ON THE MECHANICS, COMPUTATIONAL MODELING, AND DESIGN IMPLEMENTATION OF PIEZOELECTRIC ACTUATORS ON MICRO AIR VEHICLES

By

BRADLEY W. LACROIX

A DISSERTATION PRESENTED TO THE GRADUATE SCHOOL
OF THE UNIVERSITY OF FLORIDA IN PARTIAL FULFILLMENT
OF THE REQUIREMENTS FOR THE DEGREE OF
DOCTOR OF PHILOSOPHY

UNIVERSITY OF FLORIDA

2013

www.manaraa.com

UMI Number: 3584474

All rights reserved

INFORMATION TO ALL USERS
The quality of this reproduction is dependent upon the quality of the copy submitted.

In the unlikely event that the author did not send a complete manuscript
and there are missing pages, these will be noted. Also, if material had to be removed,
a note will indicate the deletion.

UMI 3584474

Published by ProQuest LLC (2014). Copyright in the Dissertation held by the Author.

Microform Edition © ProQuest LLC.
All rights reserved. This work is protected against
unauthorized copying under Title 17, United States Code

ProQuest LLC.
789 East Eisenhower Parkway
P.O. Box 1346
Ann Arbor, MI 48106 - 1346

www.manaraa.com

© 2013 Bradley W. LaCroix

www.manaraa.com

I dedicate this document to Mikayla, my partner in life, who has endured the eratic and taxing schedule that comes with completing a PhD. I also dedicate it to my parents, who have unrelentlessly encouraged and supported me through every step of my education.

www.manaraa.com

ACKNOWLEDGMENTS

Thank you to Dr. Peter Ifju for guiding me through the often large and ambiguous world of university research and keeping me focused on my end goal. In addition, thank you to my committee members, Dr. Raphael Haftka, Dr. Bhavani Sankar, and Michele Manuel for your extensive help through this process.

Thank you to Kevin Shortelle, Kyuho Lee, and Bill Graham of System Dynamics International for your endless support and patience in the numerous experiments and flight tests ran throughout the process of this research.

Thank you to Mike Sytsma for his many hours helping me at the REEF wind tunnel. Without your help, I would have been spending a lot more time at the wind tunnel and accomplishing a lot less.

Also, a big thanks to Jason Cantrell for stepping up to help whenever I needed a hand. This includes the numerous hours in the on-campus wind tunnel trying to salvage the outdated wind tunnel system.

A special thanks to Kelsey Dyal and Chris Gardiner, who have helped me immeasurably by putting in numerous hours in the design, fabrication, and testing of MAVs and test fixtures.

Finally, thank you to Anirban Chaudhuri who provided me significant advice and insight into the application of optimization to this research.

This research has been funded in part by Air Force Research Laboratories (AFRL) - Distribution A. Approved for public release, distribution unlimited. (96ABW-2013-0381)

www.manaraa.com

TABLE OF CONTENTS

www.manaraa.com

www.manaraa.com

www.manaraa.com

www.manaraa.com

LIST OF TABLES

www.manaraa.com

LIST OF FIGURES

www.manaraa.com

www.manaraa.com

www.manaraa.com

www.manaraa.com

www.manaraa.com

www.manaraa.com

www.manaraa.com

www.manaraa.com

Abstract of Dissertation Presented to the Graduate School
of the University of Florida in Partial Fulfillment of the
Requirements for the Degree of Doctor of Philosophy

ON THE MECHANICS, COMPUTATIONAL MODELING, AND DESIGN IMPLEMENTATION OF PIEZOELECTRIC ACTUATORS ON MICRO AIR VEHICLES

By

Bradley W. LaCroix

December 2013

Chair: Peter G. Ifju
Major: Mechanical Engineering

This document details the research performed on applying piezoelectric macro fiber composite actuators on micro air vehicles. The research objective was to apply the minimum number of macro fiber composites to the aircraft in an optimized manner in order to obtain complete control authority. To do this, a local-global approach was taken. Numerical predictions, experiments, and finite element models were used to model the macro fiber composites in a local manner, approximating the curvature of the actuator when bonded to a substrate. The substrate was selected to maximize the curvature when submitted to expected loads. In a global manner, the design of the aircraft was optimized, using a computational model, to provide the largest control authority under expected flight conditions. A variety of experimental tests were conducted to create an accurate aeroelastic computer model, including tests to determine material properties, static loading tests, and wind tunnel testing. Two of the optimized designs were tested in the wind tunnel to verify the predicted improvement, which confirmed the accuracy of the computer model. Other experimental results are also included, including experiments examining the unimorph fabrication technique, rigid assumptions used for the aerodynamic model, and high frequency dynamics of the macro fiber composite unimorph.

www.manaraa.com

CHAPTER 1
INTRODUCTION

1.1 Historical Background and Applications

The piezoelectric effect was first discovered in 1880 by French physicists Jacques and Pierre Curie [1]. It is derived from the Greek word meaning ”to press” and can be described as a mechanical force resulting from an electrical input or conversely, a mechanical input resulting in an electrical output. Piezoelectric devices were first implemented in the early 1920s as quartz crystal stabilized electrical oscillators and shortly thereafter incorporated into high frequency radio transmitters [2]. World War I brought great attention towards piezoelectric technology with the invention of sonar [3]. Incremental advancements have taken place due to discoveries of new piezoelectric materials such as barium titanate ($BaTiO_3$) and single crystal lithium niobate ($LiNbO_3$). These advancements have expanded the use of piezoelectrics, which have been utilized in devices ranging from phonographs to microphones to acceleration sensors to ink-jet printers.

Originally, piezoelectric actuators were limited to small displacement applications, such as precise optical positioning [4] and piezoelectric motors [5, 6], but recent advancements have allowed piezoelectric actuators to achieve new levels of strain. Macro Fiber Composites (MFCs), which are described in the next section, offer a previously unseen flexibility and actuated strain that has opened the door for several innovations and research areas. One such MFC is shown in Fig. 1-1, which measures 112 mm (4.4 inches) by 40 mm (1.6 inches) and is capable of producing 1800 $\mu\epsilon$.

Initially developed by NASA [8], MFCs have also made their way into sporting applications. In skiing, they have been implemented in skis to actively dampen vibrations [9]. In tennis, piezoelectric devices have been incorporated into the racket to orient the direction of the force while stiffening the racket for ultimate power. They also help to reduce vibrations in the racket, thereby improving comfort [10]. Piezoelectrics

www.manaraa.com

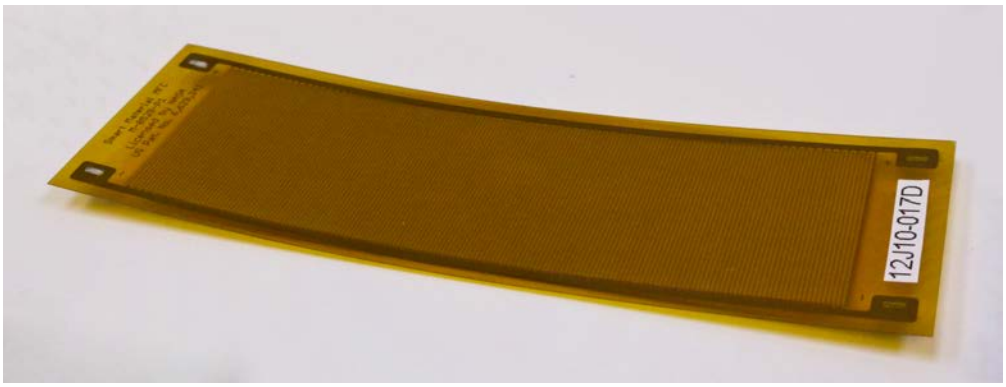

Figure 1-1. M8528-P1 MFC actuator manufactured by Smart Materials Corp. [7]. Photo taken by Bradley LaCroix.

also hold a large presence in energy harvesting, especially in remote, off-the-grid low power devices which operate for long periods of time [11]. In these applications, the piezoelectrics are able to harvest energy from vibrations or fluid oscillations.

In aerospace applications, piezoelectric actuators have been utilized in an array of aircraft. They have been used on helicopter rotors for active twist control on the order of $\pm 1^{\circ}$ without adding excessive amount of mass [12] as well as vibration dampening [13, 14]. Research has also been conducted in applying piezoelectric actuators to the vertical tail of an F/A-18, as seen in Fig. 1-2, to reduce buffet loads. In these experiments, root strains were reduced by up to 60% at high angles of attack [15, 16]. Additional tests showed that the MFCs could reduce both the bending and torsion modes of the tail fin sufficiently doubling the fatigue life [17].

MFCs have also been used in structural health monitoring of UAVs using acoustic guided waves [18, 19]. In these applications, the MFC system is able to determine delamination and damage due to debonding of joints. The research relates to health monitoring rather than actuation, and is therefore beyond the scope of the research in this document.

1.2 Macro Fiber Composites in Detail

The piezoelectric actuators studied within this project are of a specific type termed Macro Fiber Composites (MFCs). They were first developed by NASA in 1996 and

www.manaraa.com

Figure 1-2. Application of piezoelectric materials on the tail of a model F/A-18 to reduce buffeting. Photo courtesy of NASA [16].

then entered commercial production in 2002 by Smart Material Corporation [11, 20]. Piezoceramics themselves are extremely brittle and therefore cannot be easily conformed to curved surfaces. They are very susceptible to breakage during handling and bonding procedures. To resolve these issues, the piezoceramics are embedded in their fibrous phase in a composite material. These crystalline materials have a much higher strength in the fiber form, where the decrease in the volume fraction of flaws leads to an increase in specific strength. Additionally, the flexible nature of the polymer matrix allows for the material to conform to curved surfaces [20]. MFCs have an advantage over traditional piezoelectrics in that they are flexible, have improved reliability, and exhibit relatively high strain when actuated.

An expanded view of a Smart Materials Corporation MFC is shown in Fig. 1-3 (adapted from [7]). MFCs use an interdigitated electrode pattern to deliver the electric field along the entire length of the fibers. This requires solid bonding between the matrix and fibers to transfer actuation loads to the external surface of the device. In manufacturing, the fibers of the MFC are machined from low-cost piezoceramic wafers using a computer controlled dicing saw. The fibers are then placed in between two series of electrodes

www.manaraa.com

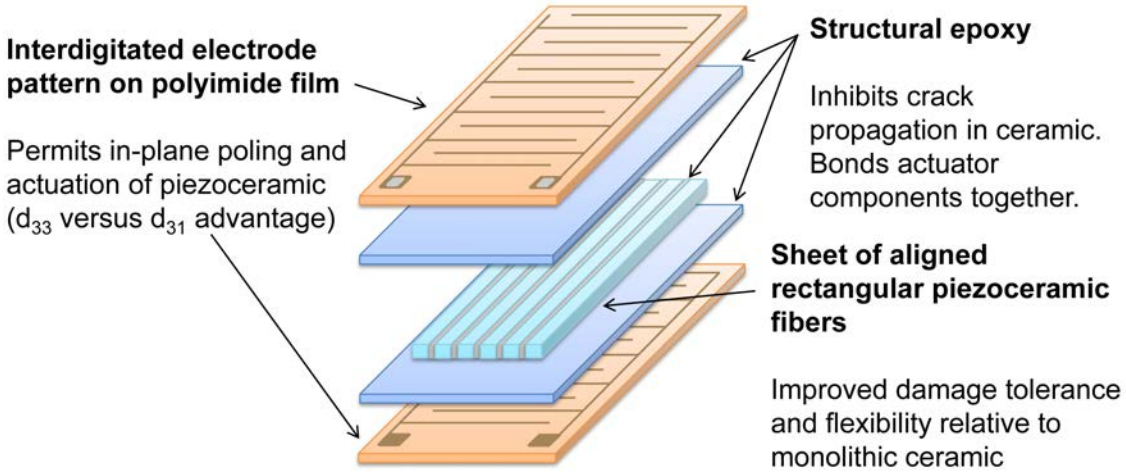

Figure 1-3. Expanded view of the material lay-up of the Smart Materials Corporation MFC (adapted from [7]).

with epoxy and vacuum pressed with heated platens. After fabrication, the piezoceramic material is poled by applying 1500 V to the interdigitated electrodes for approximately 1 minute [21].

The MFCs are available as commercial off-the-shelf components and are offered in a variety of sizes. One MFC, the M8528-P1, is quoted as being capable of a strain range of 1800 $\mu\epsilon$. The three MFCs considered thus far in this research are shown in Fig. 1-4 with the properties described in Table 1-1. The MFCs are named according to the length and width of the active area of the MFC and the actuation direction. For example, if the piezoelectric portion of the MFC is 85 mm long and 28 mm wide, it is given the designation '8528'. The 'P1' indicates that it is an elongating MFC, which utilizes the d33 effect for actuation, whereas the 'P2' and 'P3' designations are reserved for the contracting MFCs which utilize the d31 effect for actuation. There is also a twisting actuator with the fibers oriented at 45° designated by 'F1'.

Electrically, the MFCs function almost identically to capacitors. When a voltage is applied, the MFC stores the charge potential across the piezoelectric. When the voltage potential is removed, the potential remains, but it is slowly dissipated through the slightly less-than-ideal electrical insulation. All of the 'P1' type actuators accept an input voltage

www.manaraa.com

Figure 1-4. The three MFCs that were considered during the initial phase of research. From left to right: M8528-P1, M8507-P1, and M8503-P1. Photo taken by Bradley LaCroix.

Table 1-1. The three MFCs examined during the initial phase of this research.

MFC	Overall Length, mm	Overall Width, mm	Strain Range, $\mu\epsilon$	Block Force, N	Block Force per active width, N/mm
M8528-P1	112	40	1800	454	16.2
M8507-P1	101	13	1380	87	12.4
M8503-P1	110	14	1050	28	9.3

of -500 V to 1500 V which is easily connected through the exposed leads on the MFC (silver in color), as can be seen in Fig. 1-4. While this voltage is substantially higher than that supplied by traditional power systems on MAVs, it is achievable by the proper amplification hardware. Specialty systems, described in Section 5.3, allow for the high voltage to be obtained using a traditional 11.1 V LiPo battery. Furthermore, Williams notes that the MFCs can safely be actuated to 1700 V without negative effects [22],

www.manaraa.com

which could potentially increase the strain range beyond their quoted values. Additional specifications for the MFCs are provided in Appendix F.

1.3 Motivation

MAVs are ideal platforms for MFCs because of their relative size. Due to the low Reynolds numbers that MAVs fly at, airfoil thickness is no longer beneficial for flight performance. A thin undercambered airfoil is the preferred solution, reducing drag and improving stability [23, 24]. In addition, flow separation over conventional control surfaces can cause drag, whereas a smooth morphing contour can improve efficiency [25–29]. Furthermore, due to the small size of MAVs, a small actuation can produce a large response.

One potential alternative investigated early on when considering designs for MFCs on MAVs was the option to incorporate membrane material within a supporting structure. Utilizing a membrane wing, where carbon fiber laminate is replaced with a flexible membrane such as silicone or ripstop polyester can reduce the wing's flexural stiffness, thereby making morphing more easily realized. Flexible membrane MAV wings have been studied at the University of Florida for over a decade. They provide a number of performance improvements such as adaptive washout for gust rejection, flight stability, and delayed stall [30, 31]. Figure 1-5 shows an example of one of the first MAVs manufactured with MFCs and a ripstop polyester membrane wing. Chapter 8 details the various aspects of this design. Later work focused on a mainly carbon fiber wing and is covered in detail in Chapter 9. Flight tests showed that this was a more stable design and better distributed the MFC actuation across the wing for improved control authority.

Servomotors, termed servos for short, have conventionally been used in small unmanned air vehicles (UAVs). Servos are motors connected in parallel with an encoder to provide constant feedback so their position is known at any time. They provide an economical and effective way of actuating control surfaces. However, their rate of actuation is limited to approximately 1-2 Hz. MFCs are capable of actuating at more than

www.manaraa.com

Figure 1-5. One of the first MAVs manufactured with MFCs. The membrane is ripstop polyester with a DIC speckle pattern applied. MFCs are applied to the underside of the battens. Photo taken by Bradley LaCroix.

an order of magnitude faster at 25 Hz or more [29, 32]. Independent tests were also conducted with a high speed camera and the results examined in Appendix C. The short reponse time opens the possibility of active gust suppression and improved flight control.

MFCs are also solid state which provides two distinct advantages. Firstly, the MAV can be environmentally sealed, with the motor and electronics encased within the fuselage. This isolates the electronics from water and corrosion. The MFCs, placed on the exterior surfaces, are weatherproof and are not negatively affected by sand, dirt, or water which can damage gear driven servos. Secondly, the MFCs are capable of withstanding high acceleration without degradation of response, excluding inertial considerations. This opens the possibility for high acceleration maneuvers and high acceleration launches, such as ballistics.

Moreover, the profile of the MFC is extremely thin which makes the volume of the actuator negligible. Flexibility in positioning is afforded since the high voltage electronics and controls can be placed anywhere on the aircraft as opposed to a servo which necessitates a mechanical linkage to the control surface. Since the wing can be made without hinges and control rods, the part count is significantly reduced [29, 32]. Instead,

www.manaraa.com

MFCs mounted to the surface of the wing can actively morph the structure to achieve flight control. The wing structure and tail surfaces can smoothly morph into different shapes quickly and seamlessly.

By conversion of electrical energy directly to mechanical energy, MFCs eliminate complicated devices with several parts, and also offer superior energy efficiency. In an early application of piezoelectrics to UAVs, a similar MFC was measured to have a power consumption of 65 mW compared to that of a tradtional servo of 2500 mW [33]. In another research UAV, power consumption was decreased from 24 W to 100 mW and current draw was cut from 5 A to 1.4 mA [32, 34]. A majority of the power consumption is through the the loss of efficiency via the high voltage electronics rather than the MFC itself. In addition, the life cycle of an MFC is greater than 10 billion cycles [7, 11], so failure due to normal use is not a concern.

In order to optimize the overall performance of a MAV fitted with MFCs, finite element analysis (FEA) is essential. Furthermore, since the wing is relatively flexible, the FEA simulation must be iterated with fluid-structure interaction to create an aeroelastic simulation. The simulation unlocks the potential for exploring numerous design possibilities computationally rather than experimentally testing each design. A combination of MATLAB, ABAQUS (FEA), and Athena Vortex Lattice (AVL) [35] were utilized for this purpose. Furthermore, with proper validation, this model can be used to conduct a full scale optimization in which a number of variables are considered during the optimization scheme.

In the end, the work in this research was approached in a local-global manner. For instance, significant research was conducted on the local behavior of MFCs to improve the degree of actuation acheived by an independent unimorph configuration. This work examined various substrate materials and adhesion techniques. A global approach was also conducted to optimize the overall wing design to improve the control authority of the

www.manaraa.com

overall aircraft. This portion of the research examined the placement and orientation of the MFC as well as the layup of the wing structure.

The details about this research are described in the following chapters of this document. But first, a literature review is presented in the next chapter detailing previous MFC research and aircraft.

www.manaraa.com

CHAPTER 2
PRIOR APPLICATIONS OF MFCS ON UAVS

2.1 Application of MFCs on UAVs

Unmanned Air Vehicles (UAVs) have proven to be an ideal test platform for MFCs and other morphing technology due to the more manageable cost requirements, relative ease of manufacturing, and fortunate removal of concern for the safety of a human test pilot [36, 37]. As a result, a greater level of risk can be taken with UAVs. Therefore, UAVs make ideal test platforms for emerging technologies, including MFC actuators. This chapter is dedicated to the discussion of various morphing technologies and how they relate to the research in this document.

The first research discussed will be the work of Onur Bilgen, a student of Daniel J. Inman. A great deal of research on MFCs and their application to MAVs has been performed under both Daniel J. Inman and Onur Bilgen [26–28, 38–40].

In one project, a bimorph configuration was implemented in a variable camber, thin airfoil intended for a ducted fan aircraft [38]. The bimorph was a sandwich of two MFCs with a sheet of 25.4 μm stainless steel. The variable camber airfoil, shown in Fig. 2-1A, was simply supported at two points. The pin location was optimized and the setup tested at various flight conditions. The displacement was measured with aerodynamic loads for a single set of pin conditions and the results are shown in Fig. 2-1B. The trailing edge tip displacement in this case is approximately 19.5 mm for an actuation range of -1400 V to 1400 V. Hysteresis, due to the piezoelectric material, is especially noticeable at the points designated by the circles in Fig. 2-1B where the airfoil is sweeping down (red circles) and sweeping up (black circles) stopping at 0 V during each sweep.

Bilgen also made a thick airfoil section using a pair of bimorphs, in which one bimorph was the upper airfoil surface and the other bimorph was the lower airfoil surface [39]. This airfoil was also intended for use on a ducted fan MAV and again used 25.4 μm stainless steel as the substrate material. The airfoil, as well as the actuated

www.manaraa.com

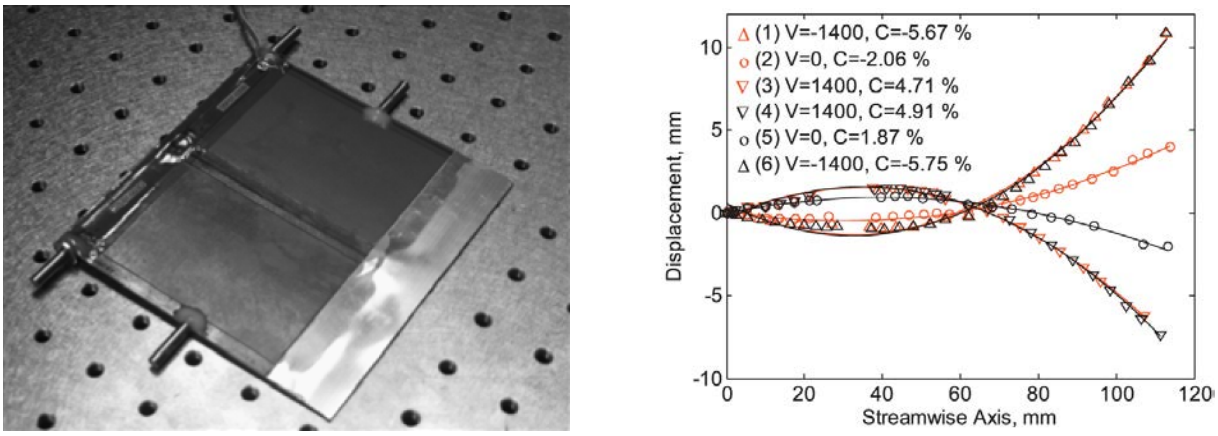

A B

Figure 2-1. Thin airfoil MFC research conducted by Bilgen [38] © IOP Publishing. Reproduced with permission. All rights reserved. A) A thin, bimorph airfoil comprised of two MFCs with a sheet of 25.4 μm stainless steel sandwiched in between. The airfoil is simply supported at two locations by the pins protruding from the edges. B) Displacement response of the airfoil when actuated from -1400 V to 1400 V and from 1400 V to -1400 V with the calculated camber for each actuation listed.

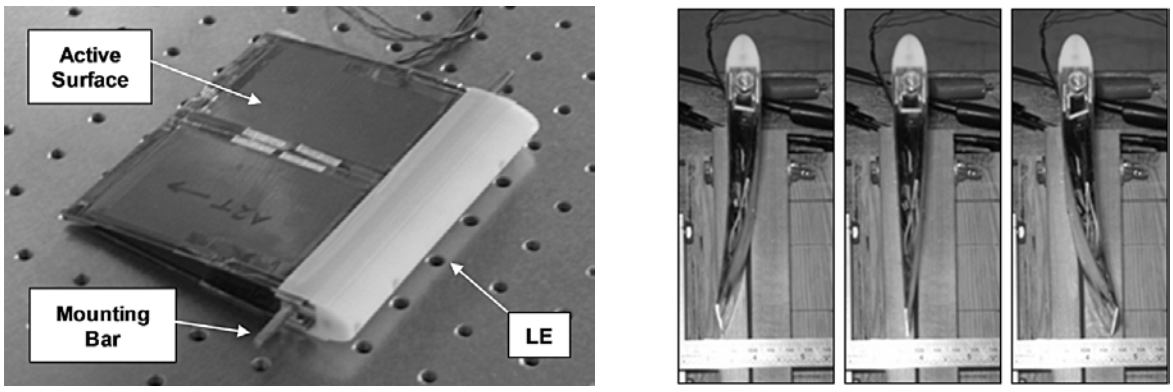

A B

Figure 2-2. Thick airfoil MFC research conducted by Bilgen. Photos courtesy of Bilgen [39]. A) Unactuated bimorph airfoil. B) Actuated bimorph airfoil to the two extreme positions as well as the unactuated position.

positions, are shown in Fig. 2-2. A total lift coefficient change of 1.54 was observed purely through the actuation of the MFCs. This is exemplified in Fig. 2-3 where the lift and drag coefficients are plotted versus MFC actuation voltage.

www.manaraa.com

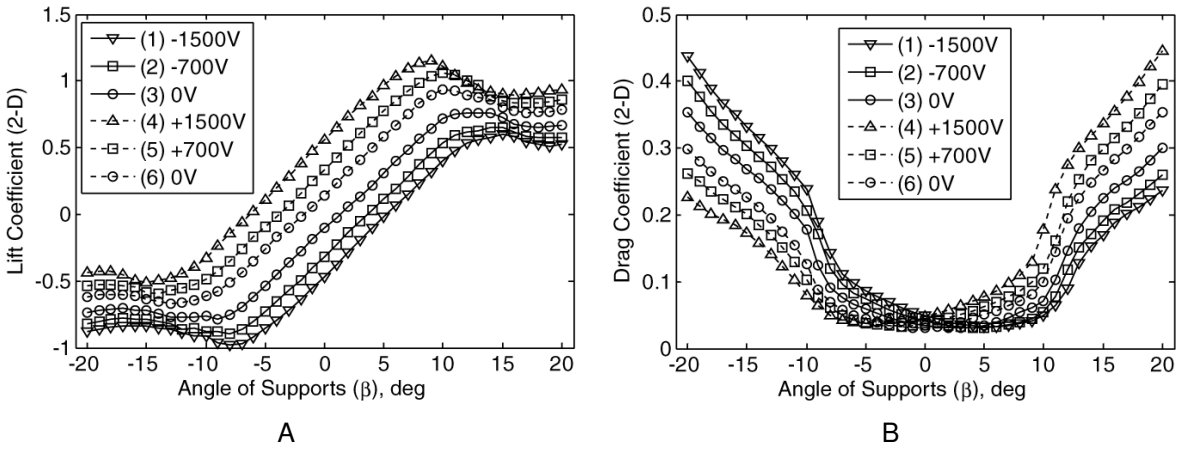

Figure 2-3. MFC actuated thick-airfoil lift and drag coefficients. Photos courtesy of Bilgen [39]. A) Lift coefficient vs angle of supports. B) Drag coefficient vs angle of supports.

Although there is no mention of trailing edge tip deflection, the effective angle of attack and camber were calculated for the actuated positions. The effective angle of attack had a range of 10.7° and the camber change was 7.59% for the peak-to-peak actuation range. Bilgen also notes that no measureable deformation occured from aerodynamic loading. Furthermore, this research showed that a significant change in lift can be achieved with a relatively small drag penalty by way of voltage actuation.

Building on this research, Bilgen built a MAV with a wingspan of approximately 2.5 feet (0.76 m), as shown in Fig. 2-4 [27, 28]. The MFCs used were M8557-P1, which are double the width of the M8528-P1 mentioned in Section 1.2. The MAV was successfully test flown for a total of approximately 15 minutes. However, the pilot noted that the aircraft's control authority was limited when using the MFCs. Although the author does not explicitly note it, it is probable that aeroelasticity and control reversal played a large role in the control authority of the aircraft. An additional pair of MFCs were added after the initial flight testing. However, wind tunnel testing showed only a small increase in control authority and in the form of mixed results due to the forward positioning of the second set of MFCs.

www.manaraa.com

A B

Figure 2-4. Micro air vehicle with MFC actuated roll control. Photos courtesy of Bilgen [39]. A) Completed MAV shown with MFCs. B) The same MAV during flight testing.

In related research, Paradies optimized the MFC and substrate section locally as well as the overall wing design [41]. In his work, he coupled the finite element solver of ANSYS©, with the computational fluid dynamics solver (CFD) of ANSYS© to iteratively calculate the deformed shape of the wing geometry and then optimize the design and placement of the MFCs. Figure 2-5 shows the final sandwich design and the location of the MFCs. The final cross-section was composed of carbon fiber composite, AIREX© foam core, and glass reinforced composite laid up using a wet lay-up method. The design was capable of 4.3 mm tip deflection which generated a roll moment of 0.17 N·m.

Work by Wickramasinghe provides yet another design, as shown in Fig. 2-6, which incorporates an Electroactive Polymer (EAP) skin along with a bimorph configuration. The bimorph is composed of an aluminum substrate, 76 μm thick, sandwiched in between two MFCs and adhered using epoxy and vacuum pressure [42]. EAPs produce increased tension when actuated. Therefore, the skin could aid in the tip displacement of the airfoil by actuating in conjunction with the bimorph. In this design, the EAP is implemented as a skin on the trailing edge of the wing in which the rib is entirely composed of the MFC bimorph. Coincidentally, the EAP actuation voltage is the same as the MFCs, 2000 V peak-to-peak. Therefore, this setup becomes more viable as a potential design option.

www.manaraa.com

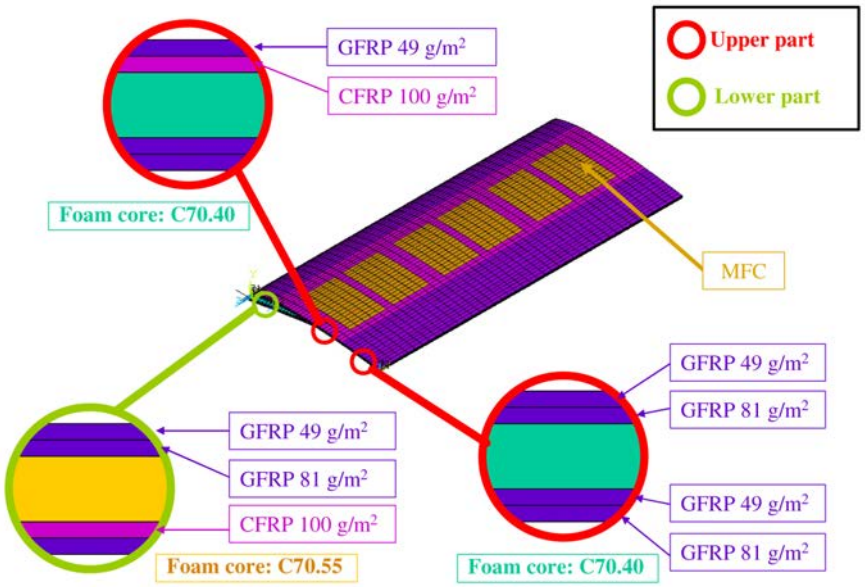

Figure 2-5. Optimized MFC wing design by Paradies [41] ©IOP Publishing. Reproduced with permission. All rights reserved.

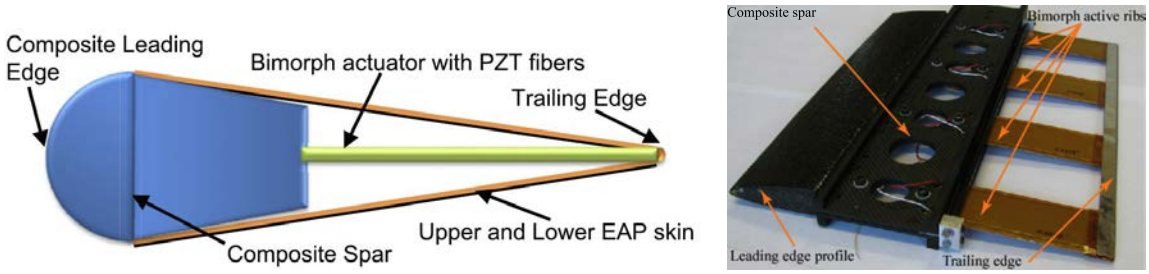

A B

Figure 2-6. EAP skin design research by Wickramasinghe [42] ©IOP Publishing. Reproduced with permission. All rights reserved. Also courtesy of the National Research Council, Canada. A) Illustration of the electroactive polymer design for increased actuation. B) Smart wing hardware model without the EAP skin.

This research showed promise in numerical models as well as preliminary experimental tests, but the skin could not be used during subsequent testing because it could not be sufficiently pre-loaded or adhered to the structure. Special care was also required to ensure that the compressive load acted exactly at the line of symmetry in order to produce equal deflection in both directions.

www.manaraa.com

Nevertheless, by utilizing latex and a 40 N pre-load, the author was able to increase the trailing edge deflection from 8.3° to 13.6°. Furthermore, the author notes that deflections of almost 30° are obtainable. However, this is with an assymmetric setup, so the resulting control actuation would be approximately ±15° for a symmetric setup. Converting this to mm displacement by estimating the acting length results in a potential tip deflection of ±2.8 cm. The author also tested the setup under aerodynamic loading and noted slight aeroelastic deflections of the trailing edge of about 1° for each case tested. Therefore, if the manufacturing method could be improved and made more reliable, this design would be very promising.

Vos and Barrett have developed a novel design for MFC actuators by incorporating them into post-buckled precompressed (PBP) bimorphs [32, 34, 43–45]. PBP bimorphs pre-stress the substrate axially in a controlled manner by heating it up during the adhesion process. Once the bimorph cools to room temperature, it is effectively pre-stressed. The PBP bimorph is then arranged in a setup where a compressive load is applied axially. The authors use primarily aluminum with a thickness of 51 μm.

With this setup, Barrett was able to achieve deflections of ±6° at rates exceeding 15 Hz. He claims that this is a 4.5 fold increase in static and dynamic deflections when compared to traditional bimorph designs. Testing of a VTOL MAV showed a 99.6% drop in power consumption, a 7-fold increase in bandwidth, 87% drop in actuator weight (excluding necessary high voltage electronics), an order of magnitude drop in part count, and a 99% cut in control surface slop [34]. Furthermore, the PBP bimorphs are designed to produce significantly higher force levels, thereby being less compliant when submitted to aerodynamic loading [43].

Flight testing for a morphing wing UAV, with components shown in Fig. 2-7, showed an increase in roll moment of 38% and 3.7 times greater control derivatives compared to conventional ailerons [32]. In this setup, bench tests showed that axial compression of the bimorph substrate increased deflection by more than a factor of 2 to

www.manaraa.com

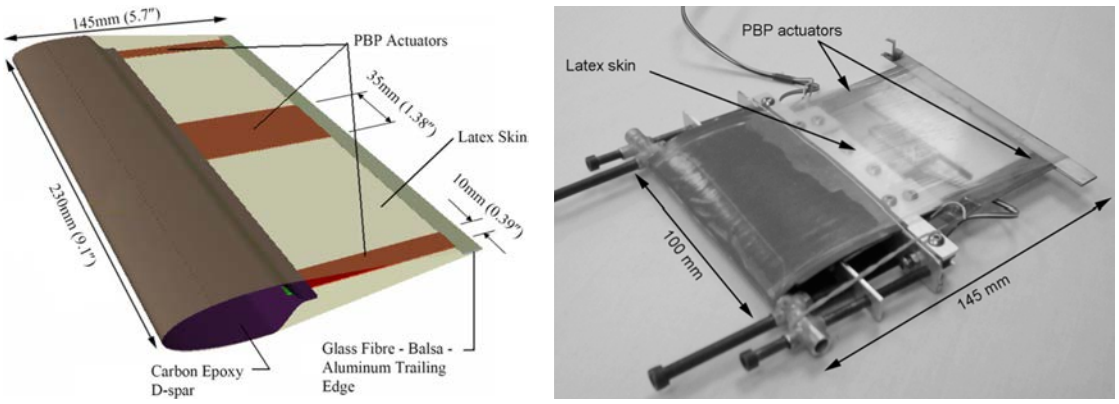

A B

Figure 2-7. Post-buckled precompressed wing geometry, designed by Vos et al. [32] ©IOP Publishing. Reproduced with permission. All rights reserved A) Illustration of wing design. B) Picture of PBP wing with latex skin.

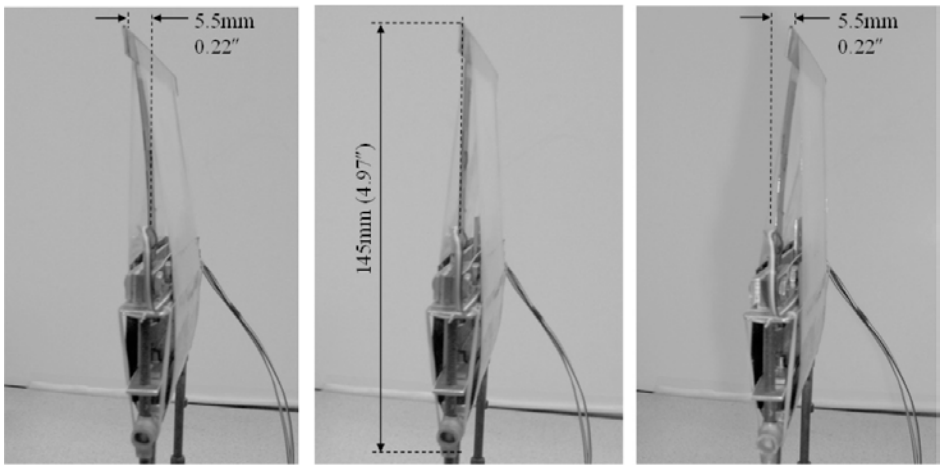

Figure 2-8. Post-buckled precompressed wing actuation. Photo courtesy of Vos et al. [32].

15.25° peak-to-peak and an actuation frequency of 34 Hz. Latex skin was used as the membrane in this prototype. The resulting wing and corresponding actuated deflection is shown in Fig. 2-8.

In Vos's most recent paper, he claimed that the PBP actuator stroke had a 300% larger actuation over a standard MFC bimorph [45]. In addition, his research studied the end rotation of the PBP as a function of axial force and external moment. Once the loading increases beyond a certain point, the PBP can no longer actuate against the

www.manaraa.com

moment and can only actuate in the other direction. Therefore, for this design, there is a tensile failure boundary that limits the curvature potential of the bimorph. As the curvature of the bimorph approaches this limit, fracture or depoling of the MFC can occur.

Ohanian also made a detailed comparison between traditional servos and MFC actuated MAVs [29]. In his research, he studied the implementation of MFCs on the Air Force Research Laboratory (AFRL) research MAV, called GENMAV. In this work, the MFCs were applied as bimorphs on the top surface of an airfoil with a passive wiper surface following the bimorph position throughout the full actuation range as seen in Fig. 2-9A. The implemented design is shown in Fig. 2-9B, where the MFC bimorphs are located on the outboard portion of the wing.

As seen by Bilgen's research, hysteresis is a reoccuring issue. Figure 2-10A shows an example of a typical response for an MFC actuated surface. By incorporating a hysteresis inversion program from a reduced-order model of the hysteretic behavior, Ohanian was able to achieve a nearly linear response as seen in Fig. 2-10B. This has significant implications regarding the incorporation of auto pilot systems.

It was also experimentally validated that smooth continuous morphing surfaces provide higher lift-to-drag ratios than traditional control surfaces, as seen in Fig. 2-11A.

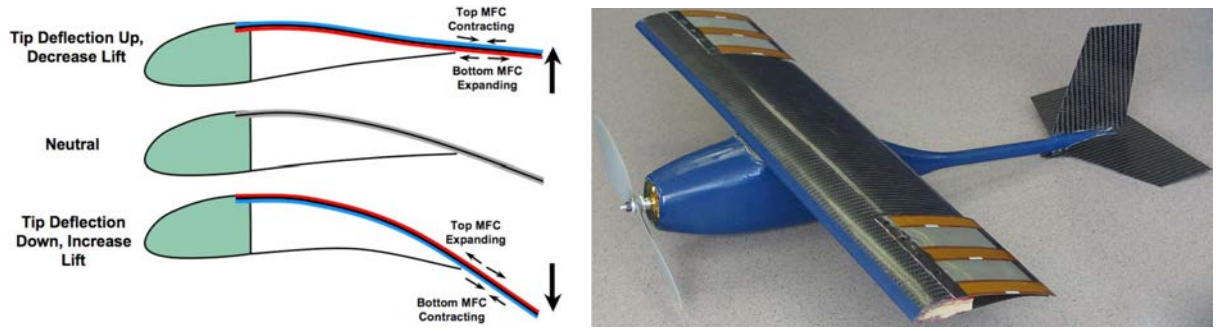

A B

Figure 2-9. MFC actuated wing design by Ohanian. Photos courtesy of Avid LLC [29] A) Illustration of concept. B) Resulting wing with bimorphs implemented.

www.manaraa.com

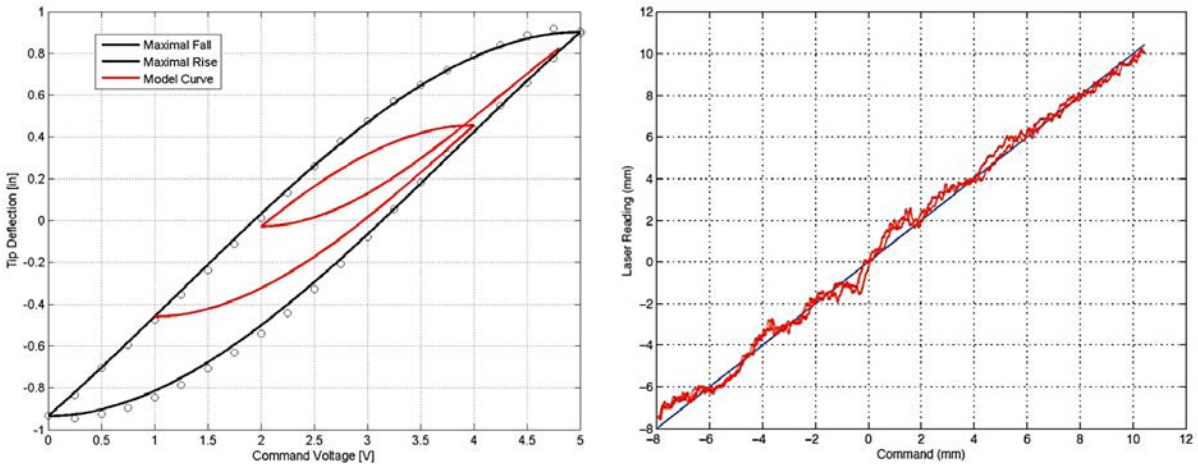

A B

Figure 2-10. MFC hysteresis measurements and linearization conducted by Ohanian. Photos courtesy of Avid LLC [29]. A) Typical response by the hysteresis-prone MFCs. B) Linearized response after implementing a hysteresis inversion from a reduced-order model of the hysteretic behavior.

In this case, the support angle is identical to the angle of attack. However, regarding error, this conclusion can only be implied, since the error bounds could potentially negate any difference between the two control methods. In a later series of tests, Ohanian observed that the morphing aircraft displayed negligible decreases in velocity while executing maneuvers, therefore demonstrating lower drag and higher efficiency [46].

Ohanian validated that the MFCs are capable of an order of magnitude greater actuation frequency than traditional servos. He also performed a detailed analysis on the part count and weight comparison between servos and MFCs. It was found that the part count was significantly reduced because the connecting rods and hinges, transmitting the load from the servo to the control surface, were unnecessary in the MFC aircraft. In addition, the weight was moderately increased, but still comparable because of the high voltage electronics.

Contrary to other research, Ohanian explored the power consumption of the entire high voltage system, rather than just the MFCs. The high voltage power board was

www.manaraa.com

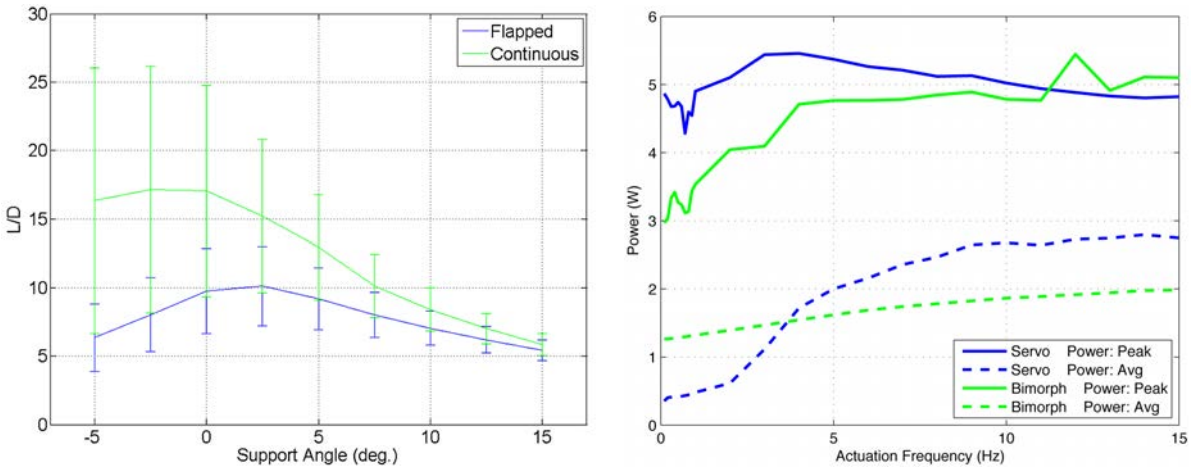

A B

Figure 2-11. Experimental lift to drag measurements and power consumption of the high voltage electronics. Photos courtesy of Avid LLC [29]. A) Lift to drag ratio of the bimorph configured wing plotted against support angle. B) Power consumption of the high voltage electronics as compared to a servo system.

designed in collaboration with AM Power Systems. The results, which show the power consumption as a function of actuation frequency, are shown in Fig. 2-11B. It can be seen that the power consumption is similar between the MFC system and the traditional servo system, even though the power consumption of the MFCs themselves are much lower than servos. Therefore, a majority of the power consumption can be attributed to the high voltage conversion.

2.2 Alternative Morphing Technologies

The previous section discussed related research regarding MFCs as manufactured by Smart Materials Corp [7]. This section introduces a few similar morphing technologies that utilize other modes of actuation to achieve morphing. The intent is to present similar morphing planforms that could have applicability in the research found within this document.

The first item of interest is an alternative macro fiber piezoelectric actuator called a lightweight piezo-composite actuator (LIPCA), which has been used in similar research [47]. The LIPCA actuator utilizes a piezoceramic found in an off-the-shelf

www.manaraa.com

component designated the Thunder 7-R©. The off-the-shelf component incorporates aluminum and stainless steel to maximize bending actuation, however, to reduce weight, the LIPCA device replaces the metal components with fiberglass and carbon fiber composites. The input voltage for this piezoceramic is much less than the Smart Material Corp's MFC, on the order of 500 V to 600 V peak-to-peak (instead of 2000 V peak-to-peak). Assuming the piezoceramic material behaves in a similar manner, this may reduce the overall strain range that can be acheived by the Thunder actuators, and therefore the overall displacement potential.

Nonetheless, this research introduces a key notion: To maximize bending actuation, the neutral axis of the cross-section must be outside of the piezoceramic material. In this research, the LIPCA-C1 actuator places the neutral axis within the piezoceramic material, which the author notes could potentially limit the overall actuator deflection. In later research, various layups were explored to attempt to adjust the position of the neutral axis as well as to maximize bending and reduce weight [48]. However, out of the different layups tested, the best deflection was only on the order of 0.7 mm.

The overall actuation was increased when two LIPCA actuators were implemented on the top and bottom of an airfoil. In this setup, they were able to produce about 1.5 cm of tip deflection [49]. While this deflection is larger than an individual LIPCA actuator, it is still relatively limited.

Shape memory alloys (SMAs) have a similar behavior to MFCs and have a higher single-stroke energy density when compared to all current adaptive materials. However, they substantially lack bandwidth, have significant hysteresis, and have high power consumption. SMA actuated systems are also significantly complex, therefore making them difficult to implement. Strelec examined the use of SMAs to morph an aircraft wing to optimize efficiency at different phases of flight [50]. However, due to the drawbacks mentioned, SMAs were not considered for this research.

www.manaraa.com

Garcia and Abdulrahim examined morphing in the form of wing twist on both a 12 inch and a 24 inch MAV [51, 52]. Their work showed that wing twist is a viable and potentially superior method for actuating roll control during flight. Their MAV was a similar size to the later models constructed for the research in this document, measuring 24 inches. Actuation was controlled by servo-driven torque rods connected to the membrane wing using kevlar string. With this setup, a roll rate of 1000° per second was achieved. Furthermore, the wing twist induced rolls experienced almost no flight path divergence, implying a nearly pure, uncoupled roll maneuver.

A couple of other twisting wing prototypes were constructed by Vos and Ricci [53–56]. In Vos's design, wing twist was imposed by utilizing an internal screw and a compliant wing structure. Preliminary wind tunnel testing showed that the lift coefficient can be increased by as much as 0.7 for angles of attack up to 12 degrees. However, this design was heavier and had a larger part count than other morphing designs. In addition, the wing must be made relatively compliant to allow for the twisting, which may be an issue at higher flow rates.

In Ricci's design, a rotating rib structure is utilized to allow for adaptability by adjusting the camber along the span. However, friction played a greater role than expected which could limit actuation performance. Overall, this mechanism contains more parts and is significantly heavier than alternative morphing structures. Regardless, it could be better for scaling up and better suited for larger aircraft.

2.3 Discussion

This chapter introduced and discussed numerous applications of piezoelectric devices in a variety of fields. Even though all of the research is not directly applicable to the research found in this document, they provide insight into possible design considerations and alternatives that may benefit the overall design. Furthermore, they demonstrate designs that did or, more importantly, did not perform well.

www.manaraa.com

The most relevant research items include the work with PBP bimorphs and LIPCAs. These two potential designs are examined using finite element modeling in Sections 6.6.2 and 6.6.3. The other research, chiefly the work by Bilgen and Ohanian, further reinforce the viability of MFCs on MAVs.

Before proceeding, it is important to note that the research reviewed in this chapter is limited in certain ways. Most of the designs only provide pitch authority or roll authority, instead of full control of the aircraft. In addition, the piezoelectric designs use multiple actuators, on the order of 6-8. This can be an economical concern since the actuators account for the largest portion of the material costs. The research in this document aims to provide complete control authority with only two actuators, therefore reducing the complexity of the necessary electronics and reducing costs. The local design, implementation, and global aircraft optimization are the primary subject of this research.

www.manaraa.com

CHAPTER 3
PRELIMINARY ANALYSIS

3.1 Overview

At the initiation of the project, it was decided to proceed in two directions. The first, was a local approach which was intended to determine the best way to mount the MFCs, and what substrate material to mount the MFCs to, in order to generate the largest deflection. It was expected that various materials and substrate thicknesses would generate varying amounts of deflection when actuated. The other plan of attack, was a global approach to determine the best MAV design to implement the MFCs on to achieve sufficient control authority for controlled flight. Preliminary results showed that MFC actuated surfaces generated a relatively small amount of deflection when compared to traditional servos. This mean that the positioning of the MFC on the planform and the design of the planform is of great importance. Before running any experiments or creating extensive computer models, a preliminary set of numerical calculations were conducted. These calculations, as part of the local approach, were used to determine the effect of the substrate material and thickness on the resulting curvature.

The MFC itself produces very little curvature when it is not bonded to a substrate. This is because the MFC is principally a linear strain actuator, but due to the slightly asymmetric layup, a small degree of curvature still results when actuated. In contrast, a majority of the curvature in a unimorph configuration is produced by bonding the MFC to a substrate, as shown in Fig. 3-1. Curvature results when two different materials are bonded together and strain of varying degrees is induced in the materials. This strain can be induced passively through temperature changes or actively, through the application of voltage in a MFC composed of piezoelectric material.

When the piezoelectric within the MFC is actuated, a linear strain results and the MFC lengthens or shortens by a small degree. When the MFC is bonded to a substrate,

www.manaraa.com

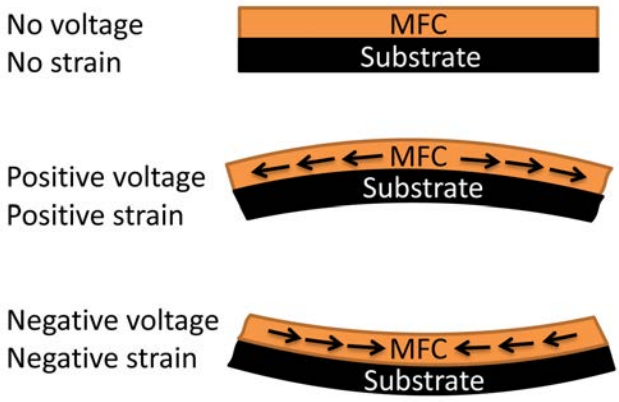

Figure 3-1. Illustration of bending in a unimorph. Out-of-plane bending is created by bonding an MFC to a substrate material.

it forms a unimorph, and the substrate resists the strain of the MFC thereby creating curvature. With no external loads applied to the unimorph composite, the curvature is relatively precise and predictable.

This chapter presents the preliminary calculations for the predicted curvature based on various substrate materials, such as carbon fiber composite, steel, and aluminum. Two approaches are addressed, Bimetallic Beam Numerical Approximation and Classical Laminate Plate Theory. Techniques for bonding the MFC to the substrate are discussed in Section 6.1.

3.2 Bimetallic Beam Numerical Approximation

The first equation used to study the impact of the substrate material on the unimorph curvature was the Bimetallic Beam Equation [57], shown in Eq. (3–1). This equation is intended to be used for two metallic materials with differing coefficients of thermal expansion and differing mechanical properties. Furthermore, this equation assumes that both materials are isotropic. This is not necessarily true with the MFC unimorph, but as we will see with Classical Laminate Plate Theory in Section 3.3, it stil provides reasonable results. The properties are designated with the following notation: α - coefficient of thermal expansion, E - Elastic Modulus, h - section thickness, and ΔT - the change in temperature from the initial temperature.

www.manaraa.com

$$\kappa = \frac{6E_1E_2(h_1+h_2)h_1h_2(\alpha_1-\alpha_2)\Delta T}{E_1^2h_1^4+E_2^2h_2^4+4E_1E_2h_1^3h_2+4E_1E_2h_2^3h_1+6E_1E_2h_1^2h_2^2} \tag{3–1}$$

This equation requires only relatively minor modificiations to achieve a formulation applicable to MFCs. Since the MFC is the only material exhibiting strain, the thermal expansion portion of the equation, $(\alpha_1 - \alpha_2)\Delta T$ can be replaced with the longitudinal strain of the MFC, ϵ_{MFC}. Next, the numerical subscripts, 1 and 2, are replaced with the material designations, *MFC* and *sub*, where *MFC* designates the macro fiber composite and *sub* designates the substrate. The resulting equation is shown below.

$$\kappa = \frac{6E_{sub}E_{MFC}(h_{sub}+h_{MFC})h_{sub}h_{MFC}\epsilon_{MFC}}{E_{sub}^2h_{sub}^4+E_{MFC}^2h_{MFC}^4+4E_{sub}E_{MFC}h_{sub}^3h_{MFC}+4E_{sub}E_{MFC}h_{MFC}^3h_{sub}+6E_{sub}E_{MFC}h_{sub}^2h_{MFC}^2} \tag{3–2}$$

This equation can be rearranged further by dividing both the numerator and denominator by $E_{sub} \cdot E_{MFC}$ and $h_{sub}^2 \cdot h_{MFC}^2$. This results in Eq. (3–3), which provides further insight into the curvature of the unimorph as a function of the substrate materials and the ratio of their properties with respect to the MFC. Since the goal is to maximize curvature, the numerator must be maximized while minimizing the denominator. Because the MFC properties are determined by the manufacturer, the numerator can only be increased by decreasing h_{sub}. The denominator can be decreased by making the ratio of material properties, $\frac{E_{sub}}{E_{MFC}}\frac{h_{sub}^2}{h_{MFC}^2}$ and $\frac{h_{sub}}{h_{MFC}}$, as close to 1 as possible. In other words, increasing the substrate modulus while decreasing the substrate thickness by a power of 2 as well as keeping h_{sub} and h_{MFC} similar in magnitude.

$$\kappa = \frac{6\left(\frac{1}{h_{sub}}+\frac{1}{h_{MFC}}\right)\epsilon_{MFC}}{\frac{E_{sub}}{E_{MFC}}\frac{h_{sub}^2}{h_{MFC}^2}+\frac{1}{\frac{E_{sub}}{E_{MFC}}\frac{h_{sub}^2}{h_{MFC}^2}}+4\left(\frac{h_{sub}}{h_{MFC}}+\frac{1}{\frac{h_{sub}}{h_{MFC}}}\right)+6} \tag{3–3}$$

At this point, the material properties for the MFC can be substituted into the expression. The properties for the Smart Materials Corporation MFCs are $E = 30.3$ GPa

www.manaraa.com

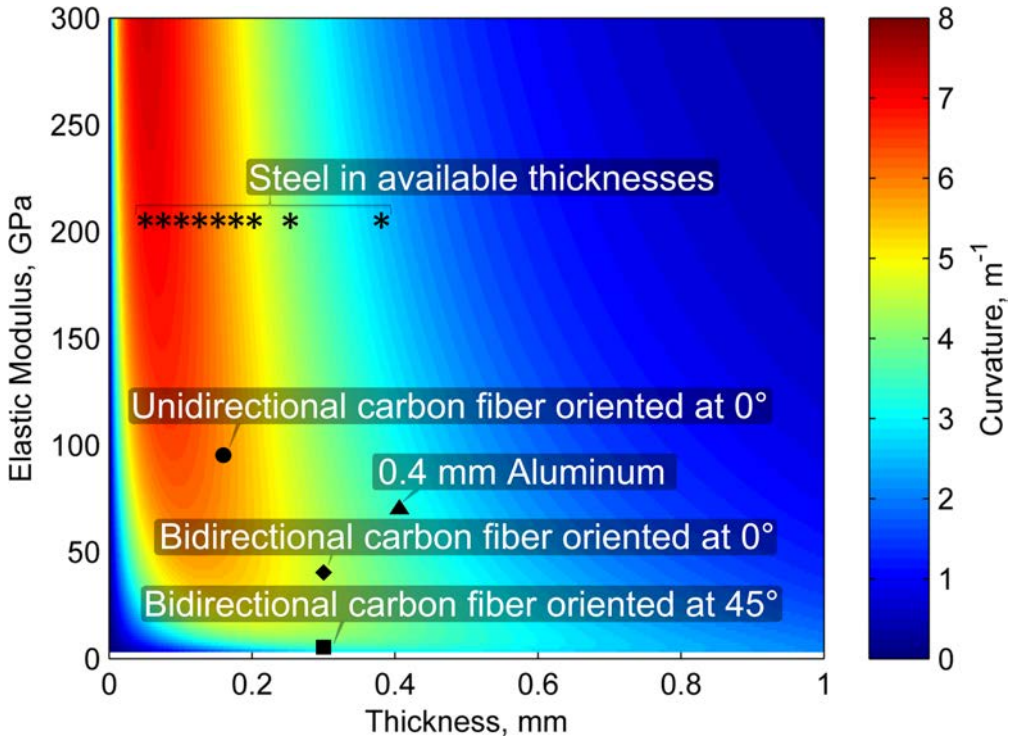

Figure 3-2. Curvature as predicted by Bimetallic Beam Theory.

and $h = 0.3$ mm. The quoted strain range for the M8528-P1 MFC is 1800 $\mu\epsilon$. With these values incorporated, there are only two variables remaining: E_{sub} and h_{sub}. MATLAB was utilized to run through a range of material properties for these two variables. The resulting plot is shown in Fig. 3-2. This figure shows that as the elastic modulus increases and the thickness decreases, the curvature increases. As the thickness approaches zero, the material is unable to resist the stress induced by the strain, which drastically reduces the resulting curvature. Various materials are superimposed on the plot to demonstrate the effects of different material substrates. It must be noted that carbon fiber pre-preg was the only material originally considered, due to its ease of use in MAV construction and availability. Later, steel and aluminum were also incorporated into the analysis.

3.3 Classical Laminate Plate Theory (CLPT)

An alternative, and possibly more accurate, method for calculating curvature can be performed by using Classical Laminate Plate Theory (CLPT) [58]. This method has been

www.manaraa.com

used to model MFC surfaces in other piezoelectric research as well [26, 44, 48, 59]. Furthermore, CLPT allows the materials to be modeled orthotropically, rather than isotropically. Since MFCs are linear strain actuators, they exhibit the same mechanical effects as orthotropic materials undergoing thermal expansion. The curvature, κ, can be predicted using CLPT with applied thermal stresses. In CLPT, the governing equation for thermal stresses in a laminate is:

$$\begin{Bmatrix} N \\ M \end{Bmatrix}_{6x1} = \begin{bmatrix} A & B \\ B & D \end{bmatrix}_{6x6} \begin{Bmatrix} \epsilon_0 \\ \kappa \end{Bmatrix}_{6x1} - \begin{Bmatrix} N_T \\ M_T \end{Bmatrix}_{6x1} \tag{3–4}$$

Where N and M are the external loads and moments, respectively. A represents the extensional stiffness, B represents the coupling matrix, and D represents the bending stiffnesses of the laminate. ϵ_0 and κ are the mid-plane strains and curvatures, respectively. N_T and M_T are the loads and moments created by the thermal stresses. Since there are no external loads ($N = M = 0$), Eq. 3–4 can be rearranged as follows:

$$\begin{Bmatrix} \epsilon_0 \\ \kappa \end{Bmatrix}_{6x1} = \begin{bmatrix} A & B \\ B & D \end{bmatrix}^{-1}_{6x6} \begin{Bmatrix} N_T \\ M_T \end{Bmatrix}_{6x1} \tag{3–5}$$

For laminates with discrete layers, the stiffness matrices can be calculated as follow:

$$[A] = \sum_{k=1}^{n} \left[\bar{Q}\right]_k \cdot h_k \tag{3–6}$$

$$[B] = \sum_{k=1}^{n} \left[\bar{Q}\right]_k \cdot h_k \cdot \bar{z}_k \tag{3–7}$$

$$[D] = \sum_{k=1}^{n} \left(\frac{h_k^3}{12} + h_k \bar{z}_k^2\right) \left[\bar{Q}\right]_k \tag{3–8}$$

Where $\left[\bar{Q}\right] = T_\epsilon^T Q T_\epsilon$, h is the layer thickness, and $\bar{z}$ is the distance of the midplane of each layer from the midplane of the laminate. Q is the inversion of the compliance

www.manaraa.com

matrix, usually denoted by S, and is given by the expression:

$$Q = [S]^{-1} = \begin{bmatrix} \frac{E_1}{1-\nu_{12}\nu_{21}} & \frac{\nu_{12}E_2}{1-\nu_{12}\nu_{21}} & 0 \\ \frac{\nu_{12}E_2}{1-\nu_{12}\nu_{21}} & \frac{E_2}{1-\nu_{12}\nu_{21}} & 0 \\ 0 & 0 & G_{12} \end{bmatrix} \tag{3–9}$$

The strain transformation matrix, denoted by T_ϵ, is simply an identity matrix since the two materials are in the same coordinate system. Therefore, $\left[\bar{Q}\right] = [Q]$. The thermal loads and moments, N_T and M_T, can be calculated by:

$$N_T = \sum_{k=1}^{n} \left[\bar{Q}\right]_k \{\alpha\}_k \Delta T_k h_k \tag{3–10}$$

$$M_T = \sum_{k=1}^{n} \left[\bar{Q}\right]_k \{\alpha\}_k \Delta T_k h_k \bar{z}_k \tag{3–11}$$

The thermal expansion coefficent, α, and change in temperature, ΔT, can be combined to represent the strain exhibited in the MFC. Since the MFC is a commercially available, off-the-shelf component, the properties cannot be changed. Therefore, plugging in the MFC material properties ($E_{1,MFC} = 30.3$ GPa, $E_{2,MFC} = 15.86$ GPa, $G_{MFC} = 5.5$ GPa, $\nu_{12} = 0.31$, $\nu_{21} = 0.16$, and $h_{MFC} = 0.3$ mm) as well as the maximum change in strain from 0 V (1350 $\mu\epsilon$ corresponds to the maximum voltage of 1500 V), the curvature can be plotted against the substrate material properties for a range of stiffness and thickness. Note, it was later experimentally determined that the strain range of the MFC was greater than 1800 $\mu\epsilon$ but this only affected the magnitude of the plot, not the contours.

The shear modulus, G_{12}, for the substrate was approximated as 5 GPa and Poisson's ratio, ν_{12}, is taken to be 0.3. Testing various values of substrate shear modulus, it was determined to have negligible effect on the shape of the plot. Figure 3-3 shows the curvature plotted against the substrate material elastic modulus and thickness. It should be noted that κ_{3x1} is actually three terms, κ_x, κ_y, and κ_{xy}. The

www.manaraa.com

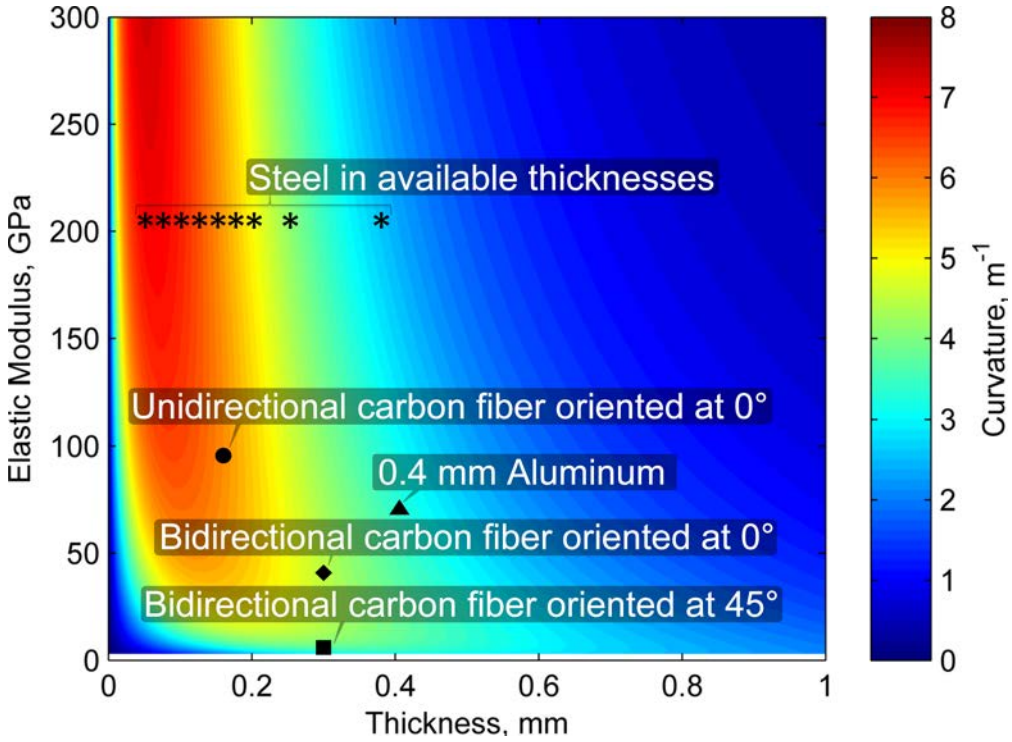

Figure 3-3. Curvature as predicted by Classical Laminate Plate Theory (CLPT).

curvature plotted is the curvature in the length direction which is obtained by the first κ_{3x1} term, κ_x.

3.4 Discussion and Further Comparison

Figure 3-3 matches the one shown in Fig. 3-2 well in terms of shape and only varies slightly in magnitude. This reinforces the two sets of independent calculations since they both provide a similar result. To illustrate the difference between the two numerical models, the percent difference, with CLPT taken as the reference, is shown in Fig. 3-4. For most of the region, the percent difference is between $\pm$1%, indicating very good agreement.

The results found in this chapter are reinforced by the work of Bilgen. Bilgen, using Rayleigh-Ritz predictions, predicted similar behavior with variations in substrates and reinforced his predictions with experimental results [26]. Chapters 6 and 7 further investigate these predictions by performing experiments and finite element analysis.

www.manaraa.com

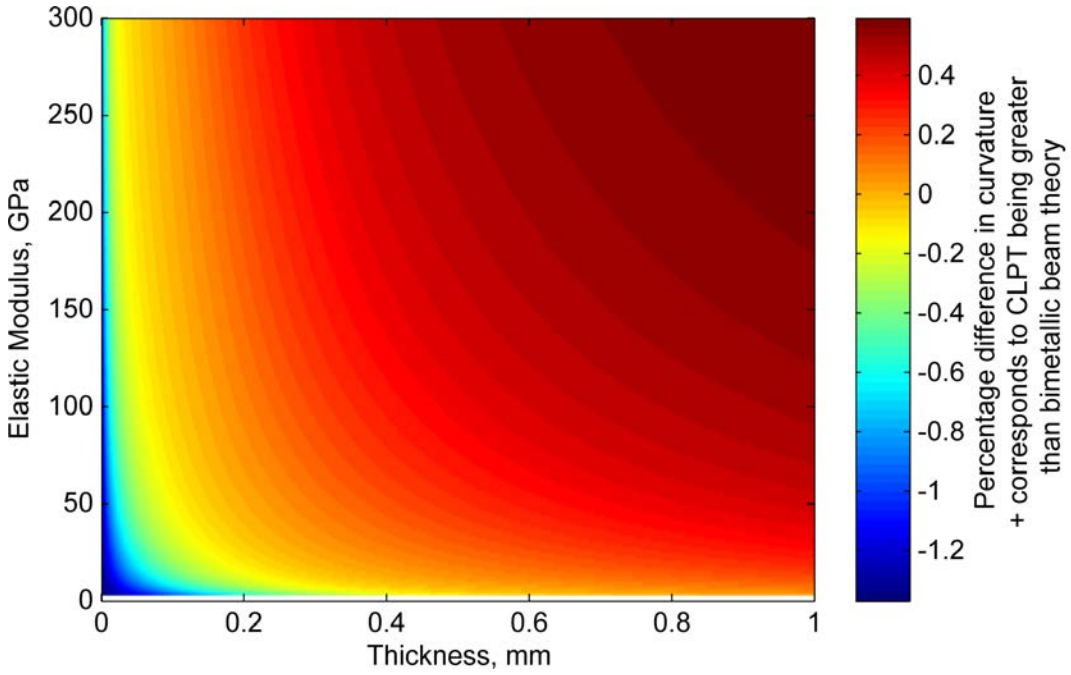

Figure 3-4. Percent difference between CLPT and Bimetallic Beam Theory.

As mentioned in Section 3.2, steel was not initially considered, since carbon fiber was readily available and easy to integrate with the current MAV manufacturing process. However, it was later included in testing and shortly thereafter incorporated into MAV designs. The plots shown in this section illustrate the predicted curvature when no loading is applied. The curvature of the unimorphs when submitted to loading will be investigated in detail in Chapters 6 and 7.

www.manaraa.com

CHAPTER 4
COMPOSITE MATERIALS TESTING

Before proceeding further, it was necessary to characterize the different materials used in MAVs. Carbon fiber composites are the primary material used for the structure of the aircraft. This research examines two particular kinds, unidirectional (in which all the fibers are oriented in one direction) and 5.7 oz bidirectional plain weave (in which the strands of fibers are perpendicular to one another and woven into a cloth). The bidirectional fabric will hereafter be referred to as simply “bidirectional.” These two composites are shown in Fig. 4-1.

The unidirectional carbon fiber provides superior strength characteristics in the longitudinal direction. However, its transverse strength and modulus are extremely low since these properties rely on the relatively weak epoxy matrix. In comparison, the bidirectional exemplifies the same strength and moduli characteristics in both the 0° direction and in the 90° direction. However, the 45° direction exhibits significantly reduced material properties, on the same order of magnitude as the epoxy matrix alone.

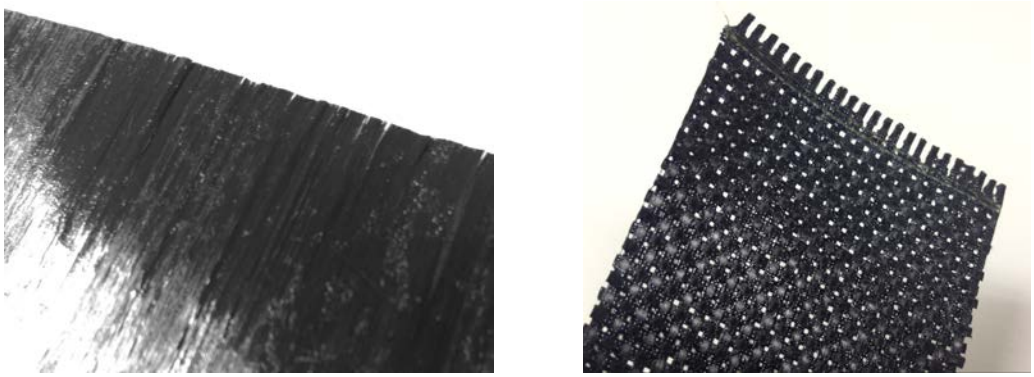

A B

Figure 4-1. The two types of carbon fiber used in the MAV manufacturing process. A) Unidirectional carbon fiber pre-preg. B) Bidirectional carbon fiber plain weave pre-preg. Photos taken by Bradley LaCroix.

The composite testing for this research was conducted in an effort to accurately model the composite materials in the finite element analysis. Two sets of tests were conducted, a series of tensile tests and a series of bending tests. For both test sets,

www.manaraa.com

a variety of fiber orientations were tested to better understand the material properties so that they could be modeled accurately in the finite elment model. These tests are described in the following sections.

4.1 Tensile Tests

In this series of tests, a variety of unidirectional samples and bidirectional samples were tested, as shown in Fig. 4-2. Three types of unidirectional were tested. Two or more of each type were created to increase the result confidence. Two 0-90 samples of bidirectional (one half of the fibers oriented with respect to the loading direction and the other half oriented perpendicular to the load) and three $\pm$ 45 bidirectional samples (fibers oriented $\pm$ 45° with respect to loading direction) were also fabricated and tested. The test samples were fabricated with additional layers at the grip locations for reinforcement. Steel samples of two thicknesses were also tested to provide a baseline comparison.

4.1.1 Setup

The tension test setup was composed of a Test Resources 315R150 tension machine, equipped with a 50,000 lb load cell. Test Resources's R-Controller software was used to control the machine and to measure the loads. The tensile tests were used in combination with Digital Image Correlation to measure strains throughout each test. Digital Image Correlation (DIC) is a method for measuring full-field displacements of a surface using a camera system and an applied speckle pattern. The basics of DIC are explained in Appendix A. For this series of experiments, the load was recorded in increments and manually synchronized with the DIC images. Therefore, the load for each image was recorded during the test allowing for the calculated strain to be measured against the load. The tensile setup is shown in Fig. 4-3.

4.1.2 Results

The displacement and load data for a couple samples obtained from the Test Resources equipment are shown in Fig. 4-4. However, this displacement data is a rough

www.manaraa.com

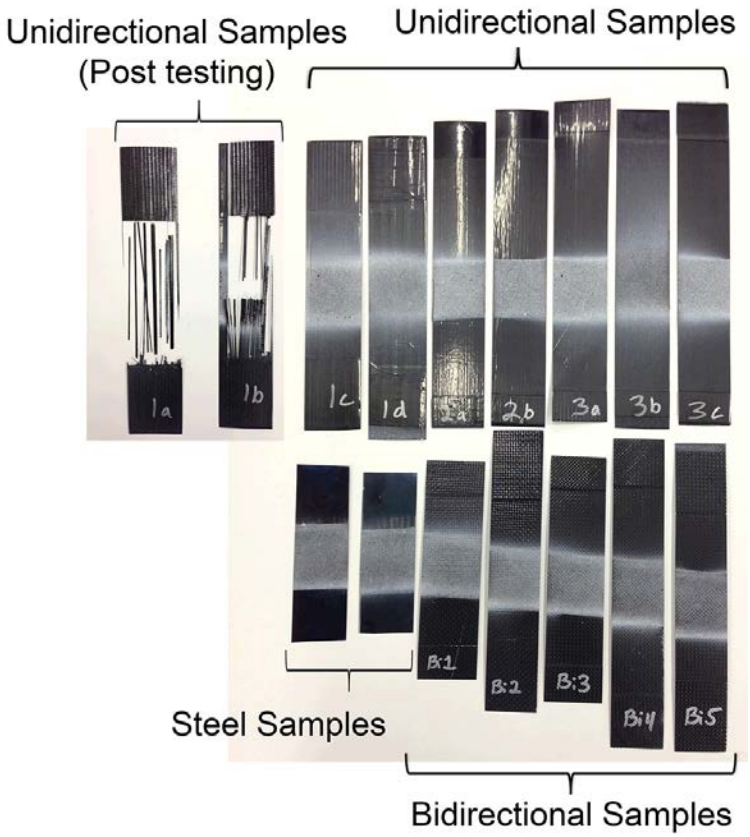

Figure 4-2. The tension test samples used to determine the elastic modulus of the available composite materials. Photo taken by Bradley LaCroix.

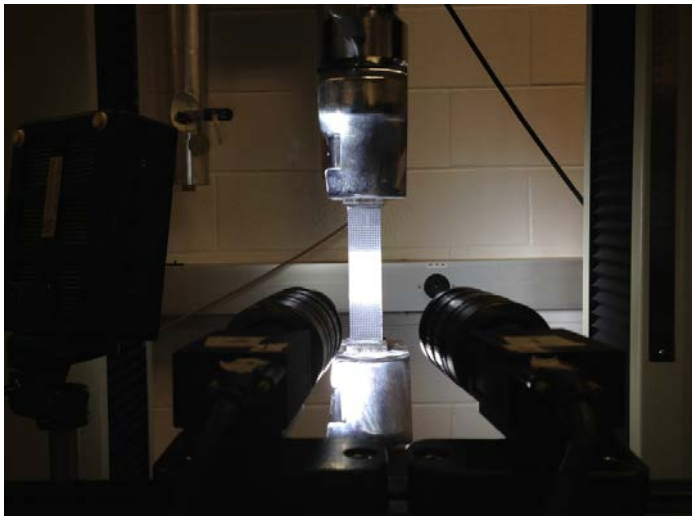

Figure 4-3. The tension test setup with the DIC cameras shown. Photo taken by Bradley LaCroix.

www.manaraa.com

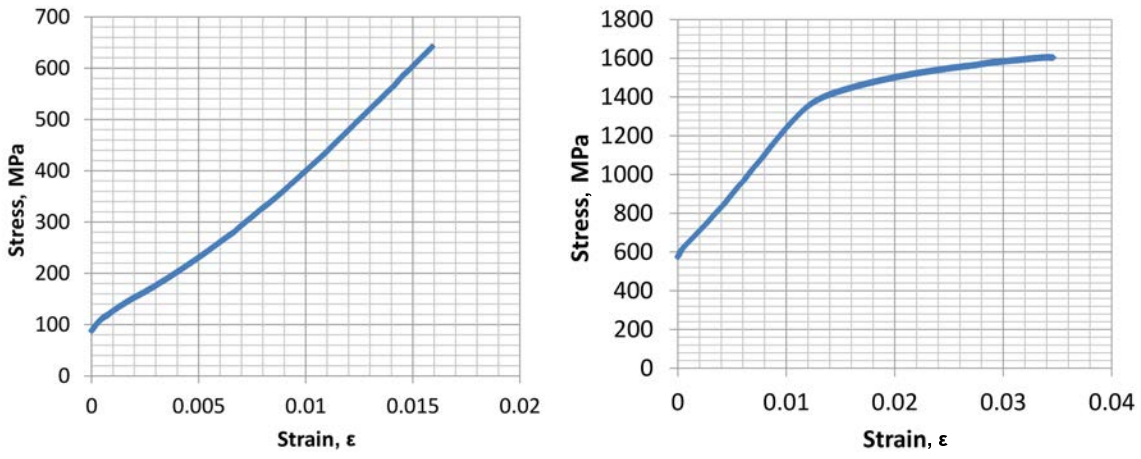

Figure 4-4. Stress-strain curves created using the displacement and loads data from the Test Resources machine. A) Stress-strain curve for the unidirectional carbon fiber specimen, sample 2b. B) Stress-strain curve for 0.004" steel.

measurement and is inaccurate due to grip slippage. Therefore, DIC data is used to calculate the strain optically, as described next. Nonetheless, these plots give a general indication of the material behavior under loading.

The positions and displacements acquired by the DIC system were converted to strains using Green's Equations, as described in Appendix B. An example of the computed strains for Sample 2b, using this method, are shown in Fig. 4-5A. The calculated strain can then be used in combination with the applied load to generate a stress-strain curve which can be used to calculate the elastic modulus, as shown in Fig. 4-5B.

The resulting elastic moduli are summarized in Table 4-1. The steel samples, used to provide a baseline, provided an elastic modulus on a similar order of magnitude as textbook values for steel, which is typically quoted as having a modulus around 200 GPa. The experimental results were slightly less, indicating that the experimental results may be, on average, less than the true values. Regarding the carbon test samples, the results show that the composite materials have a relatively low elastic modulus compared to textbook values, but are still on the same order of magnitude.

www.manaraa.com

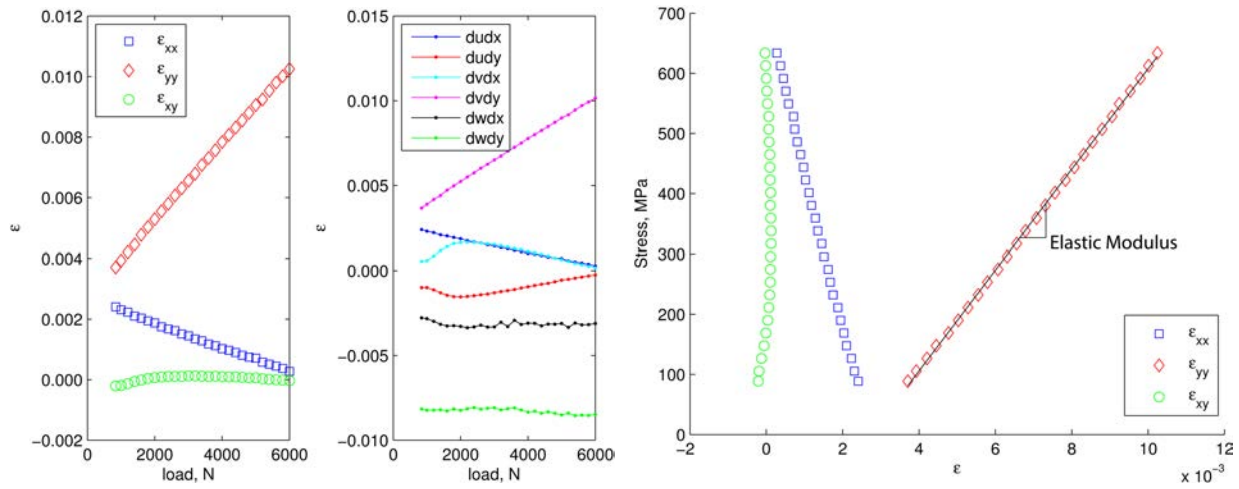

Figure 4-5. Resulting strain for the Sample 2b tensile test. A) Computed Green's strain and corresponding strain components. B) Stress-strain plot used to calculate elastic modulus using ϵ_{yy}.

Unidirectional carbon fiber with an epoxy matrix normally has an elastic modulus closer to 110 GPa, which indicates that the carbon fiber used in our lab is slightly more compliant than average.

While these results provide a significant amount of insight into the material properties of the composites used in the lab and can be a first step towards a finite element model, they don't provide an entire picture. The bending properties of composites can deviate grossly from the in-plane properties. This topic is examined in the following section.

4.2 Cantilever Tests

The properties determined in the previous section are very well suited for in-plane analysis of carbon fiber composites. However, out-of-plane bending stiffnesses for woven composites with one or two plies can vary by as much as 400% [60]. The reason for this becomes apparent when looking at the woven composite on a magnified scale, as shown in Fig. 4-6A. In the 0-90 direction, half of the fibers are in transverse direction and only half of the fibers are in the longitudinal direction and are contributing

www.manaraa.com

Table 4-1. Summary of tension test samples and their respective elastic moduli.

Sample	thickness, mm	width, mm	cross-sectional, area mm^2	calculated moduli, GPa
0.004” steel (0.1016 mm)	0.10	39.3	3.9	194.4
0.008” steel (0.2031 mm)	0.20	40.1	8.0	190.8
Bi 1 (0-90)	0.32	43.1	13.8	35.6
Bi 2 (0-90)	0.32	37.2	11.9	37.0
Bi 3 (+/-45)	0.31	41.3	12.6	5.1
Bi 4 (+/-45)	0.30	37.6	11.3	3.7
Bi 5 (+/-45)	0.31	36.8	11.4	4.9
Uni 1a	0.21	42.3	8.7	94.0
Uni 1c	0.20	41.3	8.4	92.1
Uni 1d	0.22	43.4	9.5	83.7
Uni 2a	0.19	55.2	10.2	73.0
Uni 2b	0.18	52.6	9.5	83.6
Uni 3b	0.19	45.0	8.3	92.5
Uni 3c	0.18	44.2	8.0	93.2

Figure 4-6. A closer look at woven carbon fiber. A) Magnified illustration of single-ply woven carbon fiber. B) Bending approximation of single-ply carbon fiber.

towards the bending stiffness. This effect is demonstrated, in an exaggerated manner, in Fig. 4-6B. Furthermore, the fibers are not distributed homogeneously across the thickness of the laminate and epoxy fills in a majority of the remaining space.

In addition, since the loads on the wing will be applied mainly in an out-of-plane direction, it is important to accurately model the bending stiffnesses of the various composites in various orientations. The following set of tests examined the out-of-plane bending properties of the composites used in our lab by using a cantilever setup.

www.manaraa.com

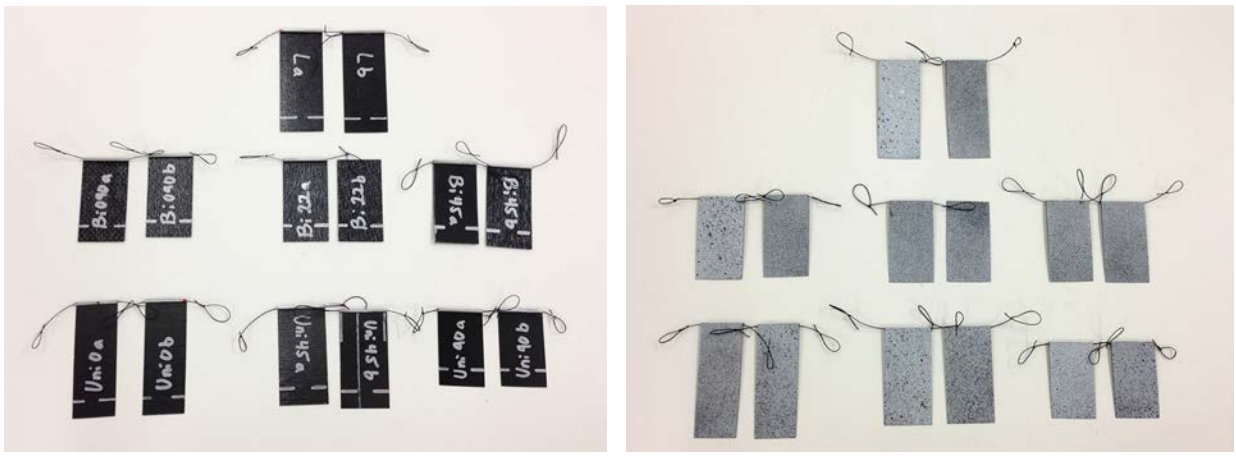

A B

Figure 4-7. Test samples used for the cantilever bending tests. A) Bottom view. B) Top view (DIC speckle pattern applied). Photos taken by Bradley LaCroix.

4.2.1 Experiments

Several test samples, shown in Fig. 4-7 were created for this set of experiments. Three pairs of unidirectional samples and three pairs of bidirectional samples were made. A third set of samples were also created. These samples were modeled after the leading edge portion of the forward swept wing prototype, which will be discussed in Chapter 9. Each of these leading edge laminates have the following layup: [Uni 49°, Bi 27°, Uni 49°]. This layup is intended to create bend-twist coupling in which bending of the sample induces twisting, or alternatively, twisting induces bending. This is described in detail in Chapter 9.

A 0°, 45°, and 90° unidirectional pair of samples were made. Each of the unidirectional samples were composed of two plys to prevent the samples from breaking during testing, since single ply unidirectional carbon fiber splits easily along the fiber direction. In addition, a 0-90, 22°, and 45° pair of bidirectional samples were made. Each of the bidirectional samples was composed of only one layer.

The samples were tested in a cantilever configuration in which one side of the sample was clamped in a vice and loads were applied to the free tip. An aluminum tube was adhered to the edge of the sample and the distance to the cantilever carefully

www.manaraa.com

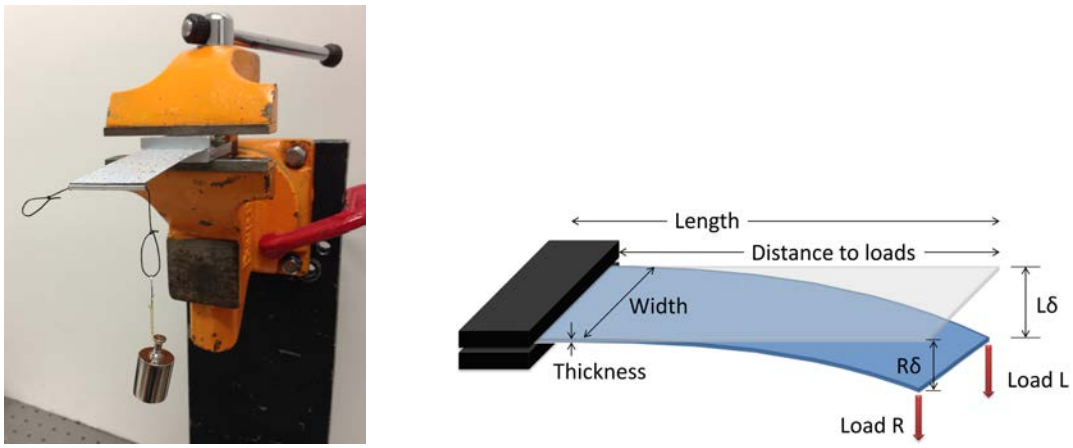

A B

Figure 4-8. Cantilever bending test setup. A) Uni 45° sample with 10 g load applied. Photo taken by Bradley LaCroix. B) Illustration of the cantilever setup.

measured. A string was passed through the tube and loops tied on each side. To apply loads, masses were attached to the string. The tube and string setup enabled quick, repeatable, and accurate load application without producing a large localized deformation. The setup with a unidirectional sample is shown in Fig. 4-8A. This loading condition demonstrates the interesting properties of a bend-twist laminate, in which the fibers are oriented at 45°. The load is applied on only one side, but due to the layup of the sample, the twist is nearly negligible and only bending occurs.

All of the samples were tested with two sets of masses. The more compliant samples were tested with 5 and 10 gram masses. The stiffer samples were tested with 10 and 20 gram masses. Prior to beginning each test, a reference image of the sample was taken with the DIC system. The displacement for each applied load could then be measured using the DIC system. Masses, in grams, were applied in the following combinations, where L designates the left side and R designates the right side: R00 L05, R05 L00, R05 L05, R00 L10, R10 L00, R10 L10. The same pairing pattern was executed for the 10 and 20 gram masses. Ultimately, the DIC results were used to quantify the displacement of each corner of the sample, as shown in Fig. 4-8B. The dimensions for each sample are summarized in Table 4-2.

www.manaraa.com

Table 4-2. Dimensions for the bending samples.

Sample	Length, mm	Width, mm	Thickness, mm	Distance to load, mm
Uni 0a	75.8	28.0	0.32	65.2
Uni 0b	”	”	0.32	64.5
Uni90a	51.7	30.7	0.33	55.0
Uni90b	”	”	0.32	54.6
Uni45a	65.8	32.8	0.34	41.1
Uni45b	”	”	0.34	41.4
Bi090a	60.0	32.0	0.30	50.0
Bi090b	”	”	0.31	48.6
Bi45a	60.1	31.8	0.31	48.9
Bi45b	”	”	0.31	49.4
Bi22a	60.0	32.1	0.31	49.1
Bi22b	”	”	0.30	49.3
La	79.1	31.9	0.57	68.8
Lb	”	”	0.57	68.4

4.2.2 Finite Element Model

The main goal of the cantilever bending experiments was to generate a data set off which to build a finite element model. As mentioned previously, if the bidirectional model was created with the properties of the in-plane tests, the bending stiffness could be drastically incorrect. To account for this, the finite element model was modified to match the experimental results.

It was found that centering the material around the centerline of the thickness, as shown in Fig. 4-9A, provided the most accurate results for a single ply of bidirectional composite undergoing bending. In this layup, the pseudo-epoxy layers made up a combined 45% of the thickness. However, when a single ply was incorporated into a multi-ply laminate, it was found that the bidirectional ply was better modeled without epoxy layers as shown in Fig. 4-9B. The material properties for both the unidirectional and bidirectional samples are shown in Table 4-3. The elements of the finite element model were quadrilateral shell elements, S4R.

www.manaraa.com

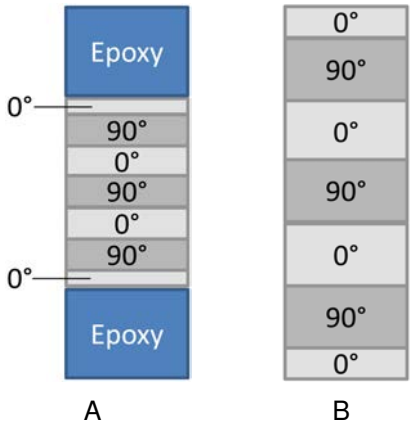

Figure 4-9. Bidirectional composite approximation for finite element model. A) Single layer bidirectional approximation. B) Bidirectional approximation when incorporated into a multi-ply laminate.

Table 4-3. Finite element properties for unidirectional and bidirectional carbon fiber.

	Unidirectional Carbon Fiber	Bidirectional Carbon Fiber
E_1, GPa	81.0	63.5
E_2, GPa	5.5	5.0
ν_{12}	0.3	0.3
G_{12}, GPa	3.0	3.0
G_{13}, GPa	3.0	3.0
G_{23}, GPa	2.0	2.0
t, mm	0.16	0.30

4.2.3 Results

The results from the experiments are summarized in Fig. 4-10. After adjusting the finite element model as described in Section 4.2.1, the experimental values matched up well with the finite element models. Overall, the finite element models had an average deviation from the experiments of 5.5%. A couple of the experiments deviated more, but this could be attributed to manufacturing defects, variations in thickness, or the position at which the sample was clamped.

After generating a successful finite element model for the composite materials, efforts progressed to analyzing the performance of the MFC actuator itself and how to apply it to substrates.

www.manaraa.com

Sample		Displacement, mm																	
		R00 L05		R05 L00		R05 L05		R00 L10		R10 L00		R10 L10		R00 L20		R20 L00		R20 L20	
		R	L	R	L	R	L	R	L	R	L	R	L	R	L	R	L	R	L
Uni0a	DIC							0.95	2.17	2.12	0.99	3.06	3.05	2.11	4.07	4.01	2.15	6.06	6.06
	FEA							0.92	2.04	2.04	0.92	2.96	2.96	1.85	4.08	4.08	1.85	5.93	5.93
Uni0b	DIC							0.92	2.23	2.08	0.97	2.91	3.15	2.06	4.12	3.95	2.13	5.84	6.15
	FEA							**	**	**	**	**	**	**	**	**	**	**	**
Uni45a	DIC	2.24	2.03	3.97	2.55	5.97	4.36	4.56	3.95	7.44	4.80	11.17	8.14						
	FEA	2.10	1.75	3.39	2.10	5.50	3.85	4.21	3.50	6.79	4.21	11.00	7.70						
Uni45b*	DIC	2.56	2.17	4.03	2.56	6.27	4.48	4.81	4.05	7.67	4.85	11.60	8.27						
	FEA	2.06	1.71	3.34	2.06	5.40	3.78	4.13	3.43	6.68	4.13	10.81	7.56						
Uni90a	DIC	1.98	2.71	2.66	1.98	4.64	4.64	4.01	5.33	5.16	3.96	8.80	8.81						
	FEA	1.91	2.49	2.49	1.91	4.41	4.41	3.83	4.99	4.99	3.83	8.81	8.81						
Uni90b	DIC	2.25	2.88	2.85	2.28	5.11	5.13	4.62	5.81	5.55	4.54	9.72	9.78						
	FEA	2.13	2.77	2.77	2.13	4.90	4.90	4.26	5.55	5.55	4.26	9.81	9.81						
Bi090a	DIC	1.61	3.14	2.88	1.72	4.54	4.77	3.46	6.08	5.54	3.57	8.71	9.17						
	FEA	1.65	2.66	2.66	1.65	4.31	4.31	3.30	5.31	5.31	3.30	8.61	8.61						
Bi090b	DIC	1.65	3.07	2.79	1.61	4.41	4.62	3.46	5.90	5.40	3.41	8.52	8.88						
	FEA	1.63	2.63	2.63	1.63	4.25	4.25	3.26	5.25	5.25	3.26	8.51	8.51						
Bi22a	DIC	2.49	2.79	3.69	2.48	6.14	5.18	4.95	5.54	6.97	4.89	11.34	9.84						
	FEA	2.19	2.64	3.39	2.19	5.58	4.83	4.37	5.28	6.79	4.37	11.16	9.65						
Bi22b	DIC	2.78	3.11	4.25	2.81	6.86	5.76	5.39	6.05	7.82	5.41	12.49	10.69						
	FEA	2.42	2.92	3.76	2.42	6.18	5.34	4.84	5.85	7.52	4.84	12.36	10.69						
Bi45a	DIC	3.72	4.36	4.29	3.77	7.64	7.78	7.05	8.20	8.15	7.23	13.78	13.96						
	FEA	2.87	3.47	3.54	2.87	6.41	6.34	5.73	6.95	7.09	5.73	12.82	12.68						
Bi45b	DIC	3.21	3.70	3.80	3.18	6.72	6.61	6.19	7.07	7.20	6.07	12.45	12.25						
	FEA	2.85	3.45	3.52	2.85	6.37	6.30	5.70	6.90	7.05	5.70	12.74	12.60						
La	DIC							1.58	1.35	2.37	1.62	3.84	2.90	3.10	2.66	4.64	3.20	7.43	5.64
	FEA							1.82	1.61	2.40	1.82	4.22	3.42	3.63	3.22	4.81	3.63	8.44	6.85
Lb	DIC							1.73	1.50	2.73	1.93	4.41	3.40	3.51	3.02	5.26	3.74	8.46	6.53
	FEA							1.78	1.58	2.36	1.78	4.14	3.36	3.56	3.16	4.72	3.56	8.29	6.72

* Switched the R and L values because the fibers were opposite of the corresponding sample

** Sample a and b were nearly identical, so a second FEA model was not created

Figure 4-10. Results from the cantilever bending tests.

www.manaraa.com

CHAPTER 5
MFC FREE STRAIN EXPERIMENTAL TESTS

The first step in creating an accurate FEA model representing an MFC structure is to experimentally determine the free strain produced by the MFC. To do this, a setup with a Digital Image Correlation (DIC) system and necessary electronics was assembled, as shown in Fig. 5-1. This setup allowed the MFC to be actuated throughout its voltage range and the deformation of the MFC quantified and converted to strain. MFCs require a high voltage system (described in Section 5.3) capable of producing a voltage range of -500 V to 1500 V. This range is slightly expanded because research has shown that the MFCs can be safely actuated up to 1700 V [22].

5.1 Setup

As mentioned in Chapter 4, DIC is an optical method in which a speckle pattern is applied to the surface of the experimental subject and tracked using a camera system to quantify the full-field position and displacements in three dimensions. DIC is described in Appendix A.

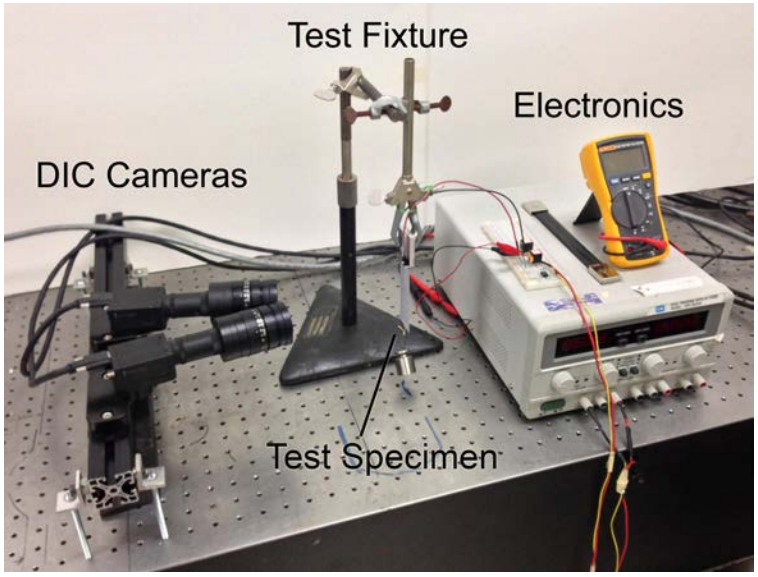

Figure 5-1. The experimental setup used to measure the strain in the M8528-P1 MFC actuator. The DIC cameras are positioned on the left, the MFC supported by the test fixture in the center, and the corresponding electronics are located on the right. Photo taken by Bradley LaCroix.

www.manaraa.com

The system used for these experiments is composed of two cameras (Point Grey Research Grasshopper®2) outfitted with Fujinon 1:1.8/75mm HF75SA-1 lenses and a computer system running Vic-Snap 2007 and VIC-3D 2009. A speckle pattern was applied to the MFC prior to the experiment using Valspar black and white spray paints. First, a uniform layer of white paint was applied, then a speckle pattern of black dots was applied to create the overall high-contrast pattern. The MFC was clamped in place and the cameras were focused on a small section of the MFC measuring approximately one square centimeter.

Since the manufactured MFC is not perfectly symmetric, it moves out-of-plane when actuated. This out-of-plane motion must be restricted due to the extremely narrow focal plane of the camera setup, as to prevent the MFC from moving out of focus. To do this, a small weight was suspended from the end of the MFC. This ensured that the MFC could still strain in the in-plane direction, but would not significantly bend out-of-plane when actuated. A variety of small weights were used to verify that the presence of the weight did not affect the measured strain.

The technique used to convert the measured MFC displacements to strain is described in Appendix B. The procedure and results are discussed in the following section

5.2 Procedure and Results

A total of four tests were conducted. The three certified masses used for these tests were 50, 100, and 500 g. Two separate sections of the MFC were examined: the center and the lower center portion. The results, shown in Fig. 5-2, demonstrate that the tests were quite consistent, with a variation in the peak-to-peak maximum difference of 8.4% in longitudinal strain and 3.0% in transverse strain at 1700 V.

The results also indicate that the longitudinal strain is higher than the quoted value by Smart Materials Corp [61]. One explanation for this result is that Smart Materials may have been referring only to the 0-1500 V range rather than the entire range.

www.manaraa.com

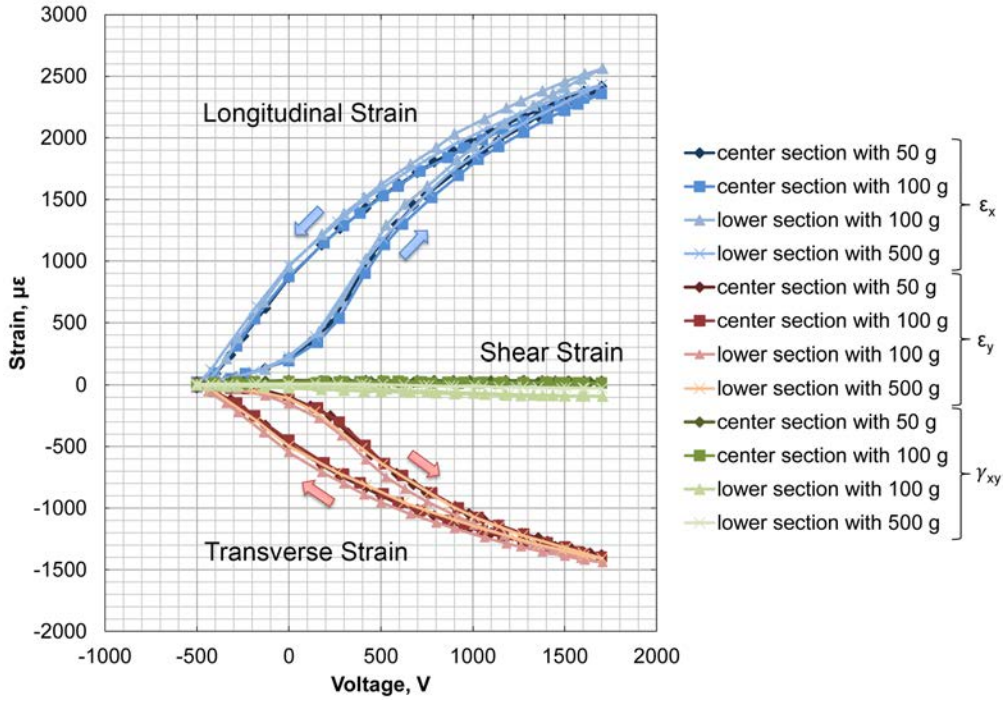

Figure 5-2. Experimentally determined free strain for the M8528-P1 MFC.

Furthermore, this experiment examines a range of -500 to 1700 V. While 1500 V is quoted as the upper limit for the MFCs, Williams and Inman conducted several tests in which they determined it was safe to operate the MFCs up to 1700 V with no decrease in performance [22]. Therefore, to encapsulate the entire operating range, tests were conducted from -500 to 1700 V.

In addition, the results show that there is significant transverse strain exhibited by the MFC, on the order of 57% of the longitudinal strain. The shear strain, as can be seen in the figure, is approximately zero.

Although ABAQUS allows for the input of specific piezoelectric parameters for a piezoelectric material, the implementation is complicated and ultimately unnecessary for a macroscopic setup such as this. Therefore, a simpler thermal relation is used to model the MFC rather than piezoelectric parameters. The strain values obtained from these experiments were converted to thermal strain values to be used in the ABAQUS FEA model. The strain values for the upper and lower parts of the hysteresis loop were

www.manaraa.com

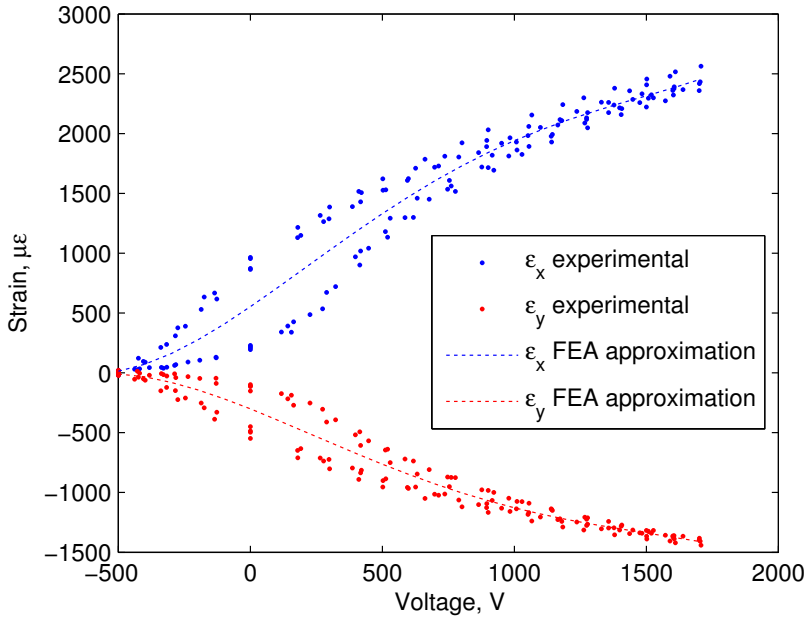

Figure 5-3. Free strain approximation for the FEA model.

averaged to provide a single set of unique values for the strain vs voltage, as shown in Fig. 5-3. These are compiled in Table 5-1. For convenience, the thermal strain is shown both in the units required by ABAQUS (strain per degree temperature change) and in absolute strain. For the FEA model, one degree temperature change in ABAQUS corresponds to one volt change in the MFC.

5.3 Electrical Setup

The electrical setup consisted of a GW GPC-3030D power supply, EMCO Q15-5 High Voltage Amplifier, a Fluke 115 multimeter, two resistors in series, and the MFC. The EMCO high voltage amplifier boosts the initial voltage by a factor of 300. Therefore, an input voltage of 5 V is amplified to a voltage of 1500 V. An illustration of the setup is shown in Fig. 5-4.

The voltage divider serves a dual purpose. Firstly, it allows the amplified voltage of 1500 V to be scaled down and measured with a multimeter, which has a maximum voltage of 600 V. Secondly, when the power is turned off to the circuit, the resistors dissipate the remaining voltage potential stored on the MFC. The resistors were carefully

www.manaraa.com

Table 5-1. Free strain values used in the ABAQUS FEA model.

Voltage, V	ϵ_x / °Temp	ϵ_y / °Temp	ϵ_x, $\mu\epsilon$	ϵ_y, $\mu\epsilon$
-500	1.08E-06	-5.84E-07	-540	292
-400	1.20E-06	-6.69E-07	-482	267
-300	1.31E-06	-7.40E-07	-392	222
-200	1.39E-06	-7.98E-07	-279	160
-100	1.46E-06	-8.44E-07	-146	84
100	1.54E-06	-9.06E-07	154	-91
200	1.56E-06	-9.22E-07	313	-184
300	1.57E-06	-9.30E-07	472	-279
400	1.57E-06	-9.31E-07	627	-372
500	1.56E-06	-9.25E-07	778	-462
600	1.53E-06	-9.13E-07	920	-548
700	1.50E-06	-8.97E-07	1053	-628
800	1.47E-06	-8.76E-07	1175	-701
900	1.43E-06	-8.52E-07	1287	-767
1000	1.39E-06	-8.26E-07	1387	-826
1100	1.34E-06	-7.99E-07	1477	-879
1200	1.30E-06	-7.71E-07	1558	-925
1300	1.26E-06	-7.43E-07	1631	-966
1400	1.21E-06	-7.16E-07	1698	-1003
1500	1.18E-06	-6.92E-07	1763	-1038
1600	1.14E-06	-6.70E-07	1828	-1072
1700	1.12E-06	-6.52E-07	1898	-1108

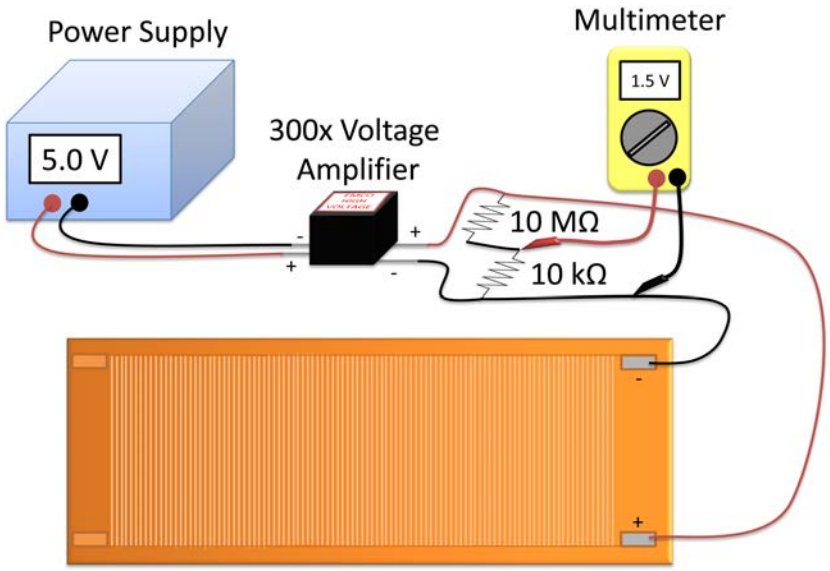

Figure 5-4. Wiring setup for MFC actuation.

www.manaraa.com

chosen to minimize the effect on the overall circuit. If the second resistor's resistance is too high, then it will interfere with the voltage measured by the multimeter. This is because the multimeter has a built-in impedance over which it measures voltage. If the resistance is too low, the voltage drop becomes unmeasureable. A resistor of 1 kΩ creates only 0.1% error, whereas a larger resistance, such as 1 MΩ, would produce an error of 10%. This trend can be seen in Fig. 5-5.

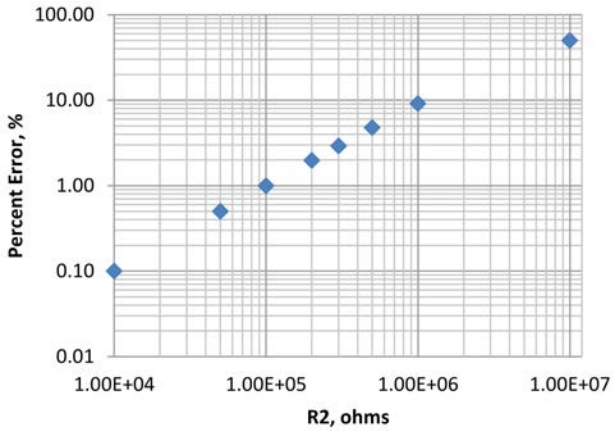

Figure 5-5. Measurement error in voltage reading based on the resistor selection for high voltage circuit.

In addition, a series of high resistance resistors is necesary since the EMCO device only produces 0.333 mA of current. Using Ohm's law, $I = \frac{V}{R} = \frac{1500\ \text{V}}{10\text{M}\Omega} = 0.15\ \text{mA}$, we can see that the resistor dissipates 0.15 mA of the 0.333 mA produced by the EMCO device. A smaller resistor would dissipate a larger portion, if not all of, the generated current. It should also be noted that the EMCO device has a input threshold of 0.7 V. Therefore, no output voltage is produced when the input voltage is less than 0.7 V [62].

www.manaraa.com

CHAPTER 6
UNIMORPH MODEL, EXPERIMENTAL VALIDATION, AND DESIGN SPACE EXPLORATION

After conducting the experiment to measure the free strain in the MFC, the next step was to generate a finite element model of a unimorph in ABAQUS and validate it with a series of experiments. It was decided to make an experimental setup similar to the configuration that would be used on a wing. For the MAV wings used in our laboratory, the leading edge is generally reinforced while the trailing edge is relatively compliant. This results in a reinforced leading edge in which one side of the MFC is approximately rigid while the other end, on the trailing edge of the wing, is relatively free. The setup most similar to this is a cantilever arrangement.

In this setup, one side of the unimorph is clamped in a way that the connecting wires are not compressed and the other end is left unrestrained. The setup, with two 10 g masses applied, is shown in Fig. 6-1A. An aluminum tube is adhered to the tip of the unimorph and a string is passed through, as shown in Fig. 6-1B. Weights are suspended from the string to apply loads on the tip of the cantilevered unimorph. The string and tube insure that the loads are applied in a precise and repeatable manner while also preventing severe local deformation.

As mentioned in Section 1.2, three sizes of MFCs were initially examined. The resulting unimorphs are shown in Fig. 6-2. The smaller MFCs were used on the initial MAV, which is discussed in Chapter 8. However, after further testing and examination of potential design concepts, it was determined that the M8528-P1 actuator was the best candidate due to its strain range and larger size. This actuator was implemented on a MAV and is introduced in Chapter 9. Some of the experimental results are shown in Section 6.2.

6.1 Adhesion Method

Two different types of adhesion methods were initially investigated. The first method was a co-curing method where carbon fiber pre-impregnated with epoxy, was laid up

www.manaraa.com

A B

Figure 6-1. Cantilevered unimorph DIC setup. A) DIC setup with the unimorph cantilevered and the loads applied to the free end. B) M8528-P1 unimorph with the aluminum tube and string attached. Photos taken by Bradley LaCroix.

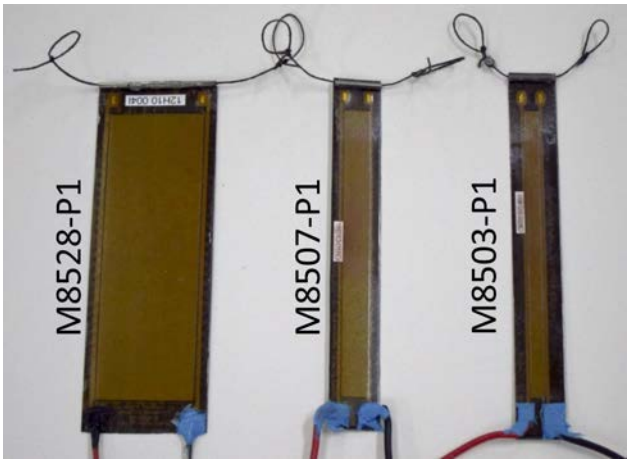

Figure 6-2. Unimorphs prepared for cantilever loading experiments. Photo taken by Bradley LaCroix.

with the MFC (shown in Fig. 6-3) and placed in the oven for curing with vacuum pressure simultaneously applied. This method provides a strong, solid bond between the MFC and the carbon fiber in a single step.

The second method is a two-step process. First, the carbon fiber is cured in the desired geometry. Next, the piezoelectric is adhered to the carbon fiber using cyanoacrylate adhesive (CA). Pressure was applied manually using weights. The main drawback to this method is the added thickness of the adhesive, which increases the

www.manaraa.com

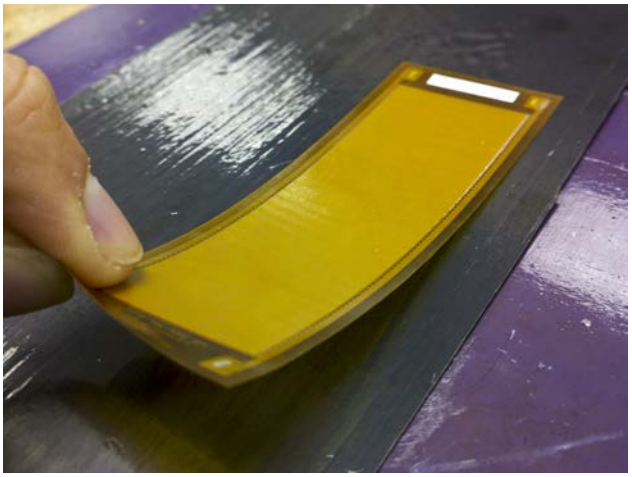

Figure 6-3. Example of bonding an MFC to unidirectional carbon fiber pre-preg. Photo taken by Bradley LaCroix.

moment of inertia of the final laminate, which in turn increases the flexural stiffness and thereby reduces the actuated curvature.

CA is available in three different viscosities: thin, medium, and thick. The lower the viscosity, the faster the cure time. Furthermore, it was expected that a lower viscosity would result in a thinner final laminate. Thickness measurements partially supported this theory, however, applying the thin CA in a uniform manner proved difficult due to the rapid curing time. The average thickness of the medium CA unimorph was 0.544 mm with a standard deviation of 0.039 mm while the thin CA unimorph was 0.534 mm with a standard deviation of 0.048 mm. Figure 6-4 shows the DIC results for the 3 different adhesion tests.

Despite being thinner in some locations, the thin CA sample proved to be no better than the medium CA sample while the co-cure sample proved to be superior to both. The relative up-deflection of the co-cure sample was 23.1 mm compared to the medium CA relative up-deflection of 17.5 mm. The down-deflection of the co-cure sample was slightly worse than the medium CA at a relative deflection of -8.8 mm compared to the medium CA relative down-deflection of -9.4 mm. Therefore, for performance critical applications, the co-curing technique applied to the unidirectional carbon fiber/epoxy

www.manaraa.com

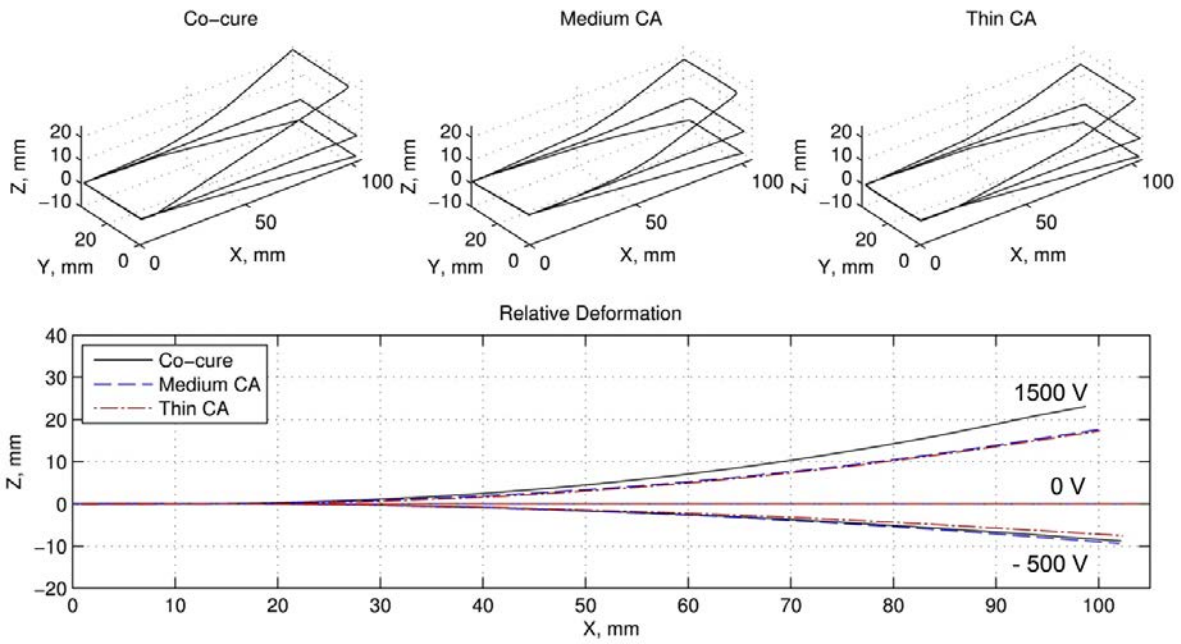

Figure 6-4. Comparison of three adhesion techniques at positive and negative actuation.

is the preferred method. Both methods result in a strong bond which makes it virtually impossible to remove and reuse the MFC. Therefore, each MFC can only be used once. This can be an economic drawback when in the early testing and development phase.

After steel was determined to be a potentially superior substrate, a slightly modified adhesion technique was developed. First, the steel surface was prepped using fine grit sand paper to remove the protective coating on the surface. A partially prepared sample is shown in Fig. 6-5. Next, the steel is placed on a teflon sheet on a flat layup surface and West Systems epoxy (105 resin and 206 hardener) is applied to the surface. The MFC is placed on top and kapton tape is placed on top of the MFC to prevent the epoxy from flowing over onto the exposed surface and electronic leads. This setup is shown in Fig. 6-6. The final step was to place the layup in a vacuum bag to apply constant and uniform pressure while the epoxy cured. After the epoxy cured, the edges could be sanded to remove excess steel and epoxy.

www.manaraa.com

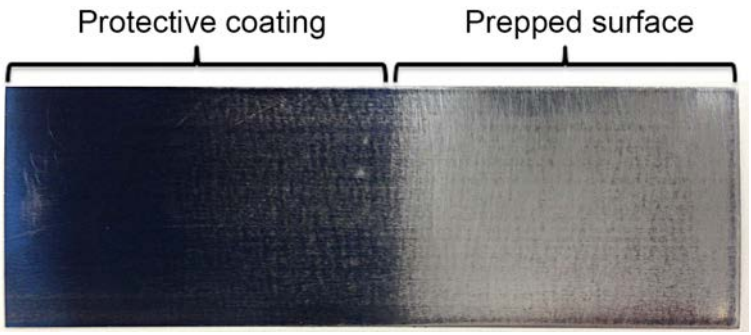

Figure 6-5. Steel substrate partially prepared for bonding. Photo taken by Bradley LaCroix.

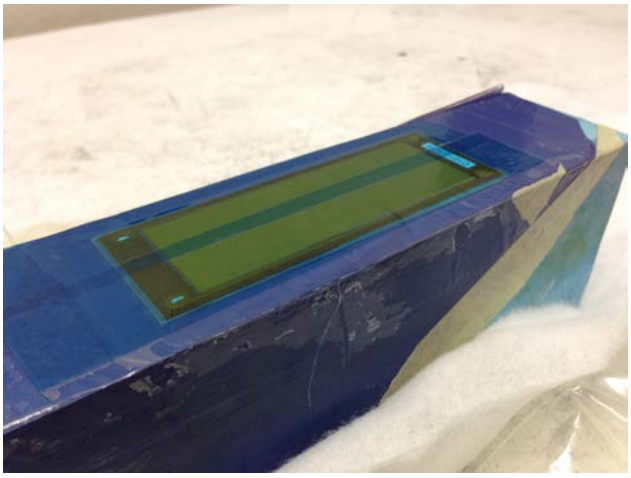

Figure 6-6. Steel substrate and MFC prepared and ready to vacuum bag. Photo taken by Bradley LaCroix.

6.2 Experimental Comparison of MFCs

Each of the unimorphs shown in Fig. 6-2 were placed in a cantilevered configuration as shown in Fig. 6-1A. The unimorphs were actuated to -500 V and 1500 V and the deformation measured with DIC. The resulting deformations are shown in Fig. 6-7.

Contrary to the expected result, the M8507-P1 unimorph has a larger actuation range than the M8528-P1. The M8528-P1 has a quoted strain range of 1800 $\mu\epsilon$ whereas the M8507-P1 has a quoted strain range of 1380 $\mu\epsilon$, as indicated in Table 1-1. Thickness measurements indicated that the M8528-P1 unimorph measured approximately 0.50 mm whereas the M8507-P1 and M8503-P1 unimorphs measured approximately 0.47 mm. This could account for part of the difference, since thinner substrates should

www.manaraa.com

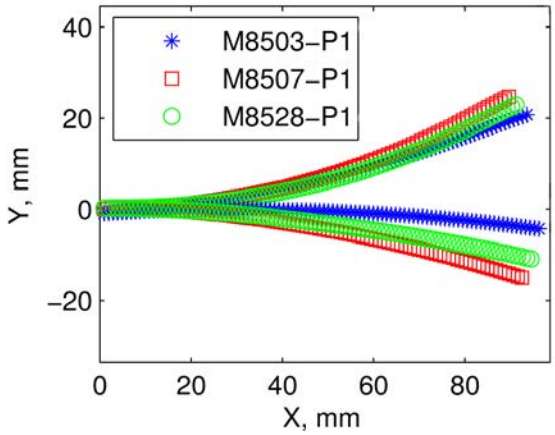

Figure 6-7. Experimental cantilever results for the three unimorphs.

produce larger deflections. In addition, the M8528-P1 MFC could have been damaged during the manufacturing process or the M8507-P1 may produce more strain than the quoted values. Regardless, due to its larger size and expected performance, the M8528-P1 was still chosen as the preferred actuator later in the design process. This decision was further reinforced by the convenient size of the M8528-P1 for a 24 inch MAV.

6.3 Substrate Comparison

Following the tests conducted in the previous section, a no-load study with the M8528-P1 was conducted in which a variety of substrates were tested with no tip load applied. Each test was started with the MFC actuated to -500 V. The voltage was increased to 1700 V in a series of steps, with the voltage recorded and DIC images taken at each step. After reaching 1700 V, the voltage was decreased to -500 V while recording each voltage and taking DIC images. The tip displacement results of these tests are shown in Fig. 6-8.

Two thicknesses of steel were tested, 0.05 mm (0.002”) and 0.10 mm (0.004”), each bonded to the MFC using West Systems epoxy (105 resin and 206 hardener) under vacuum pressure. Another substrate was pre-cured unidirectional carbon fiber bonded to the MFC using thin viscosity cyanoacrylate (CA) adhesive. The other three samples

www.manaraa.com

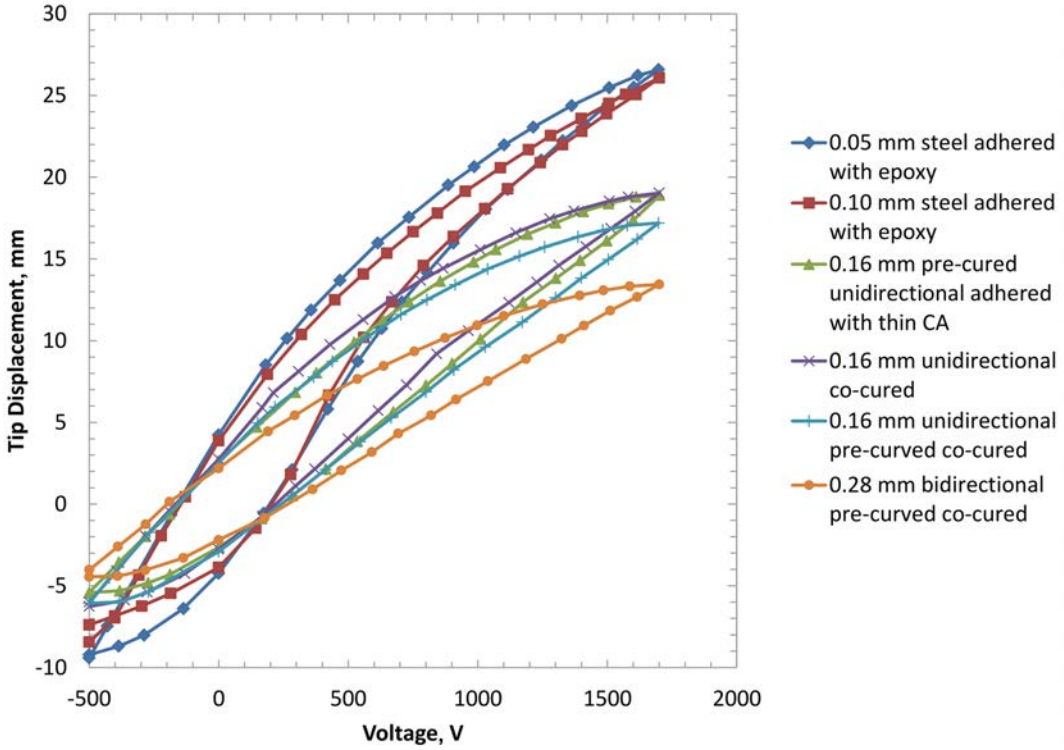

Figure 6-8. Measured tip displacement with various substrates in a cantilever setup with the M8528-P1.

were co-cured with carbon fiber preimpreganted with epoxy (usually termed pre-preg for short). The carbon fiber pre-preg, measuring approximately 0.16 mm thick, was co-cured with the MFC under vacuum pressure at a temperature of 127°C (260°F). The first of which was co-cured with unidirectional carbon fiber on a flat layup surface. The other two (one unidirectional sample and one bidirectional sample) were co-cured on a pre-curved surface. The radius of curvature for the bidirectional sample after curing was approximately 0.33 m^{-1} and 0.21 m^{-1} for the unidirectional sample.

These results reinforce those predicted by CLPT and the bimetallic beam theory, as discussed in Chapter 3. As seen in the figure, steel, the material with the highest modulus, has the largest deflection. The unidirectional carbon fiber is less, but still outperforms the bidirectional carbon fiber. Furthermore, these results clearly show the hysteresis of the MFC actuator and closely follow the trend seen in the MFC free strain results seen in Fig. 5-2 from Section 5.2.

www.manaraa.com

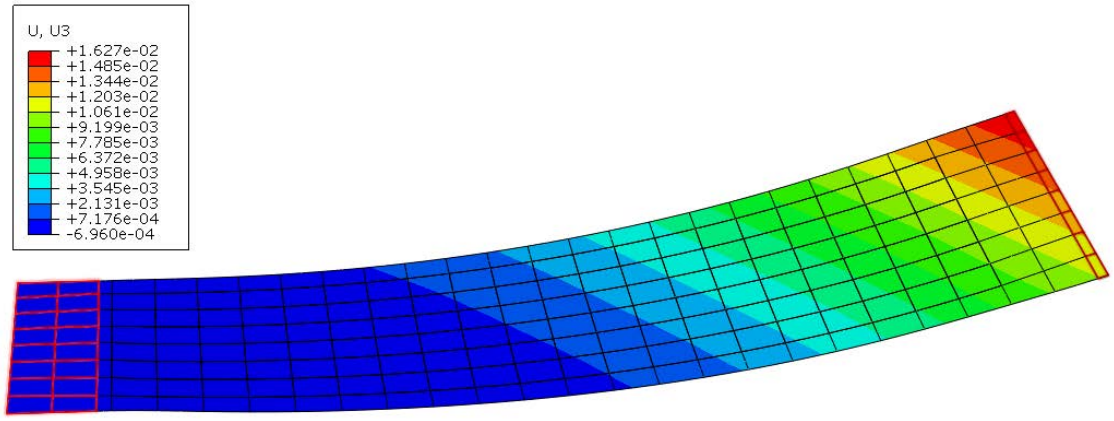

Figure 6-9. Example of FEA model with cantilever boundary condition highlighted (left) and aluminum partition highlighted (right).

6.4 Comparison Between Experimental and Finite Element Results

6.4.1 Finite Element Model

The finite element model was created in ABAQUS 6.9-2 using a quadrilateral shell model. The model was divided into partitions and the respective material properties assigned to each partition. The MFC material was assigned a coefficient of thermal expansion based on the results obtained from the free strain experiments (Section 5.2). Next, a temperature field was applied to the model to simulate the strain produced by the MFC actuation. The other materials were not assigned a coefficient of thermal expansion, therefore a temperature field did not affect them. A linear model was used since the magnitude of extensibility was assumed to be small for all cases. The complete cantilever FEA model is shown in Fig. 6-9.

6.4.2 Experimental Procedure

Digital image correlation was used to measure the shape of the unimorph through each step of the experiment. For the experiments in which no load was applied, the MFC was actuated to -500 V, 0 V, 1500 V, 1700 V, then 1500 V, 0 V, and -500 V. The deformation was captured using DIC for the upward pass (-500 V, 0 V, 1500 V) and for the downward pass (1500 V, 0 V, and -500 V).

www.manaraa.com

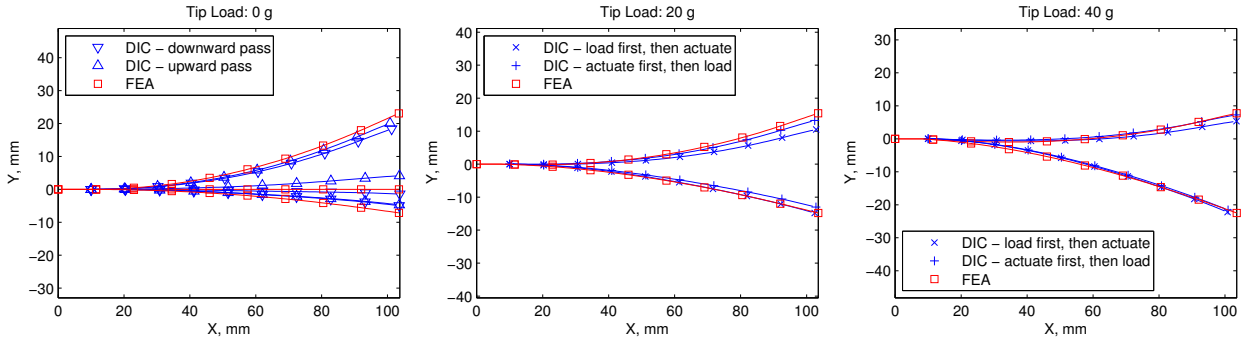

A B C

Figure 6-10. Comparison between the experimental results and the finite element model for the 0.16 mm unidirectional unimorph. A) No load applied. B) 20 g load applied. C) 40 g load applied.

For the experiments with applied loads, the loads were applied in two different ways. In the first way, the MFC was actuated to either -500 V or 1500 V and then the load was applied. In the other way, the MFC was loaded first and then actuated to -500 V or 1500 V. DIC was once again used to measure the deformation at each step. All of the results were output from VIC-3D and compiled using MATLAB.

6.4.3 Results

Three samples were chosen to be tested and compared to the FEA results. One sample was a co-cured unimorph composed of a single layer of unidirectional carbon fiber. The other two samples were the steel substrates mentioned previously, one measuring 0.05 mm and the other 0.10 mm thick. The layer of adhesive epoxy between the steel and the MFC is also modeled in each case, with a thickness of 0.05 mm. The results, as compared to the FEA models, are shown in Figs. 6-10, 6-11, and 6-12.

Due to thermal expansion during the manufacturing process, the unimorphs contained a small amount of pre-strain and therefore exhibited a small degree of curvature. To account for this, the temperature field in the ABAQUS model was shifted to effectively zero the model on the unloaded, unactuated position.

www.manaraa.com

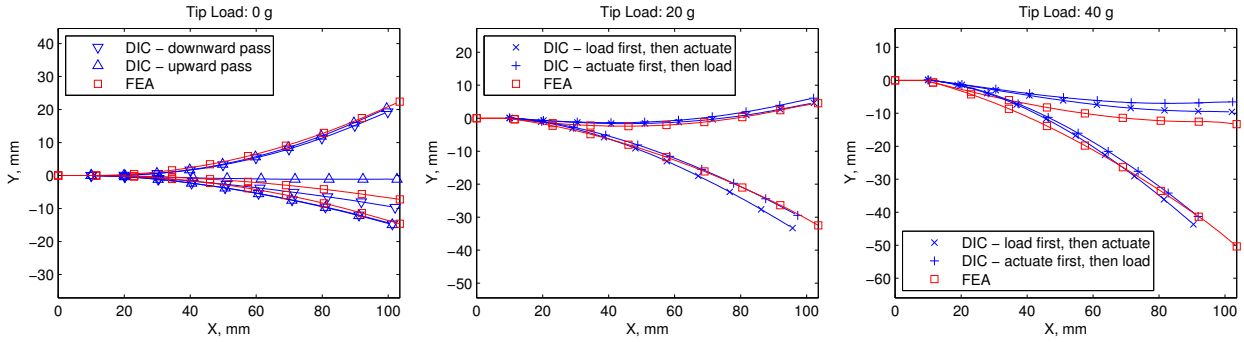

A B C

Figure 6-11. Comparison between the experimental results and the finite element model for the 0.05 mm steel unimorph. A) No load applied. B) 20 g load applied. C) 40 g load applied.

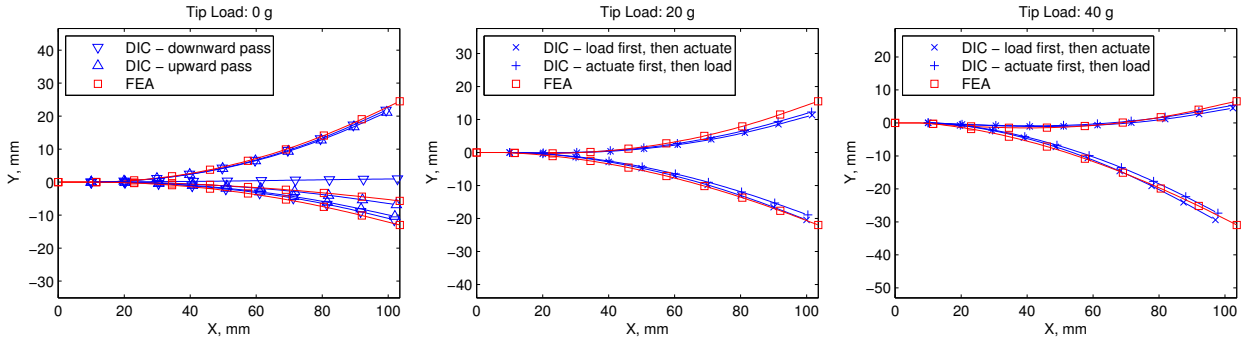

A B C

Figure 6-12. Comparison between the experimental results and the finite element model for the 0.10 mm steel unimorph. A) No load applied. B) 20 g load applied. C) 40 g load applied.

6.5 Design Space Exploration

After the FEA model was validated, it could be used to explore other design possibilities. For example, the thickness of the steel substrate could be adjusted to see its impact on the tip deflection with and without loading. Two thicker substrates were examined and compared with the 0.10 mm steel substrate and the results shown in Fig. 6-13. As can be seen in the figure, the unloaded displacement of the 0.15 mm steel unimorph is slightly less, and the 0.20 mm steel is even less, but the thicker substrates are better at opposing the applied load.

www.manaraa.com

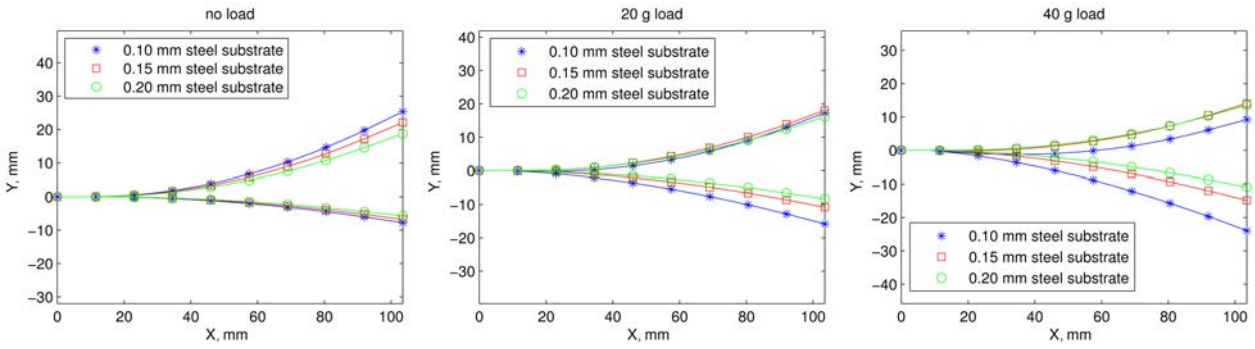

Figure 6-13. FEA unimorph comparison between three thicknesses of steel substrate. A) No load applied. B) 20 g load applied. C) 40 g load applied.

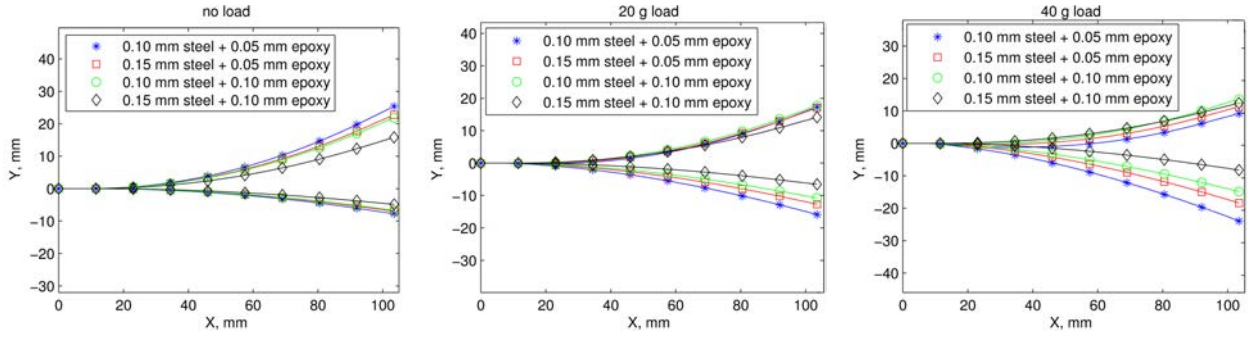

Figure 6-14. FEA unimorph comparison between two epoxy thicknesses. A) No load applied. B) 20 g load applied. C) 40 g load applied.

A similar study was conducted comparing two thicknesses of epoxy. These results are shown in Fig. 6-14. Similar to the trend shown with the other experiments, the thinnest layup has the largest unloaded tip displacement and the thickest substrate has the smallest displacement. However, the results are mixed once the load is applied, since the thicker layups hold their position better and the thinner layups have a larger initial deflection. Therefore, the thinner laminates deflect farther initially, but are displaced farther by loading, so their resulting position are similar to the thicker layups.

To gather a more widespread understanding of the impact of the substrate on the actuation of the unimorph, a large series of finite element analyses were conducted. The substrate thickness and modulus was adjusted through a range of values and the results

www.manaraa.com

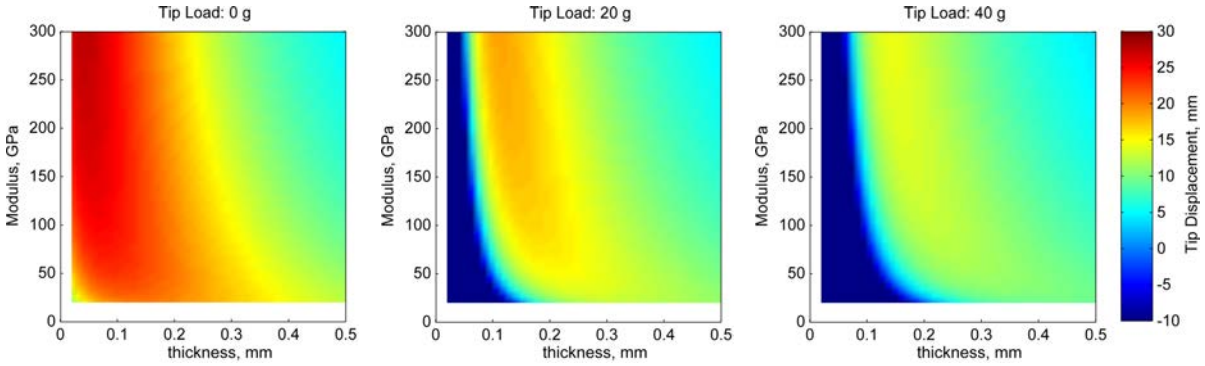

Figure 6-15. FEA unimorph tip displacement for various substrates thicknesses and moduli. The MFC is actuated to 1500 V. A) No load applied. B) 20 g load applied. C) 40 g load applied.

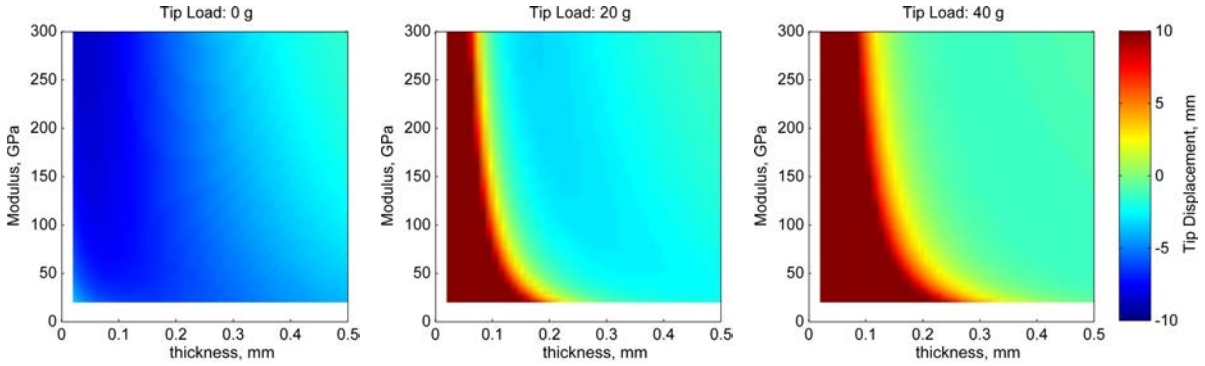

Figure 6-16. FEA unimorph tip displacement for various substrates thicknesses and moduli. The MFC is actuated to -500 V. A) No load applied. B) 20 g load applied. C) 40 g load applied.

plotted. Figure 6-15 shows the FEA results when the MFC is actuated to 1500 V with a tip load of 0 g, 20 g, and 40 g applied. Similarly, Fig. 6-16 shows the FEA results when the MFC is actuated to -500 V. In this case, the load is applied in the same direction as the direction of actuation.

6.6 Alternative Designs

A few other MFC layup possibilities, inspired from the literature, were also considered. A simple bimorph configuration is presented first. Then, two alternative designs are explored.

www.manaraa.com

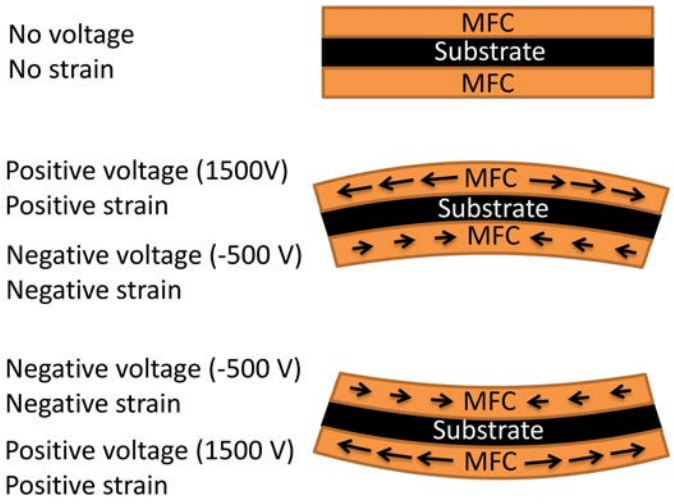

Figure 6-17. Illustration of bimorph actuation.

6.6.1 Bimorph Configuration

Building on the previous results, a bimorph configuration was explored. Although bimorph experiments were not conducted, the results from the previous set of experiments were extrapolated to offer insight into the relative performance of a bimorph configuration. Furthermore, a bimorph configuration was not considered for the MAV project since one of the main objectives was to limit the number of actuators on the aircraft to only two. A MAV incorporating a set of bimorph actuators would require four MFC actuators.

In a bimorph configuration, the bottom MFC is actuated independent of the top MFC, as shown in Fig. 6-17. In this setup, the top MFC is actuated to 1500 V while the bottom MFC is actuated to -500 V, or vice versa. The resulting curvature can be predicted using CLPT as outlined earlier, with the results shown in Fig. 6-18. Contrary to the unimorph configuration, the results show that in order to increase the unloaded curvature, it is preferential to minimize the thickness of the substrate, but elastic modulus has a minimal effect on the unloaded curvature.

A comparison can be drawn between unimorphs and bimorphs by testing a couple substrates in both configurations within FEA. This is shown in Fig. 6-19. In these figures,

www.manaraa.com

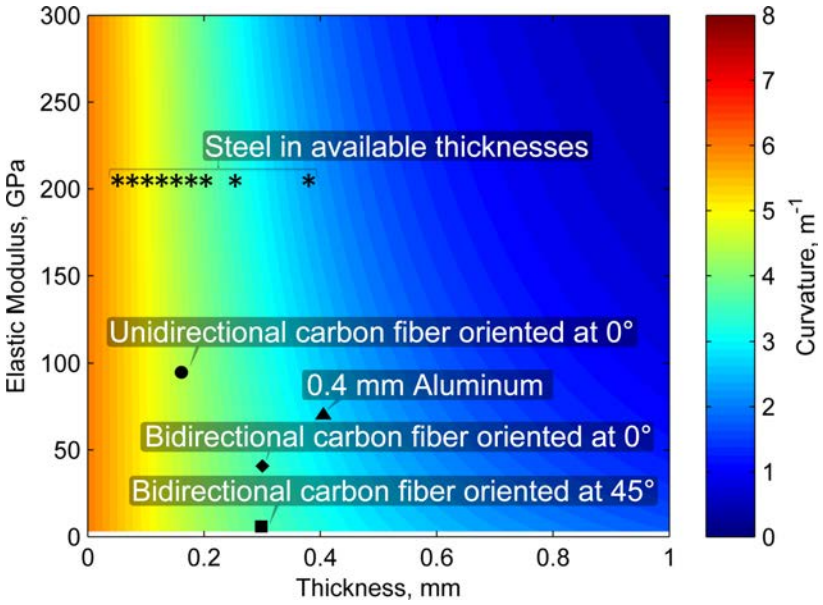

Figure 6-18. Predicted curvature of a bimorph using CLPT for various substrate moduli and thicknesses.

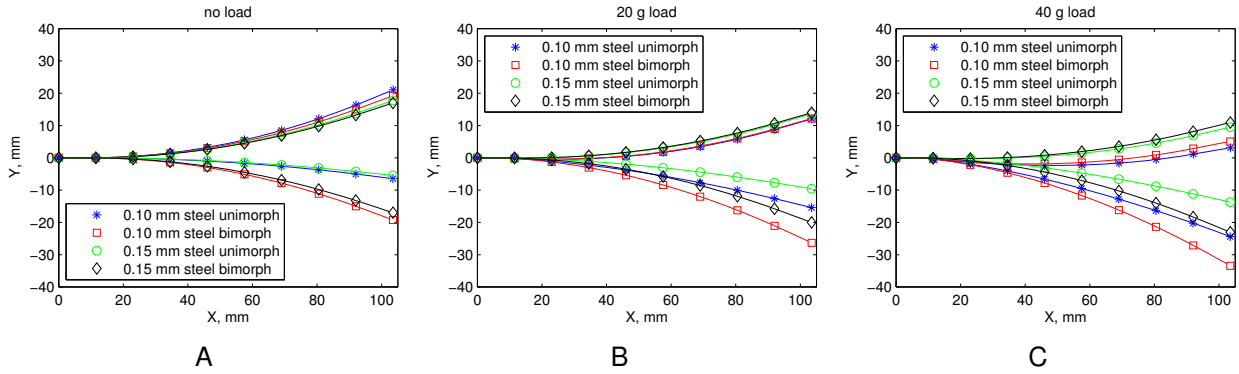

Figure 6-19. Comparison between unimorphs and bimorphs. A) No load applied. B) 20 g load applied. C) 40 g load applied.

the bimorph and unimorph have a similar unloaded tip displacement in the upward direction. However, in the downward direction, the bimorph is superior. However, when loaded with a mass at the tip, both the unimorph and the bimorphs behave similarly, with the main difference being the substrate.

To test this theory further, the modulus and thickness of the bimorph configuration was varied. Loads were applied to the tip and the tip displacement measured. The results are shown in Fig. 6-20. The FEA model indicates that lower modulus materials

www.manaraa.com

exhibit the largest tip deflections for a bimorph configuration, but a significant drop-off is observed once loading is applied. These results reveal that the bimorph configuration has a smaller tip deflection than the unimorph for all cases. This is most likely a result of the bottom MFC working to overcome the top MFC while deflecting, due to the asymmetry in actuation magnitude. In this configuration, the top MFC is actuated to only -500 V while the bottom MFC is actuated to 1500 V. However, it must be noted that a bimorph provides equal deflection in both directions, which is something a unimorph is unable to replicate. Furthermore, a bimorph would provide faster actuation for some electronic setups where the charge on the MFC is dissipated using a resistor, rather than actively adjusting the voltage to a lower value. Therefore, certain applications may make a bimorph configuration the preferred option.

As an example, we can compare a single substrate with a modulus of 200 GPa and a thickness of 0.15 mm in both configurations with M8528-P1 MFCs. In a bimorph configuration, this substrate would yield a tip displacement of 15.5 mm in each direction for a total displacement range of 30.1 mm. In a unimorph configuration, this substrate would yield an upward tip displacement of 21.7 mm and a downward tip displacement of 6.8 mm for a total range of 28.5 mm. However, when loaded with 20 g at the tip, the tip displacement of the bimorph is reduced to 12.8 mm and the unimorph is only reduced to 17.6 mm.

Lastly, Fig. 6-21 demonstrates the predicted behavior of the bimorph configuration when loads are applied in the same direction as the actuation. These results show a similar response to the plots in the previous figure. If the substrate is too thin, the structure will collapse under loading. Furthermore, if the substrate is too thick, then the structure will not displace a measureable amount. Therefore, a compromise must be found at a point in between.

www.manaraa.com

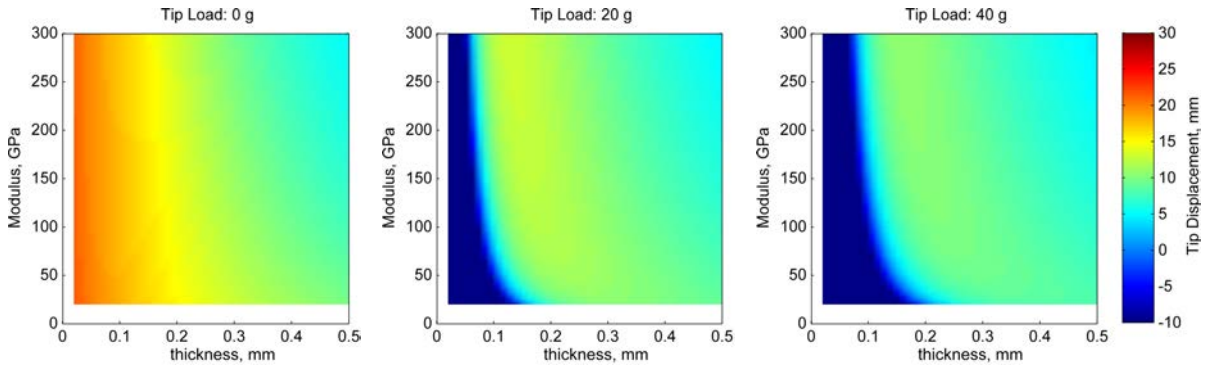

Figure 6-20. FEA bimorph tip displacement vs substrate moduli and thickness (with opposing load). A) No load applied. B) 20 g load applied. C) 40 g load applied.

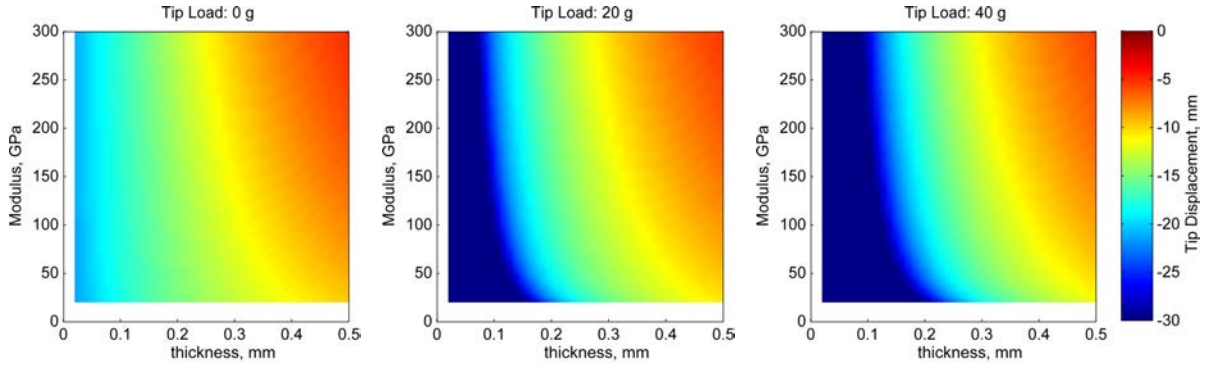

Figure 6-21. FEA bimorph tip displacement vs substrate moduli and thickness (with supplementary load). A) No load applied. B) 20 g load applied. C) 40 g load applied.

6.6.2 Precompressed Actuators

Once the finite element model was validated, additional designs were considered. One such design, similar to the results obtained by Vos and Barret [32, 34, 43–45], was incorporated into the finite element model. In this design, the MFCs and substrate are heated up during the adhesion process. Due to the coefficient of thermal expansion, the substrate expands more than the MFC. After cooling to room temperature, the substrate contracts relative to the MFCs and is held in tension while the MFCs are in compression. This was modeled in the finite element model and the results shown in Fig. 6-22.

www.manaraa.com

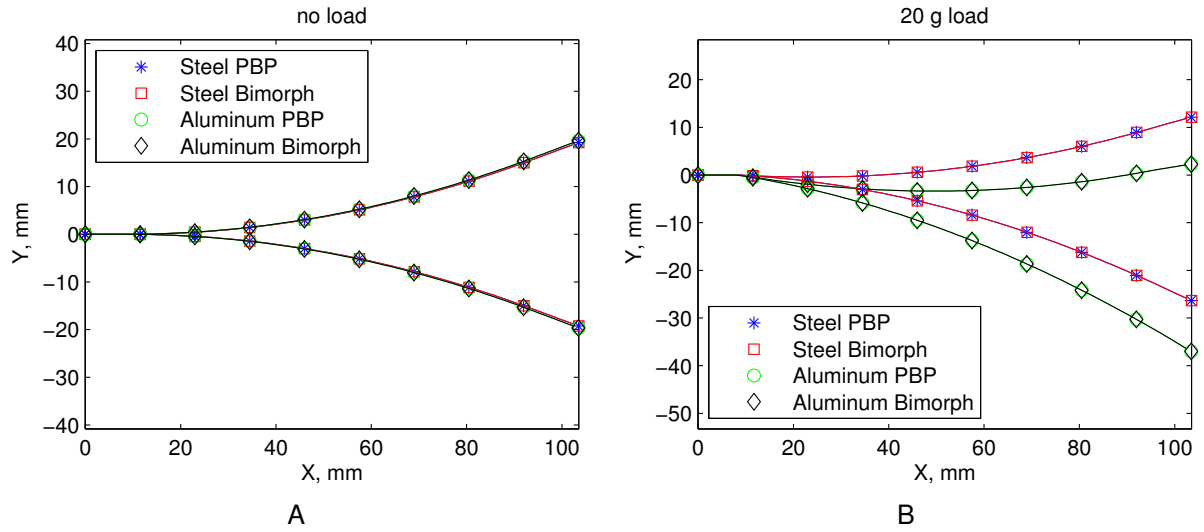

Figure 6-22. Predicted behavior of the precompressed bimorphs (PBP) vs standard bimorphs A) No load. B) 20 g load applied to the tip.

The figures compare two substrates. Each substrate is modeled as a standard bimorph and as a precompressed bimorph. The two substrates examined were: a steel substrate with a thickness of 0.1 mm, elastic modulus of 207 GPa, and coefficient of thermal expansion of 13 $\frac{\mu\epsilon}{K}$; and an aluminum substrate with a thickness of 0.1 mm, elastic modulus of 70 GPa, and a coefficient of thermal expansion of 22.2 $\frac{\mu\epsilon}{K}$. The thermal cycle was assumed to start at 22.2°C (72°F), elevate to 126.7°C (260°F), and return to 22.2°C (72°F).

As noted in the figures, the precompressed aspect does not yield a noticeable benefit. It is likely that combining this setup with a post-buckled design would yield better results, but since this design is more complex and difficult to implement on a thin undercambered wing it is not considered further. It should also be noted that an improvement in tip displacement was achieved if the temperature gradient was increased 100-fold. However, this is not a feasible option since it would require more than a 10,000°C temperature change.

www.manaraa.com

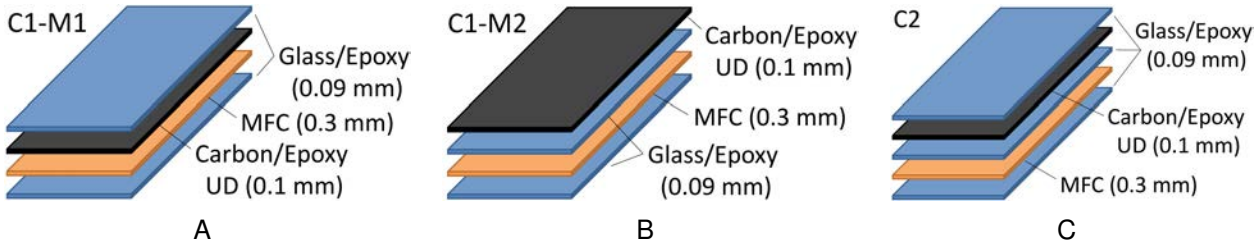

Figure 6-23. The designs modeled in FEA similar to the LIPCA layups. A) C1-M1 design. B) C1-M1 design. C) C2 design.

6.6.3 LIPCA Actuators

LIPCA actuators were also considered. In this type of actuator, the neutral axis is shifted away from the active material and into the surrounding laminate. Although the research for LIPCA actuators was conducted with lead zirconate titanate PZT actuators, it was decided to examine the potential benefits possible when implementing MFCs in a similar configuration.

In the LIPCA actuators examined [48, 49], the actuating material was incorporated into a laminate with layers of glass/epoxy and carbon/epoxy, similar to that shown in Fig. 6-23. Three designs were examined: C1-M1, C1-M2, and C2. The C1-M1 and C1-M2 designs switch the order of the top two layers and the C2 layup contains an extra layer of glass/epoxy.

The results from the FEA are shown in Fig. 6-24. The standard unimorph significantly outperforms all three of the LIPCA designs. It also deforms less when the loading is applied at the free end. Since the LIPCA actuators have a smaller actuation range and deflect more under loading, these results safely eliminate LIPCAs as a possible design option for the research in this document.

www.manaraa.com

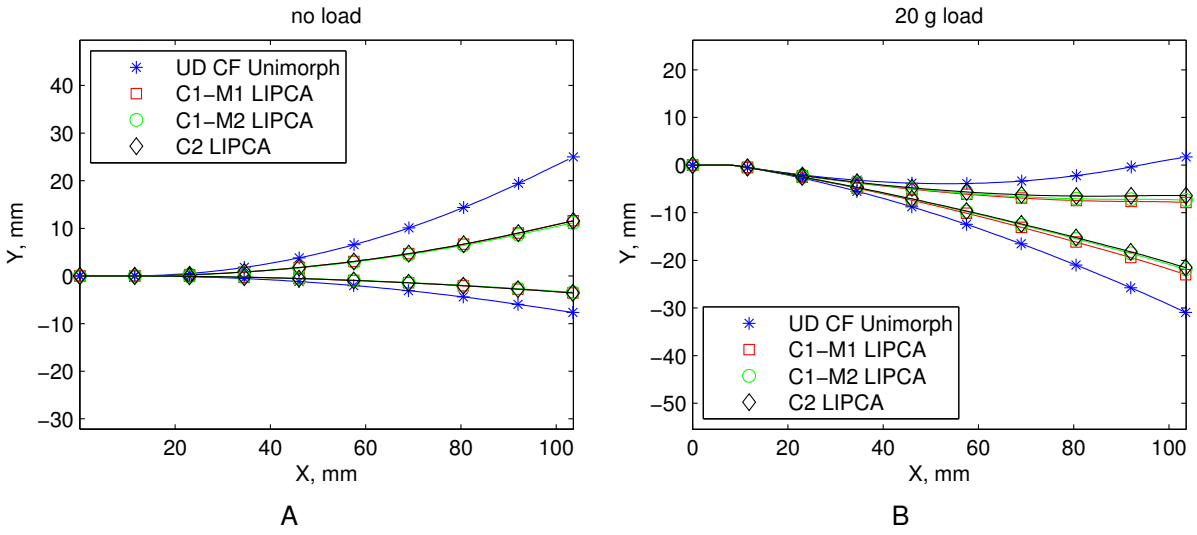

Figure 6-24. The results of the LIPCA FEA models vs a standard unimorph sample with unidirectional carbon fiber A) No load comparison. B) 20 g load comparison.

www.manaraa.com

CHAPTER 7
FOUR POINT BEND TESTS

The cantilevered unimorph experiments covered in the previous chapter provided significant insight into the performance of the actuators when bonded to various substrates. However, the displacement measured in the cantilevered tests could be especially sensitive to the clamp position. Small changes in the boundary conditions would result in large changes in displacements when various loads were applied to the actuated unimorph.

Therefore, another set of experiments were devised to test the load bearing capacity of the unimorphs during actuation. Because the unimorph's main result of actuation is curvature, it was decided that a test that applies a bending moment would be ideal, since the bending would directly oppose the curvature. With this in mind, a four point bend test was chosen since it provides a uniform and constant moment between the inner two supports. In addition, positioning a unimorph on a four point bend setup was determined to be easier than a three point bend setup. Overall, it was expected that a four point bend test would yield a more accurate characterization of the unimorph since it allows for the application of a pure moment, thereby counteracting the moment generated by the unimorph.

7.1 Setup

The setup and corresponding illustration are shown in Fig. 7-1. The supports of the four point bend setup were connected to the same Test Resources machine described in Section 4.1. To improve the test resolution, a Test Resources 10 lbf load cell (model number SM-10-294) was incorporated into the setup. The supports were spaced according to ASTM standards and positioned so that the outer supports were placed just inside of the active portion of the unimorph. This also allowed sufficient clearance for the wires to run to the MFC without interferring with the supports. During the experiments,

www.manaraa.com

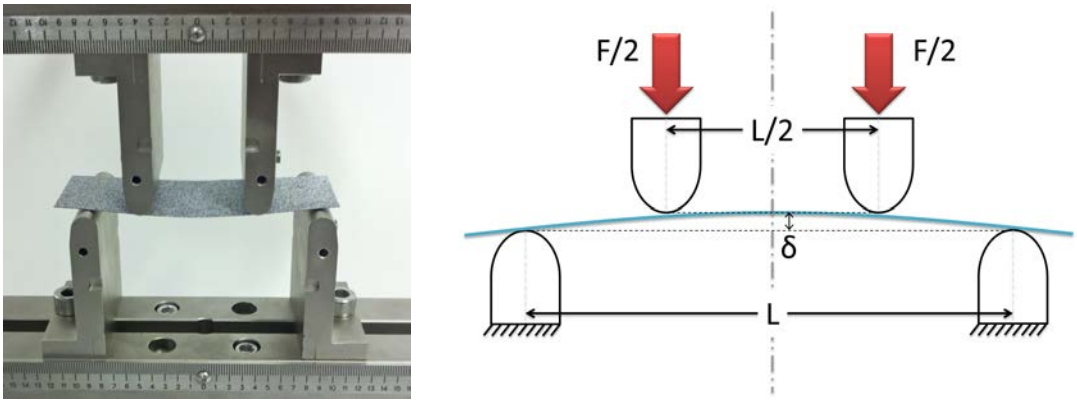

A B

Figure 7-1. Four point bend test setup. A) Example of the test setup for the four point bend test (wires not connected). Photo taken by Bradley LaCroix. B) Diagram of pin spacing and load application for four point bend test.

the outermost supports were spaced at 70 mm and the inner supports were spaced 35 mm apart.

7.2 Procedure

The 0.05 mm steel unimorph, 0.10 mm steel unimorph, and a unidirectional unimorph were tested. Two tests were conducted with each unimorph. For one test, the unimorph is actuated to 1500 V as the four point bend test is conducted. For the other test, the unimorph is inverted and actuated to -500 V while the test is conducted. The test procedure for the 1500 V case is outlined in Fig. 7-2 and the steps are detailed below.

The experimental steps were defined to minimize the effects of hysteresis. Since the curvature of the unimorph cannot be accurately predicted and replicated, except at the minimum and maximum voltages, these were chosen as the starting points for the experiment. Therefore, the experimental procedure was defined as follows:

1. Actuate the unimorph to -500 V (or 1500 V for inverted case).
2. Bring the fixture into slight contact with the unimorph so a small load is measured (0.1 N or 0.03 lbf).
3. Adjust the actuation of the unimorph to 1500 V (or -500 V for the inverted case).

www.manaraa.com

4. Record the load as the fixtures are moved apart from one another.
5. Stop and reverse the direction of motion once the load is at 0.44 N (0.1 lbf).
6. Record the load as the fixtures are moved toward one another.
7. Stop the fixtures when they return to their starting position.

For the -500 V test, the unimorph is flipped so the MFC part of the unimorph is on top. Then, the steps are repeated, except the voltages are interchanged, so that the test begins with 1500 V. The load is applied throughout the application of -500 V. The cyclic nature of this procedure allowed for the mechanical hysteresis of the unimorph to be studied. Furthermore, repetitions (not shown) indicated that the results did not vary to any significant degree.

7.3 Results

The results of the experiment are shown in Fig. 7-3. Reviewing the results, it is quickly evident that the thicker steel substrate outperforms the other two substrates in load bearing capacity. Closer examination reveals that it also outperforms in terms of overall displacement. The thinner steel has a larger displacement range than the unidirectional carbon fiber, but the unidirectional carbon fiber produces a larger load bearing capability. One remarkable aspect to these results is the fact that the MFCs are much weaker when actuated in the -500 V direction as compared to the 1500 V direction. The difference is approximately a factor of two.

These results indicate that the 0.10 mm steel is the preferred substrate for a MAV expected to encounter anything beyond very slight aerodynamic loads. As was shown with the FEA work in Section 6.5, it is possible that a thicker steel substrate may yield even more load bearing capacity than the 0.10 mm steel and may be better suited for the MAV examined in this research. This will be explored using the optimization scheme in Chapter 11.

www.manaraa.com

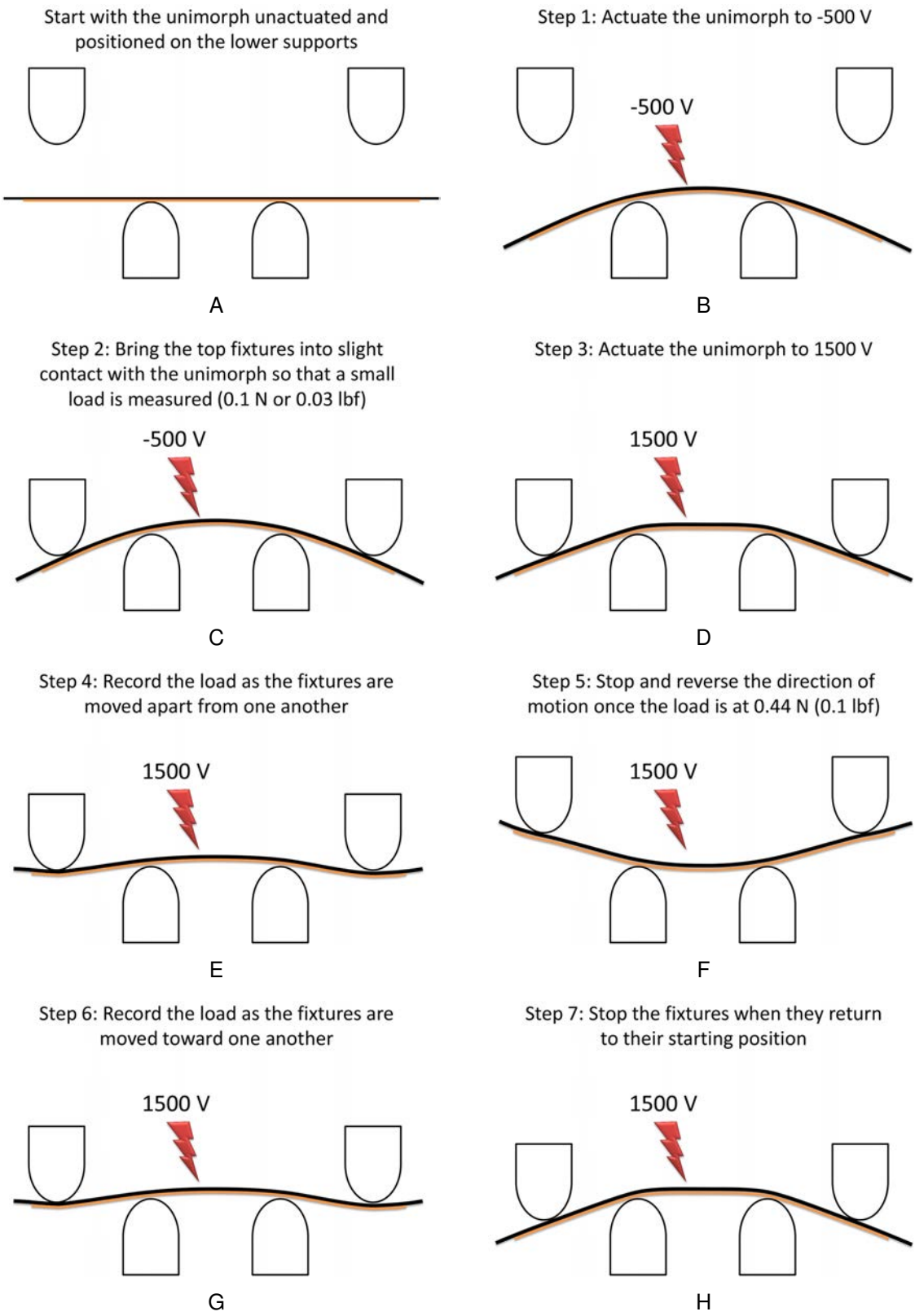

Figure 7-2. Four point bend test procedure for the 1500 V test.

www.manaraa.com

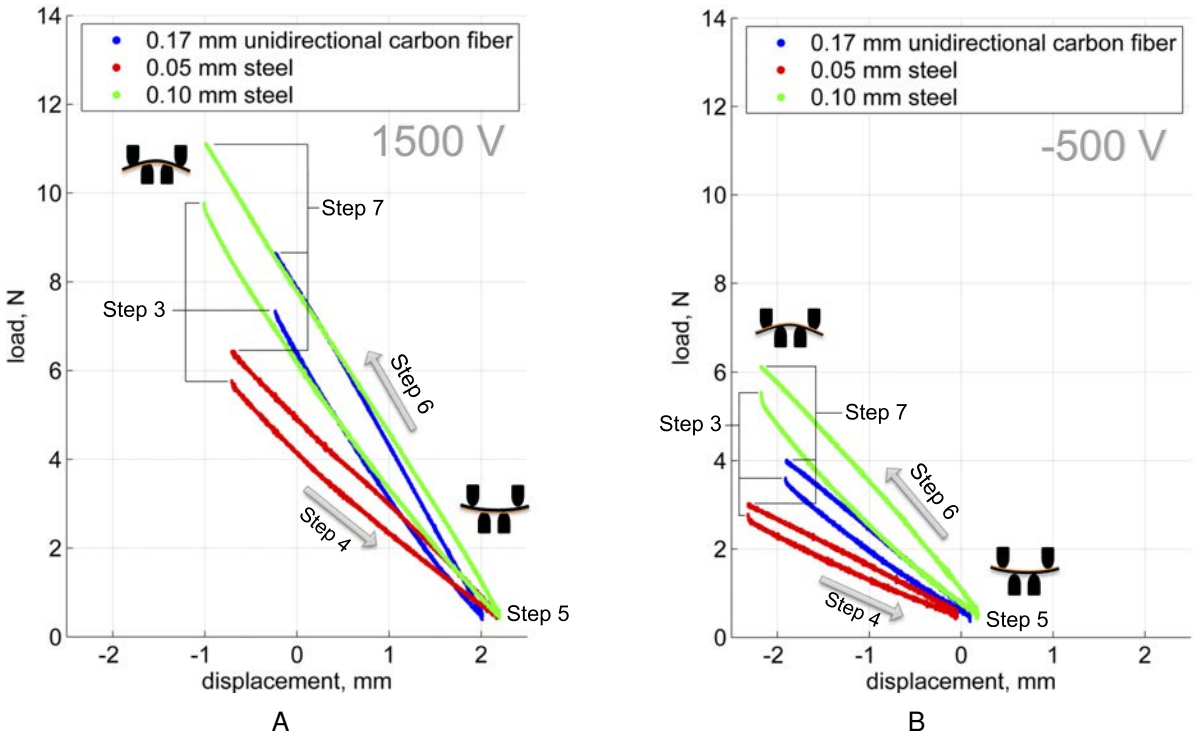

Figure 7-3. Four point bend experimental results. a) MFC actuated to -500 V, the fixtures brought into contact with the unimorph surface, then the MFC actuated to 1500 V. b) MFC actuated to 1500 V, the fixtures brought into contact with the unimorph surface, then the MFC actuated to -500 V.

www.manaraa.com

CHAPTER 8
INITIAL MAV DESIGN, LESSONS LEARNED, AND VALIDATION OF AERODYNAMIC MODEL ASSUMPTION

Shortly after the preliminary results were generated, a preliminary MAV with MFCs was manufactured. Rather then spend substantial time creating a sophisticated computer model around an unproven design, it was decided the best process was to experimentally test potential designs until one was found to provide suitable flight characteristics. Once a functional design was determined, additional resources could be contributed towards modeling and optimizing the design. The MAV discussed in this chapter is the first attempt at a MFC actuated MAV design.

The geometry of this MAV was built on a previously proven servo-controlled design which had gone through numerous revisions and improvements. To maximize the deflection generated by the MFCs, a batten reinforced membrane wing was chosen. It was expected that this would reduce the bending stiffness of the structure, allowing the MFCs to deflect further. A total of four MFCs, two M8507-P1 and two M8503-P1, were placed on the wing, as shown in Fig. 8-1. With the MFCs on each side connected in parallel, each side of the wing could be actuated independently. A servo controlled elevator and rudder were also incorporated into the design. The intent was not to couple the MFCs with the servos, but to use the servo actuated control surfaces to trim the aircraft and use only the MFCs for flight control.

8.1 Manufacturing

Manufacturing was performed using a pre-preg layup technique as shown in Fig. 8-2. The membrane was constructed of ripstop polyester and the battens were constructed of unidirectional carbon fiber. The leading edge was composed of three layers of bidirectional carbon fiber. The MFCs were laid on top of the battens before the entire layup was placed under vacuum pressure inside the oven for curing. After the curing process, the extra material was trimmed off the wing to achieve the final product.

www.manaraa.com

Figure 8-1. Images of the first MFC actuated MAV constructed under this research. Photos taken by Bradley LaCroix.

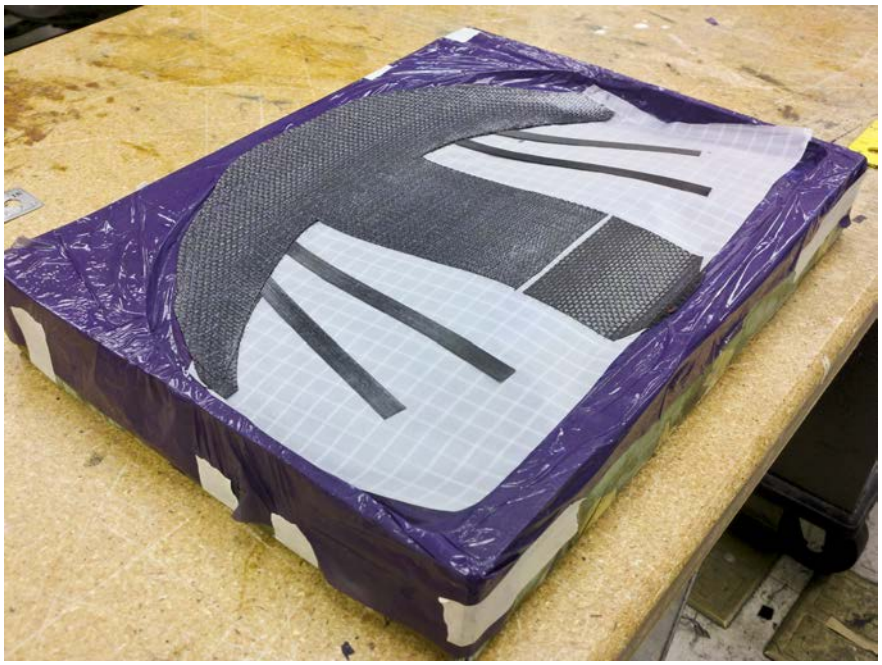

Figure 8-2. Manufacturing of the first MFC actuated MAV wing. Photo taken by Bradley LaCroix.

www.manaraa.com

Figure 8-3. DIC setup for first MFC actuated MAV wing. Photo taken by Bradley LaCroix.

8.2 DIC Testing

At this point, the wing was prepared for DIC testing, where a speckle pattern was applied to the surface of the wing. Next, the camera system and lighting was setup to illuminate the wing properly, without overexposing or silhouetting the structure. This setup is shown in Fig. 8-3. The wing was actuated through various voltages with the horizontal tail positioned in an approximate pitch-up, pitch-neutral, and pitch-down position.

Figure 8-4 shows the DIC results for three different actuated postions. A relatively large displacement can be commanded when the MFCs are actuated to the up-position. Conversely, a relatively small displacement occurs when actuating the MFCs to the down position. Furthermore, the horizontal tail strongly affects the position of the outboard portions of the wing as can be seen in Fig. 8-4C.

www.manaraa.com

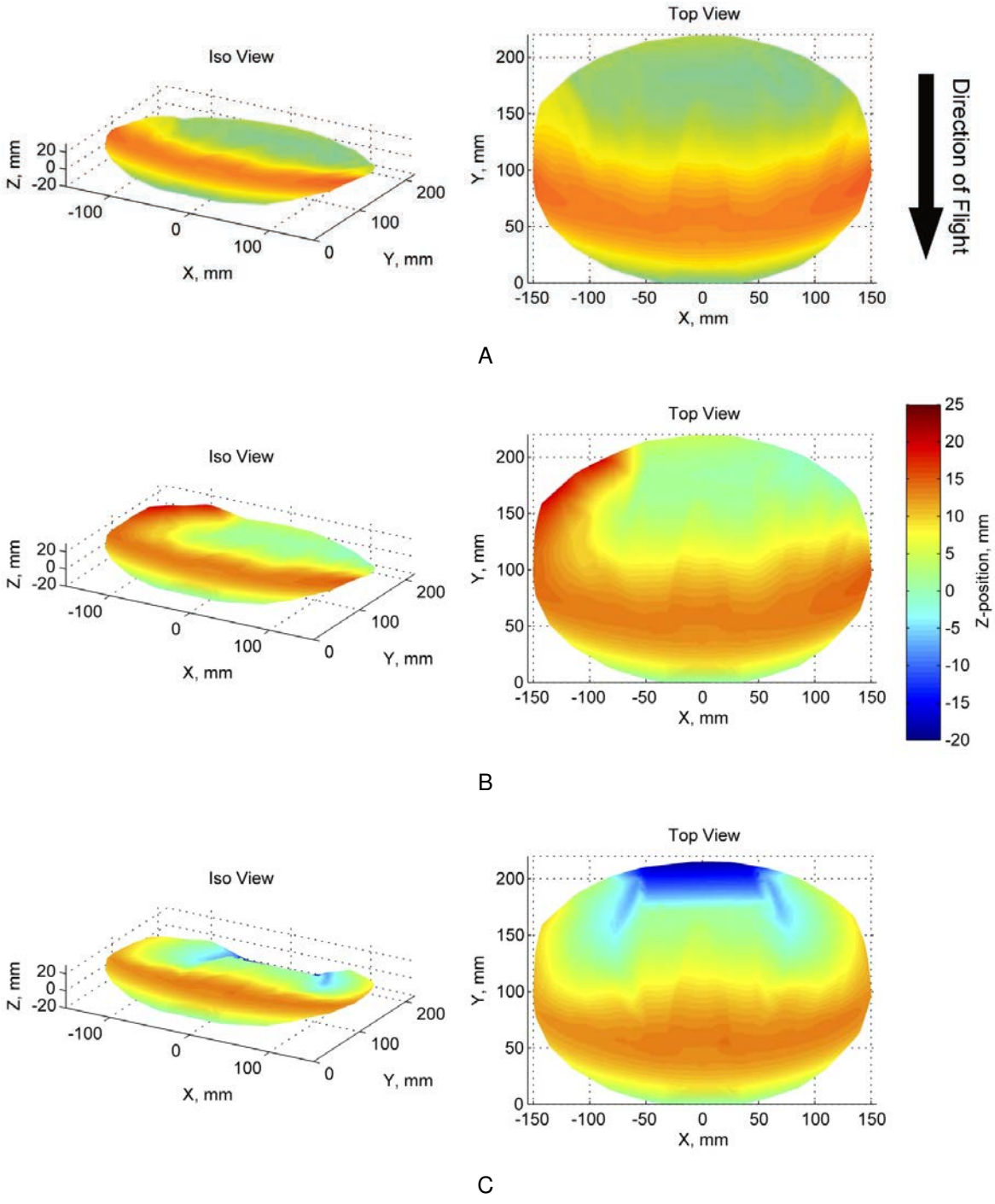

Figure 8-4. Digital image correlation results for the first MFC actuated MAV. A) Neutral position for all control surfaces. B) Full roll-left maneuver with the tail at the neutral position. C) MFCs actuated to full-up position with the tail actuated to a pitch-down position.

www.manaraa.com

8.3 Flight Testing

The flight test goal was to first trim the aircraft and reach adequate altitude and then switch to MFC control to evaluate the MFC performance. Numerous flight tests showed that the aircraft was relatively heavy for its wing area. This made it difficult to fly for more than a few seconds. Furthermore, the membrane at the wingtips appeared to allow airflow to spill over and dump lift. Additional structure was added at the tips to try to mitigate this problem. The final flight test was successful in producing roll control of the airplane with the assistance of pitch control from the servo-actuated horizontal tail, but there was still substantial room for improvement.

8.4 Discussion and Lessons Learned

One of the main aspects that may have limited the performance of the aircraft was the relatively compliant nature of the wing and MFCs. Even though the stationary actuation of MFCs was on the order of 25 mm, aerodynamic loads may have drastically reduced this. Furthermore, slack and vibration in the wing may have made stable flight an inherent impossibility. In addition, the MFCs were positioned towards the trailing edge of the battens. Due to aeroelasticity, it is likely that the MFCs were likely being pushed up or down along with the rest of the wing membrane. Lastly, the relatively low aspect ratio of the wing may have made it largely inefficient and difficult to maneuver.

There are also drawbacks to take into account when considering the computer modeling aspect of the aircraft. Due to the large difference in the material properties in the membrane wing (transitioning abruptly from carbon fiber composite to polyester), finite element modeling and aerodynamic predictions could yield a variety of problems. This would make the computer modeling aspect extremely challenging. Along with the previously mentioned negative flight characteristics, it was determined that a solid carbon fiber wing would be preferential. The next chapter details the attempts to correct these issues by investigating other potential designs. The remaining portion

www.manaraa.com

of this chapter considers the key assumption made when modeling a flexible wing in aerodynamic software.

8.5 Aerodynamic Assumption Validation

One of the key aspects of this research is the calculation of the aerodynamic load on an airframe for a particular design. To do this quickly and efficiently, a program called Athena Vortex Lattice (AVL) was used [35]. This program was developed by Mark Drela and Harold Youngren at MIT. It provides the necessary framework to calculate the aerodynamic and flight-dynamic properties of a rigid aircraft of arbitrary configuration. It utilizes an extended vortex lattice model for the lifting surfaces, as well as a slender-body model for the fuselage. One drawback of AVL is that it only gives an inviscid approximation, which tends to underestimate drag and overestimate lift. Nonetheless, it has been widely used in the research field due to its relatively fast computational time [63–68] and has been independently validated numerous times [69, 70].

A couple MAVs with a similar geometry to the revised MAV (to be discussed in Chapter 9) also use AVL for their analysis. The first MAV, mentioned in Section 2.2, was developed by Stanford and Mujahid at the University of Florida, and incorporated torque rods for actuated roll control [68]. The torque rod enables the outboard section of the wing to be twisted up or down using traditional servos. Another example from AVL is an Air Force Research Laboratory MAV, GENMAV [69], intended to be used for a variety of missions. This design was later outfitted with MFCs as shown in Ohanian's work in Section 2.1 [29].

The key assumption in AVL is that the structure is perfectly rigid and does not deform under loading. However, MAVs constructed of membrane materials and the ones found in this project, which may be constructed of only one or two layers of carbon fiber composite, can be relatively compliant. To verify that an additional phenomena is not present, such as oscillations which may cause the flow to separate or, conversely,

www.manaraa.com

improve flow attachment, a separate set of experiments were conducted. These experiments are described in detail in the following sections.

8.5.1 Background and Concept Outline

Micro Air Vehicles (MAVs) are operated at low Reynolds numbers which makes them easily influenced by small disturbances. A relatively small degree of turbulence can have profound effects on the flight stability and flight path. In addition, the tip vortices produced at the wingtips can be quite large in comparison to the wing due to the low aspect ratio. Gusts can very likely be on the same order of magnitude as the forward velocity of the MAV (up to 15 m/s), which could result in immediate instability. A flexible membrane wing shape dampens such disturbances and can help to resist flow separation, reducing erratic behavior that is commonly associated with low profile wings of this size [30, 71].

However, the flight mechanics of flexible membrane wings are not fully understood. One common assumption when generating a computational analysis for such a wing is that the deformed shape, in steady state, behaves the same as its rigid counterpart. To this extent, finite element software is normally coupled with AVL which predicts the lift, drag, and moments. The finite element software and AVL software iterate until they converge on a solution. When calculating the aerodynamic loads, AVL treats the structure as perfectly rigid. Figure 8-5 shows this general concept.

In the software setup for this research, the FEA software predicts the deformed shape of the wing under actuation. Next, AVL predicts the aerodynamic loads for this geometry. The aerodynamic loads are passed back to the FEA software, which calculates the new geometry. The process is iterated until the results converge. This process is further explained in Chapter 10. However, the assumption that the wing can be treated as perfectly rigid during the AVL analysis has never been tested. The purpose of this set of experiments is to further investigate the flight mechanics of flexible membrane wings and to determine if the perfectly rigid assumption is appropriate.

www.manaraa.com

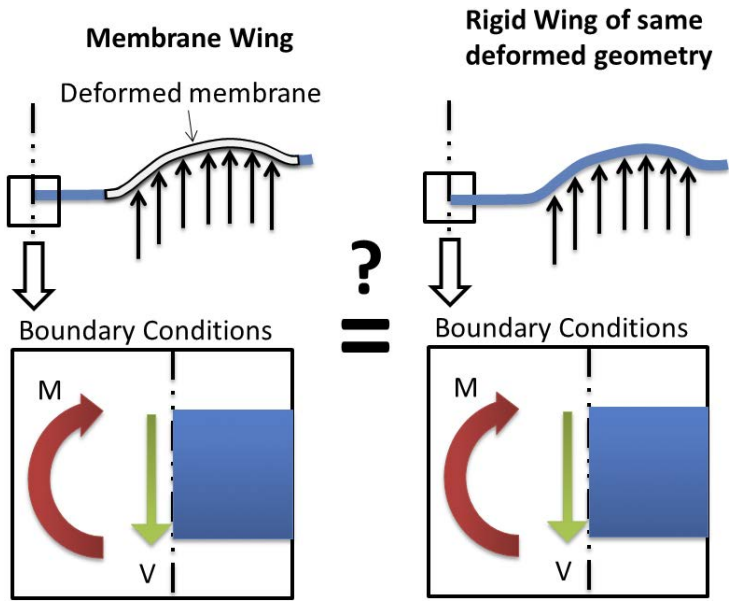

Figure 8-5. Conceptual illustration of rigid vs. flexible wing loading.

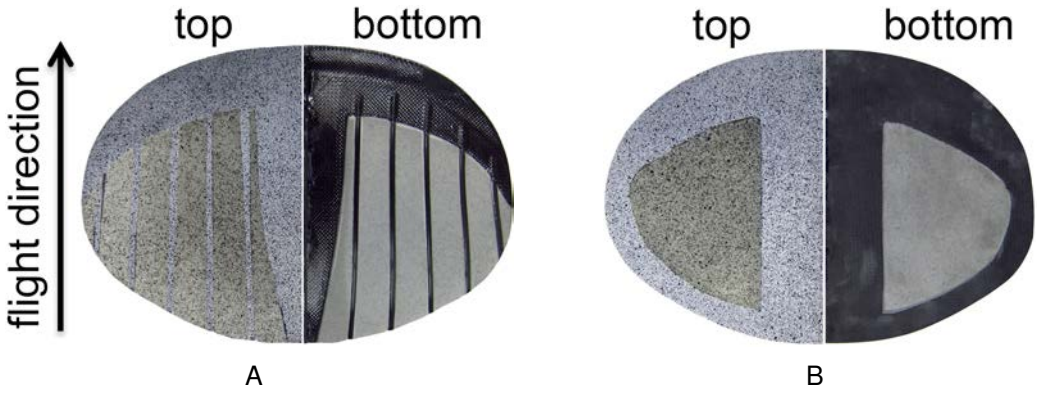

Figure 8-6. Flipside view of silicone membrane wings. A) Batten reinforced silicone membrane wing. B) Perimeter reinforced silicone membrane wing. Photos taken by Bradley LaCroix.

To test this assumption, two flexible membrane wings were manufactured, one perimeter reinforced and the other batten reinforced, shown in Fig. 8-6. Silicone was chosen for the membrane material. This is because it is relatively easy to pretension in a uniform manner and it does not degrade with time [72], which is critical for this set of experiments. DIC was used in the wind tunnel to acquire the three dimensional profiles of the wings while under different flight conditions.

www.manaraa.com

The 3D profiles for each wing were converted to CNC code and molds were manufactured representing the deformed wings while under load. Using these molds, four approximately rigid wings were fabricated: two representing the BR wing at two flight conditions and two representing the PR wing at two flight conditions.

The intent was to match up the flexible wing geometry with the rigid counterpart under the same flight conditions. Detailed measurements of the lift and drag were taken of the four rigid wings as well as the two flexible wings using a 6DOF sting balance and DIC. The DIC could then quantify the quality of fit between the rigid and flexible profiles of each wing. Afterwards, the measurements were analyzed and the flexible-rigid assumption analyzed.

8.5.2 Initial Experiments

Two sets of experiments were conducted. The goal of the initial set of experiments was to map the 3D geometry of the flexible wings at different flight conditions. This 3D geometry was then used to generate a set of rigid wings used in the second set of experiments. During this second set of experiments, the flexible wings were compared to the rigid wings at identical flight conditions in which the flexible wing deformed to the same shape as their rigid counterparts. This process is described in the following sections.

8.5.2.1 Manufacturing

Two wings were fabricated with pre-preg carbon fiber using the mold for the initial MAV. The wings were fabricated in a single process using a lay-up method where the pre-preg carbon fiber and membrane material were cut and assembled on the mold and then cured under vacuum pressure at 1 atmosphere and 260°F. This results in a heterogeneous wing manufactured as a single part.

The PR frame was made up of 4 layers of bidirectional carbon fiber. This large number of layers was used to insure that the frame of the wing would be relatively rigid, with only the membrane in the middle deforming. The BR wing had the same 4-layer

www.manaraa.com

A B

Figure 8-7. Isometric view of silicone membrane wings. A) Batten reinforced silicone membrane wing. B) Perimeter reinforced silicone membrane wing. Photos taken by Bradley LaCroix.

construction on the leading edge; however the battens were composed of 2 layers of unidirectional carbon fiber. These wings are shown in Fig. 8-7 as well as in the previous section in Fig. 8-6. The membrane material for both wings was made of pre-fabricated silicone. The silicone material allows for uniform and repeatable pretensioning [72]. Furthermore, it has been shown that treating the silicone with a corona treatment machine improves the adhesion between the pre-preg carbon fiber and silicone [73, 74]. Before applying the silicone, it was treated with a corona treatment device, Model BD-20 manufactured by Electro-Technic Products, Inc, to strengthen the bond between the epoxy in the carbon fiber pre-preg and the silicone.

After curing, the edges of the wing were sanded and trimmed such that their outlines were identical. To utilize DIC, a high contrast black and white speckle pattern was applied to the top surface of each wing. The silicone, which was already white, was masked off prior to applying a white coat of paint to the carbon fiber. Then the black speckle pattern was sprayed over the entire top surface of both wings. The silicone is only coated with black speckles, since the paint can crack and flake if applied in a uniform coat on the highly elastic silicone.

www.manaraa.com

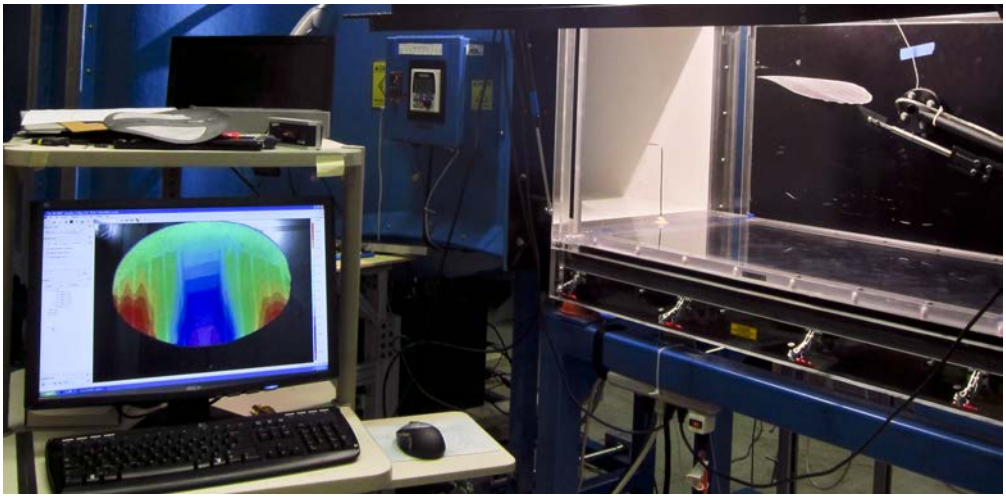

Figure 8-8. Flexible wing wind tunnel setup with DIC. Photo taken by Bradley LaCroix.

8.5.2.2 Testing Procedure

The two wings were positioned in the wind tunnel and tested under various angles of attack ranging from 0° to 15° and wind speeds of 10 to 15 m/s. Before each run, a reference image was taken of the wing positioned at its respective angle of attack. This image was used to calculate the displacement of the wing during testing. During the runs, multiple images were taken using the DIC system and accompanying VIC-Snap 2007 software. The DIC cameras used were manufactured by Point Grey Research (GRAS-50S5M-C) and the lenses are Schneider-Kreuznach Xenoplan 1.4/17-0513. Ten pictures were taken at each condition so that any oscillations could be averaged out numerically using post-processing. VIC-3D 2009 was used to analyze the images and to generate a three dimensional set of points representing the deformed shape of the wings. Figure 8-8 shows the wind tunnel setup with the DIC system on the left and the wing on a rotating angle-of-attack arm positioned within the wind tunnel on the right. Figure 8-9A shows a view of the BR wing placed on the angle-of-attack arm and Fig. 8-9B shows the positioning of the DIC camera system over the BR wing above the ceiling of the wind tunnel.

www.manaraa.com

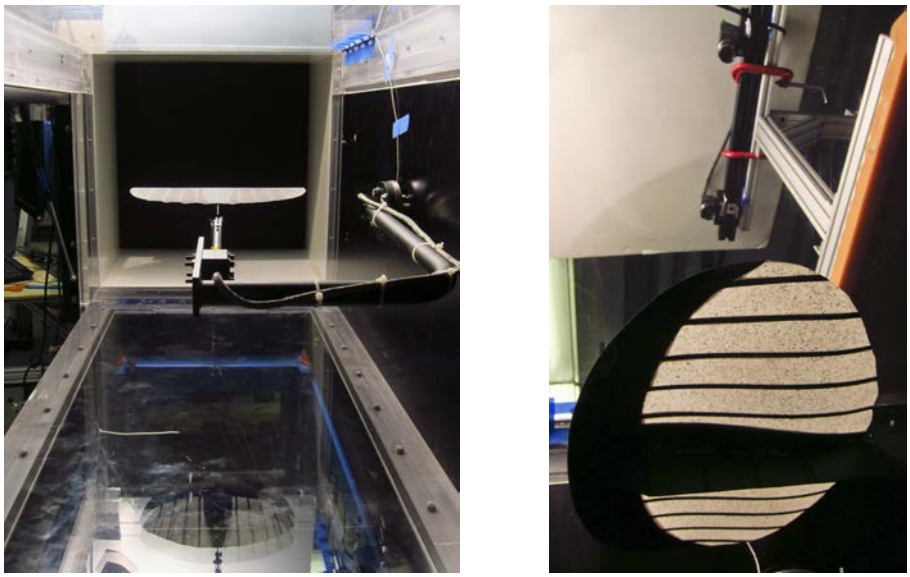

A B

Figure 8-9. Flexible membrane wing in the wind tunnel. A) Rear view of the membrane wing. B) Underside view of the membrane wing with the DIC cameras in the background. Photos taken by Bradley LaCroix.

Lift and drag measurements were not taken in this segment of testing since the flexible wings needed to be re-tested at the next stage of testing to ensure proper matching of geometry and dynamic pressure. For example, even if the same wind speed and angle of attack of the initial test is used during the second segment of testing, conditions such as temperature and humidity can change, which affects the dynamic pressure. This can have a significant effect on aerodynamic forces. Therefore, in the second stage of testing, a combination of visual differencing between the flexible wing and rigid wing took place as well as a least-squares error calculation to accurately adjust and closely match the deformed shape of the flexible wing to the shape of the rigid wing.

8.5.2.3 Digital Image Correlation Post Processing

The results of the wind tunnel tests were exported from VIC-2009 as plain ASCII text files. These text files include the X, Y, and Z coordinates of approximately 40,000 points as well as their respective displacements in the U, V, and W directions for each image. These text files were imported into MATLAB and then post-processed.

www.manaraa.com

One of the key advantages of post-processing the results in MATLAB is the precise transformation of the results into the desired coordinate system. The deformed values shown on the monitor in Fig. 8-8 make the wing appear to be asymmetrically deformed. This is because the angle-of-attack arm can pitch upwards and roll slightly when aerodynamically loaded, thereby causing a seemingly larger deformation on the left side of the wing. Furthermore, the default reference frame of the DIC may not be orthogonal with respect to the plane of the wing. MATLAB was used to effectively remove the rigid body rotation and transform the data to the desired orientation within the coordinate system using coordinate transformations.

The steps for this, which are illustrated in Fig. 8-10, are as follow.

1. After loading the data into MATLAB, the coordinate system of the reference data was transformed to the correct orientation by taking the reference X, Y, and Z coordinates and applying coordinate transformation so that the X-Y plane was aligned to the plane of the wing.
2. The coordinate transformations were also applied to the U, V, and W vectors to maintain the correct displacement directions.
3. The XYZ and UVW data was then combined (X + U, Y + V, Z + W) to generate a set of deformed data for each image.
4. This data was then interpolated into a uniform grid pattern to assure standardization across all images at a particular angle of attack and airspeed.
5. Finally, this data was transformed to subtract out the rigid body rotation of the wing due to the movement of the angle-of-attack arm.

Figures 8-11 and 8-12 show the final result of the transformations along with the out-of-plane deformation for both the PR and BR wing. The transformed geometry, as shown in Figs. 8-11A and 8-12A, illustrates the contours of the deformed surface. In contrast, the out-of-plane deformation, shown in Figs. 8-11B and 8-12B shows how much the wing deforms in the out-of-the-page sense. In other words, it is the change in the Z-position (ΔZ) rather than a specific Z-value. Additional steps are required to convert the data into CNC format which is covered in the following section.

www.manaraa.com

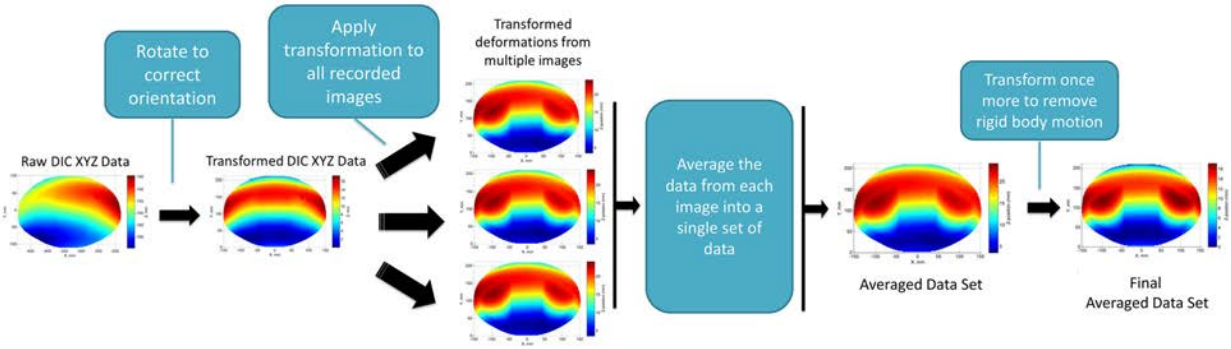

Figure 8-10. Illustration of DIC post processing procedure.

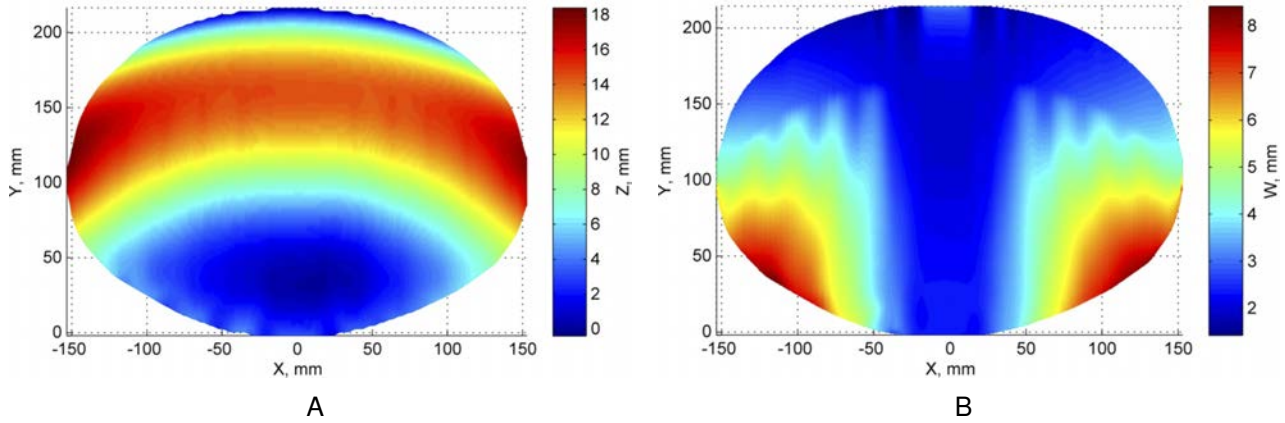

Figure 8-11. DIC results for the batten reinforced flexible membrane wing.
A) Transformed reference geometry for the batten reinforced wing.
B) Out-of-plane deformation for the batten reinforced wing.

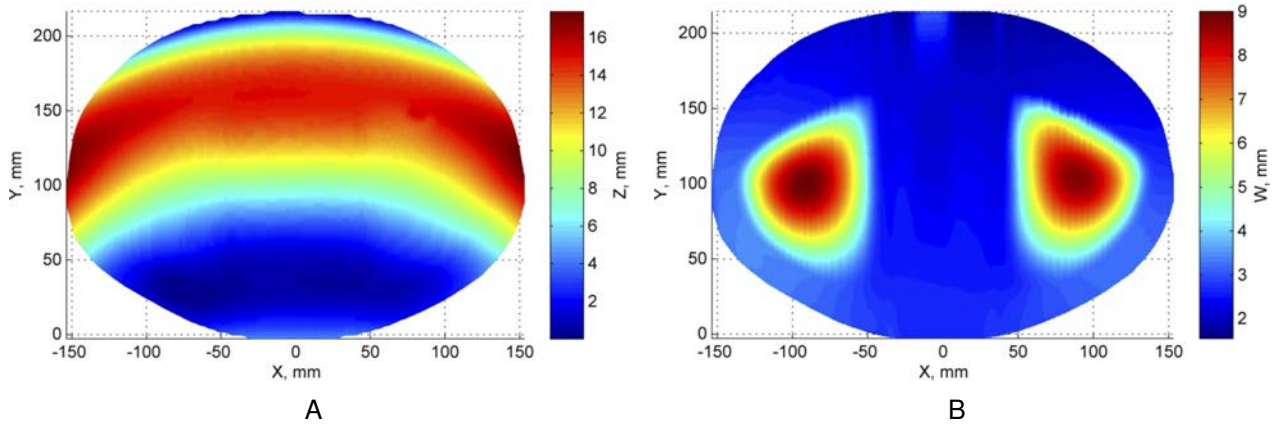

Figure 8-12. DIC results for the perimeter reinforced flexible membrane wing.
A) Transformed reference geometry for the perimeter reinforced wing.
B) Out-of-plane deformation for the perimeter reinforced wing.

www.manaraa.com

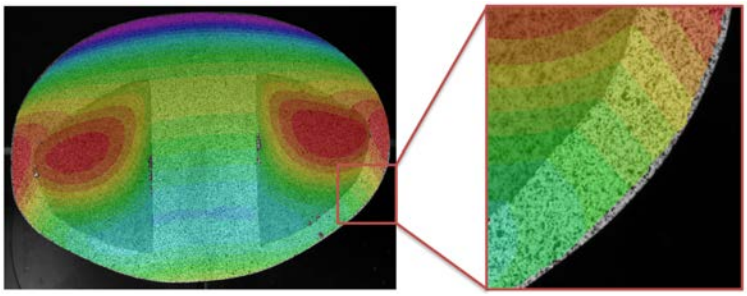

Figure 8-13. Geometric edge truncation of DIC.

8.5.3 Rigid Wing Manufacturing

One of the key drawbacks of DIC when utilizing it as a replication method is that it is unable to correlate the surface all the way to the edge. This is shown in Fig. 8-13 where the color overlay suddenly stops near the edge. This truncation can be moderately reduced by changing settings in the DIC software, but cannot be completely eliminated. Therefore, it is necessary to generate a technique by which the known geometry can be extrapolated to approximately replicate the true geometry. This is described in the following section.

8.5.3.1 Extrapolation and Conversion of DIC Data to CNC Format

Various extrapolation techniques were examined using a variety of curve fits. However, it was determined that a linear extrapolation technique was the best approach for this project. Since the extrapolation length was relatively small and also because higher order polynomials have a tendency to give asymptotic results, a linear extrapolation technique was deemed most appropriate. The extrapolation process itself takes place over three steps. The first step was to designate the points of interest for the extrapolation. With this in mind, a set number of points around the perimeter were selected, which are shown in black in Fig. 8-14. Second, the data was extrapolated row by row and column by column in two directions, the longitudinal and lateral direction, with the condition that there were two data points at that row or column. The extrapolated values are designated by the red and green circles in Fig. 8-14. The

www.manaraa.com

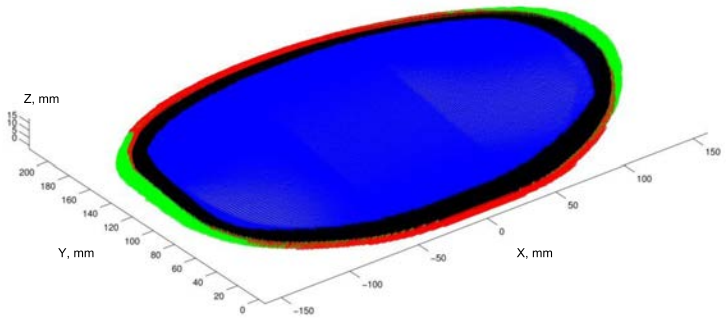

Figure 8-14. Extrapolation of DIC data to restore uncorrelated geometry. The black dots indicate the reference points for the extrapolation whereas the red points designate the longitudinal extrapolation and the green points designate the lateral extrapolation.

data for the wing was extrapolated slightly beyond its original planform dimensions to ensure that the mold would be large enough to properly fabricate the wing. Finally, any points where the data was extrapolated both in the longitudinal and lateral direction were averaged to generate a single data point.

Even though the linear extrapolation technique was determined to be the most rigorous, it still produced some resulting data points that were outliers. This can be especially problematic on a CNC machine where the outlying points can command the bit to dive deep into the material causing a large gouge. To rectify this issue, a smoothing function was utilized around the perimeter of the wing. This technique is shown in Fig. 8-15.

At this point, the data points can be arranged into a CNC code based on the desired tool path. Modified MATLAB code, originally written by Claxton [70], was used to make the conversion.

8.5.3.2 Fabrication

The manufacturing process is shown in Fig. 8-16 where the CNC toolpath, generated in MATLAB is shown, followed by the completed CNC mold, and the rigid counterpart for the perimeter reinforced wing. The CNC tool path is generated based on

www.manaraa.com

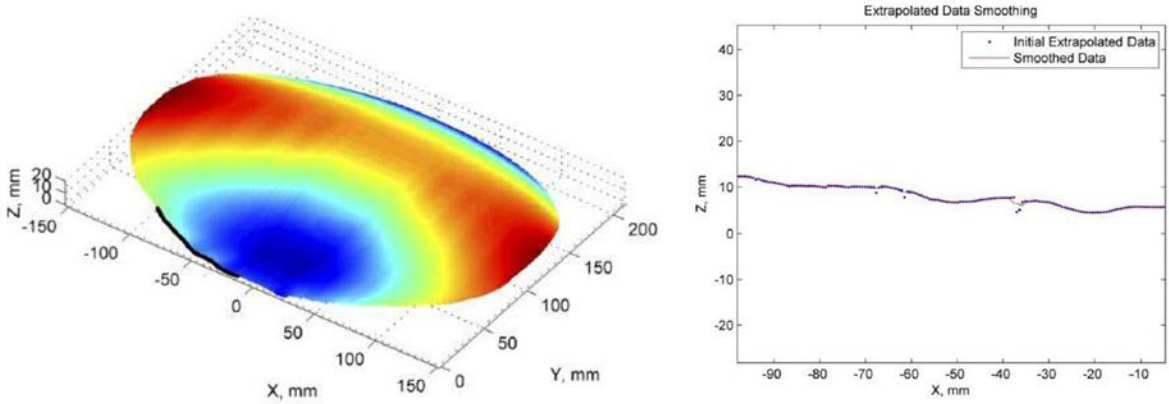

A B

Figure 8-15. Smoothing technique for extrapolated DIC data. A) Indication of trailing edge data (in black) containing outliers. B) Original data (blue dots) and smoothed data (red line).

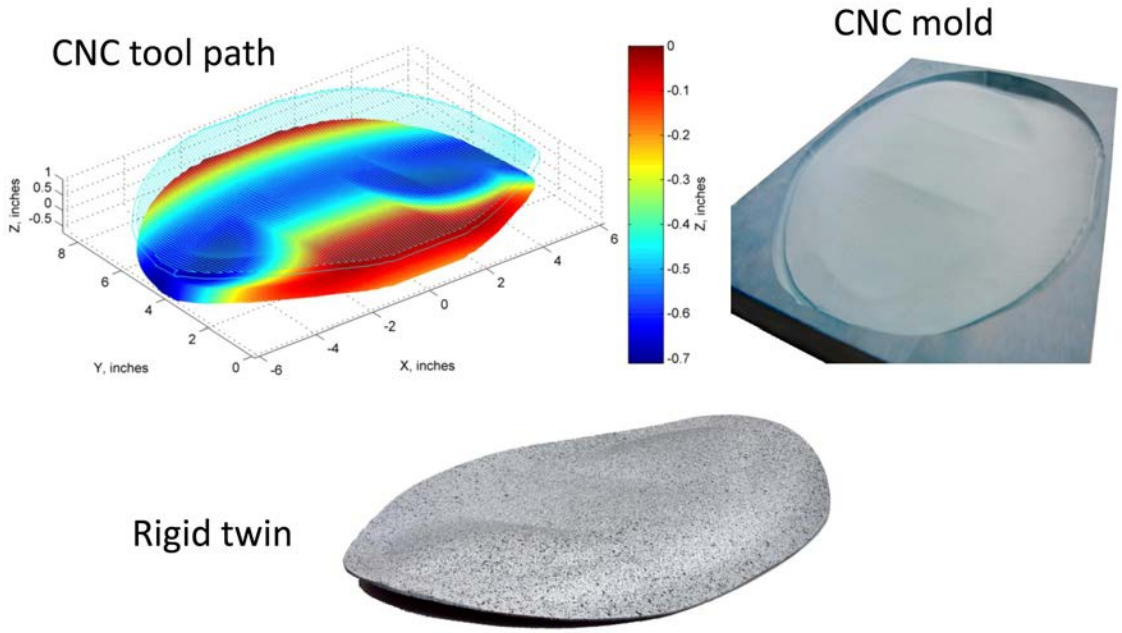

Figure 8-16. Illustrated rigid wing manufacturing process. Photo taken by Bradley LaCroix.

various parameters such as tool diameter, scallop height (ridges between tool passes), and spacing of data points.

The lay-up method for the rigid wing is similar to the flexible wings (as described in Section 8.5.2.1), but only carbon fiber pre-preg is used. 4 layers of bidirectional carbon

www.manaraa.com

Figure 8-17. Rigid wing counterparts. The perimeter reinforced wings are shown on the left and the batten reinforced wings are shown on the right. Photo taken by Bradley LaCroix.

fiber are used to fabricate a wing measuring approximately 1 mm in thickness. The four resulting rigid wings are shown in Fig. 8-17.

Benchtop DIC tests were performed on the rigid wings to verify that there was reasonable agreement between the recorded profiles for the deformed flexible wings.

8.5.4 Validation Experiments

In the validation set of tests, each respective flexible wing was tested first. The flight conditions were adjusted until the 3D profiles presented good agreement with the original recorded profiles. The new 3D profile was recorded and the lift and drag measurements taken. Then, the rigid wing counterparts were placed in the wind tunnel at the same flight conditions and the 3D profile recorded while the lift and drag was measured using the sting balance. The 3D profile for the flexible wings were then compared with the 3D profiles for the rigid counterparts. These comparisons are shown in Figs. 8-18 and 8-19.

A positive value indicates that the rigid wing protrudes above the flexible wing (out-of-the-page) whereas a negative value indicates that the flexible wing protrudes above the rigid wing. The color scale in each figure is set from -1 mm to 1 mm. The

www.manaraa.com

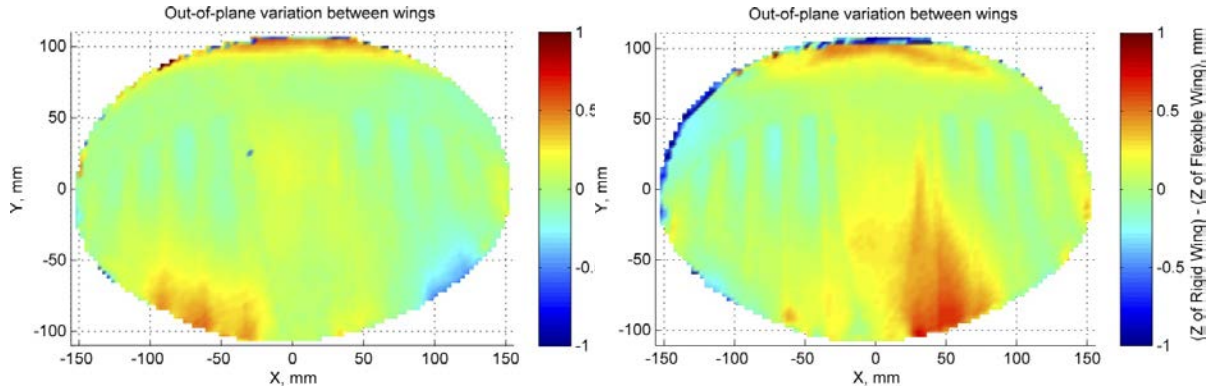

Figure 8-18. Comparison of flexible and rigid batten reinforced wings. A) Batten reinforced wing at 15 m/s and 8.5° angle of attack. B) Batten reinforced wing at 15.5 m/s and 14° angle of attack.

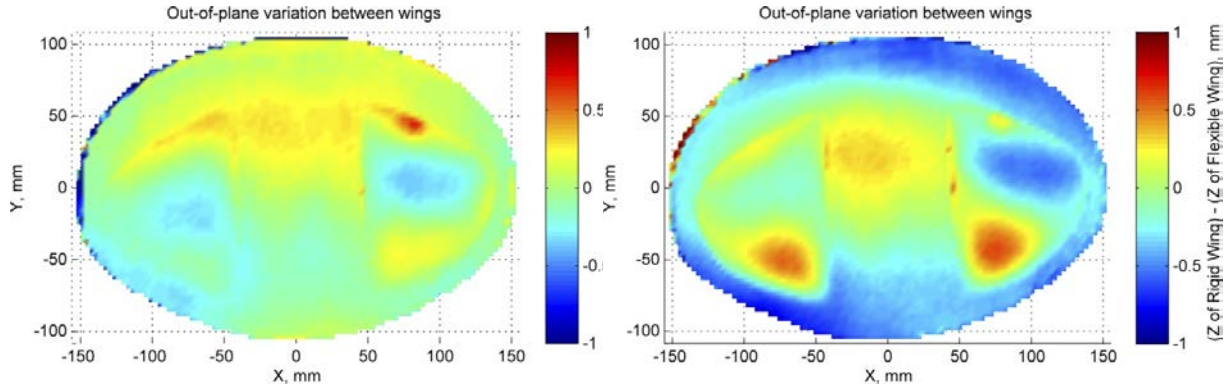

Figure 8-19. Comparison of flexible and rigid perimeter reinforced wings. A) Perimeter reinforced wing at 17 m/s and 4° angle of attack. B) Perimeter reinforced wing at 17 m/s and 8° angle of attack.

summary of flight conditions, profile agreement, and measured lift and drag forces, are shown in Table 8-1. Note that the coefficient of lift and drag are nearly identical in every case, with perimeter reinforced wing having the largest percent differences. Even though these percent differences are larger, the magnitude is still quite small, especially when considering the magnitude of the coefficients. This leads to the conclusion that there is ultimately no difference in steady state lift and drag between the flexible wing and its rigid counterpart.

www.manaraa.com

Table 8-1. Results of the rigid and flexible wing comparison.

			Profile Agreement		Rigid Wing		Flexible Wing			
	AoA (degrees)	Velocity (m/s)	RMS Error (mm)	Avg Error (mm)	C_L	C_D	C_L	C_D	% Diff in C_L	% Diff in C_D
BR 1	8.5	15.0	0.17	-0.03	1.23	0.24	1.22	0.24	-1.0	-1.6
BR 2	14.0	15.5	0.24	-0.07	1.76	0.52	1.78	0.53	1.2	0.3
PR 1	4.0	17.0	0.27	0.03	0.77	0.10	0.74	0.10	-3.3	-0.3
PR 2	8.0	17.0	0.36	0.17	1.33	0.25	1.29	0.25	-2.8	-2.4

8.5.5 Discussion

This set of experiments successfully demonstrated that a perfectly rigid wing assumption in AVL is valid as long as the deformed profile is the input geometry. This means thats a program incorporating both AVL and a finite element solver, such as Abaqus, can be used to determine the aerodynamic loads and deformed state of a wing on a MAV. Furthermore, this provides a method by which various designs utilizing MFCs can be studied relatively quickly and efficiently.

Perhaps one of the most significant results of this set of experiments is the proof of concept that DIC can be used to create a reasonably accurate copy of a 3D geometry. With a degree of error of less than ± 1 mm for a 305 mm wing, this is equivalent to a replication accuracy of $\pm 0.3\%$. This was seen with all four rigid wing counterparts.

www.manaraa.com

CHAPTER 9
FORWARD SWEPT MAV

After conducting numerous test flights with the elliptical MAV, it was decided to make a complete design revision. The goal of the initial stage of flight testing was to narrow down the design space from a broad range of options to develop a design capable of a few minutes of flight. Once a flight worthy plane was developed, further analysis could be conducted and revisions could be made to make a well rounded aircraft. Ultimately, the main goal was to develop a platform which would be capable of sufficient control authority, but with only two MFC actuators. Excluding electronics, the MFCs on a two actuator aircraft account for roughly 90% of the material costs. Therefore, doubling the number of actuators would nearly double the aircraft's cost. From laboratory testing and previous test flights, it was known that the MFCs generated relatively small deflections compared to servo-actuated control surfaces. Therefore, in developing a new aircraft, it was decided to maximize the control authority by choosing the best planform and by finding the ideal placement for the MFCs.

9.1 Concept Evaluation

Figure 9-1 illustrates the conceptual thought process behind the consideration of the three traditional aircraft designs. With a rear swept wing, placing the MFCs inboard would result in poor roll control and poor pitch control because the MFCs are located close to the Center of Gravity (CG) both in the lateral direction and in the longitudinal direction. Placing the MFCs outboard has more potential, but since the wings are relatively compliant, this design is subject to the effects of aeroelasticity and control reversal. Aeroelastic effects are a result of aerodynamic loads changing the shape of the structure. In a more severe case, the aeroelastic effects will deform the wing in such a way that a control input results in an opposite response. Therefore, a rear swept wing with the MFCs placed outboard would require sufficient structural reinforcement.

www.manaraa.com

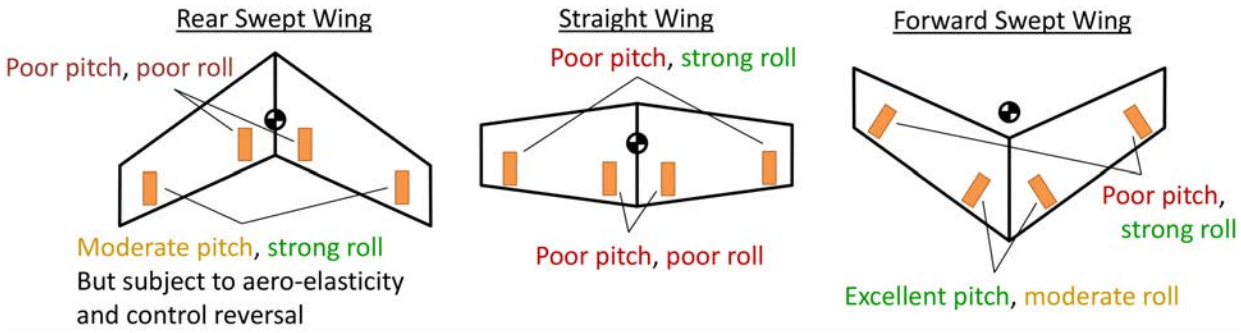

Figure 9-1. Design considerations for MFC planform.

A straight wing would be capable of very little pitch autority since the MFCs cannot be positioned more than a small distance from the CG. Roll control would be acceptable if the MFCs were placed outboard.

For the forward swept design, placing the MFCs outboard would result in very little pitch authority since the MFCs are longitudinally close to the CG, but may produce acceptable roll control with sufficient structural reinforcement. The best position for the MFCs may be near the inboard section, where they are a large longitudinal distance from the CG. Roll control would be acceptable if the deformation of the MFC actuator translates outboard on the wing. In addition, the aeroelastic response of the wing may be tuned by adjusting the fiber orientation in the wing layup.

Another concern, for MAVs in general, is the overall pitch authority. MAVs, due to their operation at lower Reynolds numbers and more flexible wings, require a large degree of pitch authority for adequate control. However, roll authority is generally within an acceptable region for most designs. For this reason, it is important to maximize pitch authority as much as possible and then maximize roll authority accordingly. Therefore, the MFCs should be placed towards the rear-most portion of the wing, which in the forward swept wing case, is towards the inboard section.

Other factors make the forward swept design slightly better than the rear swept design. For example, prop-wash can improve control surface authority due to increased air flow. This is especially true at lower speeds, when control authority is usually

www.manaraa.com

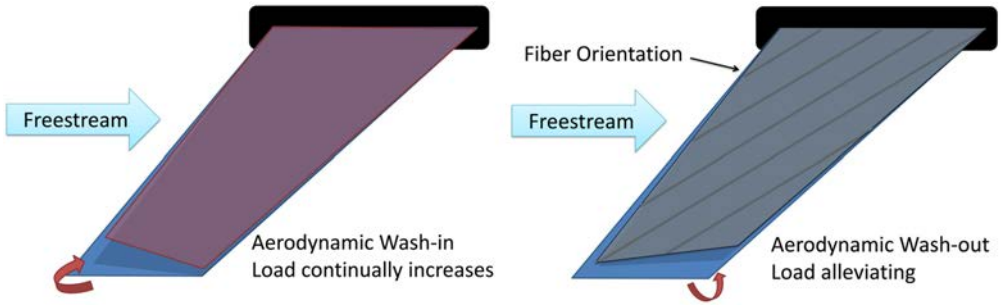

Figure 9-2. Illustration of an isotropic wing vs a bend-twist coupled wing.

reduced, due to reduced air flow. However, if the actuated area is in the prop-wash, flight control can be maintained even at lower speeds. Furthermore, if the MFCs were placed outboard on the wing, they would not be within the prop-wash region and have less control authority for a majority of the flight regime. These considerations indicate that the forward swept wing may be a superior solution when selecting a planform for the MFCs.

To mitigate aerodynamic instabilities for the forward swept wing design, bend-twist coupling can be incorporated into the wing. Bend-twist coupling is a response of orthotropic materials in which a pure bending moment results in a bending AND twisting response from the material. This behavior is demonstrated extremely well in Fig. 4-8A, where a load applied to only one corner of the cantilevered subject results in bending, but also in twisting in the opposite direction of the load. The benefit of bend-twist coupling in a forward swept wing is demonstrated by Fig. 9-2. For an isotropic forward swept wing, aerodynamic loads will lift the front edge of the wing up resulting in twist, which in return increases the aerodynamic loads even further. This can create severe instabilities during flight. The upward twist is because a majority of the lift on the wing is in front of the halfway point, near the quarter-chord location. As the isotropic wing is loaded, it will continue to twist upwards. Essentially, this is a positive feedback loop that can lead to other problems like flutter and divergence.

In comparison, when a forward swept wing incorporates bend-twist coupling by orienting the fibers in the direction shown, the twisting of the wing will be mitigated

www.manaraa.com

or even slightly reversed, therefore reducing lift. This results in a negative feedback loop in which high loads will lead to reduced loads, therefore alleviating instabilities. The forward swept wing design with bend-twist coupling will be studied in detail for the remainder of this chapter.

9.2 Motivation

Forward swept wings first made their debut during World War II, in the form of the German bomber, Junkers Ju 287. The airplane had a forward wing sweep of 25 degrees. Several years later, the Messerschmitt of Germany produced the HFB 320 Hansa aircraft. The next forward swept wing aircraft was not until 1984, with the release of the Grumman X-29.

Forward swept wings have a few advantages when compared to traditonal straight or swept wings. Firstly, they promise to be slightly more efficient, since the air flow over the wing forces air inboard rather than outboard, which reduces wing tip vortices. Secondly, assuming a well designed structure, they can be more agile when conducting complex maneuvers. However, if the structure is ill-designed, aeroelastic divergence can rapidly cause the plane to become unstable. Pamadi further adds that forward swept wings generally have favorable stall characteristics. Contrary to rear swept wings, the root regions stall first, and the stall progresses from the root to the tip. This prevents loss of roll control during stalling and therefore, forward swept designs are spin resistant [75].

Nonetheless, forward swept wings can suffer from yaw instability. This means that as the plane yaws to one side, one wing angles forward, the other rearward. This reduces the sweep of the rearward wing, which increases the drag, which pushes it farther back. This can lead to a dutch roll in reverse. However, a vertical stabilizer could help to alleviate this problem.

www.manaraa.com

9.3 Prototypes and Flight Testing

A couple prototypes with servo actuated control surfaces were constructed and tested prior to manufacturing a wing with MFCs. These prototypes, as well as the MFC prototype, are described in the following sections.

9.3.1 First Prototype - Testing the forward swept wing design

The initial prototype is shown in Fig. 9-3A. To minimize the resources invested, the first prototype wing was laid up on a flat surface, therefore, tooling was not necessary. Two layers of bidirectional carbon fiber were present throughout the wing, with additional layers of unidirectional carbon fiber placed on the leading edge. The unidirectional was angled at 22° in front of the sweep angle of the wing. This version of the plane had servo-actuated rudder and elevator control in the form of a traditional tail for flight control. Since yaw and roll are coupled, sufficient control was expected.

After the initial testing, it was quickly realized that the center of gravity was too far back and a prolonged test flight could not be completed. Therefore, the wing was moved towards the rear of the plane to effectively shift the center of gravity forward. Additionally, extra surface area was added to the rudder to increase yaw authority. This revised plane is shown in Fig. 9-3B.

This plane flew well with respect to stability, but lacked sufficient roll control. Since there was no dihedral built into the wing, the plane was only slightly more stable than neutral in the roll axis. Furthermore, the rudder was located very close vertically to the center of gravity. Therefore, if the plane entered a banked orientation during flight, the rudder was unable to roll the aircraft back to level.

To improve roll control and to make an intermediate step towards the next prototype, aileron control surfaces were added to the inboard section of the wing. This modification is shown in Fig. 9-4. After this revision, the aircraft handled extremely well and was difficult to differentiate between a traditional RC aircraft. With these results, the work began on the next prototype.

www.manaraa.com

A B

Figure 9-3. The first prototype of the forward swept wing. A) Protype with the wing in the initial position. B) Prototype with the wing in the revised position. Photos taken by Bradley LaCroix.

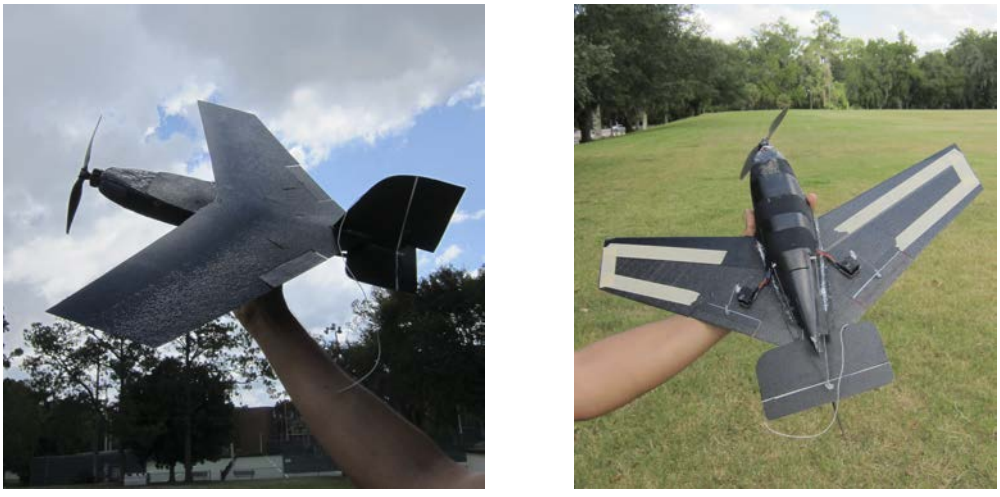

A B

Figure 9-4. The revised version of the first prototype. A) Top view. B) Bottom view. Photos taken by Bradley LaCroix.

www.manaraa.com

A B

Figure 9-5. The second prototype. A) Top view of the airplane. B) Bottom view. Photos taken by Bradley LaCroix.

9.3.2 Second Prototype - Testing elevon control

For the next prototype, the horizontal tail was removed from the design and elevons were added, as shown in Fig. 9-5. Elevons are a single set of control surfaces which serve both the role of ailerons (roll control) and elevators (pitch control). As mentioned previously, since roll and yaw are coupled, sufficient flight control can be maintained with control in one of the two axes. Therefore, the rudder was also eliminated, but the vertical tail was retained for stability.

A cambered wing design was devised using an in-house software package built for MATLAB developed by Daniel Claxton [70]. Reflex was built into the wing to eliminate the need for a horizontal tail. Once the design was complete, the software produced a CNC code which allowed for the tooling to be manufactured. The tooling provides a 3D surface on which to layup the composite wing, similar to the elliptical wing layup in the previous chapter (Fig. 8-2). The wing was composed of two layers of bidirectional throughout and a leading edge with two layers of unidirectional sandwiching the bidirectional. The unidirectional was once again placed at an angle of 22° with respect to the sweep of the wing thereby incorporating bend-twist coupling. A new smaller fuselage was also produced. Similar to the first prototype, servos were used to allow for small modifications as well as to reduce airframe costs.

www.manaraa.com

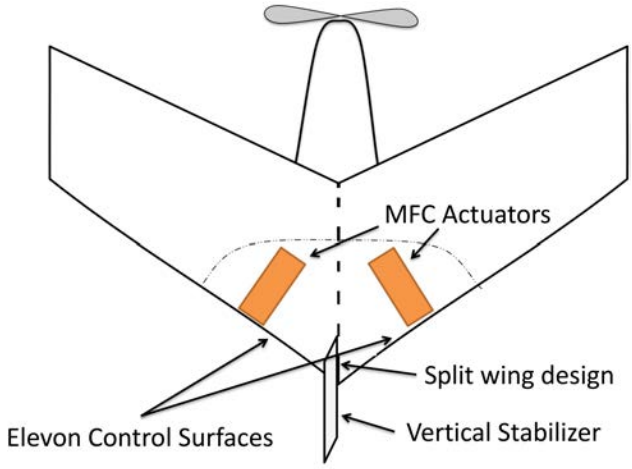

Figure 9-6. Initial forward swept wing design concept.

Flight testing showed that this version of the plane was stable as long as the airspeed was maintained. In addition, both roll and pitch authority were sufficient with this configuration. With the success of this prototype and the previous prototype, work began on the MFC version.

9.3.3 Third Prototype (MFC1) - Implementing MFCs

The first two prototypes showed that a forward swept wing with bend-twist coupling was a feasible option for a MAV measuring 0.61 m (2 ft). However, both of these MAVs were controlled using traditional servo motors for actuation. The next step was to eliminate the servos and incorporate MFCs into the design. The initial design concept for the MFC forward swept wing is shown in Fig. 9-6.

The intent was to place the MFCs inboard near the very rear of the aircraft so that they could produce the largest possible pitching moment. In addition, the actuation of the MFCs would also translate outboard on the wing, therefore allowing roll control. It was anticipated that positioning the MFCs farther inboard or farther outboard on the wing would allow for a balance between roll and pitch control.

The MFC prototype, termed MFC1, was laid up on the same wing tooling as the second prototype. The substrate for the MFCs was unidirectional carbon fiber due to ease of manufacturing. To fabricate the wing, each layer of the wing was cut and

www.manaraa.com

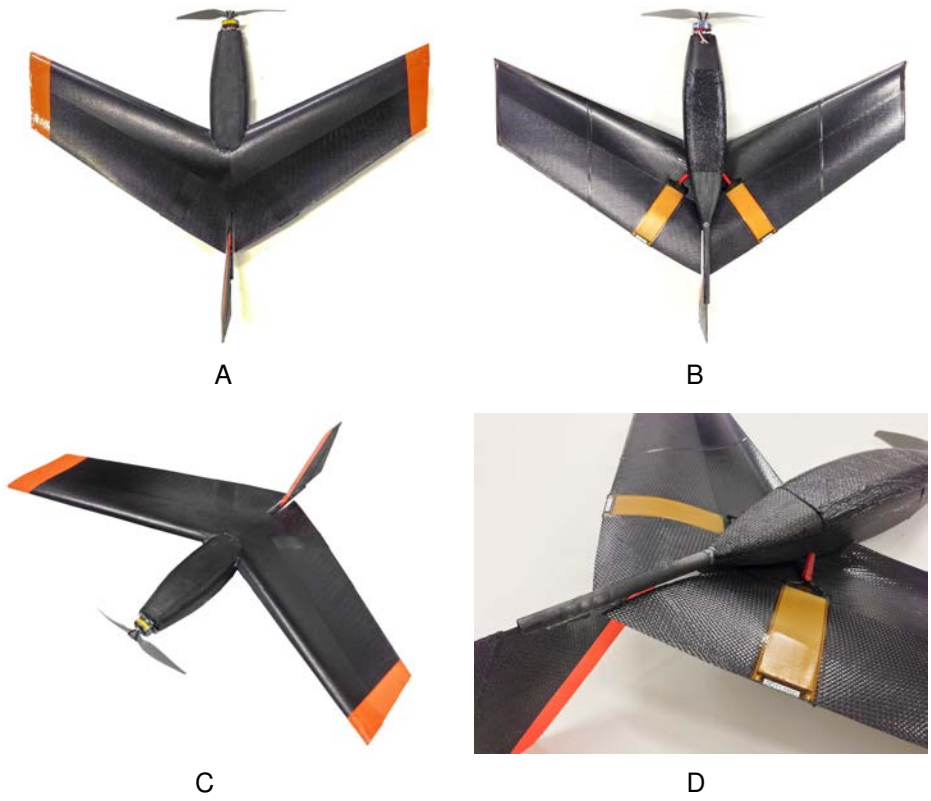

Figure 9-7. The first MFC prototype, MFC1. A) Top view. B) Bottom view. C) Angled view. D) Close up of MFC actuator. Photos taken by Bradley LaCroix.

placed into position, including the unidirectional carbon fiber for the MFC. The last step was placing the MFCs on top of the uncured layup and then placing the layup inside a vacuum bag. The layup was cycled through a lay-up cycle which holds a temperature of 126.7°C (260°F) for four hours. After curing, the wing, tail, and fuselage were assembled. The final result is shown in Fig. 9-7.

The layup for this wing was composed of a single layer of bidirectional to facilitate more compliance for the MFC actuation. The leading edge was composed of two layers of unidirectional carbon fiber, one layer on top of the bidirectional and one layer on the bottom. The unidirectional was again placed at 22° with respect to the sweep angle of the wing. Battens, in the form of unidirectional stiffeners, were added to the wing for reinforcement to prevent the outboard section of the wing from being too compliant.

www.manaraa.com

Flight testing was an immediate success. The first flight was more than five minutes. During this time, it was observed that the airplane was stable and had decent control authority. The largest issue was a lack of sufficient roll authority, but the test pilot noted the pitch authority was sufficient. The test flight ended when the pilot entered a steep bank and was unable to recover.

9.3.4 Fourth Prototype (MFC2) - An attempt to improve roll control

The next prototype, termed MFC2, was the first to implement steel substrates into the wing. To do this, it was necessary to combine a pre-preg layup with a wet layup. Since standard epoxies used in wet layups start to degrade at higher temperatures, it was decided the best option was to use high temperature epoxy. To perform this kind of layup, the composite layers of the wing were assembled just as they were in the previous prototypes. A section of material, the size of the active area of the MFC, was removed and steel placed in the void. To bond the MFC to the steel, high temperature epoxy was applied to the steel and the MFC placed on top.

This process was first tested with an inoperative MFC on a half wing test piece to verify its effectiveness. The resulting test piece is shown in Fig. 9-8. The steel is held in place due to the bond to the MFC. The MFC overlaps between the steel and the rest of the wing. In other words, the steel is set within the surface of the wing and the MFC is placed on the surface of the wing where it overlaps both the carbon fiber and the steel.

Once the process was demonstrated, the MFC prototype was constructed. The battens were determined to be unnecessary and were not included in this prototype. This also had the added benefit of making the FEA model less complex. The number of layers in the layup and fiber orientation remained the same as MFC1. In an attempt to increase roll authority, the MFC actuators were moved farther outboard. It was also anticipated that the steel substrate would produce larger deflections, therefore increasing both roll and pitch authority. These results are discussed in Section 9.4. MFC2, completed after assembly, is shown in Fig. 9-9.

www.manaraa.com

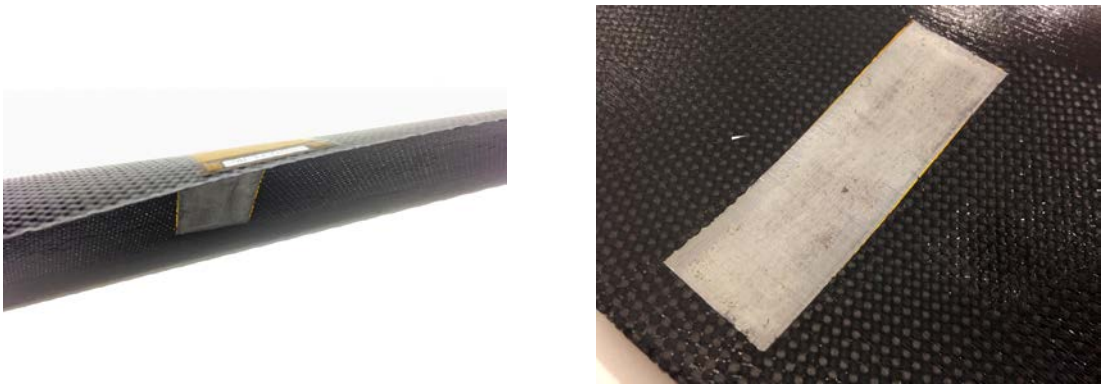

A B

Figure 9-8. Steel substrate test section. A) View of wing from the trailing edge. B) Closeup of the top section of the wing. Photos taken by Bradley LaCroix.

Figure 9-9. The second MFC prototype, MFC2. Photo taken by Bradley LaCroix.

This aircraft did not undergo flight testing, but its characteristics and performance were examined in static workbench testing as well as wind tunnel testing. Both the MFC1 and MFC2 underwent static workbench tests with DIC as a way to validate the FEA model of each airplane. These tests and results are discussed in the following section. The wind tunnel tests provided a way to study the aeroelastic nature of the aircraft, in which the interaction between the wing structure and aerodynamic loads was

www.manaraa.com

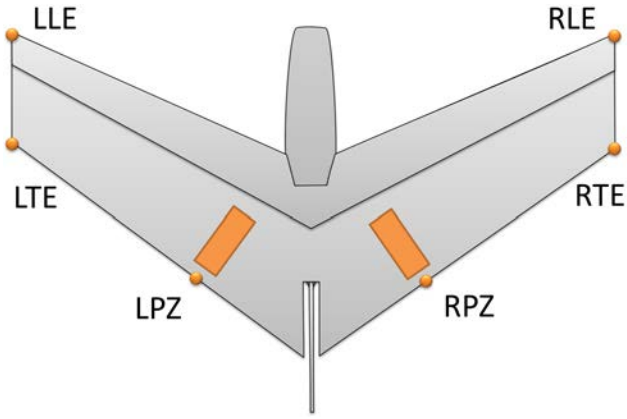

Figure 9-10. Diagram of the loading points for the workbench tests. LLE - Left leading edge, LTE - Left trailing edge, LPZ - Left MFC, RPZ - Right MFC, RTE - Right trailing edge, RLE - Right leading edge.

studied with a combination of DIC and load measurements. These results were used to validate the aeroelastic model and are discussed in Chapter 10.

9.4 Workbench Testing

This section discusses the static test setup and execution for both the MFC1 and MFC2 aircraft. In these tests, the aircraft were mounted in a rigid manner and various masses suspended from key points on the wing. DIC was used to measure the full-field deformation of the wing and the results used to validate the FEA model in Section 9.6. The masses were positioned at three locations on each side of the wing as shown in Fig. 9-10. Staples, bent into the shape of hooks, were used as attachment points for the masses. Cyanoacrylate adhesive (CA) was used to bond the hooks to the wing. A small piece of string, less than 0.1 g, was tied to each mass so that it could be easily placed on the attachment hooks. The hooks, masses, and attachment points for MFC1 and MFC2 are shown in Fig. 9-11.

9.4.1 MFC1 Tests

In this setup, the MFC1 aircraft was placed in a vice which was secured to a large optical table. The DIC cameras were positioned over the aircraft as shown in Fig. 9-12. The aircraft performed flight tests prior to performing the workbench tests mentioned

www.manaraa.com

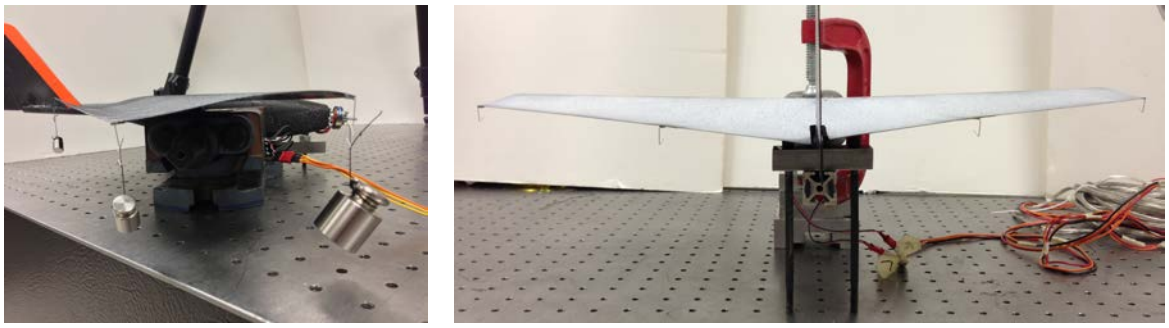

A B

Figure 9-11. Loading points for the MFC1 and MFC2. A) MFC1 with masses applied. B) MFC2 attachment points. Photos taken by Bradley LaCroix.

here. During the flight test, the pilot lost control of the aircraft and it crashed nose-first into the ground. Shortly after beginning the workbench tests, the left MFC failed and would not respond to voltage inputs. It is likely that the left MFC was damaged during the crash. Regardless, a number of tests were still conducted and used for the validation of the FEA model.

9.4.2 MFC2 Tests

A similar setup was used for the MFC2 aircraft. To further analyze the structure, two main setups were used. The first, was similar to that used for the MFC1, and is shown in Fig. 9-13A. The second, is an inverted setup in which the plane was positioned upside-down and the cameras were placed below, shown in Fig. 9-13B.

9.5 Finite Element Model

9.5.1 Model Setup

The finite element model was setup in a similar way to the unimorph models in Chapter 6 and also used the composite material properties derived in Chapter 4. The model itself was composed of both quadrilateral reduced integration shell elements (S4R) and triangular shell elements (S3). The resulting layouts for both the MFC1 and MFC2 wing, with a seed spacing of 5 mm, are shown in Fig. 9-14. In both cases, the portion attached to the fuselage is assigned a fixed boundary condition.

www.manaraa.com

Figure 9-12. The workbench setup for MFC1. The DIC cameras are positioned above the aircraft and the aircraft is mounted to the table via a large vice. Photo taken by Bradley LaCroix.

9.5.2 Convergence Analysis

To ensure a economical balance between computational time and accuracy, a convergence analysis was performed. The main interest in performing a convergence analysis is to determine how fine to make the finite element mesh in order to achieve sufficient accuracy. Making the mesh too coarse can result in large errors, while making the mesh too fine can result in excessive computational time. It is especially important to determine a satisfactory balance in computational time and accuracy when running a finite element analysis on the order of hundreds or thousands of times, such is the case in this research, when using the model for optimization.

Four points of interest were examined on the MFC2 wing for the finite element convergence analysis. These configurations are shown in Fig. 9-15. The first two points assessed the unloaded MFC actuation of the wing, with 1500 V applied to the left side

www.manaraa.com

A B

Figure 9-13. The workbench setup for the MFC2. A) The standard loading setup. B) The inverted loading setup. Photos taken by Bradley LaCroix.

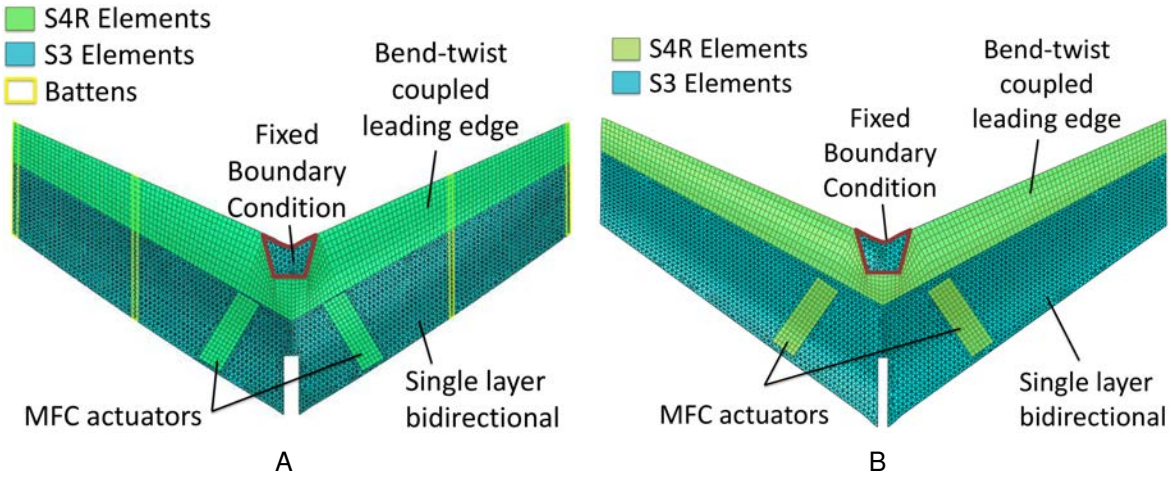

A B

Figure 9-14. FEA layout. A) MFC1. B) MFC2.

www.manaraa.com

and -500 V applied to the right side. In this configuration, the displacments for the left and right side of the wing were measured. The measured points were at the trailing edge of the wing nearest the centerline of the aircraft. Next, the wing was placed into the unactuated configuration and a 100 g load applied in the upward direction on the outboard leading edge of the wing. The final point examined was a combined actuation and loaded configuration. In this configuration, both sides of the model were actuated to 1500 V and a 20 g load was applied to the outboard corner of each trailing edge.

Nine mesh densities were tested, ranging from 776 elements to 24,470 elements. Each of the 9 meshes are shown in Fig. 9-16. The results of the convergence analysis are shown in Fig. 9-17 and Fig. 9-18.

The results show that there is a significant increase in the number of elements after seed spacing drops below 5 mm. Since the computational time is proportional to the number of elements, it increases rapidly as well. Taking a look at the change in displacements, there is not a significant change after seed spacing is reduced to 5 mm. Therefore, it is decided the most balanced mesh size is the mesh with a seed spacing of 5 mm and slightly more than 6,000 elements.

9.6 Model Validation

A set of experiments, as described in Sections 9.4.1 and 9.4.2, were performed to validate the results of the FEA model. A few comparisons are given in this section, however, a majority of the data is presented in Appendix D.

9.6.1 MFC1

The first result in this section is a comparison between both sides of the wing being actuated to -500 V, shown in Fig. 9-19. Keep in mind, this is before the left MFC failed, so it may have been functioning at a reduced capacity. These results show that the experimental results match the FEA model well on the right side, but the experiment does not achieve the same degree of deflection on the left side.

www.manaraa.com

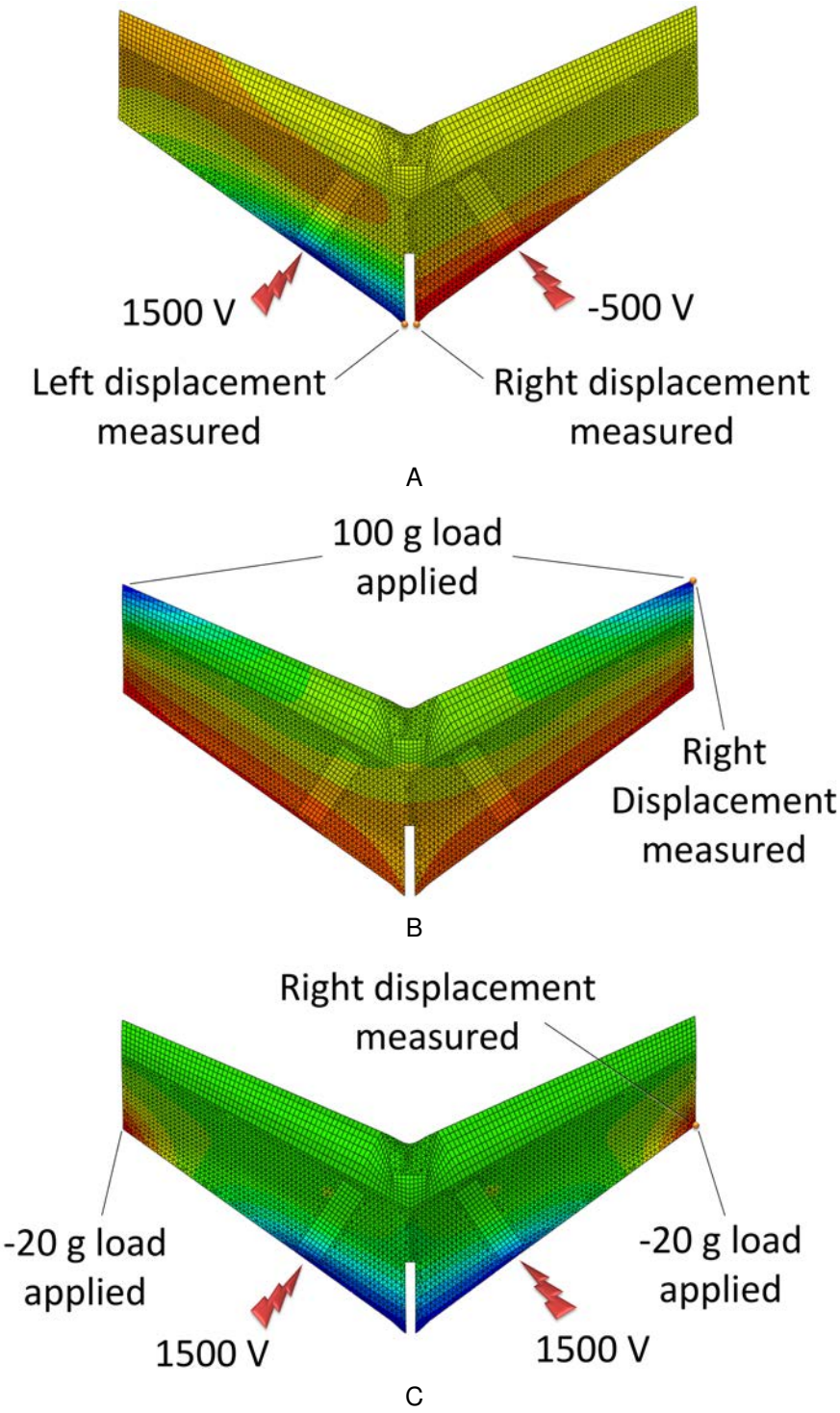

Figure 9-15. Points examined for the convergence analysis. A) Case 1. B) Case 2. C) Case 3.

www.manaraa.com

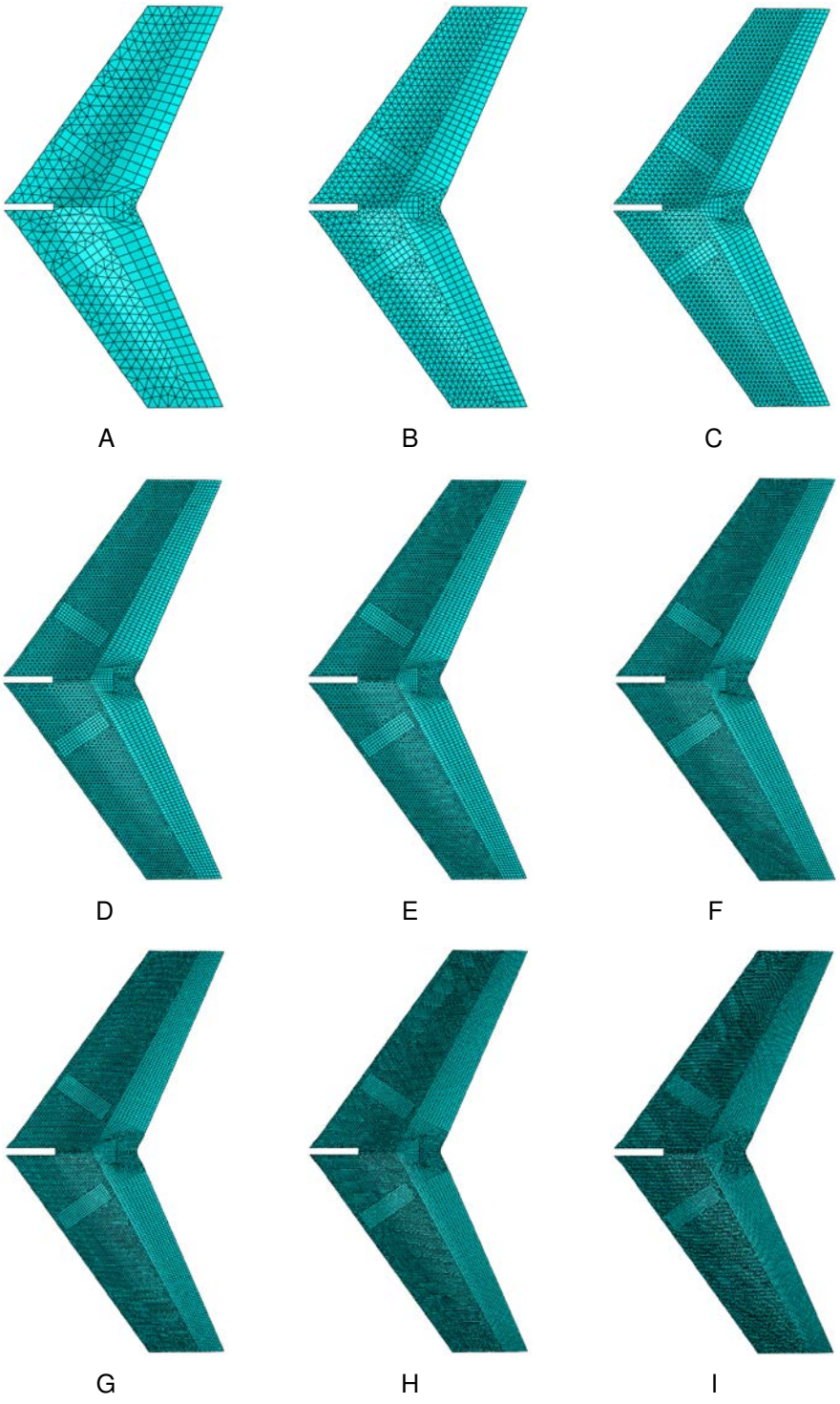

Figure 9-16. Meshes considered in the convergence analysis. A) 776 elements. B) 1,651 elements. C) 2,819 elements. D) 6,278 elements. E) 7,655 elements. F) 9,564 elements. G) 12,721 elements. H) 16,940 elements. I) 24,470 elements.

www.manaraa.com

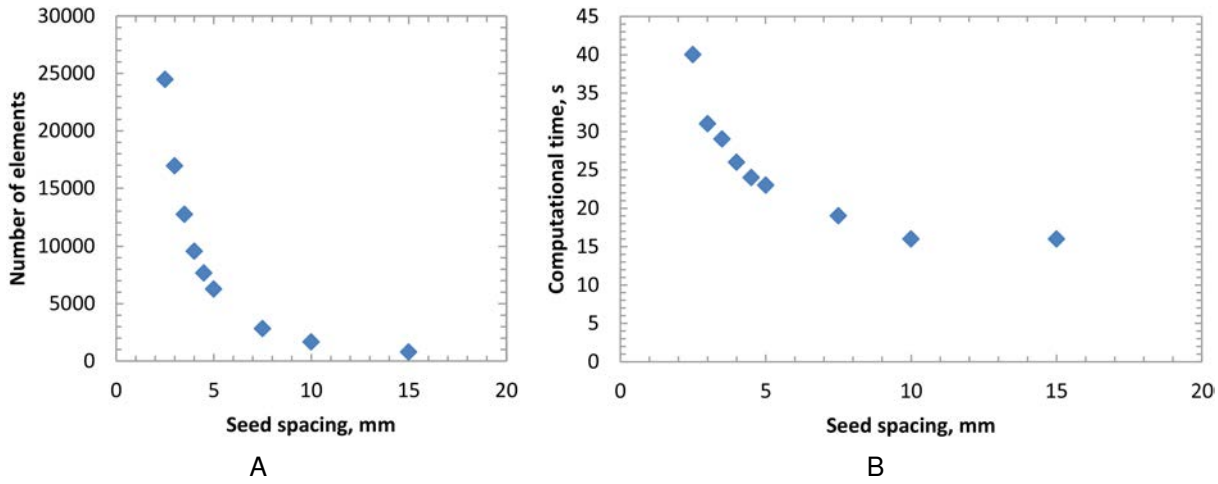

Figure 9-17. Results of the convergence analysis. A) Seed spacing vs number of elements. B) Seed spacing vs computational time.

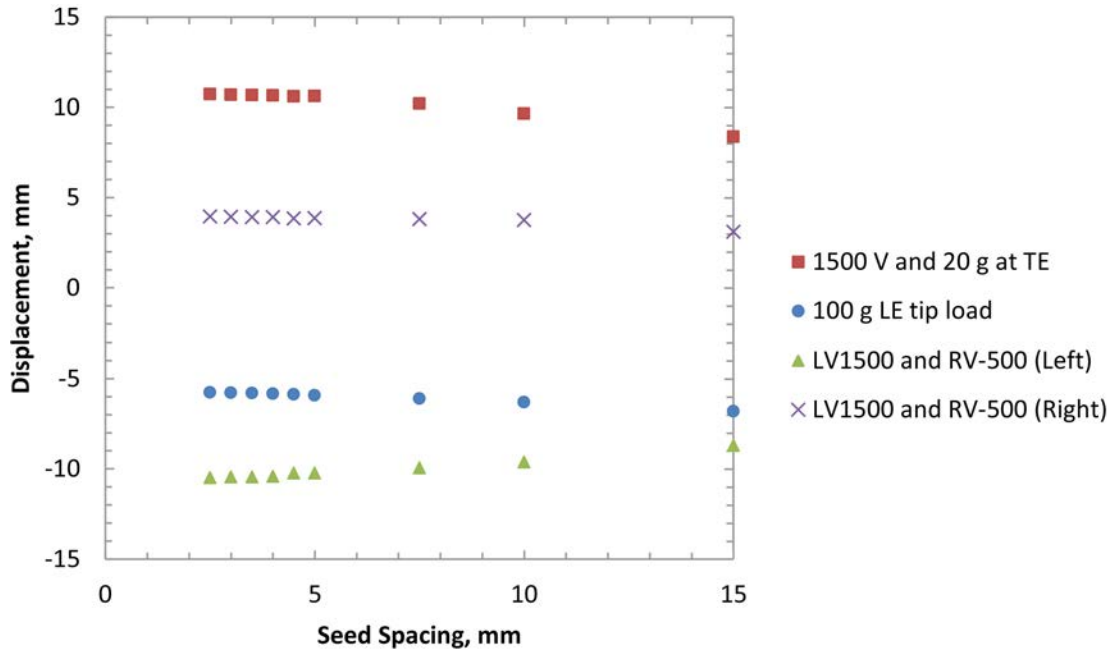

Figure 9-18. Seed spacing vs. resulting displacements.

www.manaraa.com

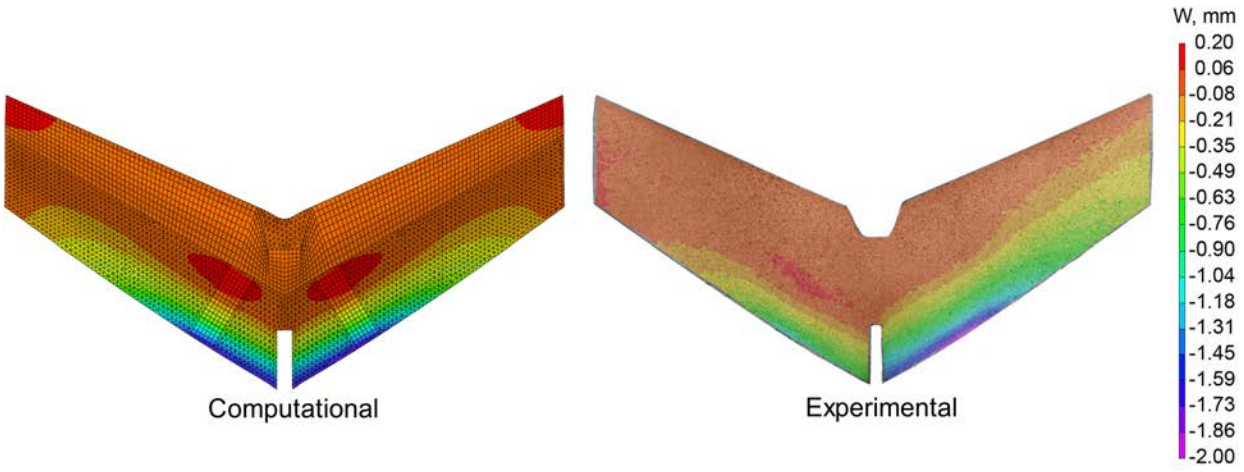

Figure 9-19. MFC1 workbench comparison LV-500 RV-500.

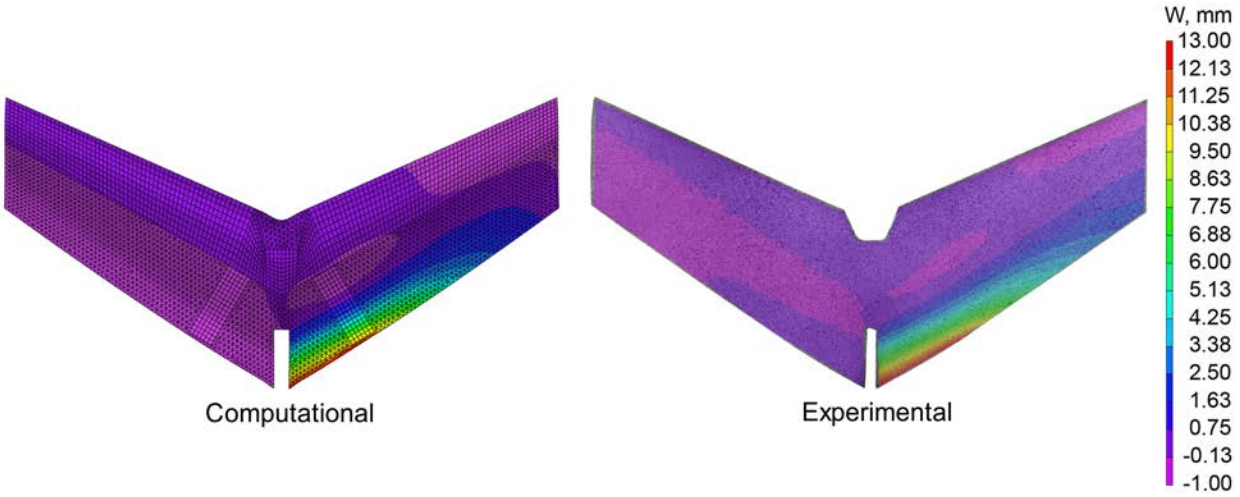

Figure 9-20. MFC1 workbench comparison LV0000 RV1500.

The next comparison, shown in Fig. 9-20, demonstrates the right side of the wing actuated to 1500 V. These results match extremely well.

Next, loads are applied to the wing, with 100 g being applied to the leading edge in the first load comparison, shown in Fig. 9-21. The displacement of the leading edge matches up well between the experiment and the FEA model. However, the displacement of the trailing edge of the wing differs. This may be caused by the FEA model not accurately representing the bend-twist coupling for this particular case. It may also be possible that the fiber orientation of the leading edge was not correctly

www.manaraa.com

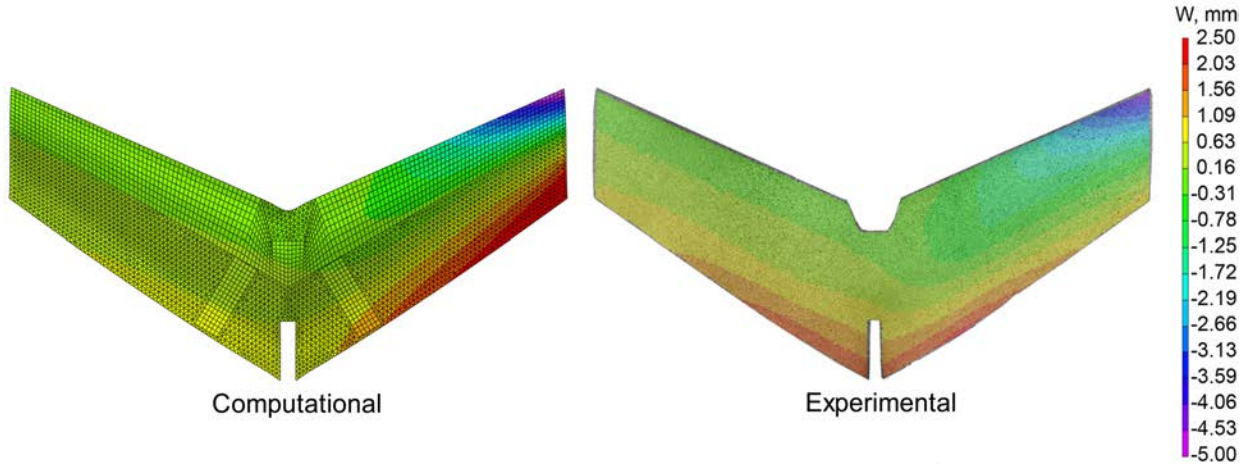

Figure 9-21. MFC1 workbench comparison LV0000 RV0000 RLE100.

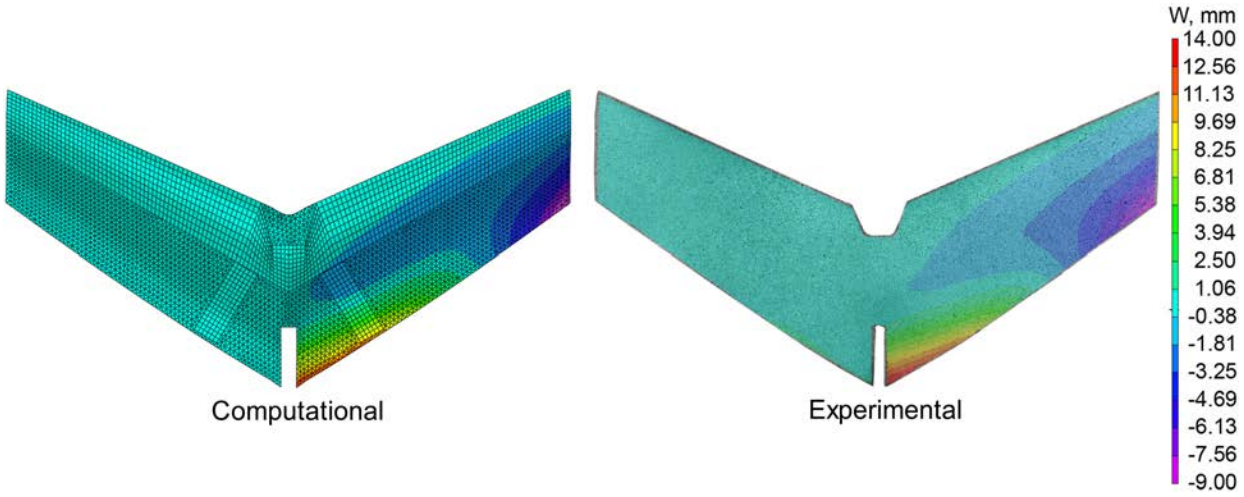

Figure 9-22. MFC1 workbench comparison LV0000 RV1500 RTE20.

applied during the layup procedure. Since the other results matched up well, this slight mismatch was not a large concern.

The final comparison shown in this section is a scenario where the right side of the wing is actuated to 1500 V and the right trailing edge of the wing is supporting a 20 g load, shown in Fig. 9-22. These results match well, including the contours near the center of the right side of the wing. Additional comparisons are shown in Appendix D.

www.manaraa.com

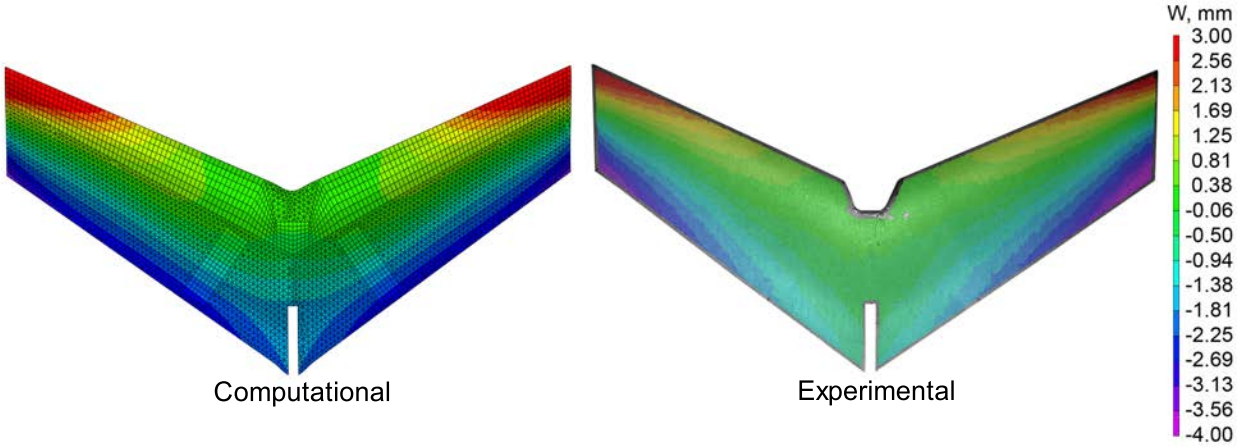

Figure 9-23. MFC2 LV0000 RV0000 LLE-100g RLE-100g.

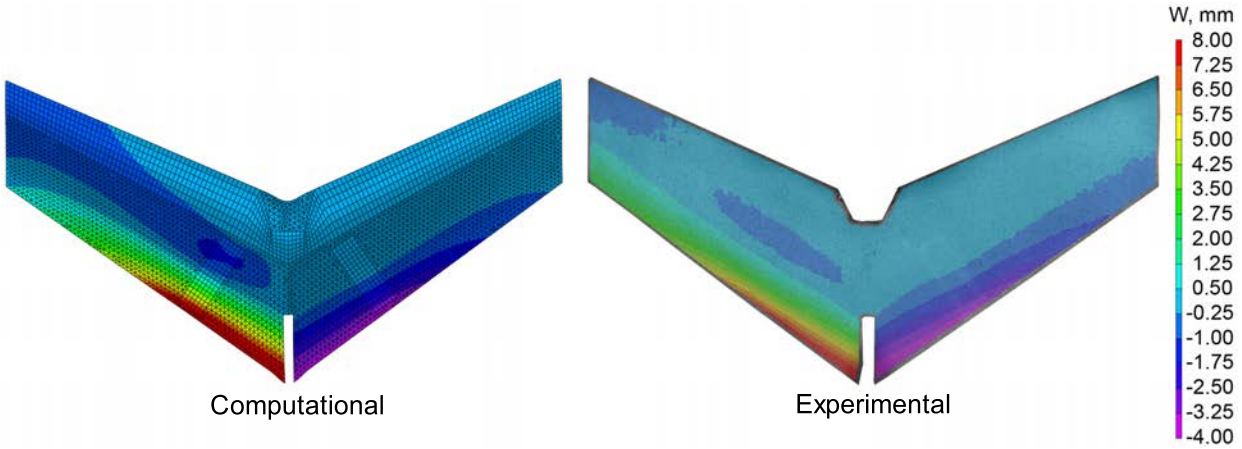

Figure 9-24. MFC2 LV1500 RV-500.

9.6.2 MFC2

A small portion of the MFC2 static testing results are presented in this section. The remaining comparisons are presented in Appendix D. The first comparison is an unactuated configuration, with 100 g loading applied in the upward direction at the leading edge of the wing tips. These results are shown in Fig. 9-23.

The next comparison is an no-load actuated configuration, with the MFCs actuated in an assymetric manner. These results are shown in Fig. 9-24.

www.manaraa.com

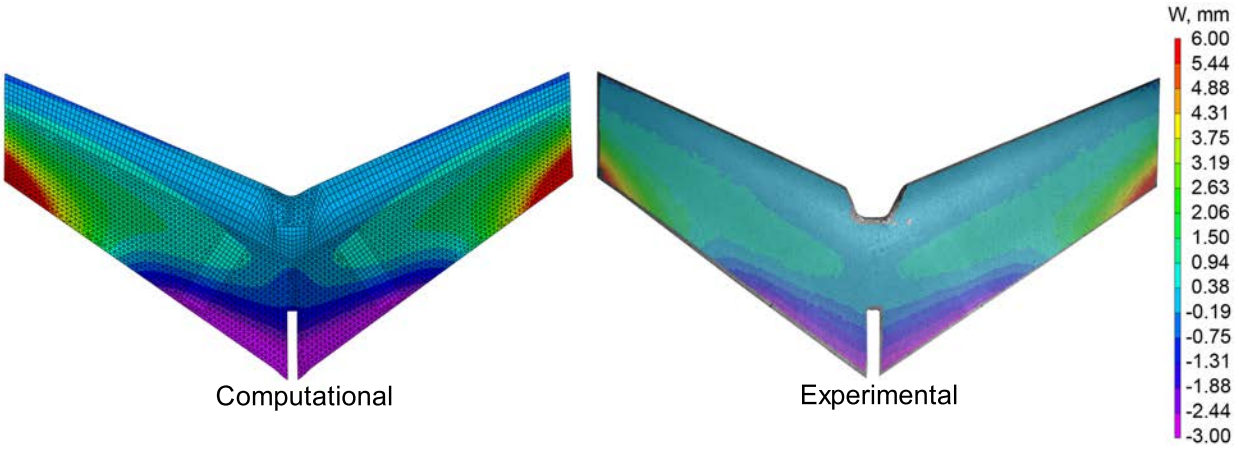

Figure 9-25. MFC2 LV-500 RV-500 LTE-20g RTE-20g.

The final comparison shown in this section is a combined loading and actuation setup. In this comparison, shown in Fig. 9-25, the MFCs are actuated to -500 V and loading is applied in the opposing direction on the trailing edge of the wing tips.

Overall, the MFC1 has a larger trailing edge displacement than the MFC2 when the MFC is actuated to 1500 V, but the MFC2 creates a larger spanwise displacement (more of the trailing edge is deformed). This indicates that the MFC2 may produce better roll authority than the MFC1.

9.6.3 Discussion

The results presented in the previous sections show that both the MFC1 and MFC2 aircraft have good agreement with the finite element model under static loads. The MFC1 showed a greater discrepancy in some cases, but this was attributed to the more complex geometry which includes battens. The aircraft MFC2 and successive designs are built without battens. This simplifies the finite element model and yields better agreement between the FEA model and experimental results. The next step of the project, discussed in the following chapter, will be to apply aerodynamic loads and to calculate the aeroelastic interaction computationally.

www.manaraa.com

CHAPTER 10
AEROELASTIC MODEL

After the finite element model was validated, it was possible to add the next layer of analysis: the coupling of aerodynamic loads with the finite element model. This is a vital aspect to the model, since the MAVs considered in this research are compliant structures susceptible to significant deformation under loading. This chapter examines the design and setup of the aeroelastic model and compares the wind tunnel results to the computational predictions.

10.1 Computational Model

10.1.1 ABAQUS

When setting up the FEA model in ABAQUS, meticulous care was taken to allow for changes to be made to the model, such as overall geometry, composite layup, partitioning for the MFCs and leading edge, and aerodynamic loading. If aspects of the code used to generate the model are not implemented correctly, changes to the earlier parts of the model will prevent the model from being regenerated properly. If implemented correctly, changes can be made to the model autonomously and a large set of models can be examined without user intervention.

This is critical, since the optimization routine, discussed in Chapter 11 examined hundreds of possible designs and it would be far too time consuming to implement these changes manually. In addition, this allowed for the aerodynamic loads to be calculated and input automatically, also eliminating an extensive amount of manual user input.

ABAQUS provides three options on how to create a model. The most common option used is the Graphical User Interface (GUI). This allows the user to visually go through their design step-by-step and specify each portion of their model, such as geometry, materials, and loads. The user is able to see the model changes as they construct the model in a way similar to a Computer Aided Graphics (CAD) environment. This method is generally the best option when setting up a model that will be examined

www.manaraa.com

under a small number of loads or conditions. However, this method becomes tedious to specify a larger number of scenarios since the user must input changes manually.

If the user wishes to input a large number of design possibilities or scenarios, then they have two options. The user can choose to create an input file (.inp) or develop a python script (.py). An external program, such as MATLAB, can then be used to execute these files without using the ABAQUS GUI. ABAQUS creates both of these files when using the GUI, so depending on the parameters being changed from one scenario to the next, the user may be able to use one of these generated files without implementing very many changes. For instance, if the only aspect being changed is a point load, and the load is acting on the same point in all scenarios, then the user can create a short routine in MATLAB which will change the load value in the python or input file before running the analysis each time.

However, if more complex changes are necessary, such as a change in geometry, then the differences between the input file method and the python script method begin to arise. The input file method gives the user more control over how the model is created in ABAQUS. In this method, the user must specify every aspect of the model geometry, such as the position of every node and how the nodes are connected to form elements. This could be advantageous if a very specific finite element mesh is desired, however, it requires substantial programming to execute. Furthermore, a similar level of detail is involved when defining distributed loads or boundary conditions, since the loads are applied to the nodes and elements individually.

For the python script method, the user specifies the shape of the geometry and partitions, but ABAQUS is responsible for generating the mesh. Therefore, ABAQUS determines how to arrange the nodes and elements based on its own algorithms. This relieves some of the work load from the user and makes it easier to define an array of designs using a python script routine. In addition, distributed loads and boundary conditions are specified for entire sections of the model and ABAQUS calculates how to

www.manaraa.com

apply these properties across the nodes and elements. It is also possible to generate outputs using this method so that the external program, such as MATLAB, can retrieve specific results from the analysis and determine how to adapt the next run.

Regarding this research, the best method was determined to be the python script method. This method allowed for the geometry, partitions, and distributed loads of the model to be changed quickly and autonomously without user input. With proper scripting, the user could specify changes like wing sweep, MFC position, and loading conditions by specifying the values in MATLAB and everything else would be executed autonomously.

10.1.2 Athena Vortex Lattice (AVL)

One of the main criterion for calculating the aerodynamic loads on the wing was the required computational costs. Reducing the time required to run the aerodynamic code meant that the aeroelastic model could iterate faster and reach a solution in less time. Therefore, full scale Computational Fluid Dynamics (CFD) was considered too time consuming.

A faster, yet proven program was required. An extensive number of journal articles and conference proceedings have been published detailing the performance and limitations of Athena Vortex Lattice (AVL) program developed by Mark Drela and Harold Youngren at MIT [35, 63–69, 76, 77]. AVL is a program used for aerodynamic and flight-dynamic analysis of rigid aircraft for nearly any geometry. It utilizes an extended vortex lattice model for the lifting surfaces, together with a slender-body model for fuselages and nacelles. It has been shown to provide reasonable predictions for lift, roll, pitch, and yaw, as well as dynamic stability. It is notoriously poor at calculating drag, but that is not a primary requirement for this research.

AVL operates in a DOS-like environment requiring keystroke commands by the user to specify text files containing aircraft design, airfoils, and mass files. Fig 10-1 is an example of the interface with some commands. While it is primitive by todays standards,

www.manaraa.com

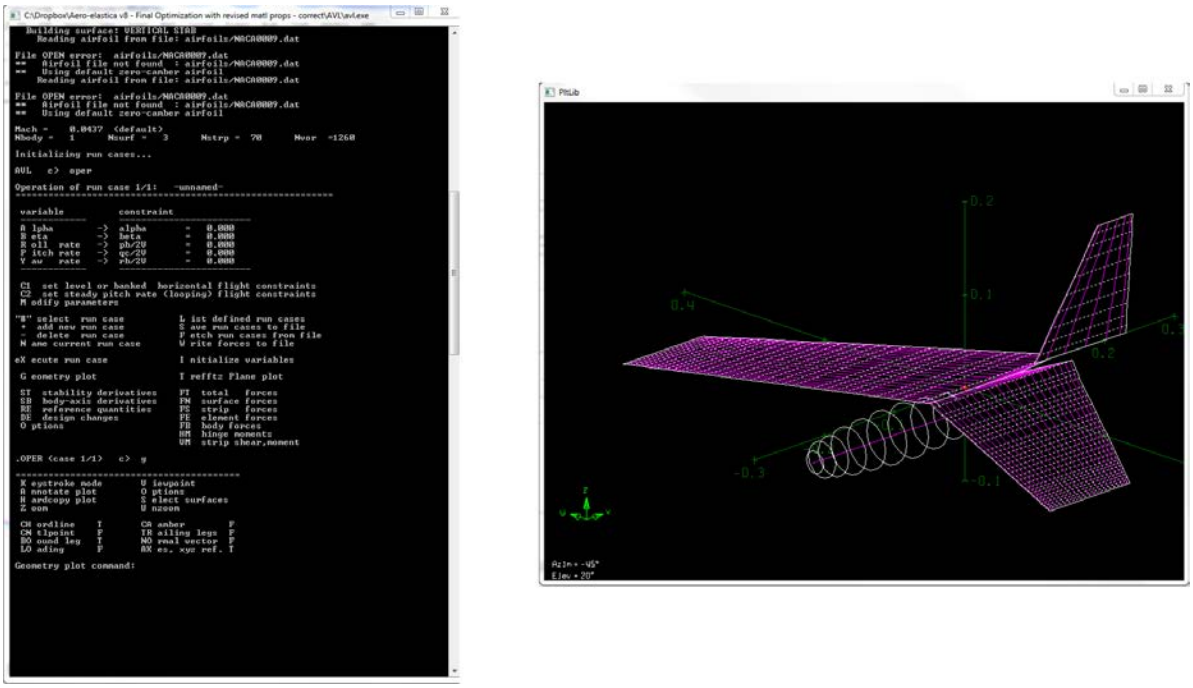

Figure 10-1. Example of the Athena Vortex Lattice (AVL) interface.

these same characteristics make it relatively straightforward to build programming around.

One of the main limitations of AVL is its rigid aircraft assumption. It assumes that any geometry specified is perfectly rigid and does not deform under aerodynamic loads. More recent programs, such as ASWING [78], incorporate the stiffness of the wing similar to a cantilever beam, but this type of model would not work for this research. This is because the MFCs actuate to deform the compliant structure, rather than acting like a control surface, so there is no way to incorporate the MFCs into a code like this.

However, it is possible to iterate the structural model (ABAQUS) with the aerodynamic model (AVL) to create an aeroelastic model. Similar methods have been used before [68]. In addition, the assumption that a compliant structure deformed under aerodynamic loading in a quasi-static manner behaves like a rigid structure with the identical geometry was tested and is described in Chapter 8. The results indicate that it is possible to derive accurate predictions using a combination of ABAQUS and AVL.

www.manaraa.com

10.1.3 Coupling ABAQUS and AVL

The aeroelastic calculation starts with MATLAB. The user, or optimization scheme, defines an aircraft design within a MATLAB file, called an m-file, with details such as the wing shape, MFC position, and material composition. Next, the MATLAB code assembles this information into a python script and passes it to ABAQUS. ABAQUS assembles the model and conducts a preliminary run which calculates the wing deflection as a result of the MFC actuation. This geometry is then passed to AVL, which calculates the aerodynamic loads based on the geometry. These aerodynamic loads are passed back to ABAQUS where they are applied to the same FEA model and the new geometry is calculated. The new geometry is passed to AVL and the process continues until there is no significant change from one iteration to the next. No significant change is defined as less than 0.1 mm for all cases. This process is illustrated in Fig. 10-2.

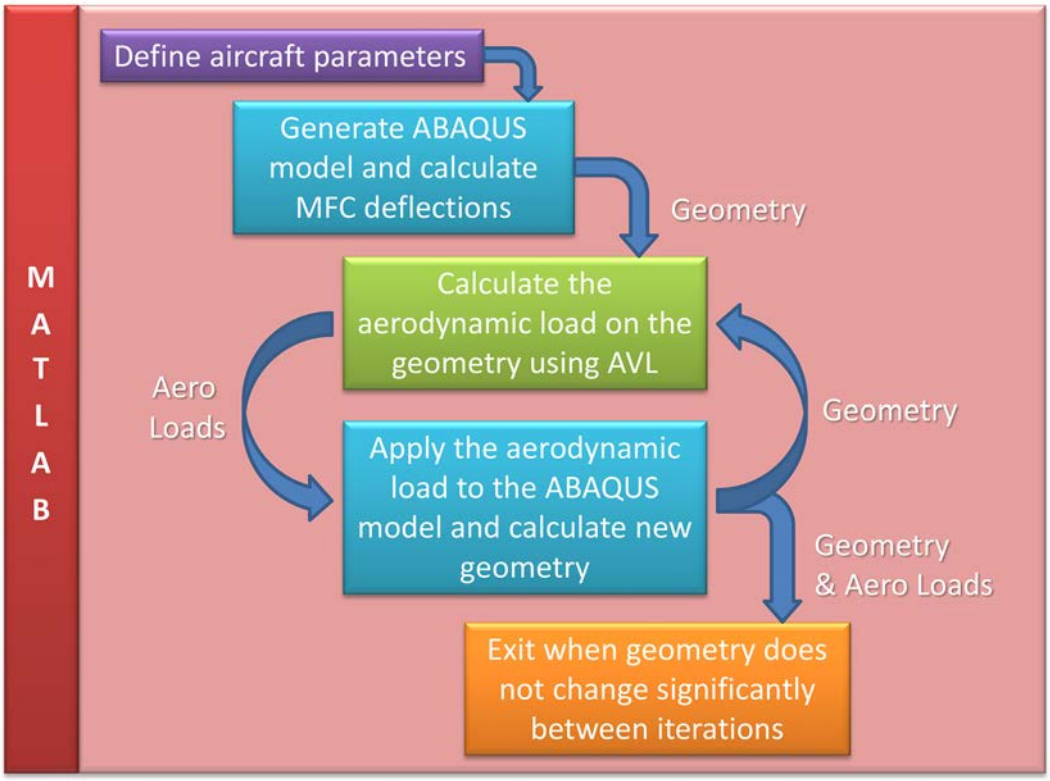

Figure 10-2. Overview of the programming architecture for the aeroelastic model.

www.manaraa.com

Typically, six or seven iterations were necessary to reach convergence. The geometry of the wing and the predicted aerodynamic loads were the main outputs from the analysis. The results of the computational analysis will be presented and compared with the experiments in Section 10.3. The next section describes the wind tunnel tests and accompanying procedure.

10.2 Wind Tunnel Tests

10.2.1 Facilities

The wind tunnel tests were completed at a remote University of Florida facility, known as the Aerodynamic Characterization Facility (ACF) located in the Research and Engineering Education Facility (REEF) in Shalimar, FL. Although the University of Florida has a number of wind tunnel facilities on its main campus in Gainesville, FL, these were undergoing renovation at the time of this research. The ACF, designed by Engineering Laboratory Design, Inc. (ELD), became operational in November of 2007. It is an open section wind tunnel with a 1.07 m (42 inch) square cross-section and a length of 3.0 m (10 feet). The axial fan was manufactured by Howden Buffalo and is powered by a 50 HP Reliance Electric motor. A pitot tube connected to a heise is placed at the beginning of the test section to measure the incoming wind speed. The temperature and absolute pressure are also measured digitally and included in the wind tunnel calculations. Pictures of the wind tunnel are shown in Fig. 10-3.

Two linear motors work in combination to control the height and angle of attack of the test arm. A digital inclinometer is attached at the rear of the test arm to measure the angle of attack during testing. A JR3 30E12 load cell (I40 bolt pattern) is mounted to the end of the test arm to measure the loads. A close-up of these items are shown in Fig. 10-4. The distance from the reference point on the load cell to the CG of the aircraft was measured in both the longitudinal and vertical direction. Finally, all aspects of the wind tunnel are controlled through a suite of LabVIEW software.

www.manaraa.com

A B

Figure 10-3. The REEF wind tunnel. A) View from outside the wind tunnel room. B) View from inside the wind tunnel room (MFC2 shown). Photos taken by Bradley LaCroix.

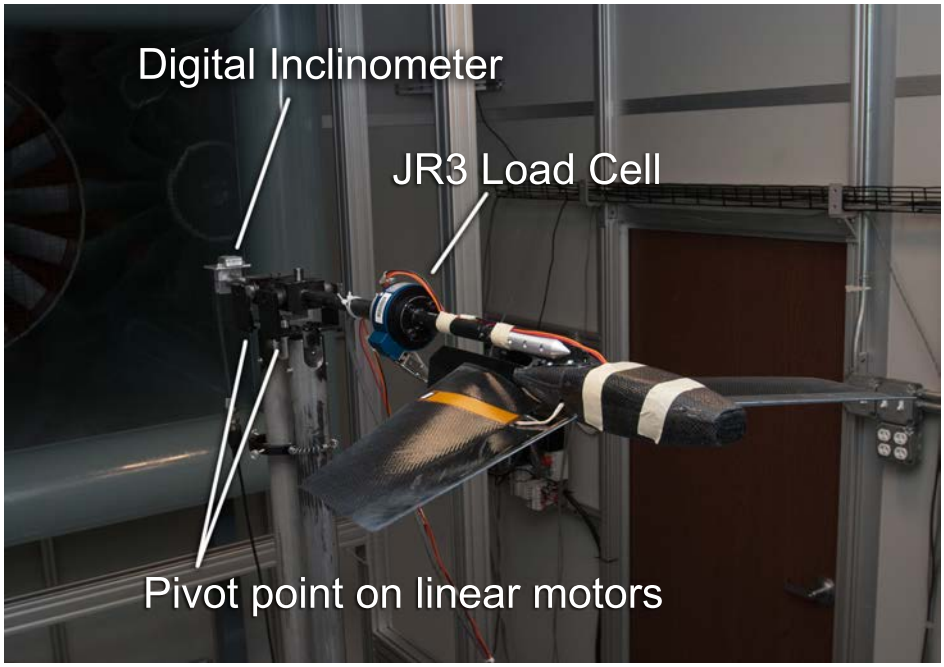

Figure 10-4. A close-up of the wind tunnel setup. Photo taken by Bradley LaCroix.

www.manaraa.com

10.2.2 Setup

The flight tested MFC1 aircraft was taken to the wind tunnel along with two MFC2 wings. Since testing was conducted at a remote facility, it was critical to have a backup test wing. Two MFC2 wings were produced as a precaution in the event one might fail either due to manufacturing defects or handling. Altogether, three wings were prepared for testing.

As mentioned in Section 9.4.1, the MFC1 aircraft suffered an MFC failure during workbench testing. However, it was still included in the testing to observe its performance with one MFC. In addition, it was discovered after arriving at the REEF that the MFCs in one of the MFC2 wings were also damaged. When applying voltage, the MFCs began to short out and quickly stopped working. The damage likely occured during the intial testing of the wing, which was performed while it was on a power supply. It is possible that the voltage potential between the MFCs and the power supply was great enough to cause permanent damage to the MFCs. Fortunately, the other MFC2 wing maintained functionality.

The DIC system was also an integral part of the experiments. To minimize the infrastructure required to setup the DIC, it was decided to test the wing in an inverted orientation. This allowed the cameras to be placed near the floor which required minimal structural addition to the existing setup. It also allowed easier access to the cameras for adjustments such as focus and aperture. The main assumption in this inverted setup is that the wing does not deform significantly under gravitational loads. This was expected to be true based on visual inspection. Figure 10-5 shows the wind tunnel setup including the DIC cameras.

10.2.3 Procedure

Prior to beginning the wind tunnel experiments, the load cell was powered on overnight to reach steady state. Before testing each aircraft, a set of tares were taken for the entire range of angle of attacks. During the tare procedure, the wind tunnel would

www.manaraa.com

Figure 10-5. The overall wind tunnel setup. The DIC cameras are located below the aircraft. Photo taken by Bradley LaCroix.

run for 60 seconds to bring the load cell to thermal equilibrium. Then the wind would be shut off and the program would run through the angles of attack in a random order, to mitigate the effects of hysteresis.

Next, a series of configurations were tested. The MFC1 plane was configured to:

- LV0000 RV0000
- LV0000 RV1500
- LV0000 RV-500

The MFC2 plane was configured to:

- LV0000 RV0000
- LV1500 RV1500
- LV-500 RV-500
- LV1500 RV-500
- LV-500 RV1500

www.manaraa.com

Each wing was tested at 10 m/s and 15 m/s, but for brevity, only the 15 m/s cases are included in this document. DIC images were taken at each angle of attack for each configuration. Each test included running through the angles of attacks in a random order at a given velocity.

10.3 Results

In this section, the predictions from the aeroelastic model are compared to the wind tunnel tests. Only a small sample of the results are presented in this section, with the remaining data being shown in Appendix E.

10.3.1 DIC Results

DIC was performed on each wing in both static conditions (no wind) and with wind applied at 15 m/s. In addition, even though the computer model was built off of the DIC results for the static, unactuated wing, there is still a small discrepancy in the shape. Therefore, the out-of-plane difference between the computer model and the static, unactuated wing is calculated for both the MFC1 and the MFC2 wing. This process is illustrated in Fig. 10-6. This difference is taken as the tare and subtracted from the other images in the group. The difference in most cases is no more than 1 mm in either direction. This discrepancy can be caused by variations in manufacturing including the thermal expansion of the composite materials. Furthermore, the mounting of the wing to the fuselage can cause a slight change in the shape of the wing.

The tare for the MFC2 wing is shown in Fig. 10-7A. This tare value is subtracted from the other results for the wing as it is actuated. The results for the wing as it is actuated through various configurations are shown in parts B, C, and D of Fig. 10-7. These results are calculated by taking the out-of-plane position of the experimental results (DIC) and substracting the finite element model (FEA) out-of-plane position. Therefore, positive values indicate the experimental results are higher than the finite element model and negative values indicate the experimental values are lower than the finite element model.

www.manaraa.com

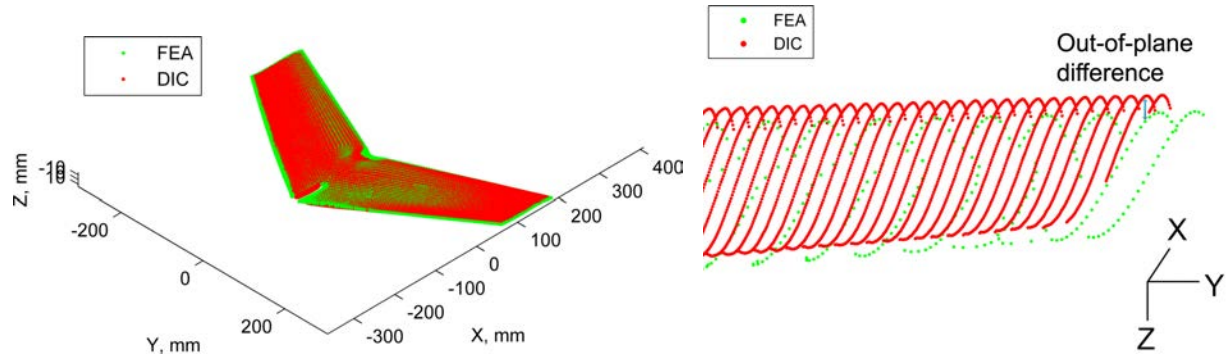

Figure 10-6. Illustration of the out-of-plane tare. A) Overall view of the computational model (FEA) and the experimental results (DIC) overlayed on one another. B) Close-up view of the same model demonstrating the out-of-plane difference between the two results.

Table 10-1. MFC2 quality of fit for each configuration tested.

Velocity, m/s	Configuration	Number of points	RMS error, mm
0	LV0000 RV0000	43437	0.38
	LV1500 RV1500	43269	0.53
	LV-500 RV-500	43273	0.15
	LV-500 RV1500	43009	0.33
15	LV0000 RV0000	42903	0.19
	LV1500 RV1500	43225	0.48
	LV-500 RV-500	43352	0.35
	LV-500 RV1500	42989	0.46

The wind tunnel arm, although relatively stiff, still has a small degree of compliance in all directions. To further enhance the fit between the computer model and the wind tunnel results, an optimization routine was invoked. The optimization routine adjusted the fit of the models to reduce the overall RMS error. The RMS error was calculated by taking the out-of-plane distance between each corresponding point on the wing, squaring it, and then summing all the points. Then, the square root was taken to produce a single value corresponding to the overall fit of the FEA and DIC models. These values, for MFC2, are tabulated in Table 10-1. The number of points analyzed is slightly more than 40,000. The RMS error averages to 0.36 mm for all 8 cases. Similar values for MFC1 are presented in Appendix E.

www.manaraa.com

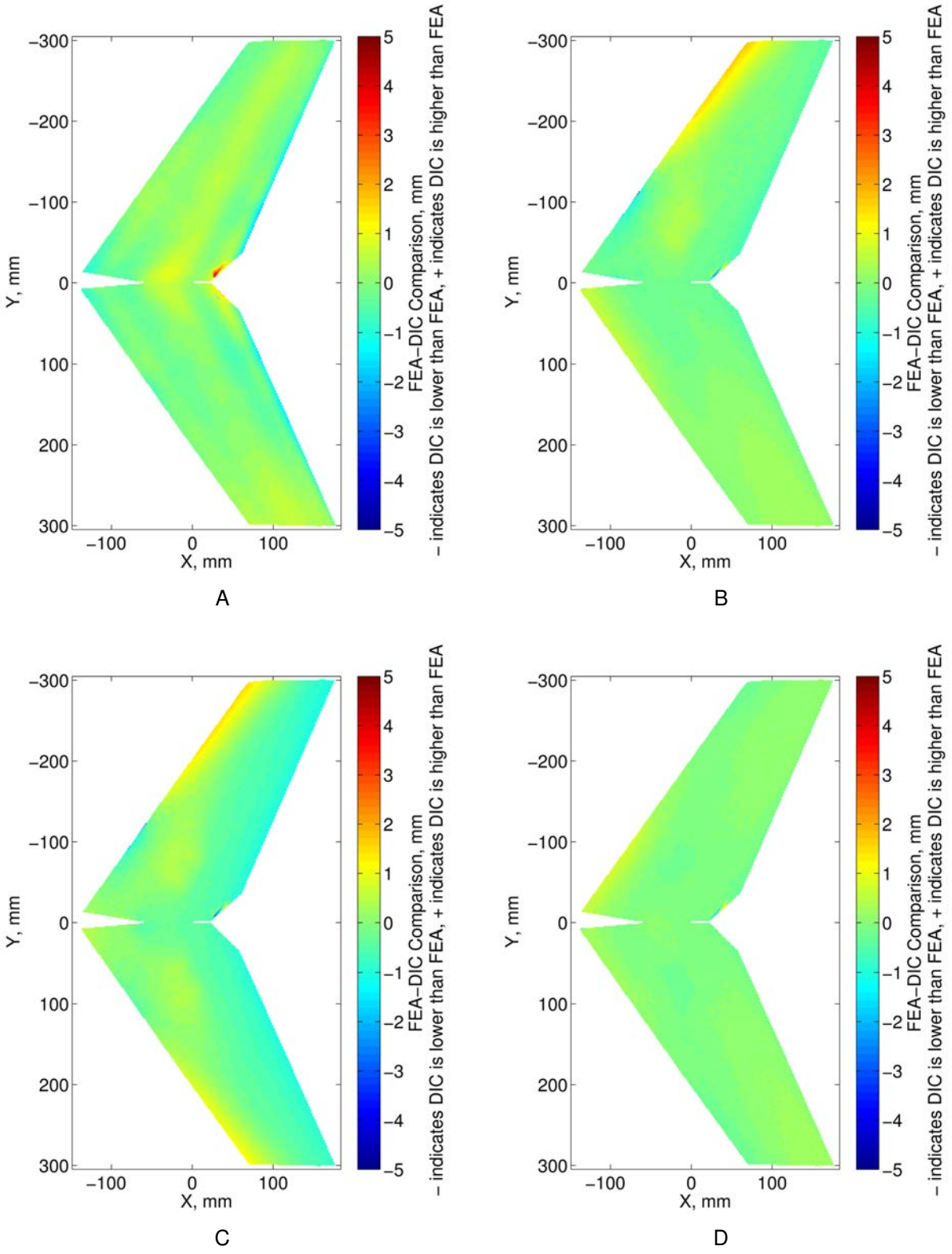

Figure 10-7. Comparison of the MFC2 finite element model to the experimental results under static conditions. A) No actuation. B) Actuated to LV1500 and RV1500. C) Actuated to LV-500 and RV-500. D) Actuated to LV1500 and RV-500.

www.manaraa.com

The same results are shown for the MFC2 wing when submitted to 15 m/s conditions as shown in Fig. 10-8. All of these results indicate extremely good agreement, with the largest error being on the order of 2 mm. Similar results are shown for MFC1 in Appendix E. However, the results for the MFC1 aircraft have slightly worse agreement and are on the order of a 3-4 mm. This is likely due to difficulties in accurately modeling the battens in the finite element model. This is not a large concern, since the MFC2 and successive models will not incorporate battens.

10.3.2 Aerodynamic Results

The aerodynamic load measurements follow a trend similar to that of the the DIC results and match reasonably well. The first results are shown in Fig. 10-9. This figure shows the aerodynamic loads for the MFC1 aircraft as the right actuator is actuated at 0 V, 1500 V, and -500 V. Only one side is actuated since the left MFC actuator failed during testing as previously mentioned.

These results show good agreement between the computational model and the experimental results. In particular, the distance between each line match up well for the pitch and roll coefficient. This means that the model predicts the pitch and roll authority well. The experimental results for the roll coefficient also indicate that the wing is undergoing unsymmetric twisting as it is loaded, which makes the roll coefficient change with respect to angle of attack. In addition, the slope of the pitch coefficients are negative. This is a preferred characteristic which indicates the plane's tendency to nose down will increase as the angle of attack increases. Lastly, the lift coefficient changes as the wing is actuated. This is expected since the lift coefficient is a direct result of the wing camber. Since the MFC changes the overall wing camber, this will have a proportional affect on the lift coefficient.

Going one step beyond the experiment, the pitch and roll authority for the MFC1 aircraft can be calculated by simulating what would happen if both actuators were active and the results compared to the MFC2 results. This will allow for a better comparison

www.manaraa.com

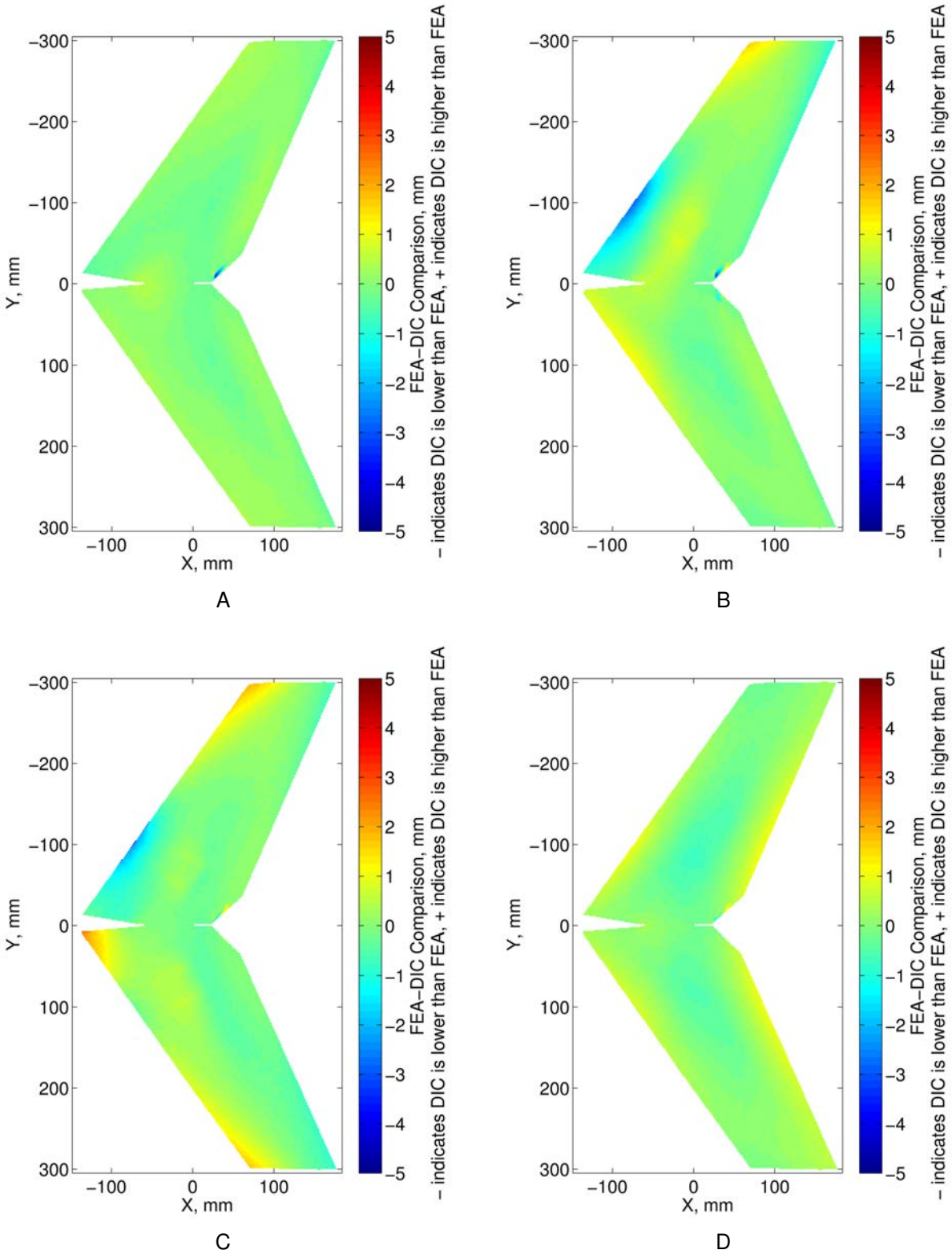

Figure 10-8. Comparison of the MFC2 finite element model to the experimental results at 15 m/s. A) No actuation. B) Actuated to LV1500 and RV1500. C) Actuated to LV-500 and RV-500. D) Actuated to LV1500 and RV-500.

www.manaraa.com

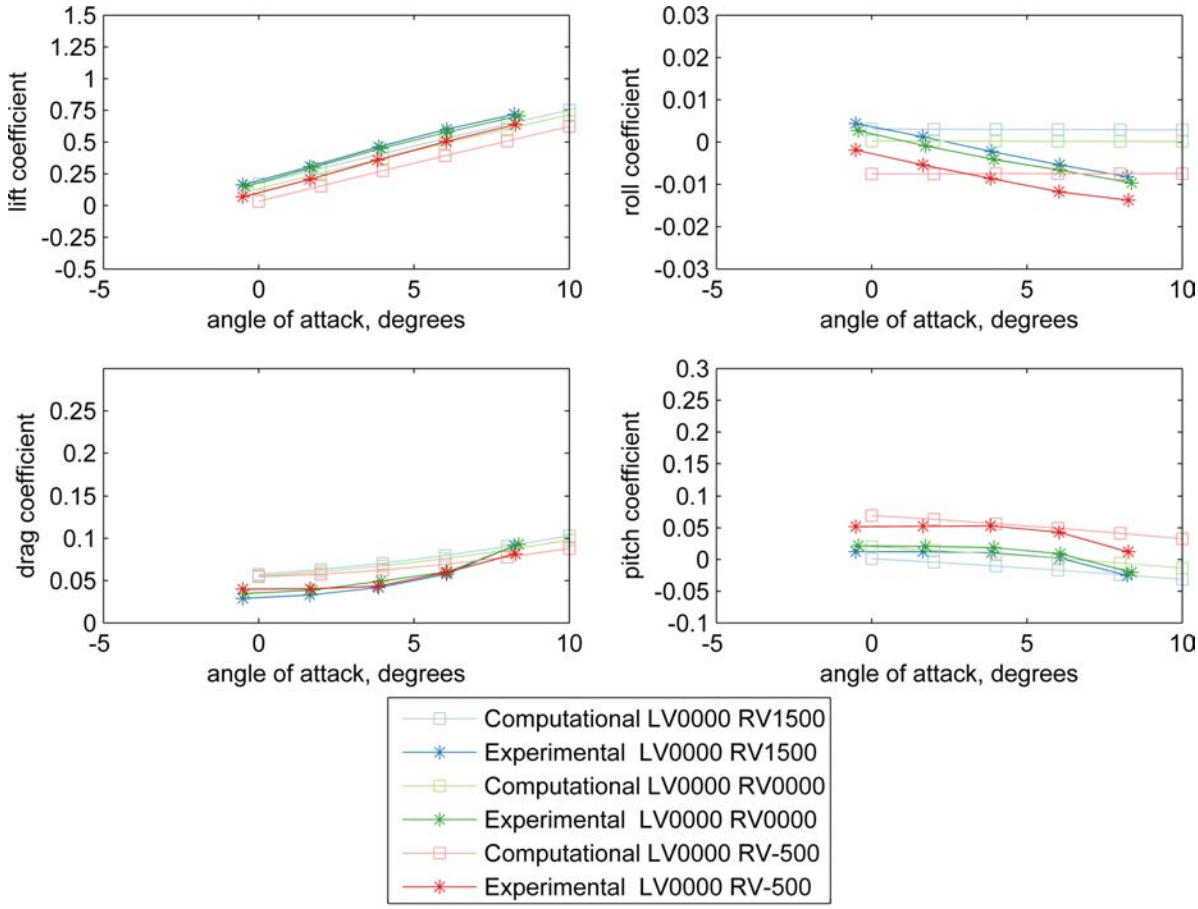

Figure 10-9. Comparison between the computational and experimental results for the MFC1.

between the two aircraft. The change in pitch authority is shown in Fig. 10-10. As can be seen in the figure, the pitch coefficient in both directions is approximately doubled. Next, the roll authority can be compared, as seen in Fig. 10-11. These results are similar because the overall roll range is doubled.

These results can be compared to the results for the MFC2 aircraft, which are shown in Figs. 10-12 and 10-13. The pitch range for the MFC1 with both actuators active is approximately 0.135. For MFC2, the pitch range is approximately 0.125. Comparing the roll coefficients, the MFC1 has a roll coefficient of approximately 0.0105, whereas the MFC2 has a similar roll coefficient of 0.0100. Overall, the experimental

www.manaraa.com

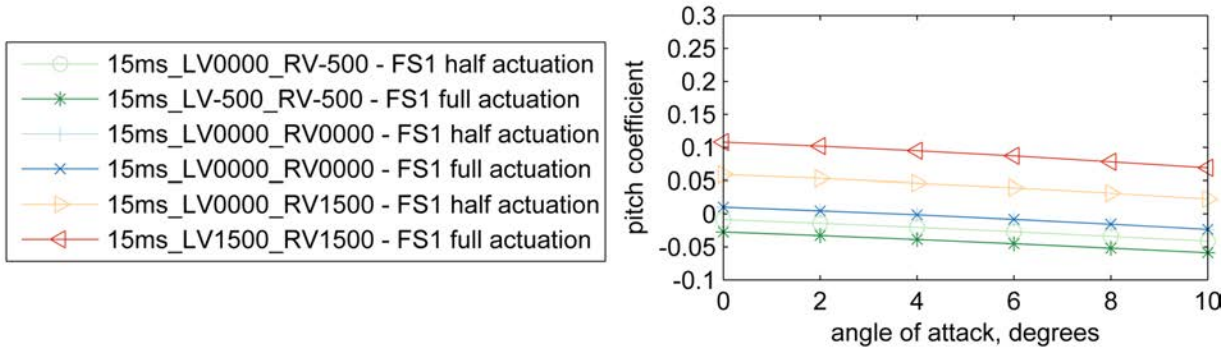

Figure 10-10. Pitch comparison between two computational models of the MFC1. One is only actuating the right MFC and the other is actuating both MFCs.

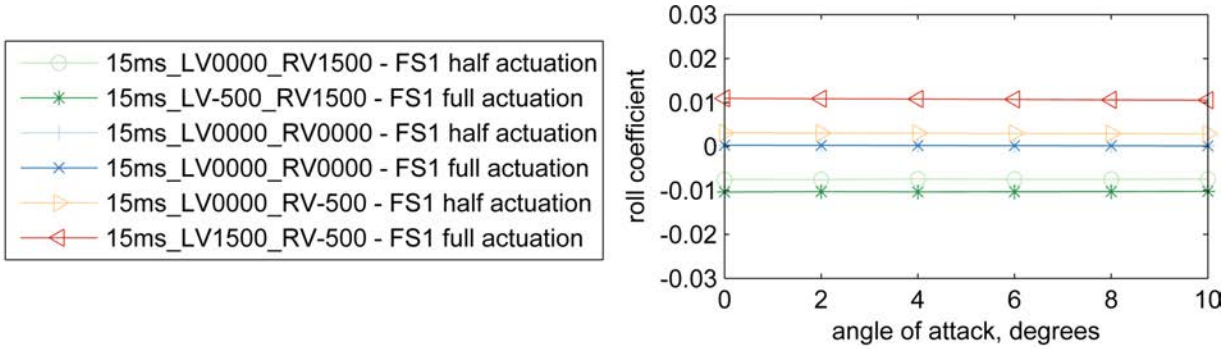

Figure 10-11. Roll comparison between two computational models of the MFC1. One is only actuating the right MFC and the other is actuating both MFCs.

pitch and roll coefficients match the aeroelastic model reasonably well, but the model slightly overpredicts both.

Two sets of measurements were recorded with the MFC2 on two different visits to the REEF. The results shown in Figs. 10-12 and 10-13 are based on the second visit. The results from the first visit indicate a slightly larger actuation. These results are shown in Figs. 10-14 and 10-15. It is possible that the actuators were compromised at some point between the two visits or during transport and did not actuate to the same range on the second trip to the wind tunnel. This could account for part of the discrepancy.

www.manaraa.com

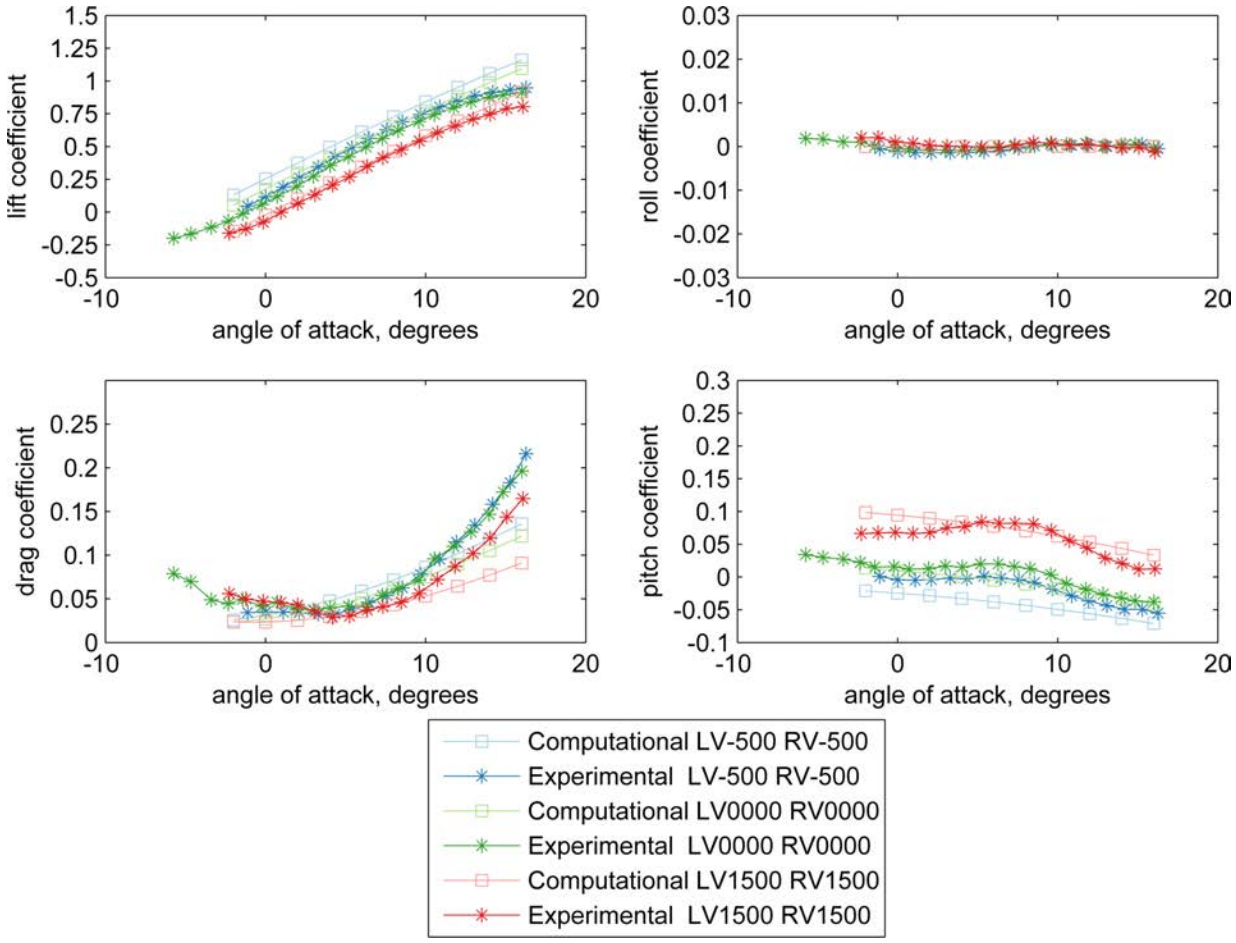

Figure 10-12. Pitch comparison between the computational and experimental results for the MFC2.

10.4 Discussion

The aeroelastic model was able to predict the lift, drag, pitch, and drag coefficients quite well for the MFC1 and MFC2. Differences between the experimental results and computational model can be attributed to variations in manufacturing. The next step will be implementing the aeroelastic model into an optimization scheme to determine the best configuration. To cut down on computational costs, the model was only examined at 15 m/s, 0° angle of attack. Additional specifics are discussed in Chapter 11.

www.manaraa.com

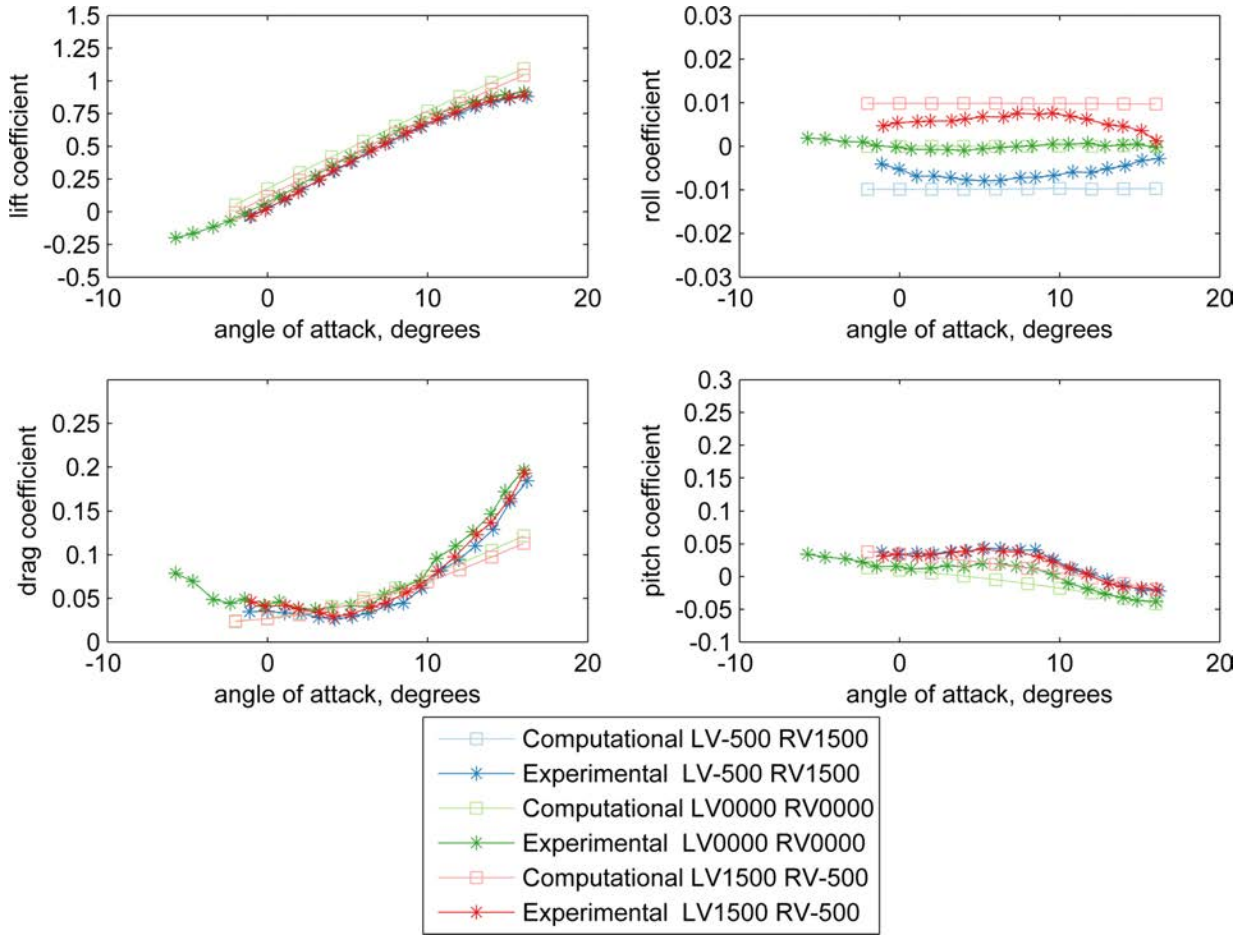

Figure 10-13. Roll comparison between the computational and experimental results for the MFC2.

www.manaraa.com

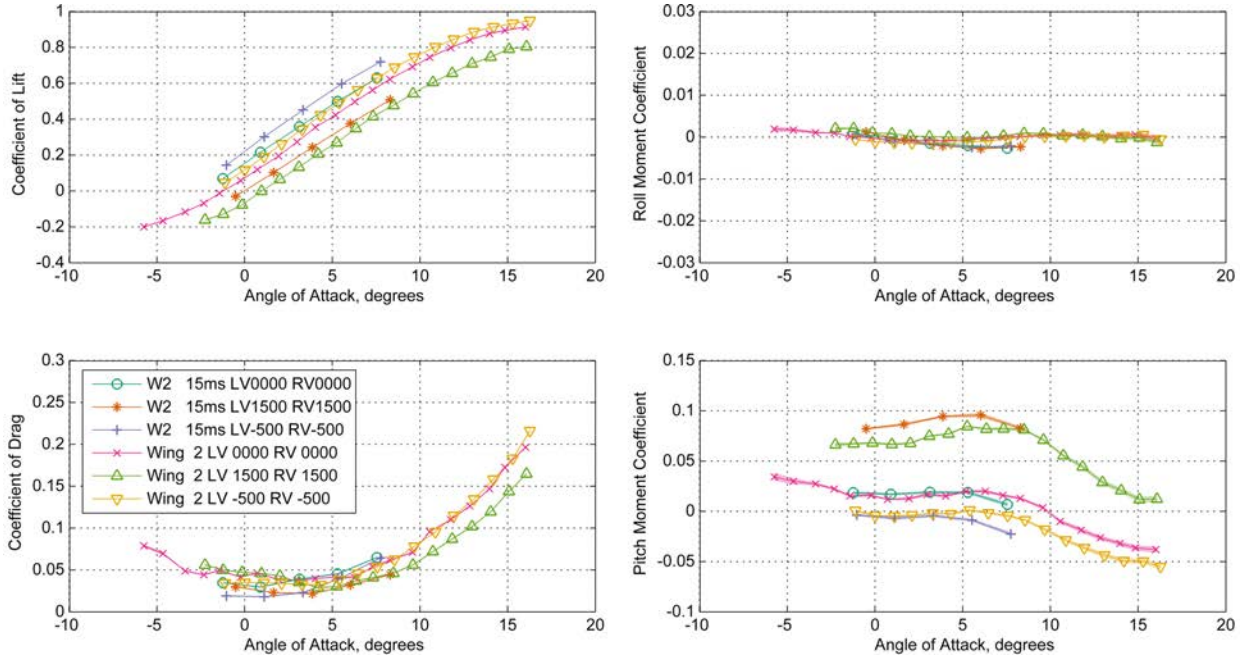

Figure 10-14. MFC2 comparison between first and second set of measurements (pitch maneuver).

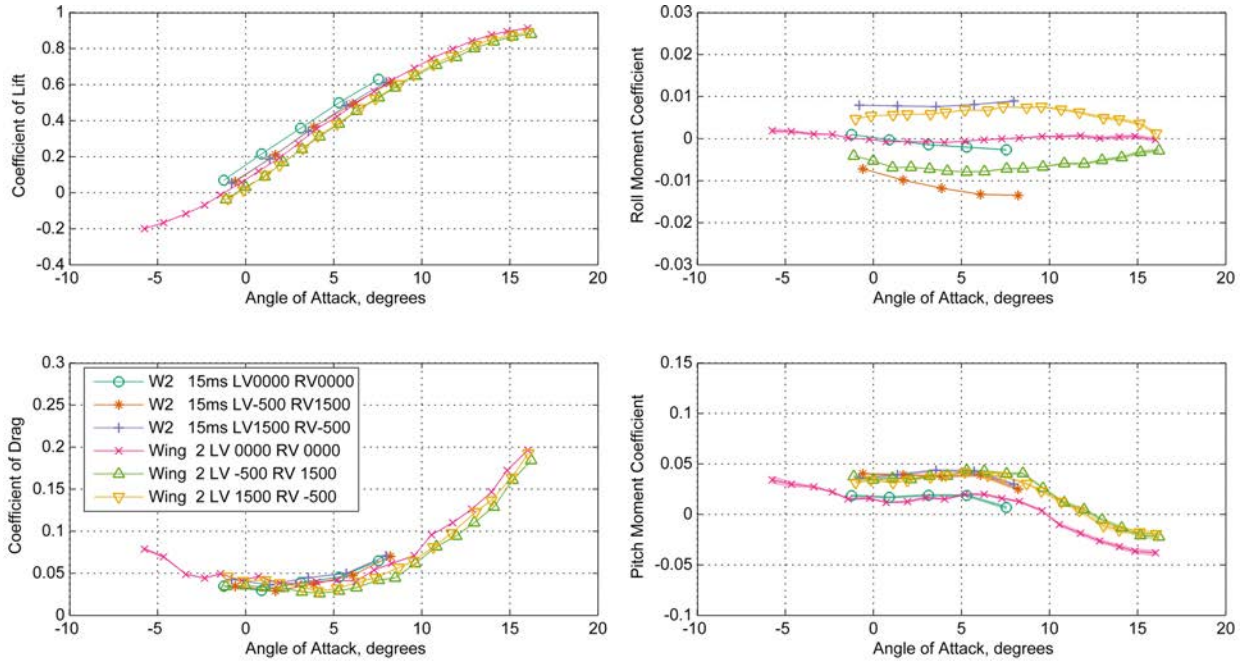

Figure 10-15. MFC2 comparison between first and second set of measurements (roll maneuver).

www.manaraa.com

CHAPTER 11
OPTIMIZATION ROUTINE

After completing and validating the aeroelastic model, it was possible to begin the optimization process. Flight testing showed that the MFC1 provided sufficient pitch authority, but lacked roll authority. Therefore, the overall goal of the optimization was to improve roll authority while maintaining, or slightly improving, pitch authority. This was to be done with the same wing geometry and wing tooling, thereby minimizing costs. Furthermore, as mentioned previously, the end goal was to limit the number of MFC actuators to only two per aircraft.

Before beginning the optimization process, a sensitivity analysis was conducted. This analysis consisted of adjusting each design parameter a small amount and observing its affect on the roll and pitch as calculated by the aeroelastic analysis. The sensitivity analysis was a necessary step, since the aircraft design is composed of dozens of parameters, and each parameter included in the optimization drastically increases the size of the design space. This drastically increases the time required to run an effective optimization.

Figure 11-1 and 11-2 show the results of the sensitivity analysis. The pitch and roll are given as percentage improvements, where the baseline model used throughout the optimization scheme is the MFC2 aircraft. The flight conditions used for all parts of the optimization are 15 m/s with the wing at 5° angle of attack. 5° angle of attack corresponds to 0° for the wind tunnel data, but this is taken into account for all figures and data presented in this document. The dynamic pressure for the aeroelastic model was assigned based on room temperature, 22.2°C (72°F), and pressure was set for sea level at 101,325 Pa (14.7 psi).

Four configurations were analyzed during the optimization routine. To run one function evaluation (analyze one design) at one angle of attack and one velocity with

www.manaraa.com

these four configurations took approximately 20 minutes. The four configurations examined for each design were:

- LV 0000 RV 0000
- LV 1500 RV 1500
- LV -500 RV -500
- LV 1500 RV -500

From the results shown in Figs. 11-1 and 11-2, ten parameters were chosen, and are listed below:

- number of leading edge unidirectional carbon fiber layers (top of laminate)
- number of leading edge bidirectional carbon fiber layers (middle of laminate)
- number of leading edge unidirectional carbon fiber layers (bottom of laminate)
- chordwise length of the leading edge section at wing root
- chordwise length of the leading edge section at wing tip
- angle of unidirectional carbon fiber in the leading edge
- spanwise position of the MFC
- chordwise position of the MFC
- angle of the MFC
- thickness of MFC substrate

Surprisingly, the leading edge layup had a significant affect on the performance of the aircraft. Other properties, such as MFC angle and substrate thickness, were previously considered to have a large impact on aircraft performance. The following sections will describe how these 10 variables are incorporated into the optimization and describe each step of the optimization process.

www.manaraa.com

Summary	Pitch up %	Pitch down %	Roll %
Leading Edge Root (decrease size)	-0.03	-1.05	-3.30
Leading Edge Tip (decrease size)	-0.15	-0.29	-0.08
Leading Edge Root (increase size)	-0.18	0.62	1.49
Leading Edge Tip (increase size)	-0.30	-0.14	0.74
MFC spanwise position (move outboard)	-21.64	-20.25	1.24
MFC chordwise position (move rearward)	-0.07	-0.72	-1.98
MFC chordwise position (move forward)	0.21	-0.62	1.16
MFC angle (decrease from 35 to 25 degrees)	8.31	6.23	-9.99
MFC angle (decrease from 35 to 30 degrees)	3.93	3.66	-4.71
MFC oriented at 40 degrees	-5.60	-5.54	3.72
Add layer of unidirectional on LE (on top)	-0.10	-0.40	8.09
Add layer of unidirectional on LE (on bottom)	-0.60	-0.40	7.76
Add layer of bidirectional inside LE	-1.53	-1.38	17.18
Make leading edge 2 layers bidirectional	-0.15	-0.87	9.83
Make leading edge 3 layers bidirectional	-1.80	-2.03	21.55
uni(22),uni(22),bi,bi,uni(22),uni(22)	-2.53	-1.85	22.13
uni(22),uni(42),bi,bi,uni(42),uni(22)	-2.31	-1.70	22.63
Extra layer of uni on top and bi in the middle	-1.97	-1.30	19.98
extra layer of uni on top and bottom	-0.83	-0.54	13.63
Reduce steel substrate thickness to 0.002"	-16.70	-15.14	-14.53
Increase steel substrate thickness to 0.006"	2.65	1.99	2.31
Increase steel substrate thickness to 0.008"	-1.73	-2.14	-1.57
Increase steel substrate thickness to 0.010"	-9.27	-9.71	-8.92
Increase steel substrate thickness to 0.012"	-17.24	-18.36	-17.51
Replace steel substrate with unidirectional carbon fiber	-6.03	-6.41	-4.95
Change orientation of bidirectional carbon fiber to +/-45	-8.83	-6.66	-7.93
Change unidirectional carbon fiber so it follows LE sweep	-1.28	-0.72	-3.96
Change unidirectional CF so its perpendicular wrt flight direction	-3.16	-3.66	11.15

Figure 11-1. Variable sensitivity. The variables are normalized and color-coded according to improvement (Page 1 of 2).

www.manaraa.com

Summary	Pitch up %	Pitch down %	Roll %
Adjust uni CF so its at -22 degrees	-2.85	-3.01	7.51
Adjust uni CF so its at -18 degrees	-2.40	-2.57	4.38
Adjust uni CF so its at -14 degrees	-2.07	-2.21	1.73
Adjust uni CF so its at -10 degrees	-1.79	-1.85	-0.91
Adjust uni CF so its at -6 degrees	-1.53	-1.52	-2.56
Adjust uni CF so its at -2 degrees	-1.09	-1.01	-3.63
Adjust uni CF so its at 2 degrees	-1.03	-0.80	-3.88
Adjust uni CF so its at 6 degrees	-0.92	-0.83	-3.47
Adjust uni CF so its at 10 degrees	-0.76	-0.33	-2.56
Adjust uni CF so its at 14 degrees	-0.55	-0.43	-1.82
Adjust uni CF so its at 18 degrees	-0.15	-0.29	-0.50
Adjust uni CF so its at 26 degrees	0.34	0.04	0.50
Adjust uni CF so its at 30 degrees	0.72	0.14	0.74
Adjust uni CF so its at 34 degrees	0.98	0.14	0.74
Adjust uni CF so its at 38 degrees	1.09	0.36	0.74
Adjust uni CF so its at 42 degrees	1.28	0.51	0.91
Adjust uni CF so its at 46 degrees	1.68	0.91	1.57
Adjust uni CF so its at 50 degrees	1.76	0.98	2.31
Adjust uni CF so its at 54 degrees	1.98	0.76	3.55
Adjust uni CF so its at 58 degrees	2.04	1.10	5.12
Adjust uni CF so its at 62 degrees	2.00	0.62	7.27
Adjust uni CF so its at 66 degrees	1.73	0.54	9.41
Adjust uni CF so its at 70 degrees	1.56	0.47	11.48

Figure 11-2. Variable sensitivity. The variables are normalized and color-coded according to improvement (Page 2 of 2).

المنارة للاستشارات
www.manaraa.com

11.1 Implementation of Optimization Scheme

The optimization routine takes the aeroelastic simulation developed in the last chapter and essentially executes it like a black box system. A set of input values are defined based on the parameters specified in the previous section and the roll and pitch values are output in the form of the objective function. The objective function is a way to resolve multiple performance aspects of the design into a single value which the optimization uses to rank each design. It is essentially a grading rubric. In this case, it combines the roll and pitch coefficients into a single value on which to rank the design.

Both the pitch range and roll were normalized before calculating the objective function. The normalized pitch range was calculated as follows:

$$\text{pitchrange}_{norm} = \frac{\text{pitchup}_i - \text{pitchdown}_i}{\text{pitchup}_{MFC2} - \text{pitchdown}_{MFC2}} \tag{11–1}$$

Where i designates the current design being considered and $MFC2$ designates the pitchup and pitchdown coefficients for the MFC2 aircraft. The normalized roll was calculated by simply dividing by the MFC2 roll coefficient. The objective function is calculated as shown in Eq. 11–3.

$$\text{ObjectiveFunction} = -\frac{\text{pitchrange}_{norm} + \lambda \cdot \text{roll}_{norm}}{1 + \lambda} \tag{11–2}$$

A weighting factor, λ, was included to increase the optimization's preference for increasing roll. This is because the pitch authority was sufficient in the test flight of MFC1, but the roll authority was significantly lacking. λ was set to 2 at the beginning of the EGO optimization and gradually reduced to 1.05 at the end. The objective function is recalculated for all of the designs each time λ changes.

11.1.1 Latin Hypercube Sampling (LHS) of Design Space

Before beginning the optimization routine, it was necessary to explore the design space. The intent was to produce a surrogate representing the design region. A surrogate is a way to connect the inputs of the model to the outputs of the model,

www.manaraa.com

essentially mapping the design region. In the case of this research, it is how each of the 10 parameters affect the objective function.

The main goal of a surrogate is to create a description of the design space using as few function evaluations as possible. Since each function evaluation takes 20 minutes to run, it is infeasible to map the entire design space in detail (it would take one week to run about 500 function evaluations if running continuously). Therefore, Latin Hypercube Sampling (LHS) is chosen to map the design space in the most strategic way possible with a given number of points.

Contrary to intuition, exploring a multi-dimensional design space with a grid-like pattern is highly inefficient. It requires far too many points to map the design space effectively. If placing a point at each corner of a 3 variable design space (a cube), it would require 8 function evaluations. However, in a 10 variable design space, it would require 2^{10} function evaluations, or a total of 1,024. This would take about two weeks to run if the program was ran continuously. However, the time mapping the design space must also be balanced with the optimization routine. The goal is to sufficiently map the design space so that the optimization routine can progress towards the global optimum. Too much time evaluating the design space, and the optimization routine is hardly utilized. Too little time mapping the design space and the optimization routine will spend too much time trying to find the general location of the optimum or converge on a lesser local optimum.

LHS design provides a way to map the design space in a more effective way with fewer points. The result may seem similar to random sampling, except it strategically places the points within the design space to generate a better set of data for the surrogate. It works by breaking the design space up into a grid format. It then places points within the grid so that each point occupies a different row and column then all the other points. This is shown in a two variable case in Fig. 11-3. An extra property

www.manaraa.com

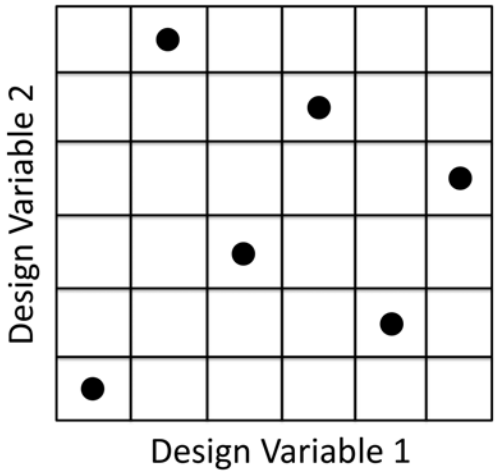

Figure 11-3. LHS design methodology for a two variable design space.

defined within MATLAB was a “maximin function.” This maximizes the minimum distance between points in the LHS design by iterating through multiple cases.

The LHS design started out with 250 points. It was known from performing a small LHS design, that roughly 40% of the points would be infeasible. Therefore a larger initial group size was chosen. After eliminating the points that created conflicts in geometry (the MFC protruding from the wing), 146 points were left. The feasible points were then evaluated. Both the feasible and infeasible points are shown in Fig. 11-4. The box in this figure illustrates the design space considered, albeit in only three dimensions. The true design space is in ten dimensions. Three examples of designs evaluated in the LHS method are shown in Fig. 11-5. Included among these is one example in which the MFC protrudes from the perimeter of the wing, which was designated an infeasible point due to the geometry conflict. To encourage the optimization to avoid infeasible regions of the design space, the objective function is automatically set to 1.2, which is greater than the baseline, but still less than the better designs.

To limit the design space to only the area with the liklihood of having the best designs, bounds are placed on the LHS design and the successive optimization. The bounds on the design space are given in Table 11-1. The maximum number of layers for the leading edge is specified as 9, due to weight concerns. However, weight is not

www.manaraa.com

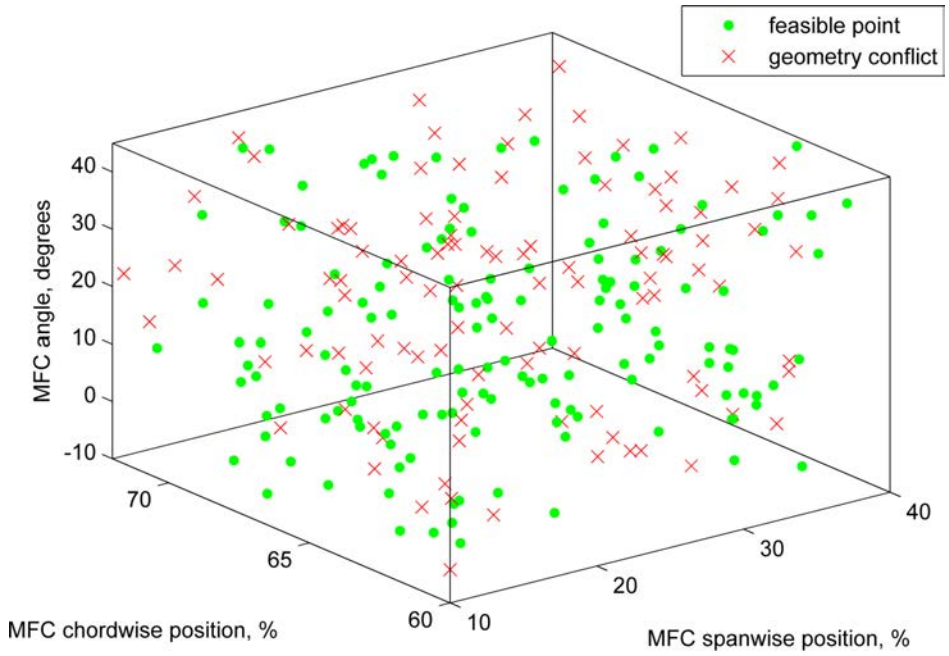

Figure 11-4. LHS design region, with the feasible and infeasible points shown.

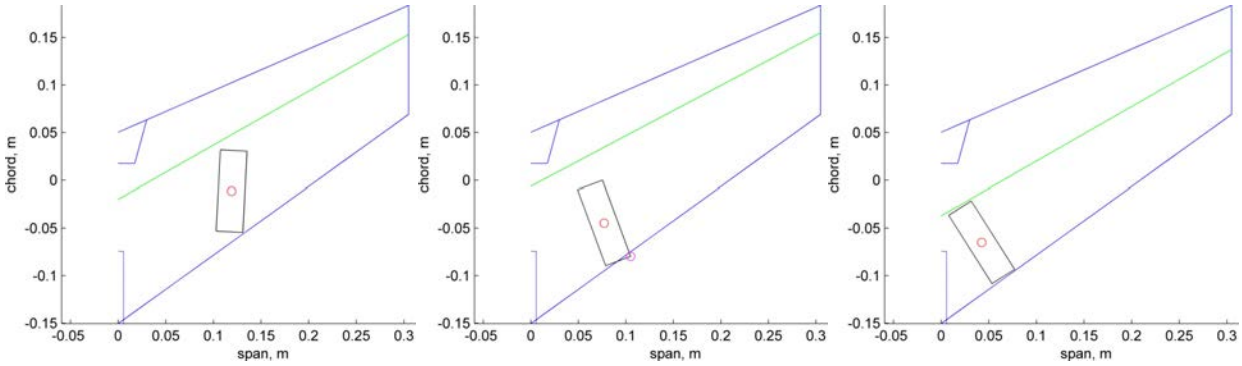

Figure 11-5. Examples of three LHS designs. A) LHS 167 - Feasible geometry. B) LHS 168 - Infeasible geometry. C) LHS 170 - Feasible geometry.

considered during this part of the analysis. The other bounds are chosen based mainly on geometrical constraints.

11.1.2 EGO Optimization

Efficient Global Optimization (EGO) is a relatively new optimization scheme first discussed in a 1998 journal article [79]. Additional work has built on this core concept with great success [80–87].

www.manaraa.com

Table 11-1. Bounds for forward swept optimization design region.

Design Property	Lower bound	Upper bound
Uni layers on top of LE	1	3
Bi layers in LE	1	3
Uni layers on bottom of LE	1	3
LE chord root, %	21	45
LE chord tip, %	21	45
LE uni angle, degrees	14	30
MFC spanwise position, %	10	40
MFC chordwise position, %	60	72
MFC angle, degrees	-10	45
substrate thickness, mm	0.10	0.15

The fundamental goal of EGO is to balance exploration and exploitation. Exploitation is strategically placing the next point in an area where the surrogate suggests an improved objective function. This point generally has low uncertainty. On the other hand, exploration is when a point is placed in an area with high uncertainty which also offers an opportunity for improvement. Evaluating this point decreases the uncertainty of the surrogate and improves the placement of future points. This practice is best illustrated by Fig. 11-6 [88], in which a one variable design space is shown. In this case, the function is being minimized.

In this series of figures, $y(x)$ represents the true function, evaluated data points are represented by circles, $y_{KRG}(x)$ is the Kriging surrogate, and y_T is the targeted improvement. In Kriging, the uncertainty goes to zero at the data points. In addition, the shaded area represents the uncertainty associated with the Kriging surrogate. Therefore, there are three areas which might yield an improvement. These areas lie around 0.21, 0.62, and 0.75. Based on the uncertainty and the expected improvement, EGO will select one of the three points. The surrogate will then be refit to the original data points plus the new data point. Then, the process will repeat.

There are two predominant adaptations of EGO, each with many variations. “Probability of improvement” (PI) was the first option explored and was later followed with “expected improvement” (EI). The initial authors favored PI over EI. However, setting

www.manaraa.com

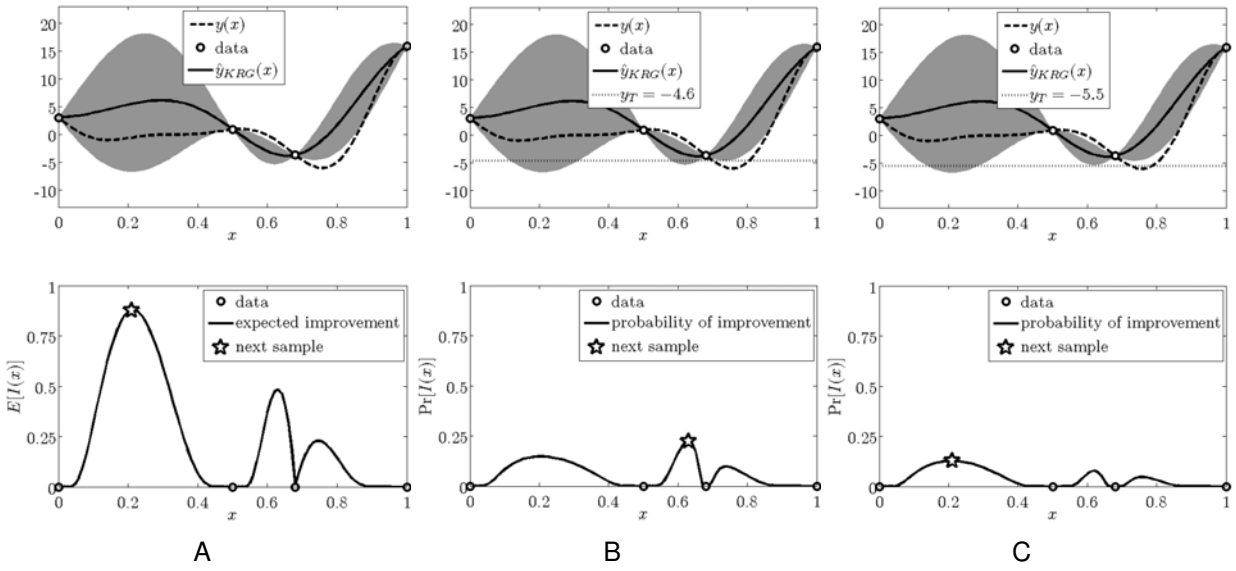

Figure 11-6. Conceptual illustration of EGO methodology. Images courtesy of Viana [88]. A) EGO EI - Maximization of expected improvement. B) EGO PI - Maximization of the probability of improvement with target set at -4.6. C) EGO PI - Maximization of the probability of improvement with target set at -5.5.

the target for PI was a challenging task in many scenarios. Therefore, EI was widely adopted.

EI follows the optimization scheme shown in Fig. 11-6A. EGO EI produces the curve shown on the bottom based on the uncertainty of the function. This function is essentially a representation of uncertainty in the function and the possibility of improvement. Therefore, since the area around 0.21 has the largest uncertainty and may produce an improvement beyond the present best solution (point at 0.68), EGO EI chooses this point to evaluate next.

EGO PI requires the user to specify a target. It uses this target to determine where to place the next point, as shown in Figs. 11-6B and 11-6C. This method determines which potential point will have the highest probability of improvement based on the function's uncertainty, rather than simply a possibility of improvement. Recent work by Chaudhuri [89], has produced a new EGO methodology. This method, called "Adaptive Targeting," adjusts the target after each iteration. Therefore, if the target is set too

www.manaraa.com

high or too low, it will be adjusted to lie in the correct region. Early results suggest that EGO AT may perform better than EGO EI, showing continuous improvement from one iteration to the next, rather than plateauing, as is common with EGO EI.

For this research, the EGO optimization process was conducted in several parts. The initial series of runs were conducted with EGO EI. After conducting several EGO EI iterations, a combination of EGO AT and EGO IE were utilized. However, the initial EGO EI improved vastly on the initial design and left little room for the later optimizations to continue to improve.

The results of the initial LHS design and EGO optimizations are shown in Fig. 11-7. Both the normalized pitch range and normalized roll are shown with the objective function. The LHS design is clearly seen at the left side of the figure since the design points are spread across a large range of values. The EGO routine quickly finds a few designs that improve on the initial MFC2 design. Anything with a value greater than 1 (above the horizontal grey line) is an improvement. In other words, a value of 1.2, can be considered a 20% improvement on the MFC2 design. As mentioned previously, a λ of 2 was used at the beginning of the EGO optimization and gradually reduced to 1.05 towards the end.

Figure 11-8 shows the EGO points superimposed with the LHS design points for the three features affecting MFC position. It can be seen in the figure that the EGO optimization was seeking an optimium near the point where the MFC spanwise position was between 20 and 30%, the MFC chordwise position was near 60% boundary, and the MFC angle was between 25 and 35%. The other 7 variables are not shown in this plot.

As mentioned, a combination of EGO EI and EGO AT were used to search for an optimum design. Since each function evaluation takes approximately 20 min, optimization runs were grouped in sets of 20-30. This meant the optimization could run for 7-10 hours without manual intervention and then the results evaluated to make

www.manaraa.com

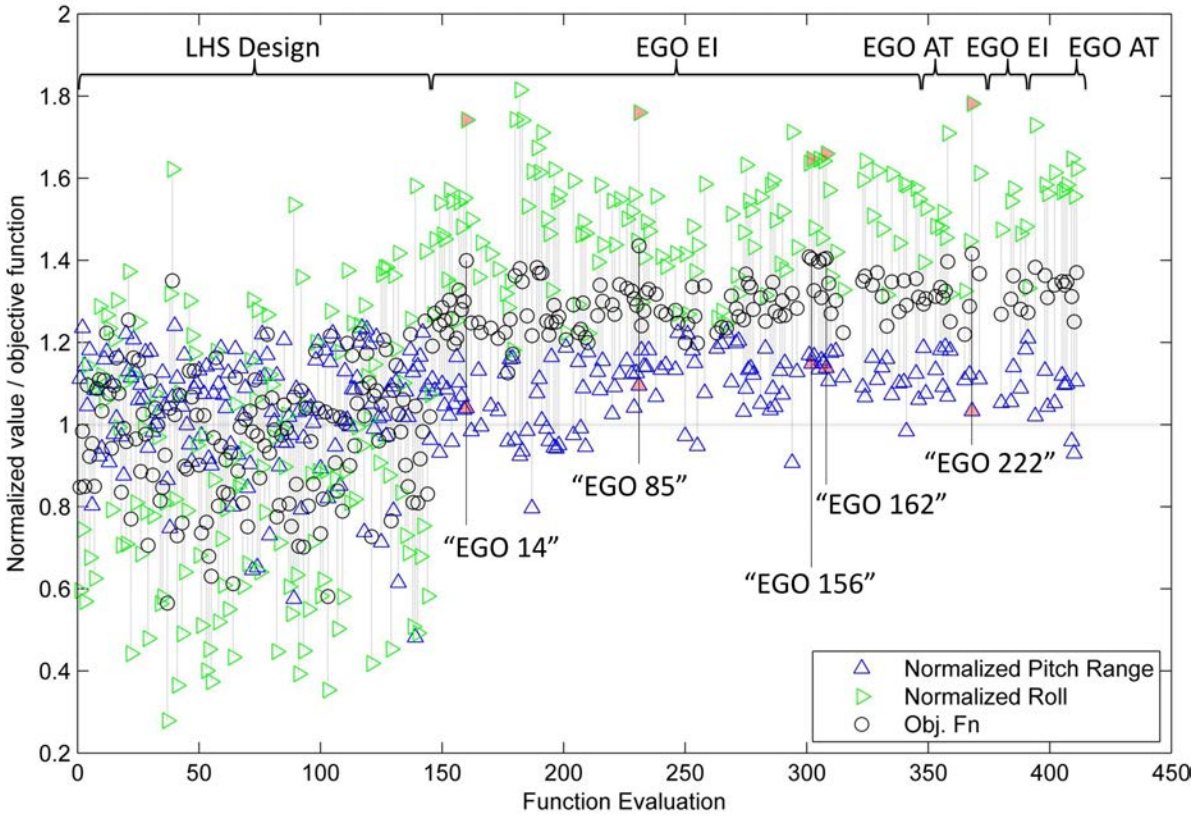

Figure 11-7. LHS Design and EGO results. ($\lambda = 1.05$)

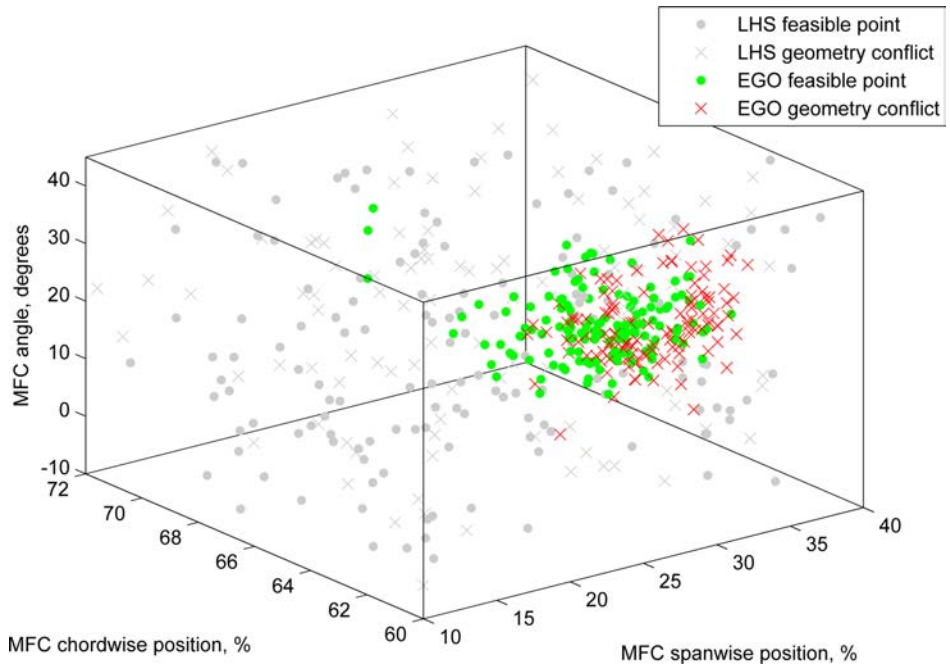

Figure 11-8. LHS and EGO design points, with the feasible and infeasible points shown.

www.manaraa.com

any adjustments, such as λ, for the next set. In addition, each time a new design was evaluated, the results were incorporated into the surrogate which improved the optimization.

Another way to view the results is by plotting the present best solution during each step of the optimization. The present best solution is the design with the best objective function, which may not be the most recent evaluation. This type of plot shows how the optimization is improving during the course of the optimization and if it has reached a plateau. Figure 11-9 shows the present best solution over the course of the EGO optimization cycles along with the objective function for each cycle. As the figure demonstrates, the EGO optimization was quick to improve on the design, producing a design within 14 iterations with a 40% improved objective function. It is not until the 85th iteration that this is improved upon for a total improvement of 43.5%. This is noteworthy since iteration 14 produces about 92% of the total improvement. None of the succeeding iterations improve on the objective function after iteration 85, however, some come close and represent alternative designs.

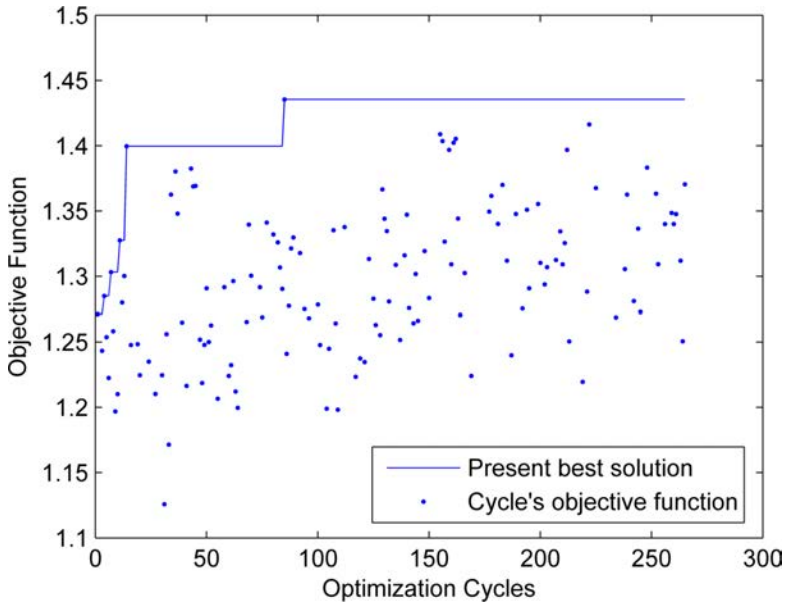

Figure 11-9. EGO present best solution during the optimization cycles. The objective function for each cycle is also shown.

www.manaraa.com

Five designs stand out from the group and are noted in the figure. The normalized pitch range and roll values for each of these five designs are highlighted. These five designs are the ones that ranked the best according to the objective function and also represent designs with notable differences. The five designs are superimposed on each other in Fig. 11-10. In addition, the specifics of these results are summarized in Tables 11-2 and 11-3.

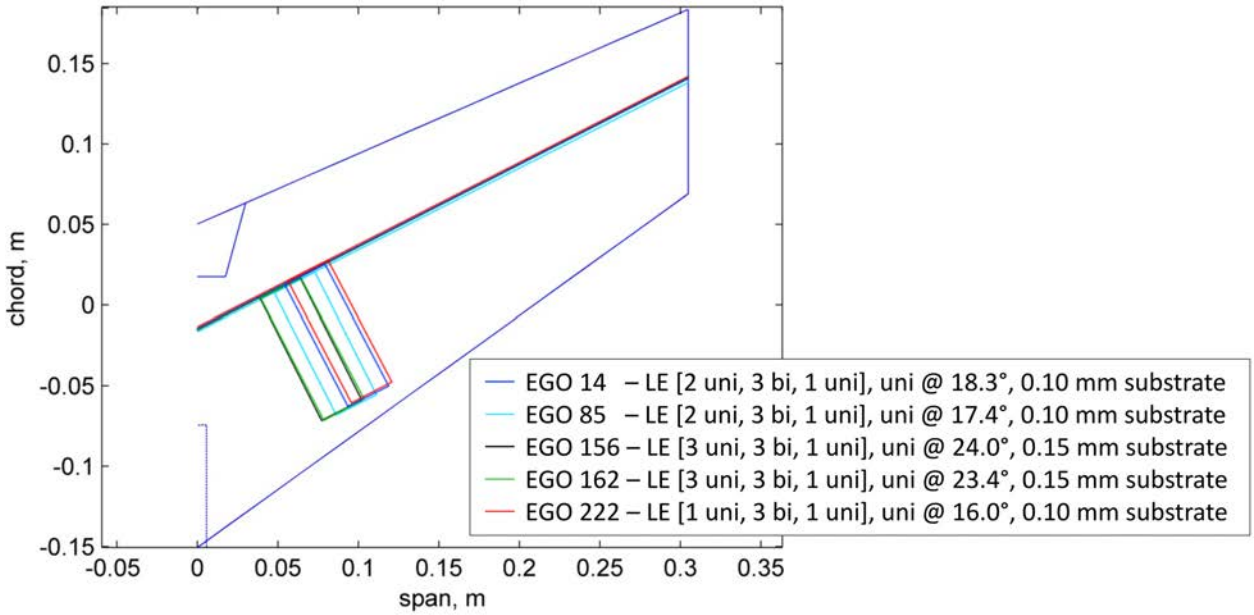

Figure 11-10. The top five EGO designs.

After conducting the global optimization, it was decided that there should be an equal number of layers of unidirectional carbon fiber in the top and bottom of the leading edge. This is because warping takes place whenever a layup is unsymmetric due to orthotropic thermal expansion of the composites during the curing process. An example of an unsymmetric [2 uni, 3 bi, 1 uni] layup is shown in Fig. 11-11. This layup was performed on a flat surface, yet due to residual strains, the laminate is curved. This could have a significant effect on the wing design by unintentionally modifying the wing twist.

www.manaraa.com

Figure 11-11. Example of an unsymmetric layup exhibiting warping. The layup is [2 uni, 3 bi, 1 uni]. Photo taken by Bradley LaCroix.

11.1.3 Fmincon

The final step of the optimization process is to apply a local optimizer. Fmincon operates by starting at a user specified point, perturbing each design variable a small amount, and then moving in a direction based on that information. In other words, its decision is based on the numerical derivatives from the pertubations. Once it arrives at the next data point, it evaluates the result and then decides which direction to move next. Fmincon does not take into account data from any prior point in the optimization, such as the EGO or LHS design results. Tables 11-2 and 11-3 show the design results of the EGO optimization, initial fmincon points, and the final fmincon results. Figure 11-12 and 11-13 show the evaluation of each point during the fmincon optimization.

For this part of the optimization, 30 function evaluations were conducted for each design. As mentioned in the previous section, the top and bottom layers of the leading edge layup are constrained to be an equal number of layers and less than 3 (i.e. 1 and 1, 2 and 2, 3 and 3). This is incorporated in order to prevent warping. In addition, a penalty for each layer added is incorporated into the objective function. This is intended to prevent the optimization from stiffening the wing too much. Stiffening the wing was inferred to be aerodynamically beneficial, but determined not to be beneficial from a weight perspective. Therefore, each additional layer added to the leading edge layup had a penalty on the objective function of 0.015. The best resulting designs were

www.manaraa.com

Table 11-2. Best cases from EGO and the initial and best points from fmincon. Leading edge properties. (Table 1/2)

Design	Layers of uni on top	Layers of bidirectional	Layers of uni on bottom	Root chord %	Tip chord %	LE uni angle
EGO 14	2	3	1	32.0	37.0	18.3
EGO 85	2	3	1	33.0	40.0	17.4
EGO 156	3	3	1	33.0	37.0	24.0
EGO 162	3	3	1	32.0	37.0	23.4
EGO 222	1	3	1	32.0	36.0	16.0
Fmincon13 initial point	1	2	1	32.3	38.0	24.2
Fmincon14 initial point	2	3	2	33.0	40.0	17.4
Fmincon13 best point	2	3	2	32.3	38.3	24.2
Fmincon14 best point	2	3	2	32.9	40.3	17.4

Table 11-3. Best cases from EGO and the initial and best points from fmincon. General wing properties and results. (Table 2/2)

Design	MFC Spanwise %	MFC Chordwise %	MFC angle, degrees	Substrate thickness, mm	Pitch Range (coefficient)	Roll (coefficient)
EGO 14	28.4	60.5	27.5	0.10	0.1211	0.0199
EGO 85	26.1	61.2	26.9	0.10	0.1275	0.0201
EGO 156	23.2	60.0	26.7	0.15	0.1337	0.0188
EGO 162	23.4	60.0	27.4	0.15	0.1325	0.0189
EGO 222	29.1	60.0	27.5	0.10	0.1202	0.0203
Fmincon13 initial point	24.5	60.0	27.0	0.10	0.1348	0.0168
Fmincon14 initial point	26.1	61.2	26.9	0.10	0.1261	0.0190
Fmincon13 best point	25.3	60.0	26.9	0.15	0.1311	0.0212
Fmincon14 best point	26.4	61.0	27.4	0.15	0.1296	0.0211

www.manaraa.com

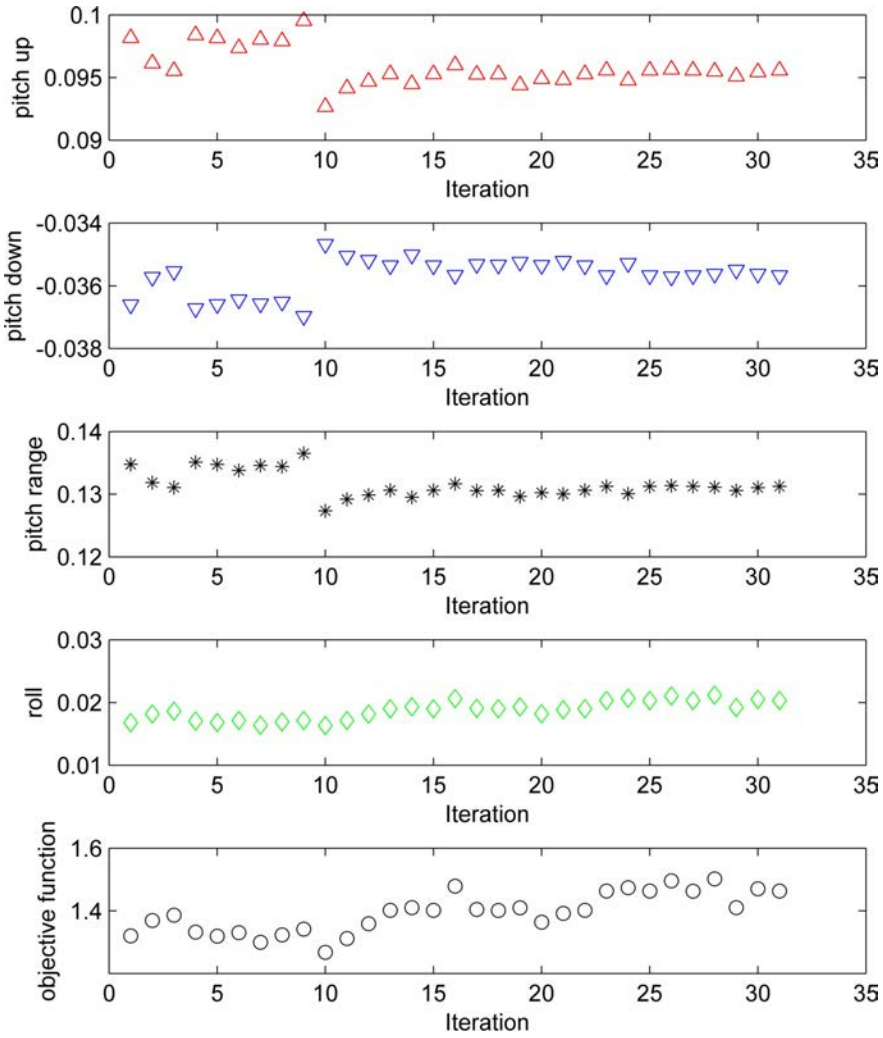

Figure 11-12. Local fmincon optimization for the fmincon13 design.

determined to be iteration 28 of Fmincon 13 and iteration 29 of Fmincon 14. These designs will be termed MFC13 and MFC14 for the remainder of this document.

A Pareto front for the optimization process is shown in Fig. 11-14. This plot compares the roll authority and pitch authority of each design and is useful in illustrating the tradeoff between the two objectives. The top five EGO points occupy a point near the Pareto front, but are not on the front because EGO tends to function in an exploratory manner rather than exploitatory. In other words, EGO continues to look for other “good” points rather than focusing in on a region to determine “great” points. The local optimizer, fmincon, follows up on the EGO results by producing two additionally

www.manaraa.com

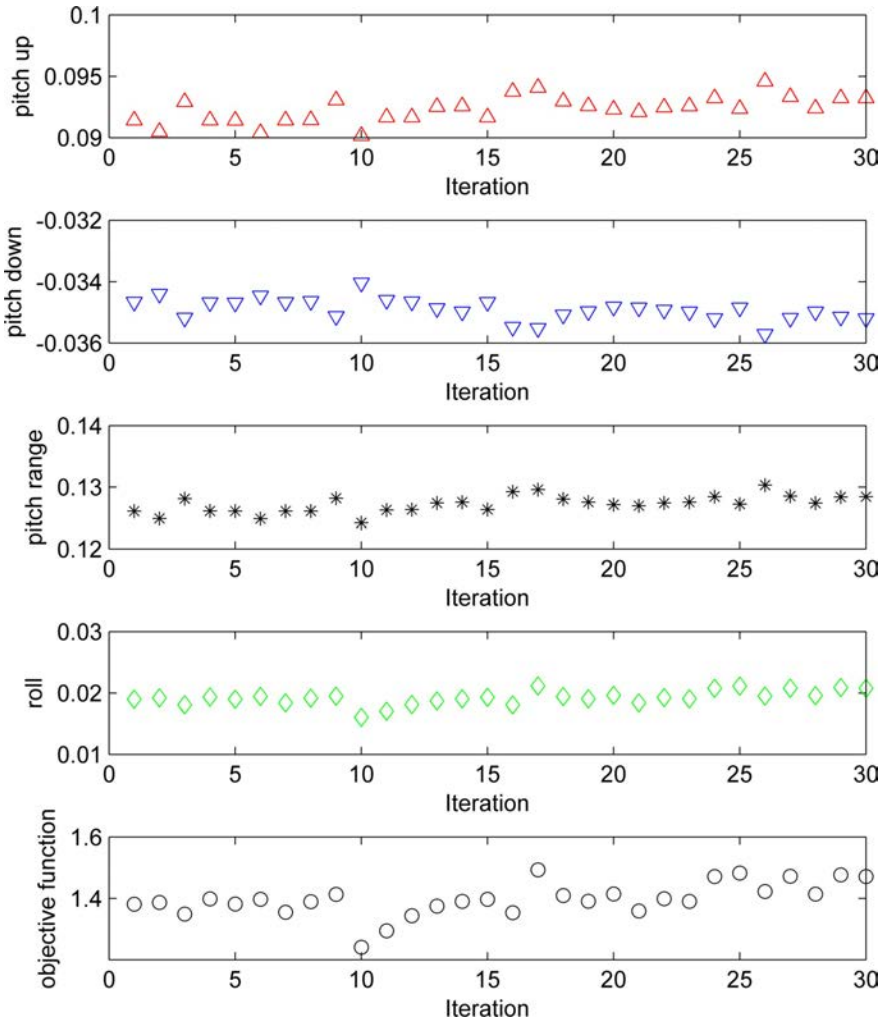

Figure 11-13. Local fmincon optimization for the fmincon14 design.

improved designs, which are likely on the Pareto front. The roundness of the Pareto front region indicates that roll and pitch are competing objectives and sacrificing some pitch authority would result in a small increase in roll authority and vice versa.

11.1.4 Results and Discussion

Overall, the optimization predicts that MFC13 will have an 86% improved roll authority and a 13% improved pitch authority when compared to the original MFC2 prototype. The optimization also predicts that MFC14 will have 83% improved roll authority and 10% improved pitch authority over the original MFC2 prototype. These designs were built and tested and the results discussed in Chapter 12.

www.manaraa.com

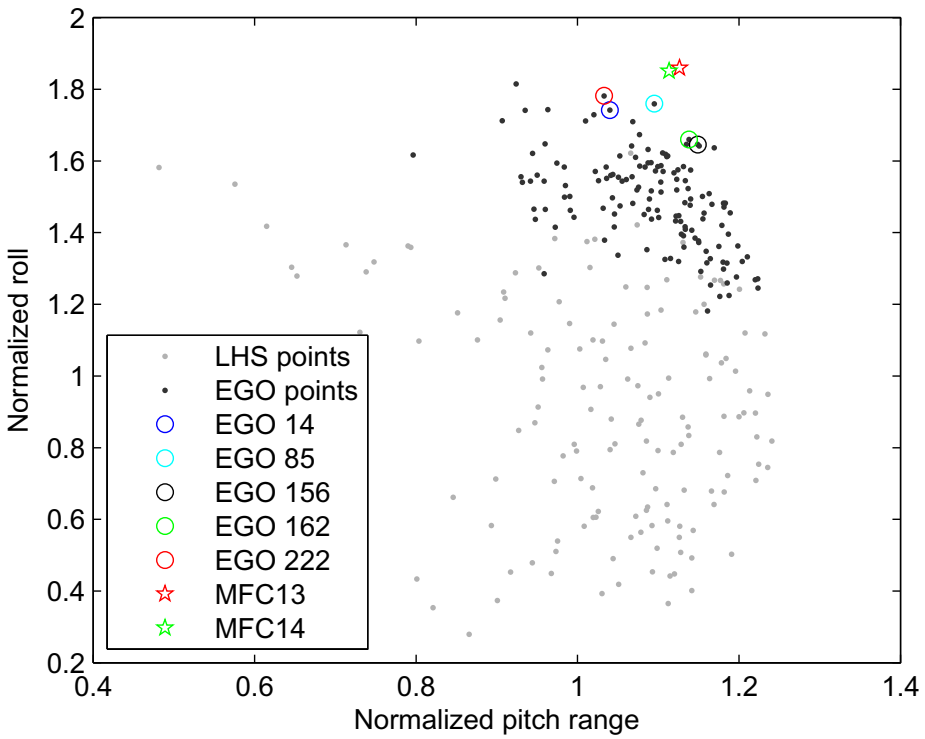

Figure 11-14. Pareto front for the forward swept optimization.

The comparison between the designs of the MFC1, MFC2, MFC13, and MFC14 are shown in Fig. 11-15. The dark blue line indicate the perimeter of the wing for the MFC2, MFC13, and MFC14, whereas the light blue color indicates the MFC1 design. Variations in manufacturing led to a different perimeter, however, additional care was taken to make MFC13 and MFC14 match up with MFC2. Overall, it appears that the largest factors corresponding to an improvement in performance is the proximity of the MFC to the leading edge (closer is better), substrate material and thickness, and the leading edge stiffness. Other factors were the layup geometry and the fiber orientation.

MFC1 seemed to parallel these requirements quite well by coincidence. However, the substrate material selection was not optimized. In addition, the location of the MFC on the MFC13 and MFC14 are farther forward and the leading edge is also narrower. The next chapter will detail the testing for the final round of experiments. These experiments are then used to validate the model predictions.

www.manaraa.com

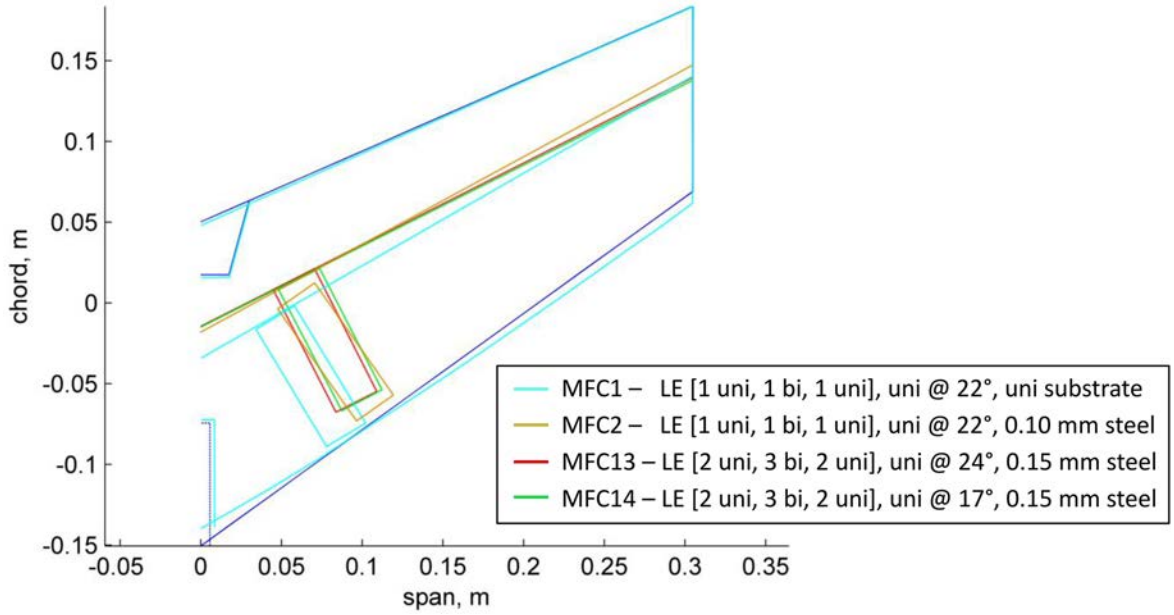

Figure 11-15. Comparison between the original MFC prototypes and optimized designs.

11.2 Application to a Rear Swept Wing Design

The method described in the first part of this chapter can be used to examine other aircraft designs, including a rear swept wing design. A rear swept design is particularly interesting in the case of this research since it may provide a planform with similar pitch and roll characteristics to the forward swept design. In such a design, the MFCs would be placed farther outboard (and rearward), so that they can provide sufficient pitch authority, as was demonstrated in Fig. 9-1 in Chapter 9. The goal of this section is to determine whether an optimized rear swept design would provide a satisfactory alternative design and how such a design would compare to the forward swept design.

11.2.1 Maintaining an Analogous Comparison

To make a fair comparison, a number of variables were held fixed and others, which could not be held constant, were carefully modified. Variables that were held constant include the wing area, airfoil shape, and taper ratio. The slot for the vertical stabilizer in the trailing edge section of the wing was maintained in the rear swept wing, even though

www.manaraa.com

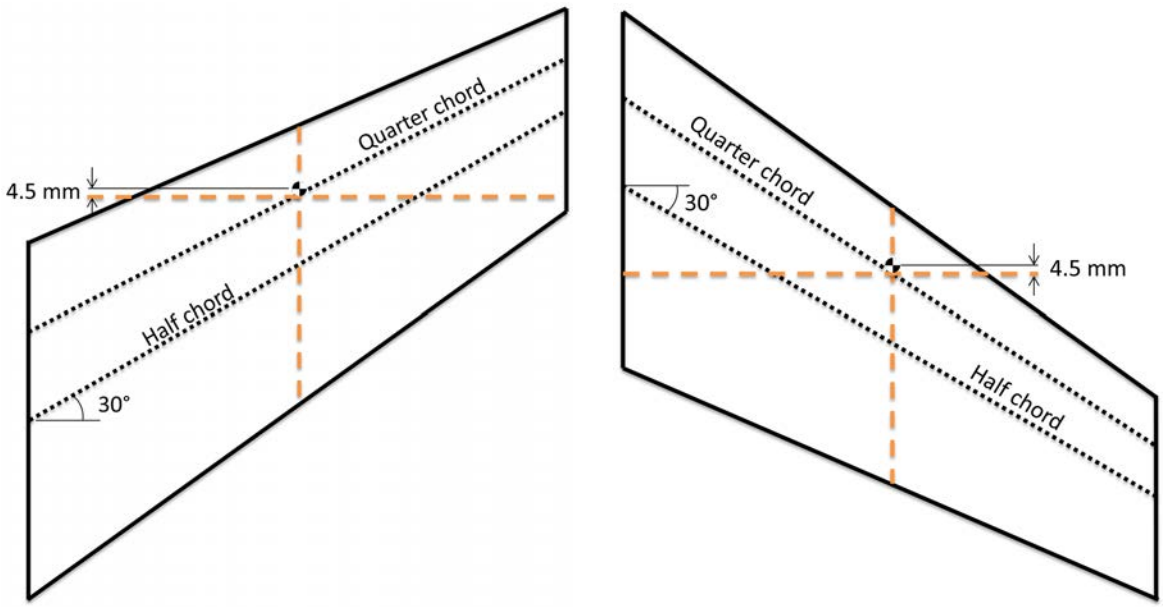

Figure 11-16. Center of gravity determination for the rear swept wing. A) Center of gravity for the forward swept wing. B) Center of gravity for the rear swept wing.

the vertical stabilizer was moved farther back and behind the wing. The sweep angle was maintained, but reversed, with respect to the half chord.

The two variables which could not be held constant, but had to be adjusted carefully were the center of gravity (CG) position and the boundary conditions for the fuselage. The position for the CG, which was determined during the flight testing of MFC1, was maintained with respect to the bisection of the quarter chord. The sweep angle and center of gravity determination are shown in Fig. 11-16. To determine the point of reference for the CG, the quarter chord line was drawn on the wing and the reference point taken at the half-span point. Then, the CG was moved forward the same amount for both cases.

The other variable, the boundary conditions for the fuselage, was modified slightly for the rear swept design. To maintain a fair comparison, the perimeter length of the

www.manaraa.com

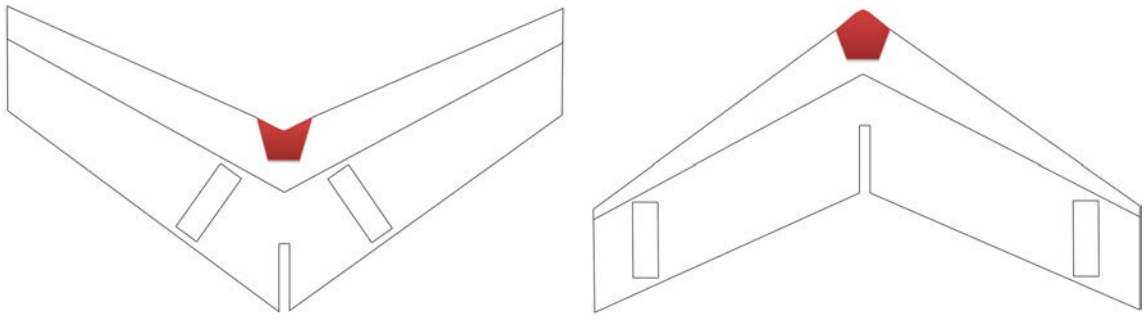

Figure 11-17. Forward and rear swept boundary conditions. A) Boundary conditions for the forward swept wing. B) Boundary conditions for the rear swept wing.

boundary conditions was maintained. The shape of the rear portion of the boundary conditions was also maintained. This is shown in Fig. 11-17.

11.2.2 Latin Hypercube Sampling (LHS) of Design Space

The same optimization variables used for the forward swept wing were used for the rear swept wing optimization. One minor revision, which was implemented during the fmincon phase of the optimization for the forward swept wing, was the combination of the leading edge layup variable for the number of layers of unidirectional carbon fiber. As mentioned in Section 11.1.2, to maintain a symmetric layup and prevent warping, the number of unidirectional layers on the top of the leading edge and the bottom of the leading edge must be equal. Therefore, the number of design variables for the rear swept wing was reduced from 10 variables to 9.

The bounds for the optimization are shown in Table 11-4. As mentioned previously, the MFC position was moved farther outboard on the rear swept wing so that it would be at a reasonable longitudinal distance from the CG. In addition, the bounds for the chord of the leading edge partition at the root was increased to provide additional capacity for material reinforcement. The bounds for the chord at the tip were also adjusted to allow more space for the MFC.

The LHS process was reduced from 250 initial points to 150 to reduce computational time. Each iteration for the rear swept design took approximately 40 minutes rather than

www.manaraa.com

Table 11-4. Bounds for rear swept optimization design region.

Design Property	Lower bound	Upper bound
Uni layers on top/bottom of LE	1	3
Bi layers in LE	1	3
LE chord root, %	27	50
LE chord tip, %	1	30
LE uni angle, degrees	-15	15
MFC spanwise position, %	55	91
MFC chordwise position, %	55	68
MFC angle, degrees	-25	25
substrate thickness, mm	0.10	0.15

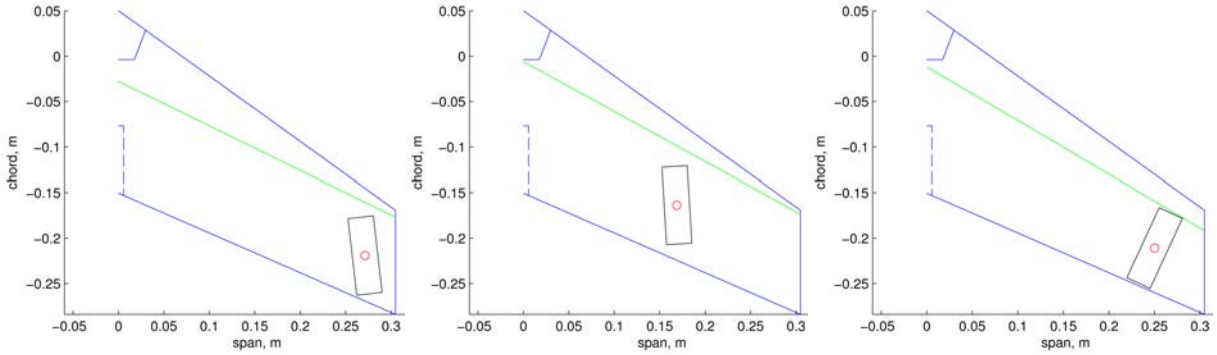

Figure 11-18. Examples of three rear swept LHS designs. A) LHS 2. B) LHS 48. C) LHS 86.

20 minutes, since the aeroelastic convergence required additional iterations to reach the convergence criteria. Reducing the number of points in the LHS design was considered acceptable since the 250 points for the forward swept wing design seemed to provide a very thorough investigation of the design space as indicated by the rapid optimization. In addition, the number of variables in this case was reduced from 10 to 9. After eliminating the infeasible design, 67 feasible points remained. Figure 11-18 shows three feasible rear swept designs that were examined during the LHS design space exploration. These provide an illustration of the range of geometries examined during the optimization process. To encourage the optimization to avoid infeasible regions of the design space, the objective function for the infeasible points was set to a value of approximately 90% of the present best design during each stage of the optimization.

www.manaraa.com

11.2.3 EGO Optimization

After the LHS design, several small runs of EGO were again used to try to improve the pitch authority of the rear swept wing design. The objective function was modified to place additional weight on the pitch authority as follows.

$$\text{ObjectiveFunction} = -\frac{\lambda \cdot \text{pitchrange}_{norm} + \text{roll}_{norm}}{1+\lambda} \tag{11–3}$$

The pitch and roll coefficients were normalized based on the optimized forward swept MFC13 design. This makes it easy to determine which designs are better or worse in terms of roll and pitch authority. Anything with a value less than 1 has less control authority than MFC13 and vice versa. Figure 11-19 shows the results of the LHS design and the subsequent EGO optimizations. The top five iterations with the highest normalized pitch coefficient are noted in the figure. Once again, both EGO AT and EGO EI were used. λ was increased during each subsequent run without any notable effect. For the last 10 runs, the objective function was modified so that its value was simply the normalized pitch coefficient, taking the roll coefficient completely out of the equation. It was expected that this may yield a design with a larger pitch coefficient, but the results did not surpass the previous EGO iterations.

Figure 11-20 shows the present best solution over the course of the EGO optimization cycles along with the objective function for each cycle. As the figure demonstrates, the EGO optimization was quick to improve on the design, producing a superior design within 13 iterations. None of the succeeding iterations improve on the objective function after this design, although some come close. The geometry and other specifications of the top five designs are illustrated in Fig. 11-21.

11.2.4 Fmincon

After completing the EGO portion of the optimization, fmincon was used as a local optimization. A total of 30 function evaluations were conducted, with an elapsed time of about 20 hours. The best design is shown in Tables 11-5 and 11-6 where it is also

www.manaraa.com

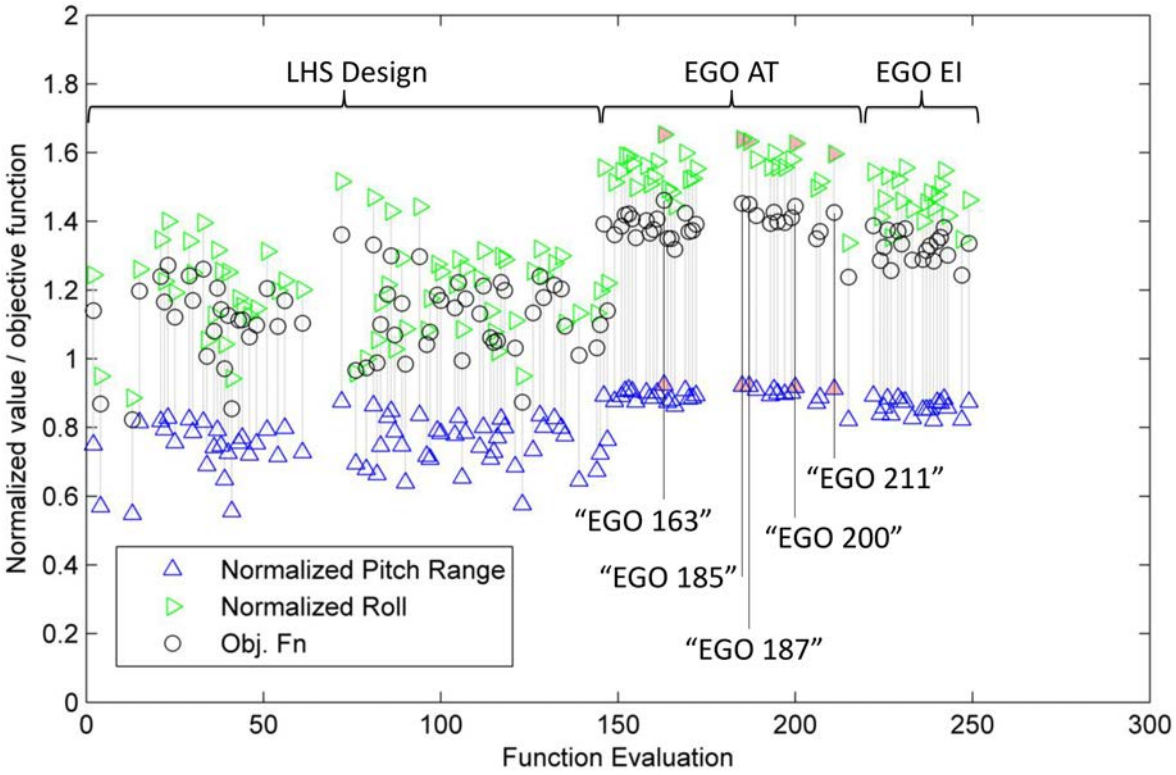

Figure 11-19. LHS design and EGO results for the rear swept wing. The top five designs with respect to pitch authority are noted. The objective function values were calculated with $\lambda = 3.0$.

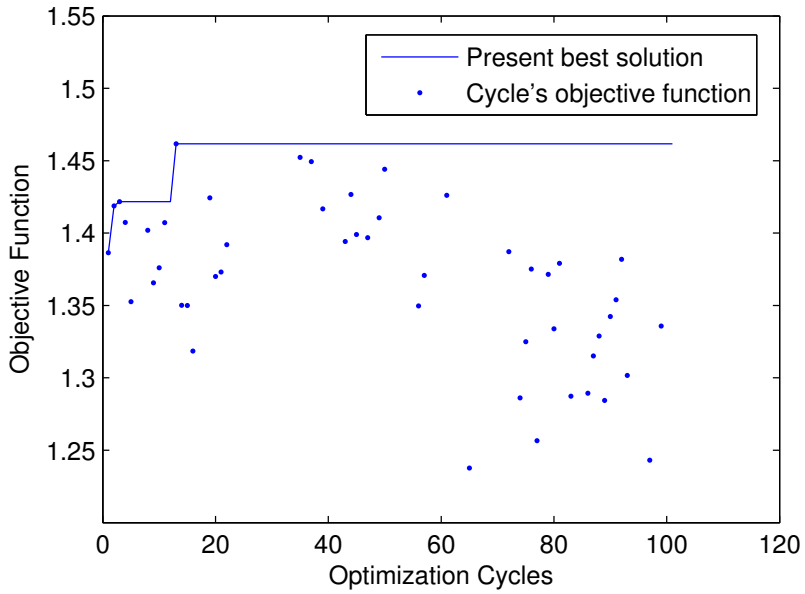

Figure 11-20. EGO present best solution during the optimization cycles. The objective function for each cycle is also shown.

www.manaraa.com

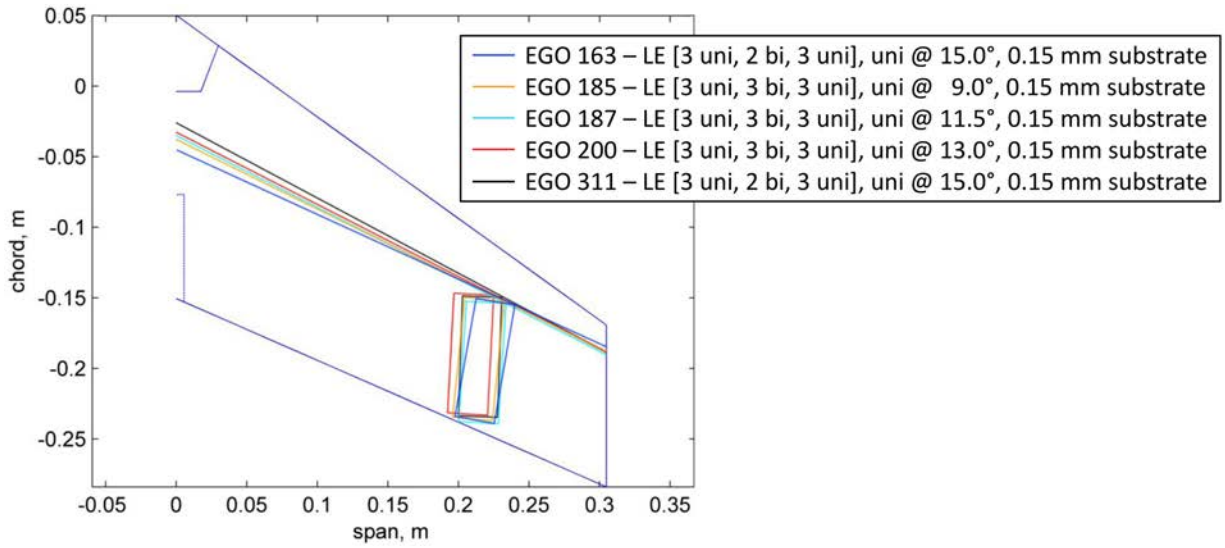

Figure 11-21. LHS design and EGO results for the rear swept wing. The top five designs with respect to pitch authority are noted. The objective function values were calculated with $\lambda = 3.0$.

compared to the initial fmincon design and top five EGO designs. The optimized design has 95% of the pitch authority as the forward swept design and 75% more roll authority. However, the optimized design requires 9 layers of carbon fiber for the leading edge in order to produce these results.

The progression of the fmincon optimization is illustrated in Fig. 11-22. One of the initial pertubations failed due to infeasible geometry, therefore it is not shown in the plot. After the initial sequence of pertubations (first 8 points), the optimization steadily increases the pitch and roll authority. Point 25 yields the best solution out of the points evaluated. Figure 11-23 shows a side-by-side comparison of the optimized rear swept design and the optimized forward swept design. It is important to note how in both cases, the MFC is oriented in a way which follows the curvature of the wing. In this way, it is not actuating against the stiffness produced by the wing curvature, but is actuating in the most compliant direction.

A Pareto front for the rear swept wing optimization is shown in Fig. 11-24. Contrary to the Pareto front shown for the forward swept optimization (Fig. 11-14), this Pareto front indicates that the two objectives are not competing. Generally speaking, an

www.manaraa.com

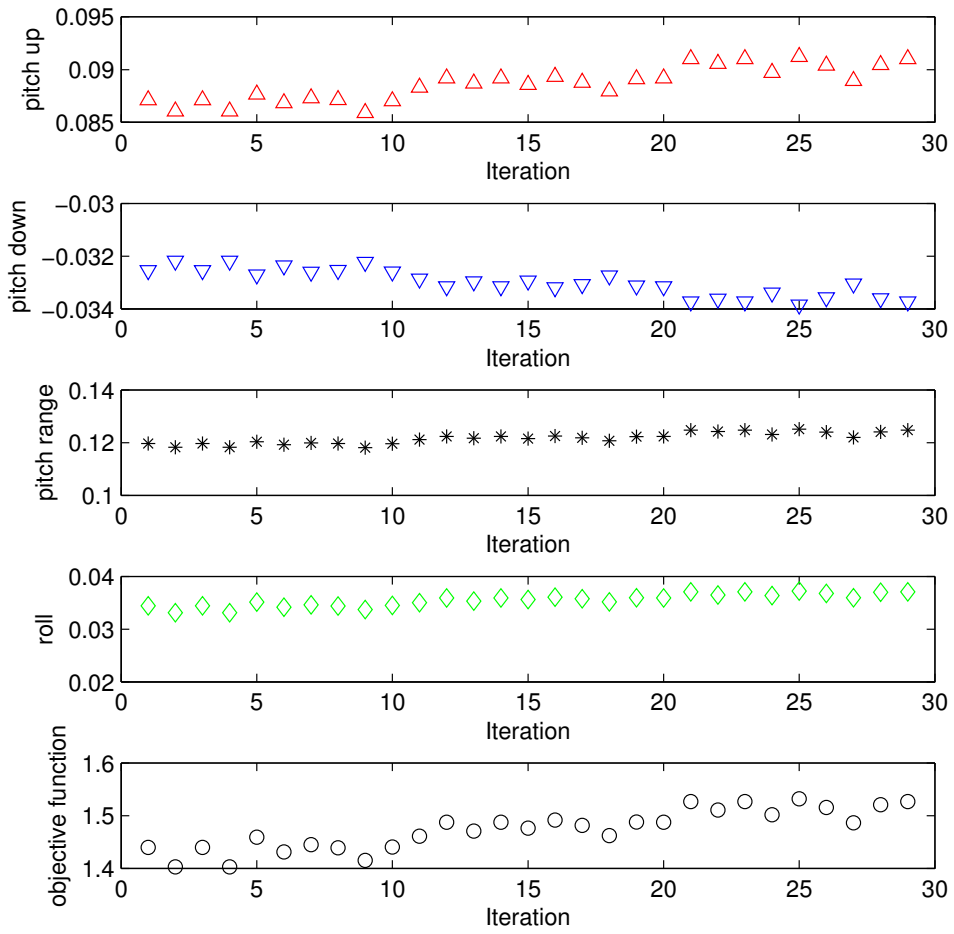

Figure 11-22. Local fmincon optimization for the rear swept design.

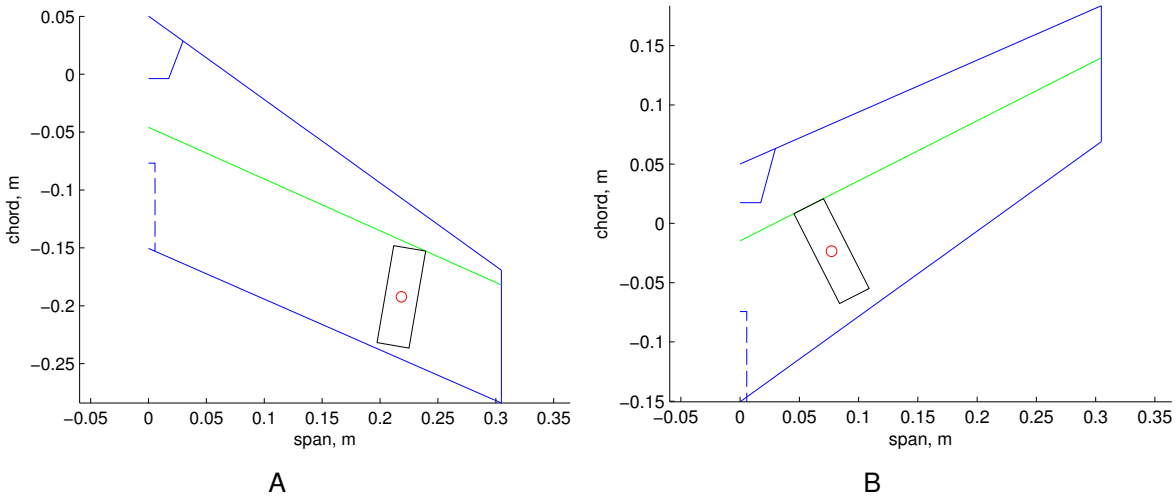

Figure 11-23. Side-by-side comparison of optimized forward swept and rear swept designs. A) Layout of rear swept design. B) Layout of forward swept design.

www.manaraa.com

Table 11-5. Best cases from EGO and the initial and best points from fmincon for the rear swept wing. Leading edge properties. (Table 1/2)

Design	Layers of uni on top	Layers of bidirectional	Layers of uni on bottom	Root chord %	Tip chord %	LE uni angle
EGO 163	3	2	3	47.4	13.4	15.0
EGO 185	3	3	3	43.8	16.4	9.0
EGO 187	3	3	3	42.3	18.4	11.5
EGO 200	3	3	3	41.3	16.9	13.0
EGO 211	3	2	3	37.9	16.7	15.0
Fmincon initial point	3	2	3	47.4	13.4	15.0
Fmincon best point	3	3	3	47.8	11.1	17.9

Table 11-6. Best cases from EGO and the initial and best points from fmincon for the rear swept wing. General wing properties and results. (Table 2/2)

Design	MFC Spanwise %	MFC Chordwise %	MFC angle, degrees	Substrate thickness, mm	Pitch Range (coefficient)	Roll (coefficient)
EGO 163	71.8	62.8	-9.9	0.15	0.1212	0.0350
EGO 185	70.3	63.7	-5.7	0.15	0.1207	0.0347
EGO 187	71.2	64.2	-3.6	0.15	0.1207	0.0346
EGO 200	68.5	63.4	-3.1	0.15	0.1202	0.0345
EGO 211	70.7	61.9	-1.9	0.15	0.1194	0.0339
Fmincon initial point	71.8	62.8	-9.9	0.10	0.1197	0.0344
Fmincon best point	71.7	61.3	-9.8	0.15	0.1251	0.0372

increase in roll authority will result in an increase in pitch authority. The fmincon result further improves on the EGO results as demonstrated by its position on the plot.

11.2.5 Manual Test Case

One final check on the rear swept optimization was conducted. This was a manual test case, in which the MFC was placed farther outboard on the wing near the wingtip and oriented longitudinally, without any angle of rotation. This design, shown in Fig. 11-25, was expected to give good results since the MFC was placed farther away from the center of gravity in both the lateral and longitudinal directions as compared to the optimized designs. However, this design had 27% less roll authority and 9% less

www.manaraa.com

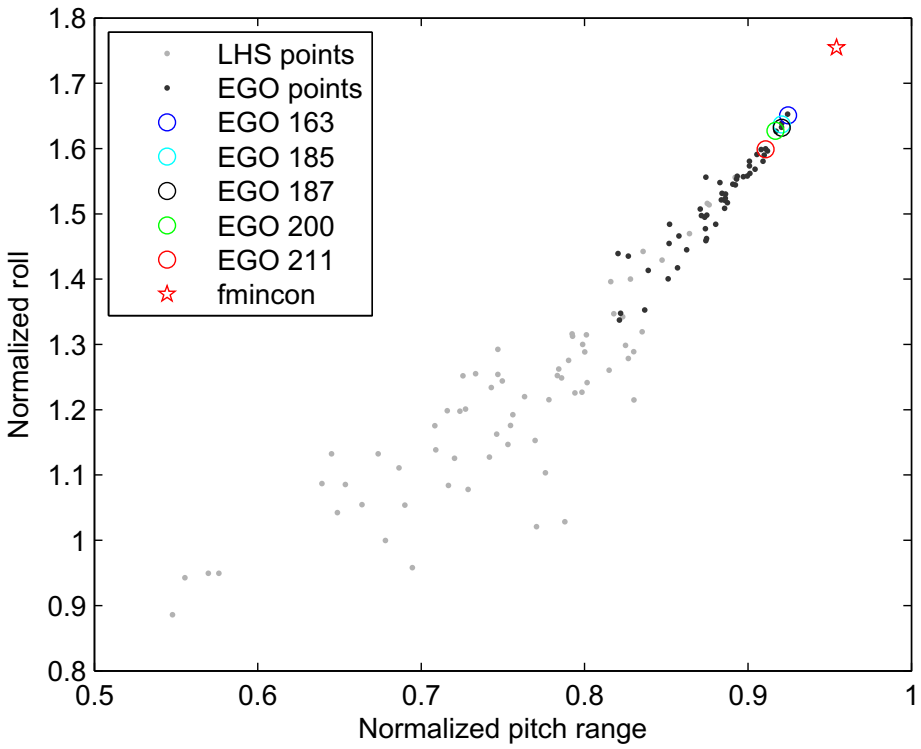

Figure 11-24. Pareto front for the rear swept optimization.

pitch authority as compared to fmincon design. Therefore, the optimized fmincon design still performs the best. This is likely because placing the MFC farther outboard results in less wing area being actuated as well as the MFC acting against the 3D curvature of the wing.

11.2.6 Discussion

In the end, the optimized rear swept design has slightly less pitch authority and significantly more roll authority than the optimized forward swept design. Additional considerations which are not included in the analysis include the effects of prop-wash on the control surface authority throughout the various flight regimes. As mentioned previously, for the forward swept design, the MFCs are located in the prop-wash region, which may increase their effectiveness for low to moderate flight speeds. Coupling this with the favorable stall characteristics of a forward swept wing further improves the potential advantages of a forward swept wing over a rear swept design. The forward

www.manaraa.com

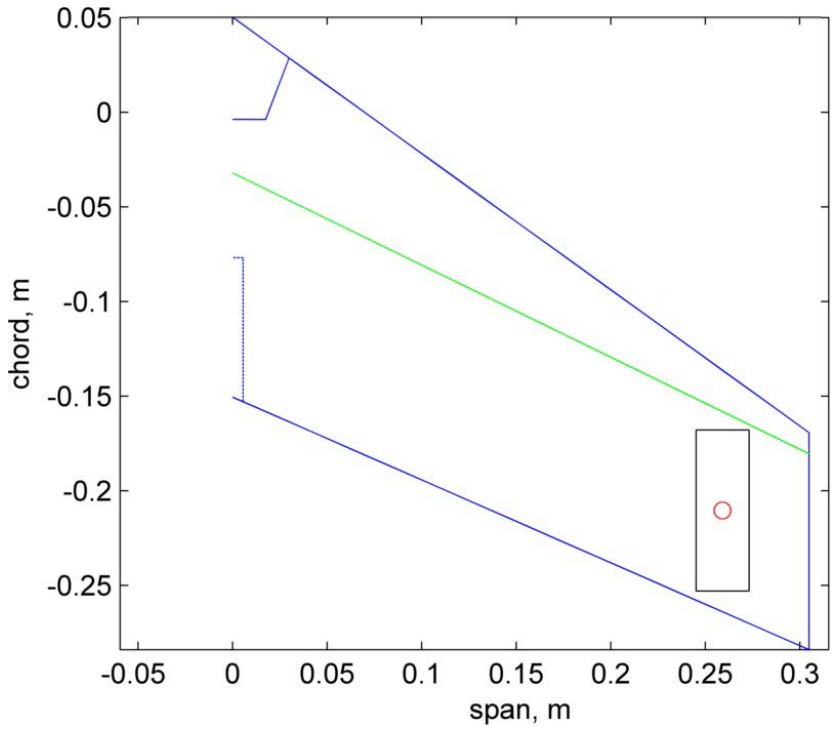

Figure 11-25. Rear swept user-specified test case.

swept geometry is also favorable for the placement of the MFCs on the wing surface, whereas the rear swept design has more space restrictions. In addition, the forward swept design provided a research topic with a challenging combination of disciplines by incorporating bend-twist coupling with the standard aeroelastic modeling aspects. Finally, even though the forward swept design has slightly better pitch authority than the comparable rear swept design, it is possible that a further optimized rear swept design (with an optimized airfoil, wing sweep, or geometry) could perform better.

www.manaraa.com

CHAPTER 12
CONCLUDING TESTS

This chapter presents and analyzes the results from the final set of wind tunnel tests. Three wings were tested, the MFC2, MFC13, and MFC14, where the MFC2 is the baseline design and the MFC13 and MFC14 are the optimized designs. The same setup and equipment, described in Section 10.2, used in the first series of tests was used again for this set of tests. The DIC setup was modified slightly and is shown in Fig. 12-1.

12.1 Manufacturing

The fabrication of the wing took place in a similar manner to that described in previous chapters and in Section 9.3.4. An area of the pre-preg wing was cut out for the steel substrate and the substrate placed in the void. High temperature epoxy was used to adhere the steel substrate to the MFC. The steel substrate placed into the wing mold is shown in Fig. 12-2A. A close-up of the resulting wing is shown in Fig. 12-2B.

12.2 Procedure

The same configurations were tested in this series of tests as were used for the MFC1 and MFC2 first round of tests (Section 10.2.3). However, due to the stiffer leading edge of the MFC13 and MFC14, a larger range of angle of attacks could be examined. In addition, the MFC2 was tested under a slightly larger range of angle of attacks. Significant flutter was noted for the MFC2 at negative angles of attack beyond -2° and beyond 15°. Therefore, testing was limited in these regions.

During testing, the left MFC on MFC13 began to short out. This behavior was noted during the preliminary tests prior to visiting the REEF. It is suspected that while removing the tape protecting the MFC's electrical leads, excessive pressure was placed near the edge of the MFC. As a precaution, once arriving at the REEF a round of wind tunnel tests were completed at half power (750 V), in which shorting was not observed. After acquiring sufficient data, the MFCs were tested at 1500 V, at which point the left MFC began to short.

www.manaraa.com

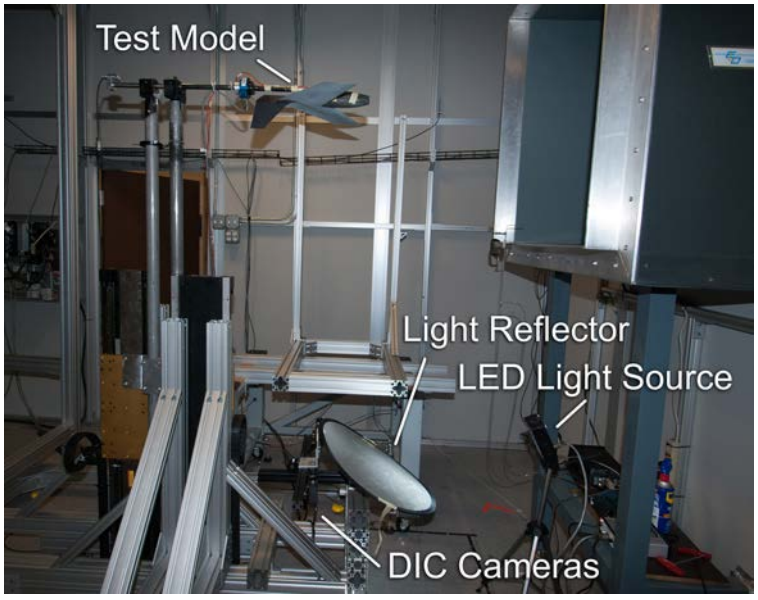

Figure 12-1. Wind tunnel setup for second series of tests. Photo taken by Bradley LaCroix.

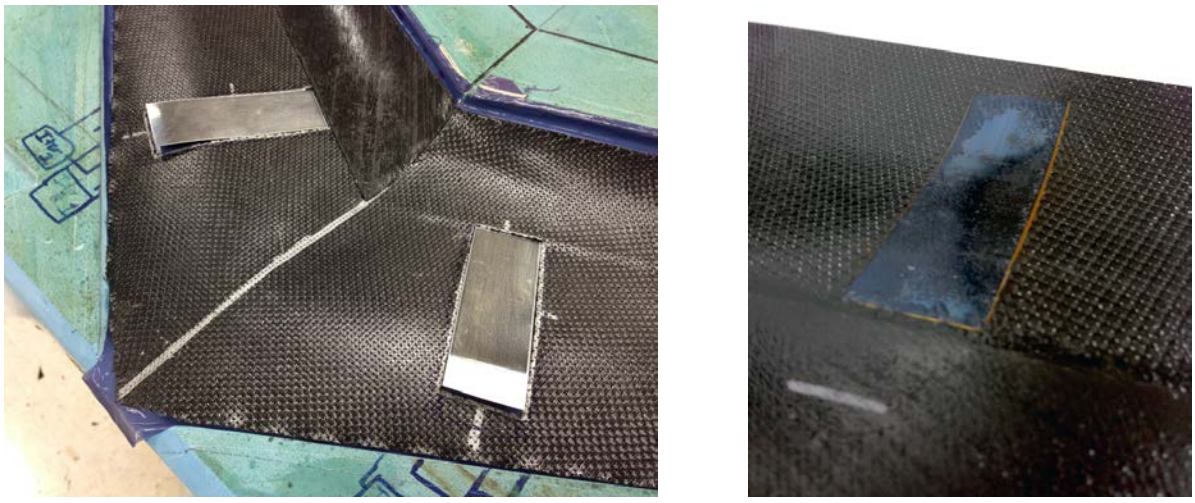

A B

Figure 12-2. Manufacturing of the MFC13 wing. A) Steel substrate placed in the cutout section of MFC13 prior to curing. B) Picture of the MFC13 wing, post-cure. Photos taken by Bradley LaCroix.

www.manaraa.com

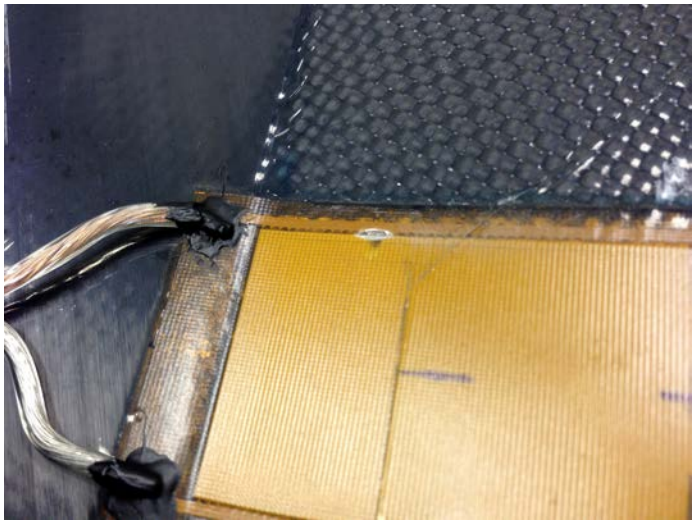

Figure 12-3. Repair made to the MFC on MFC13. Photo taken by Bradley LaCroix.

It was determined that the best course of action was to attempt a repair on the MFC. If the area in which the short was occuring was removed from the circuit, then ideally the problem should be resolved. A Dremel© and a grinding disk were used to carefully cut the electrical connections leading to the damaged area of the MFC. The result is shown in Fig. 12-3, in which the black shorted area is removed from the circuit via the cut made in the MFC. After making the cut, a coat of insulating adhesive was applied to prevent the exposed connections from arching. Testing revealed that the repair had successfully resolved the problem.

12.3 Results

The results from the wind tunnel tests are grouped into three sections. The first section presents the DIC results comparing the geometry of the aeroelastic computer model to the experimental results obtained using DIC. The second section presents a comparison of the actuated wings at various speeds to examine the affect of loads on the wing deformation. The third section examines the aerodynamic load results.

12.3.1 DIC Results

A comparison between the aeroelastic computer model and the experimental results for the MFC13 wing is shown in Fig. 12-4. These results are for static conditions

www.manaraa.com

Table 12-1. MFC13 quality of fit for each configuration tested.

Velocity, m/s	Configuration	Number of points	RMS error, mm
0	LV0000 RV0000	43908	0.75
	LV1500 RV1500	43308	0.59
	LV-500 RV-500	43388	0.56
	LV-500 RV1500	43356	0.56
15	LV0000 RV0000	N/A	N/A
	LV1500 RV1500	43575	0.53
	LV-500 RV-500	43411	0.63
	LV-500 RV1500	43410	0.57

in which the MFCs are actuated to various positions. Some sharp variations in color are present in these images. This is due to the DIC software being unable to correlate properly for these areas due to the combination of insufficient contrast in the DIC speckle pattern and glare on the wing.

Just as in Chapter 10, the first image is with the MFCs placed in the unactuated position, and is used as a tare value for the other wings. This removes any initial discrepancy between the experimental model and the computer model. Overall, the results indicate that the computer model matches the experimental results within ± 1 mm.

The next figure, Fig. 12-5, provides a comparison between the computer model and the experimental tests at 15 m/s. No data was recorded for the unactuated position for this wing. Regardless, the results show that the model matches the experiment very well with a discrepancy of less than ± 1 mm.

The quality of fit of the computer models with respect to the wind tunnel experiments is tabulated in Table 12-1. This table was calculated in the same way as specified in Section 10.3. The RMS error is slightly more, on average, for this set of results (averaging 0.60 mm compared to 0.36 mm). This can be attributed to the fact that the model was tuned to match up well with the MFC2 results, but was not adjusted for this set of results.

www.manaraa.com

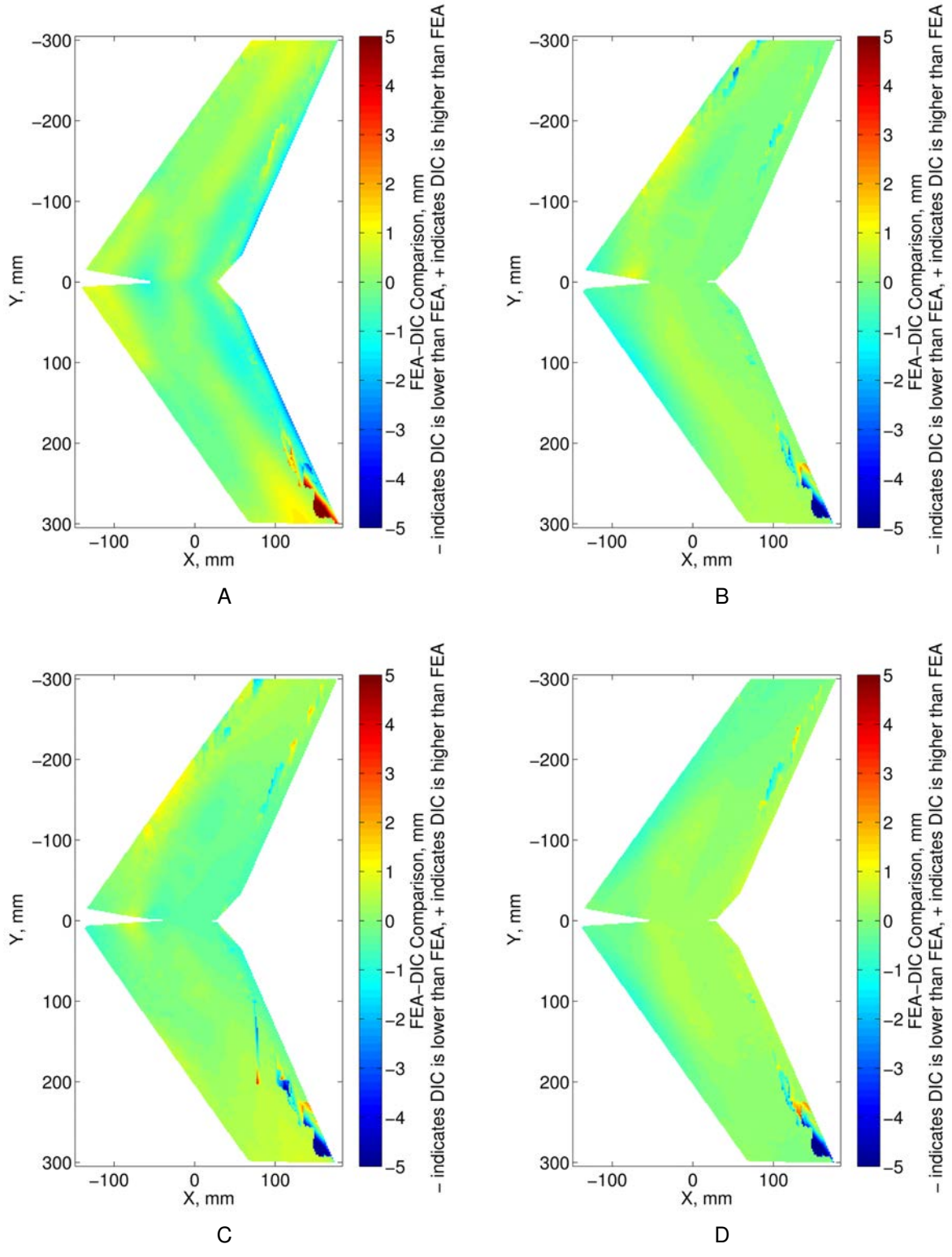

Figure 12-4. Comparison of the MFC13 finite element model to the experimental results under static conditions. A) No actuation. B) Actuated to LV1500 and RV-500. C) Actuated to LV1500 and RV1500. D) Actuated to LV-500 and RV-500.

www.manaraa.com

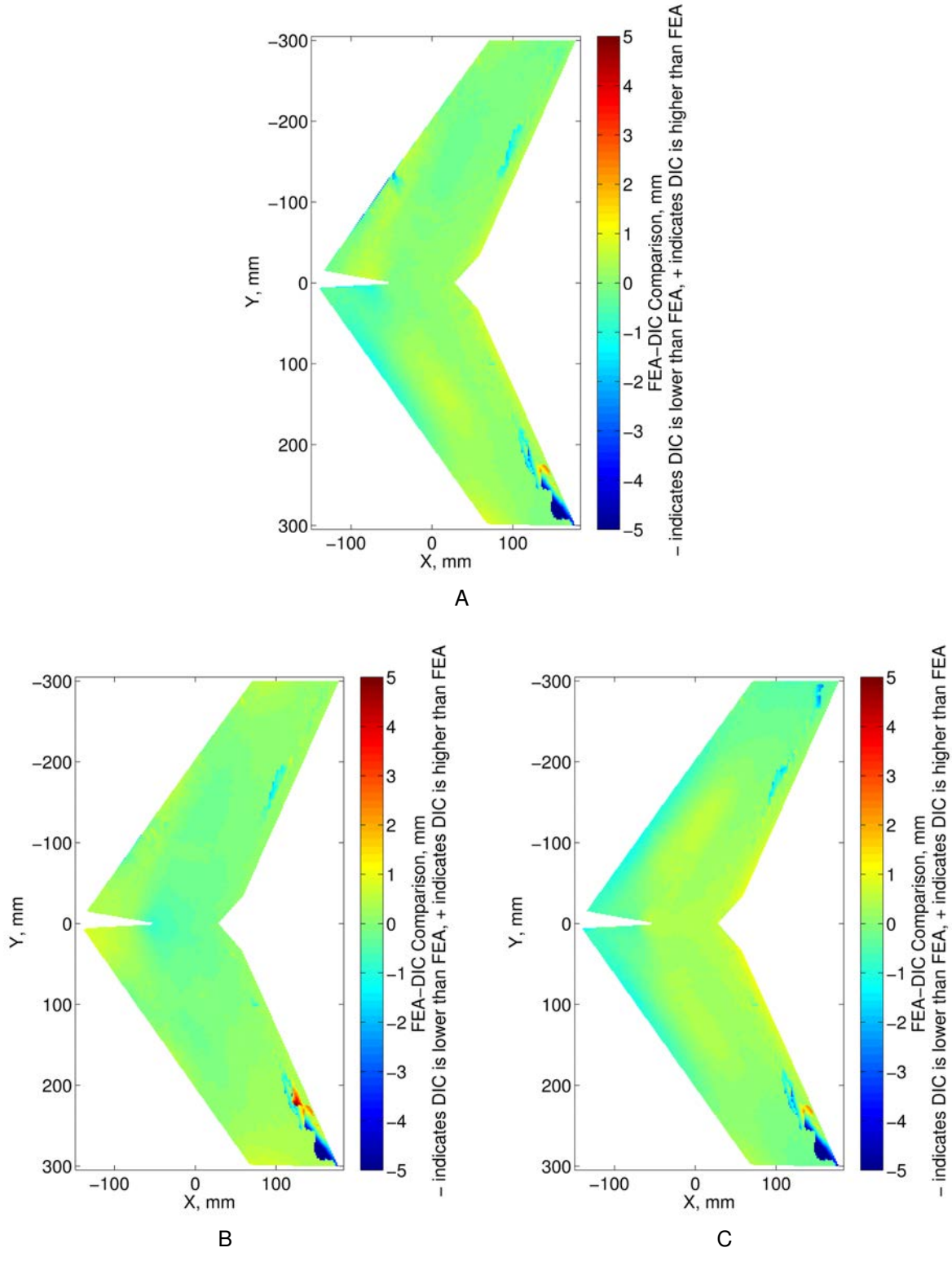

Figure 12-5. Comparison of the MFC13 finite element model and the experimental results at 15 m/s. Note: No data was recorded for the unactuated experiment. A) Actuated to LV1500 and RV-500. B) Actuated to LV1500 and RV1500. C) Actuated to LV-500 and RV-500.

www.manaraa.com

Table 12-2. MFC14 quality of fit for each configuration tested.

Velocity, m/s	Configuration	Number of points	RMS error, mm
0	LV0000 RV0000	44578	0.50
	LV1500 RV1500	44283	0.43
	LV-500 RV-500	44479	0.27
	LV-500 RV1500	44273	0.31
15	LV0000 RV0000	44086	0.43
	LV1500 RV1500	44228	0.36
	LV-500 RV-500	44084	0.55
	LV-500 RV1500	44109	0.41

A similar series of results are shown in Figs. 12-6 and 12-7 for the MFC14 wing. Once again, the results match up very well with nearly the whole surface being with $\pm$1 mm.

The quality of fit for these results are shown in Table 12-2. As the values indicate, the MFC14 results match up slightly better, with an average RMS value of 0.41 mm.

12.3.2 Effects of Speed

An extra series of tests were conducted for this round of testing. To examine the affects of aerodynamic loads on the actuated wing, each wing was put through a series of velocities. The results are shown in Figs. 12-8 and 12-9. It is evident from these figures that due to the reflex in the trailing edge part of the wing, the -500 V actuated part of the wing is further assisted by aerodynamic loads, pushing it farther down as the velocity increases. For the 1500 V side, the aerodynamic loads oppose the actuation and push it down as the velocity increases. This is the case for both wings and to a similar degree.

12.3.3 Aerodynamic Results

The following series of figures compare the aeroelastic computer model results to the experimental results measured in the wind tunnel. All tests were conducted at 15 m/s. The first figure, Fig. 12-10, shows the pitch range when the MFC13 is actuated through its pitch up and pitch down actuations. Similarly, Fig. 12-11 shows the MFC13

www.manaraa.com

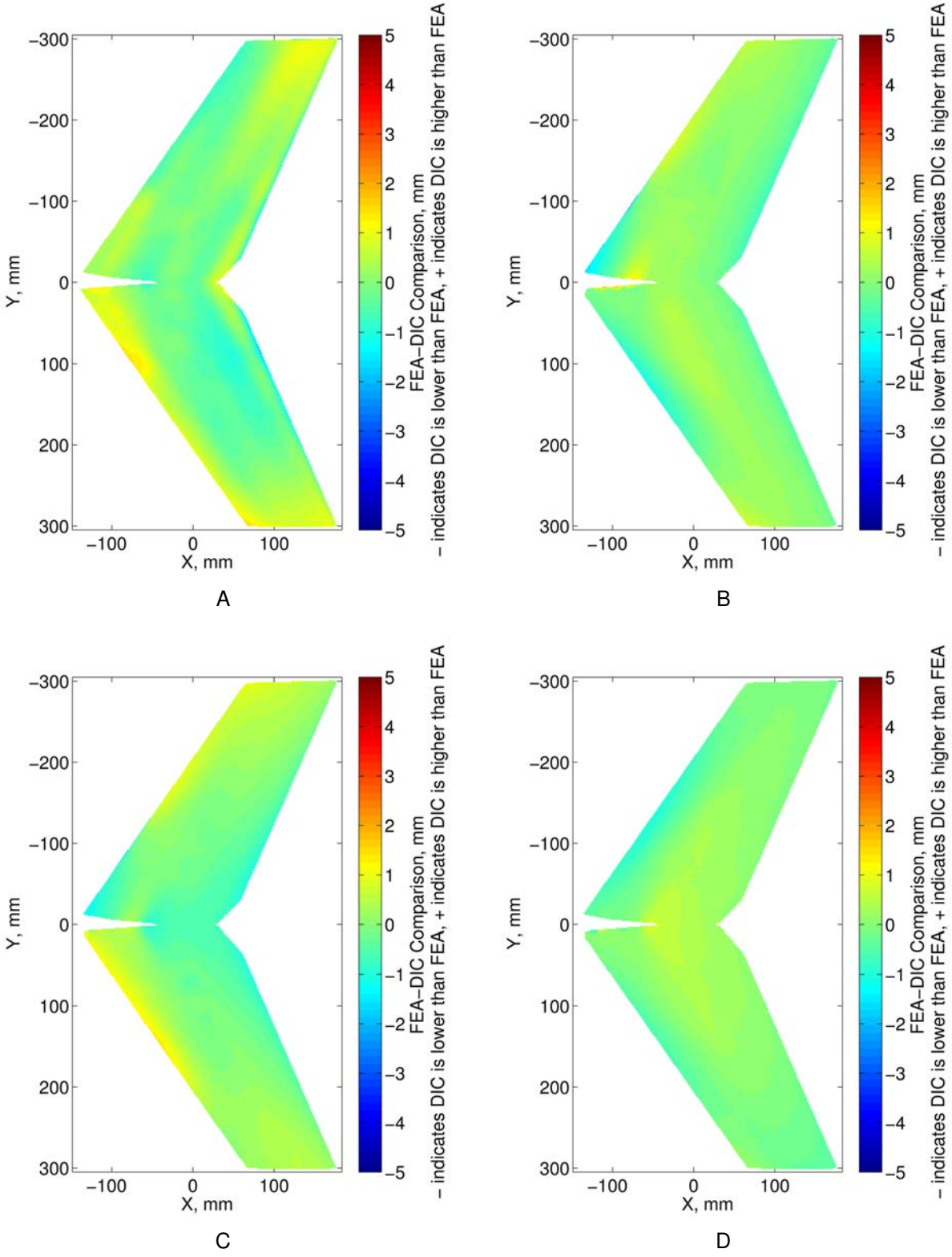

Figure 12-6. Comparison of the MFC14 finite element model and the experimental results under static conditions. A) No actuation. B) Actuated to LV1500 and RV-500. C) Actuated to LV1500 and RV1500. D) Actuated to LV-500 and RV-500.

www.manaraa.com

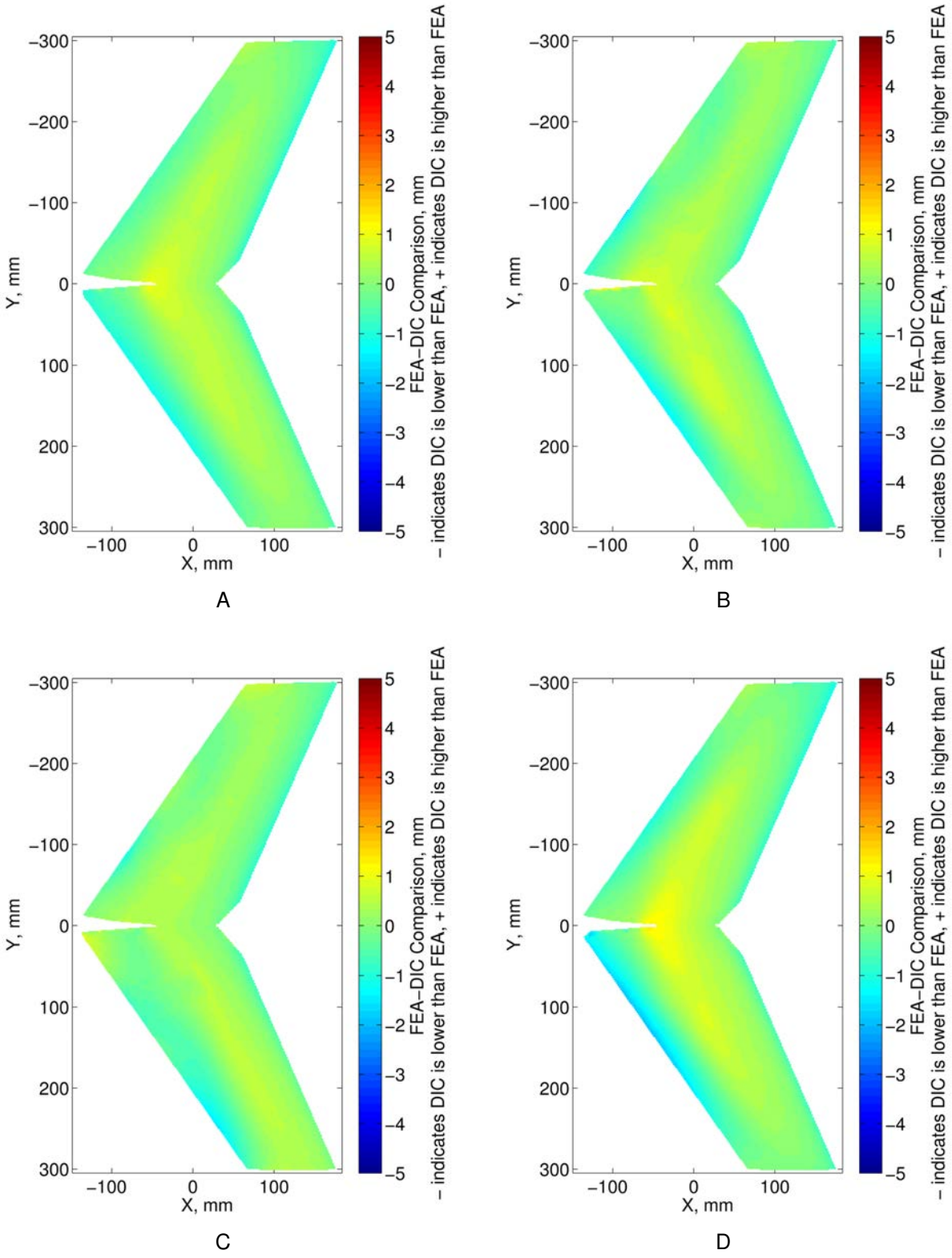

Figure 12-7. Comparison of the MFC14 finite element model and the experimental results at 15 m/s. A) No actuation. B) Actuated to LV1500 and RV-500. C) Actuated to LV1500 and RV1500. D) Actuated to LV-500 and RV-500.

www.manaraa.com

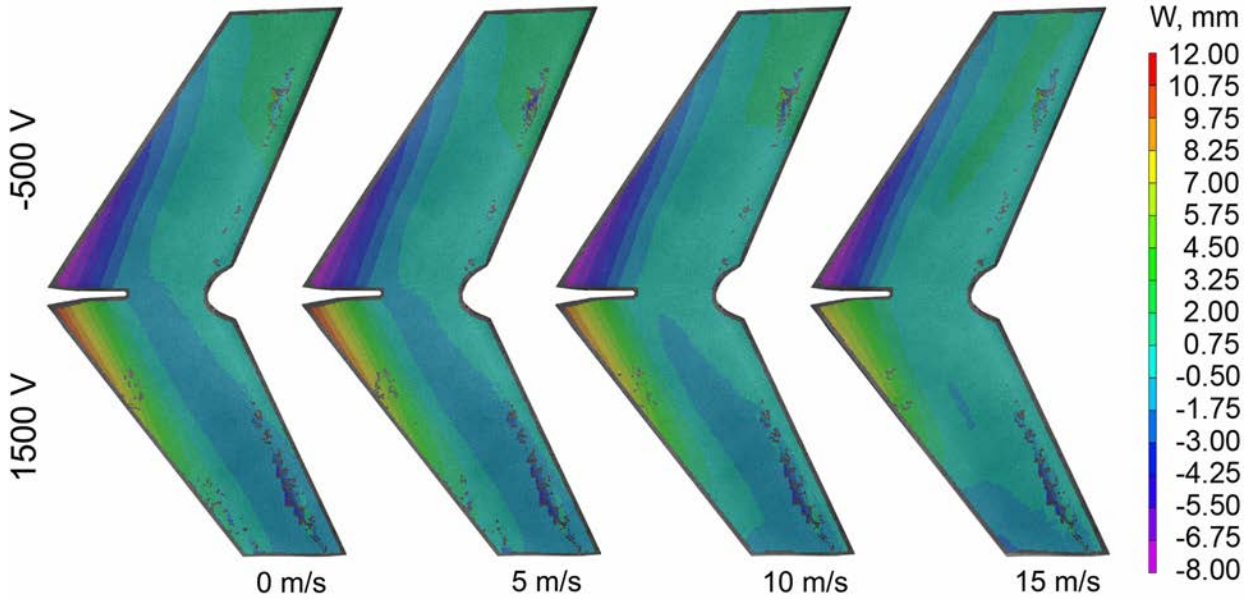

Figure 12-8. MFC13 deformation under various velocities when actuated to LV1500 RV-500 at 0° angle of attack.

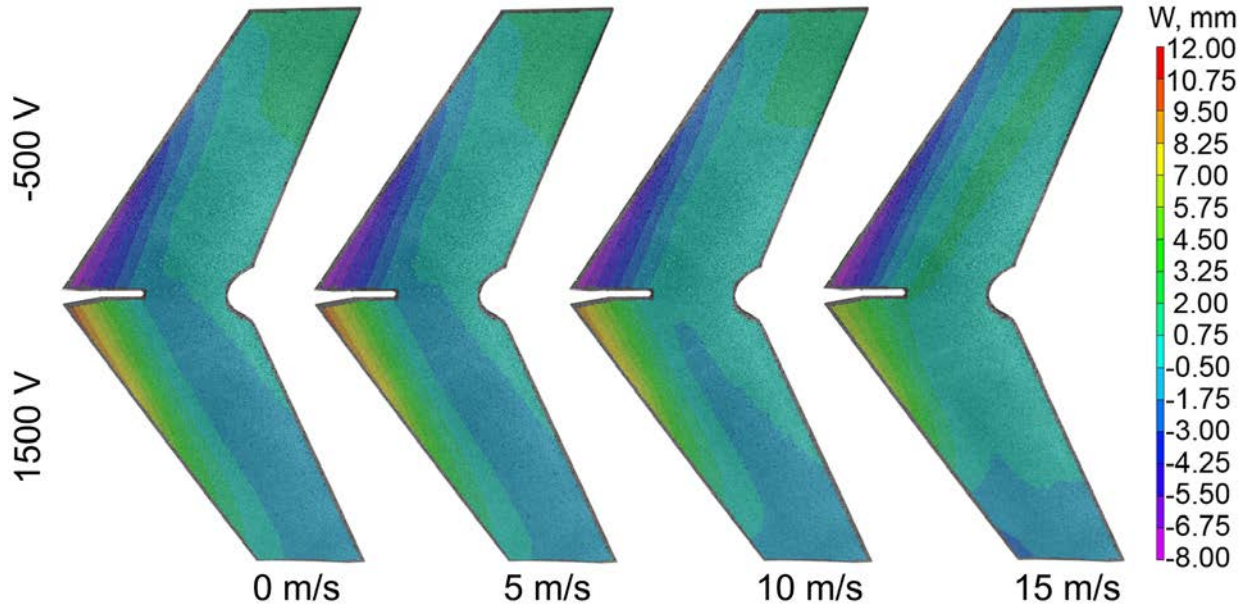

Figure 12-9. MFC14 deformation under various velocities when actuated to LV1500 RV-500 at 0° angle of attack.

www.manaraa.com

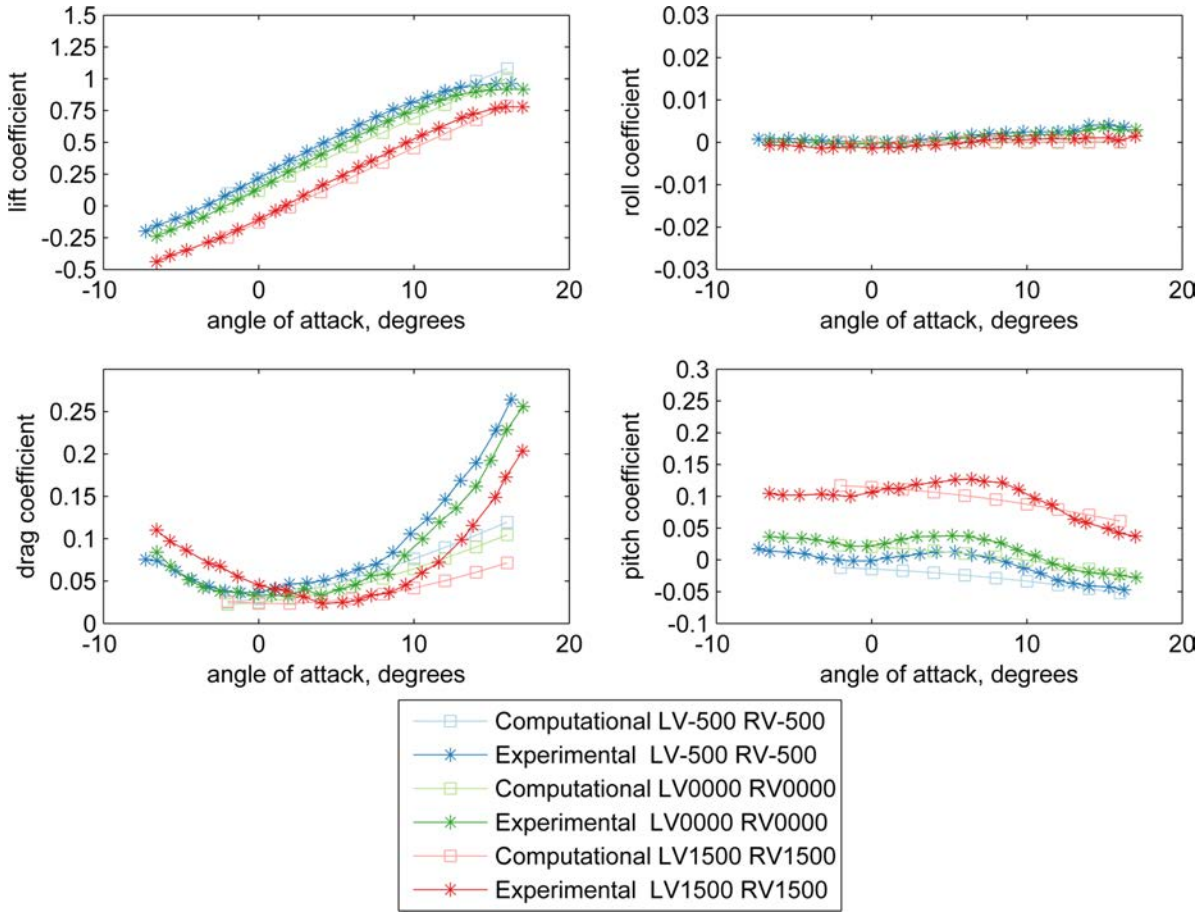

Figure 12-10. MFC13 pitch comparison between the computational and experimental models.

wing configured in the two roll configurations. The results in both cases match extremely well, with the computer model beginning to deviate at the higher angles of attack.

Also worth noting is when the MFC repair took place. LV0000 RV0000, LV-500 RV1500, and LV-500 RV-500 configurations were tested before the left MFC began to exhibit problems. The MFC was then repaired and the other tests performed, LV1500 RV-500 and LV1500 RV1500. Even with the repair, the roll range is symmetric and the roll when pitching up is nearly zero, indicating symmetric actuation.

Similar results are shown in Figs. 12-12 and 12-13 for the MFC14 aircraft. The pitch coefficient values match up very well, but the experimental roll range is less than the

www.manaraa.com

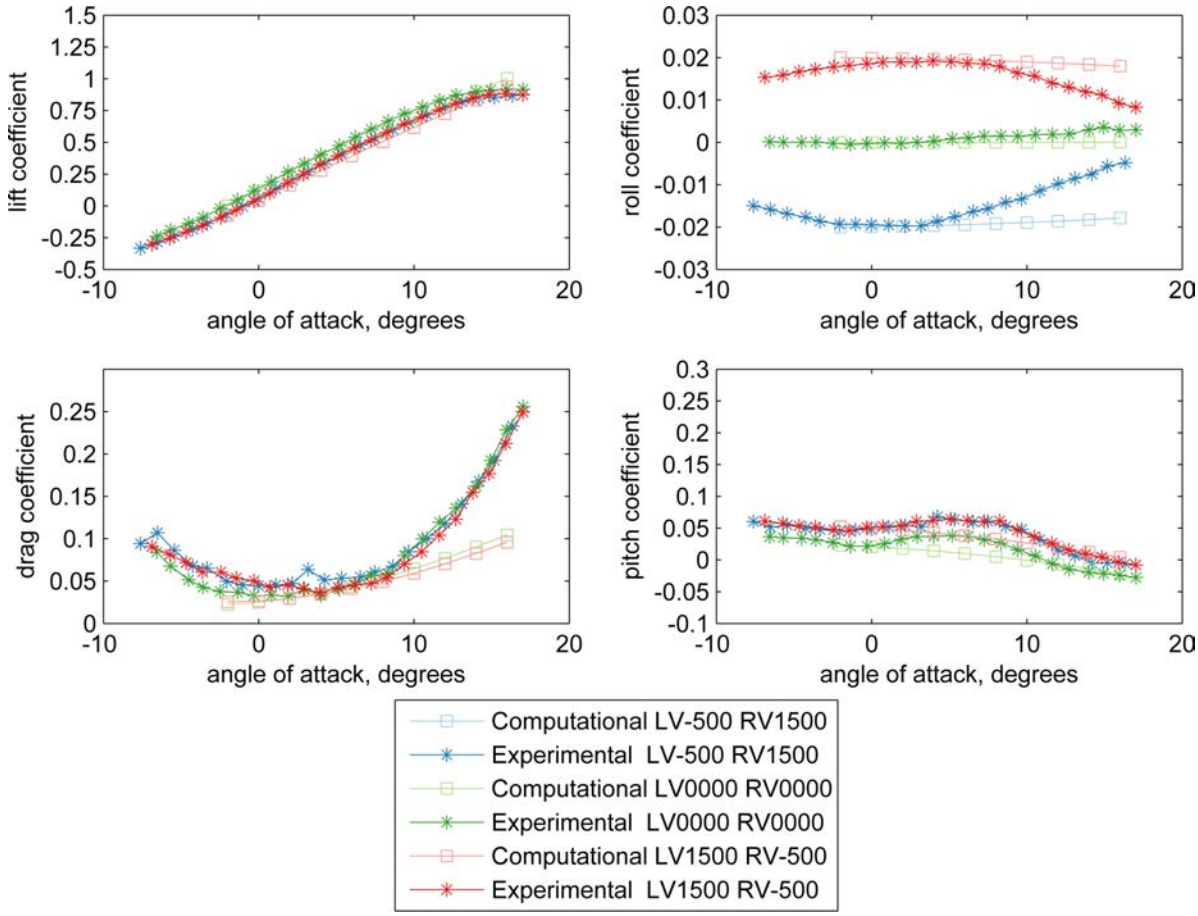

Figure 12-11. MFC13 roll comparison between the computational and experimental models.

predicted values. The roll actuation is also not symmetric. Both of these issues may be due to variations in manufacturing.

The values for roll are comparable to the results obtained by Ohanian. During his testing with the GENMAV, mentioned in Section 2.1, he obtained roll coefficient values of 0.0324 and 0.0382 for two of his MFC actuated aircraft [46]. The first aircraft utilized 4 sets of M8514-P1 bimorphs positioned at the outboard section of wing (two bimorphs on the left side and two bimorphs on the right side). The second aircraft utilized 4 sets of M8528-P1 bimorphs positioned at 45° angles on a thin airfoil wing. The roll coefficient for these MAVs is approximately 53-80% more than the MFC13. However, when compared to the optimized rear swept design in Section 11.2, the optimized

www.manaraa.com

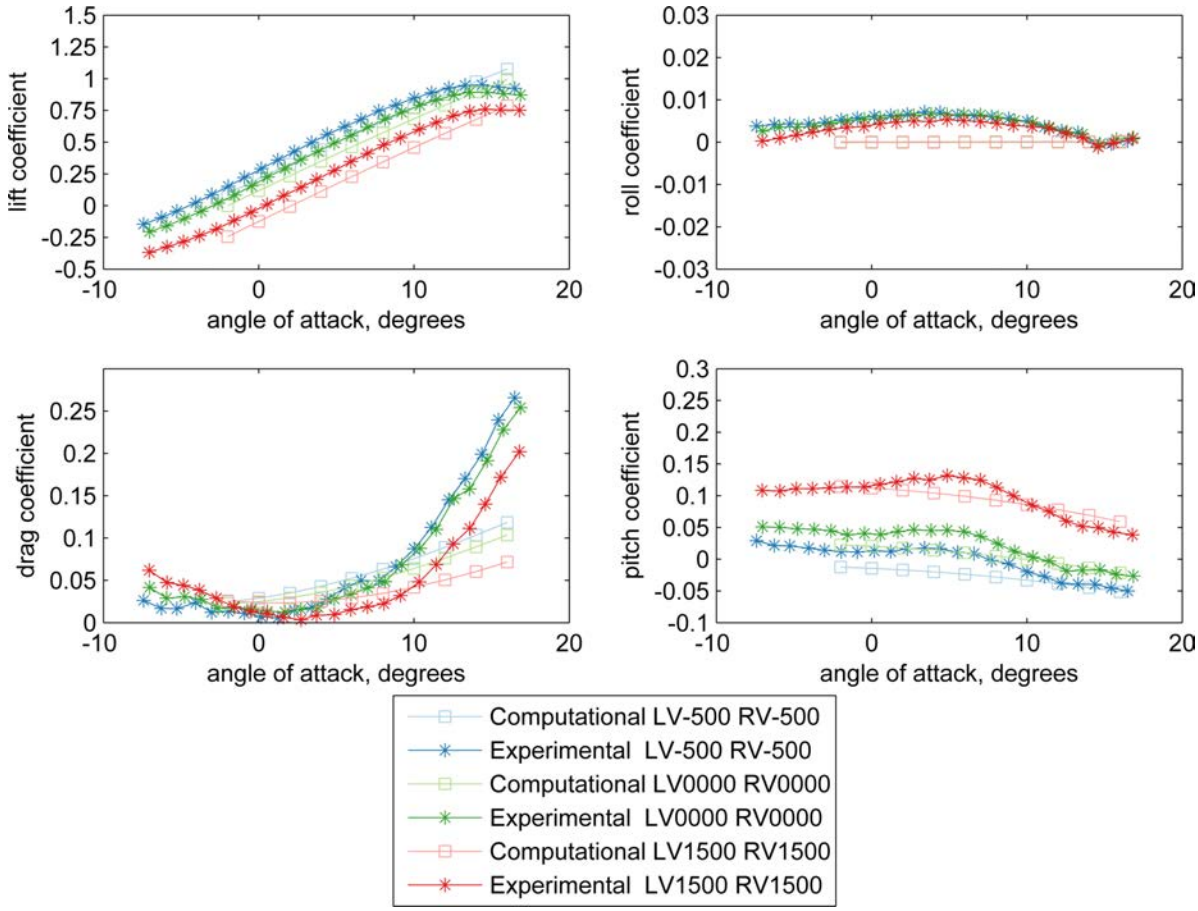

Figure 12-12. MFC14 pitch comparison between the computational and experimental models.

design produced 15% more roll than the Ohanian's first design and only 3% less than the second design. These results are especially noteable considering Ohananian's aircraft used 8 actuators for roll control, compared to the 2 actuators used on the MFC13 and rear swept design.

Although the stability of the optimized designs was not evaluated, it is likely that the improved designs have similar stability traits to the original design, MFC1. This is because the wing geometry has remained virtually the same and the wing structure is the only aspect that has changed. In addition, the improved designs are stiffer and deform less than the original MFC1, therefore, aeroelastic instabilities would be less of a

www.manaraa.com

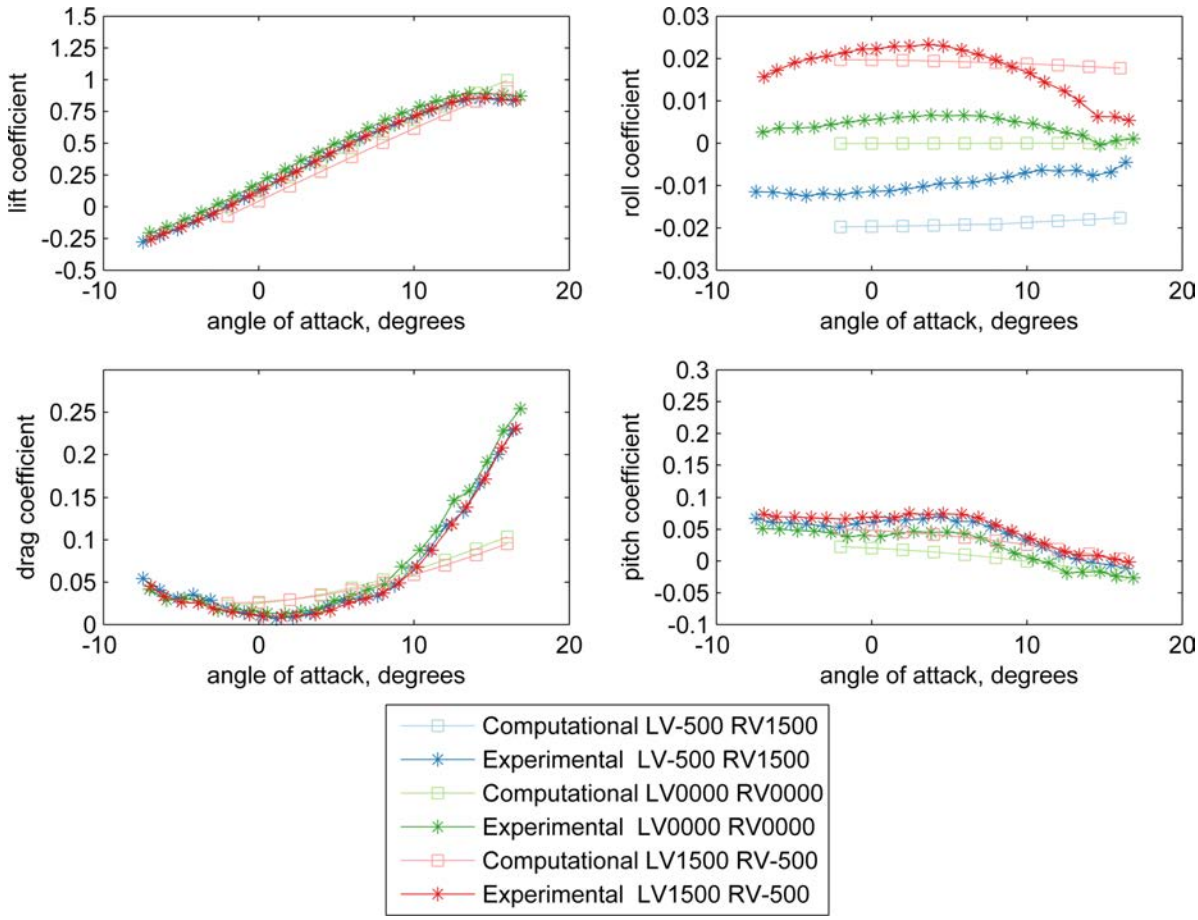

Figure 12-13. MFC14 roll comparison between the computational and experimental models.

consideration. As a result, since the MFC1 exhibited acceptable flight characteristics, it is likely the improved designs would also exhibit acceptable flight characteristics.

12.4 Conclusion

In the end, the MFC13 and the MFC14 are both much improved over the original prototypes. The MFC13 produces about twice the roll as the MFC2 and the MFC14 produces about 75% more. The MFC13 had significantly more roll than the MFC14, and slightly more pitch authority. The factors most important for these improvements are likely the substrate material, placement of the MFC near the leading edge, and the stiffer leading edge containing more layers of composite.

www.manaraa.com

This process has progressed through optimization on both the local scale, looking at the independent unimorph performance, as well as on the global scale, looking at the overall wing geometry and layup. Initial tests examining the MFC actuation, unimorphs, and composite materials paved the way for a more accurate computer model. This is especially critical when conducting an optimization, since defects in the computer model can be exploited by the optimization routine.

Ultimately, this research has been successful in demonstrating that two MFC actuators are sufficient to adequately fly an aircraft. This is beneficial in terms of weight, electronic complexity, and cost. Furthermore, the research contained within this document would be beneficial to other groups who may be interested in achieving more actuation from their MFC actuators for a variety of applications, not limited to MAVs.

www.manaraa.com

APPENDIX A
DIGITAL IMAGE CORRELATION (DIC)

Digital Image Correlation (DIC) is a class of non-contacting methods that acquires images of an object, stores the images in digital form, and performs image analysis to extract full-field shape and deformation measurements. It is sometimes referred to as Visual Image Correlation (VIC), however, this terminology is mildly redundant. The digital image correlation setup used within this research is a 3D system, which makes use of two Grasshopper©2 cameras, manufactured by Point Grey Research. The images are recorded using VicSnap 2007 and processed using VIC-3D 2009. By using stereo triangulation, the system is able to reconstruct a three dimensional geometry utilizing two pre-calibrated imaging sensors. This concept is shown in Fig. A-1A.

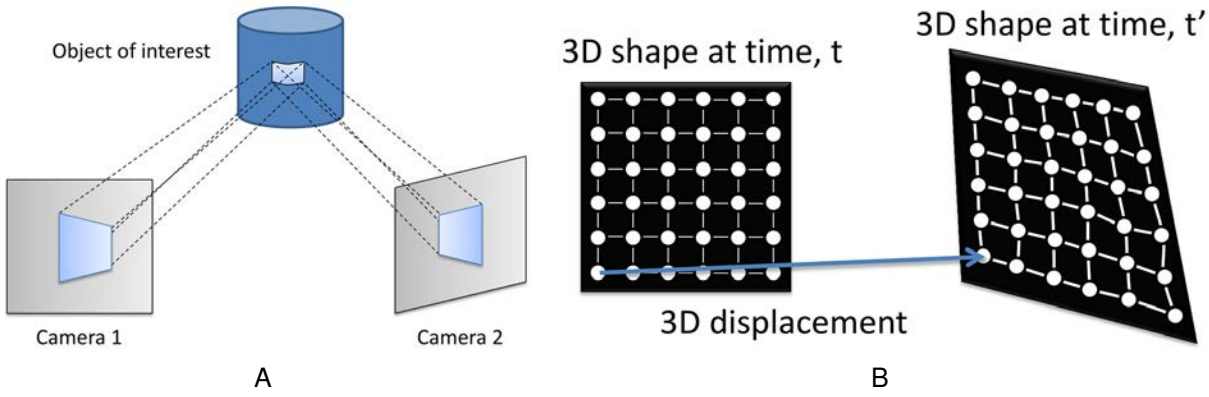

Figure A-1. Digital image correlation conceptual illustration. A) Demonstration of the 3D perception when viewed through the stereographic system. B) Measurement of 3D displacement with respect to time.

Before conducting a DIC experiment, a black and white speckle pattern is applied to the surface of interest. This provides a distinct, high-contrast pattern that can be tracked by the system. Since the pattern is unique, the translation, rotation, and strain can be acquired from the correlation. Furthermore, since the system uses stereo triangulation, displacement can be measured in all three coordinate directions. This principle is illustrated in Fig. A-1B. The same concept is illustrated with a standard speckle pattern in Fig. A-2, where the translation of the dots is measured by the DIC system. DIC tries

www.manaraa.com

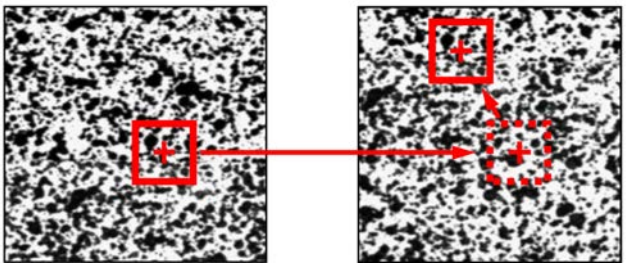

Figure A-2. Digital image correlation example pattern.

to find a region in the deformed image that maximizes a cross-correlation function corresponding to a small subset within the un-deformed image.

DIC is scalable to a large variety of length scales, ranging from tens of meters to micrometers. 2D surface deformations at the nanoscale using atomic force microscopy and scanning electron microscopy have been performed [90]. Optimal accuracy is obtained when cameras are positioned at 90° with respect to one another, but 45-90° is generally accepted. Less than 45° reduces out-of-plane accuracy, but the correlation analysis can still be performed.

The imaging process takes place starting with the conversion of intensity of light on each pixel to a numeric value. The intensity of light is converted with 8-bit resolution to a value ranging from 0 to 255. An intensity value of 255 indicates that the pixel is oversaturated. DIC utilizes grey-value interpolation schemes, which allows for optimal sub-pixel accuracy. Because of this, in-plane accuracy is on the order of $1/50^{th}$ of a pixel and out-of-plane accuracy is on the order of Z/50,000 where Z is the distance from the camera to the subject. This is assuming the camera system is positioned with at least a 45° angle.

Figure A-3 illustrates the DIC setup used for the cantilevered unimorph experiments described in Chapter 6. In this setup, the DIC cameras were positioned over the cantilever setup while the MFC was actuated to various voltages and different loading conditions were applied. The DIC system allowed for the full-field 3D displacement of the unimorph to be measured at any given time.

www.manaraa.com

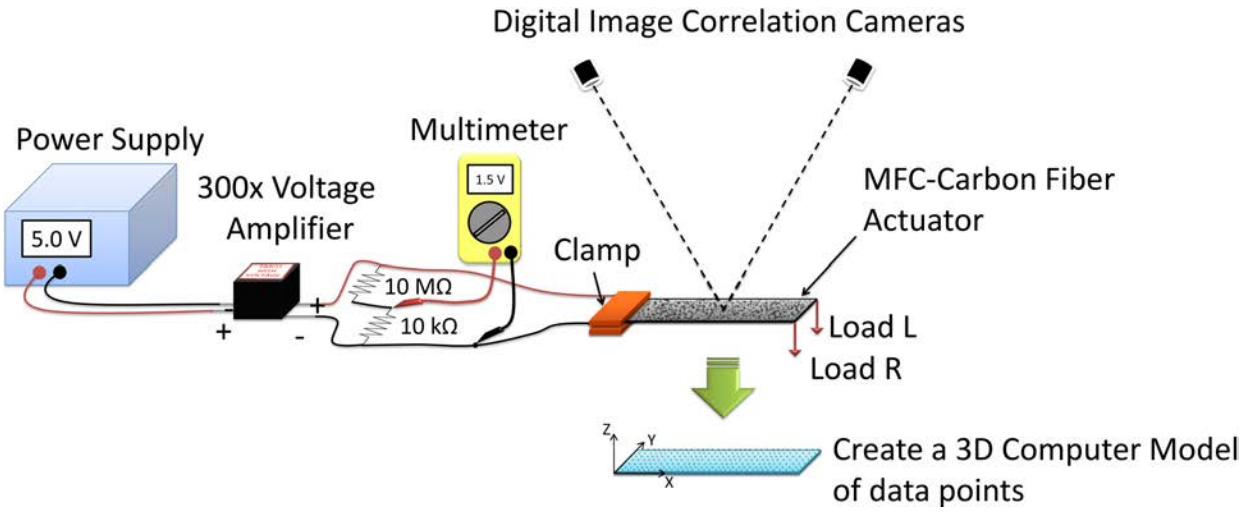

Figure A-3. DIC setup for cantilever experiment.

There are a variety of issues that can arise when using a DIC system. Possible problems include continuity of correlation regions when a disconinuity is present, such as a crack, hole, or shadow. Loss of contrast can also occur due to debonding or delamination of the speckle pattern. In addition, a change in the diffuse reflectivity of the surface during loading can result in loss of contrast in the recorded images. If such a discontinuity or surface imperfection is present, the correlation will only take place on the starting subset area and will not be able to progress across the entire surface.

This was a consideration when using DIC in the wind tunnel on the membrane wings, as shown in Fig. A-4. The lighting and reflective surfaces had to be carefully positioned to prevent any shadow or silhouetting from occuring. Too much back-lighting and the carbon fiber portion of the wing becomes silhouetted. Too much front lighting and portions of the wing can become over-exposed. In either case, the DIC system would be unable to correlate the entire wing surface.

Two other parameters that must be considered when setting up a DIC system include shutter speed and aperture. Shutter speed is the duration over which the image is captured. This may have very minute effects for quasi-static systems, but if the user is attempting to capture a surface that is in motion, a high shutter speed must be used.

www.manaraa.com

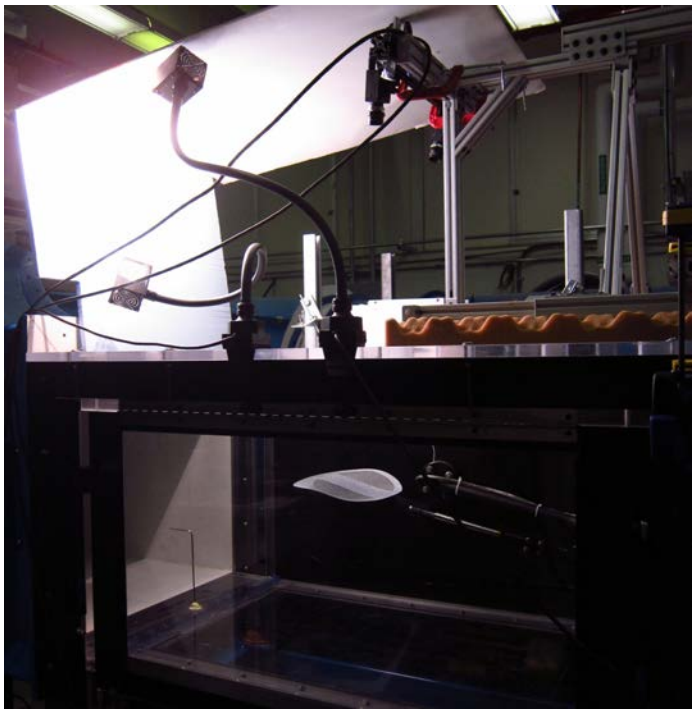

Figure A-4. Digital image correlation setup in the wind tunnel with carefully adjusted lighting. Photo taken by Bradley LaCroix.

If a high shutter speed is not an option, an alternative would be to use a strobe flash to illuminate the surface for a brief period of time, on the order of a thousandth of a second, while the camera shutter is open. This will essentially freeze the object in motion, as demonstrated with a set of propeller experiments I conducted in Fall 2009 (Figure A-5). The same technique has also been used extensively for the flapping wing project at the University of Florida [91–95].

Aperture adjustment is crucial for obtaining valid DIC results. The camera aperture determines the proportion of light that reaches the sensor. But the aperture setting also effects the depth of field. If the depth of field is small, items within the field of view that are outside of the focal plane will appear extremely out of focus. If the depth of field is large, then items within the field of view that are near the focal plane will still appear to be in focus and the focal plane will be less distinct. Optically, the depth of field is inversely related to the aperture size. Therefore, a large aperture, which allows a large amount of light to fall on the sensor, will produce a small depth of field. So only the items

www.manaraa.com

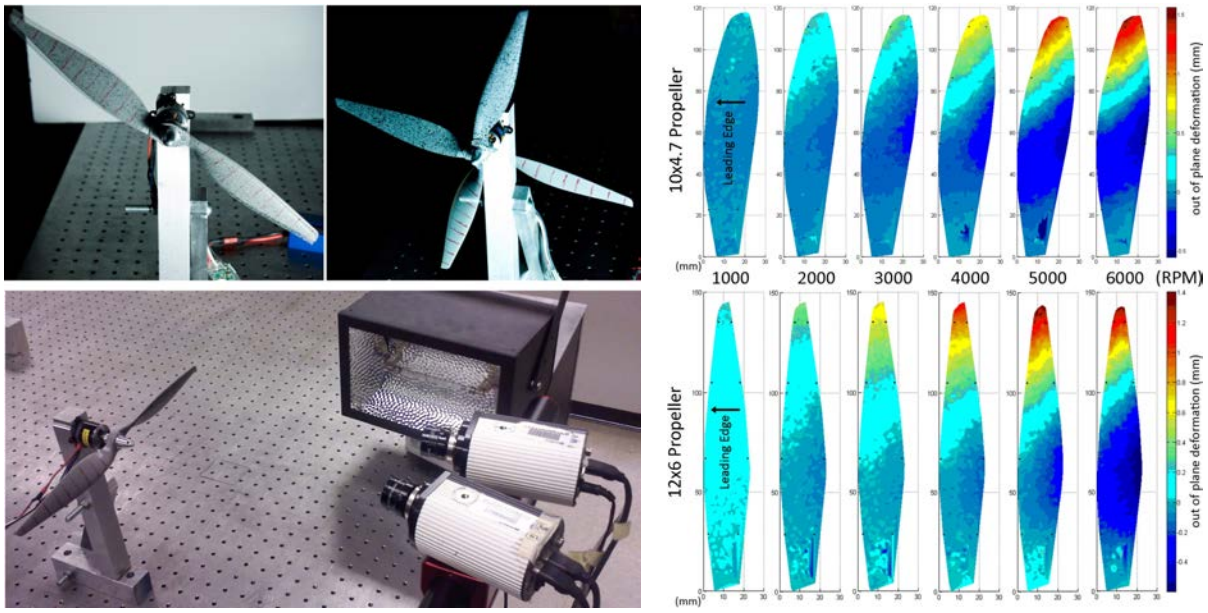

A B

Figure A-5. Digital image correlation of a rotating UAV propeller. A) The experimental setup with the propeller frozen in motion using the strobe light. Photo taken by Bradley LaCroix. B) Results of the DIC analysis for two propellers.

located at the focal plane will be sharply in focus. Conversely, a small aperture, which would limit the light falling on the sensor, would create a large depth of field and more items would be in focus.

All of these options must be carefully weighed when setting up a DIC system and performing an experiment. In certain situations, compromises may have to be made to achieve satisfactory results. Nonetheless, DIC provides a relatively quick and simple architecture by which a large variety of experiments can be performed. With the right setup, full-field displacements and 3D profiles can be accurately captured and modeled in 3D.

www.manaraa.com

APPENDIX B
USING DIC DISPLACEMENTS TO CALCULATE STRAIN

The primary output from VIC-3D software are 3D positions and displacements (X, Y, Z, and U, V, W). VIC-3D offers the user an option to convert the results into strain, but since the area of interest in some applications is relatively small compared to the overall sample, the strain is expected to be constant in each direction. With this in mind, the longitudinal strain ϵ_{xx}, transverse strain ϵ_{yy}, and shear strain ϵ_{xy}, were calculated based on Green's strain equations shown in Equations B–1, B–2, and B–3 using the measured positions and displacements from VIC-3D.

$$\epsilon_{xx} = \frac{\partial u}{\partial x} + \frac{1}{2}\left[\left(\frac{\partial u}{\partial x}\right)^2 + \left(\frac{\partial v}{\partial x}\right)^2 + \left(\frac{\partial w}{\partial x}\right)^2\right] \tag{B–1}$$

$$\epsilon_{yy} = \frac{\partial v}{\partial y} + \frac{1}{2}\left[\left(\frac{\partial u}{\partial y}\right)^2 + \left(\frac{\partial v}{\partial y}\right)^2 + \left(\frac{\partial w}{\partial y}\right)^2\right] \tag{B–2}$$

$$\epsilon_{xy} = \frac{1}{2}\gamma_{xy} = \frac{1}{2}\left(\frac{\partial v}{\partial x} + \frac{\partial u}{\partial y} + \frac{\partial u}{\partial x}\frac{\partial u}{\partial y} + \frac{\partial v}{\partial x}\frac{\partial v}{\partial y} + \frac{\partial w}{\partial x}\frac{\partial w}{\partial y}\right) \tag{B–3}$$

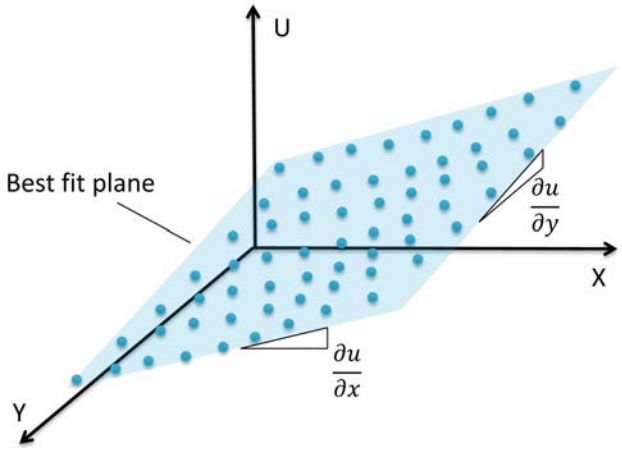

Figure B-1. Illustration of how the strain components are calculated using positions and displacements.

www.manaraa.com

To do this, each displacement (U, V, or W) is plotted against the X and Y positions, as shown in Fig. B-1. A plane fit is then applied to the data. The strain components are obtained from the slope of the plane, which can then be plugged into the above equations.

www.manaraa.com

APPENDIX C
UNIMORPH BANDWIDTH MEASUREMENT

Flight control of a MAV requires precise and rapid control surface actuation, usually on the order of 2 Hz or greater. To verify that MFCs could obtain an actuation at this rate and to quantify the exact dynamics, a series of high speed camera tests were conducted. These tests provided insight into the high speed dynamics of the actuator and are explained in the following sections.

C.1 High Speed Camera Setup

The setup, shown in Fig. C-1A, consists of a high speed camera, unimorph in a cantilevered setup, and proper lighting. The proper electronics to drive the unimorph from -500 V to 1500 V at various frequencies was also included in the setup.

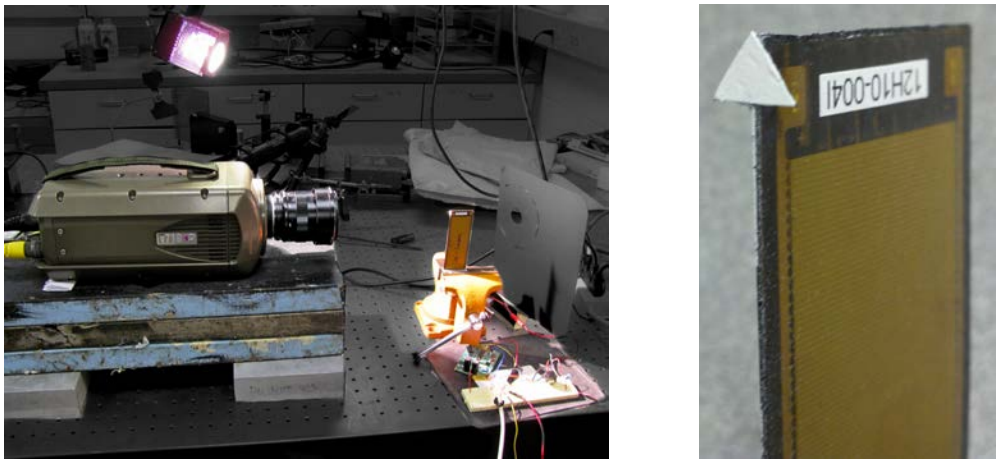

A B

Figure C-1. A) High speed camera setup for dynamic testing. B) Triangle adhered to the tip of the unimorph to visually track the tip displacement. Photos taken by Bradley LaCroix.

A triangle, made out of carbon fiber and spray painted white, is adhered to the tip of the unimorph, as shown in Fig. C-1B. This allowed the tip of the unimorph to be visually tracked throughout its range of motion. Since there was only one camera, it was important to keep the camera perpendicular to the plane of motion to minimize the effects of perspective.

www.manaraa.com

C.2 Analysis

The unimorph was actuated through a range of frequencies and the displacements captured using the high speed camera. Based on the dimensions of the triangle, a mm-to-pixel ratio was developed and utilized to measure the tip displacements of the unimorph. MATLAB was used to find each corner of the triangle for each image and compile the results into a plot. This process is illustrated in Fig. C-2.

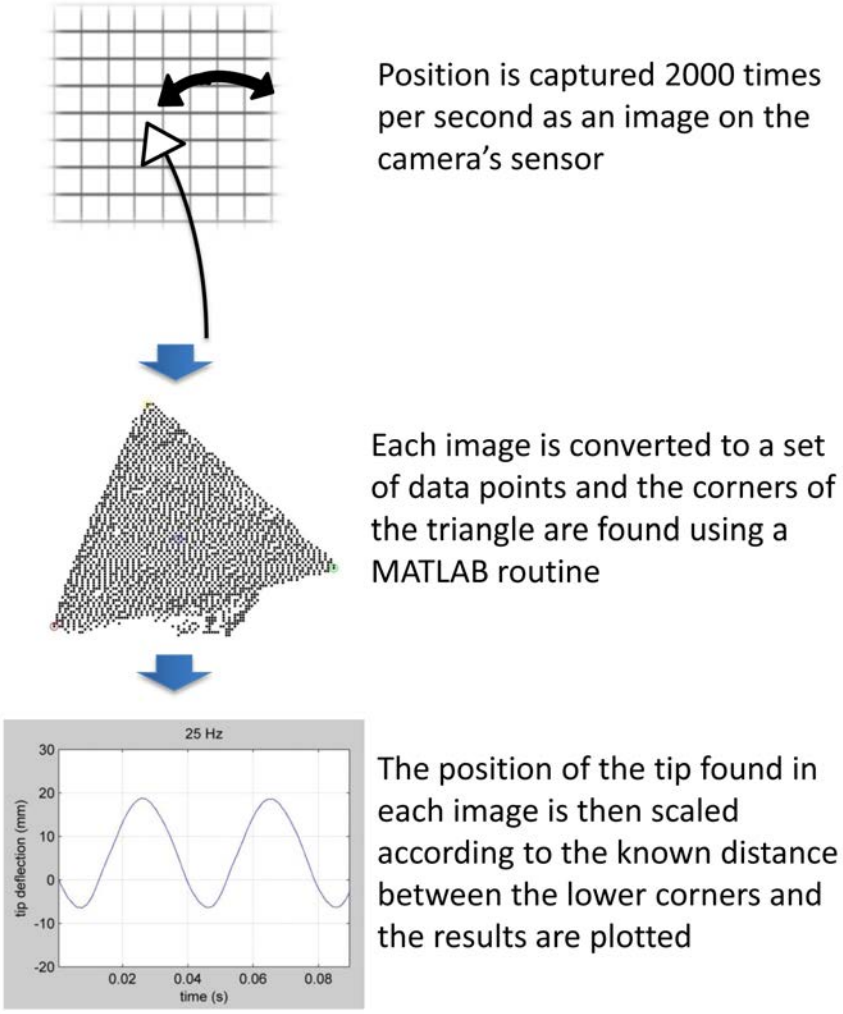

Figure C-2. Unimorph dynamics post-processing.

C.3 Results

The results of the high speed dynamic tests and the subsequent MATLAB analysis are shown in Figs. C-3 and C-4. The 1 Hz response is an ideal example of the natural

www.manaraa.com

frequency of the unimorph, where the small oscillations are an artifact of the natural frequency and the large displacement is commanded by applying the change in voltage. This is apparent in the 5 Hz plot as well, but is less evident in the other plots. The tip displacement is highest at 23.3 Hz, which is the natural frequency, and then begins to decrease as the frequency increases. From these results, it can be concluded that the MFCs can be actuated on the order of 20 Hz or more, with higher frequencies dependent on the natural frequency of the overall structure.

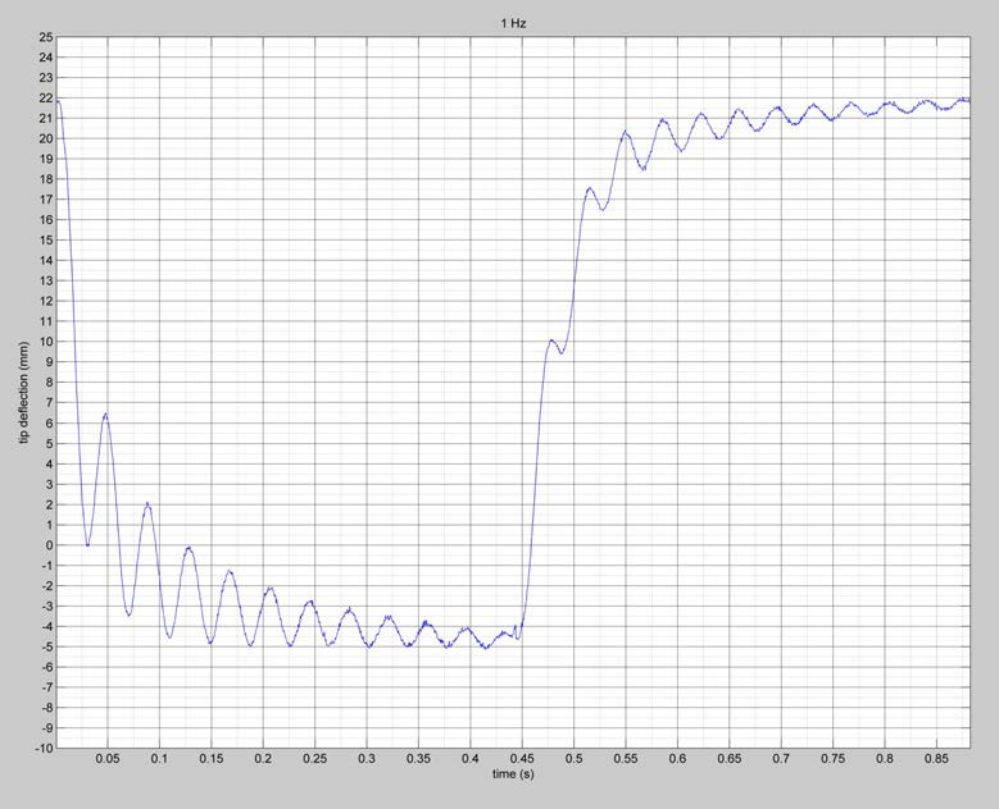

Figure C-3. M8528-P1 unimorph dynamics for 1 cycle at 1 Hz.

www.manaraa.com

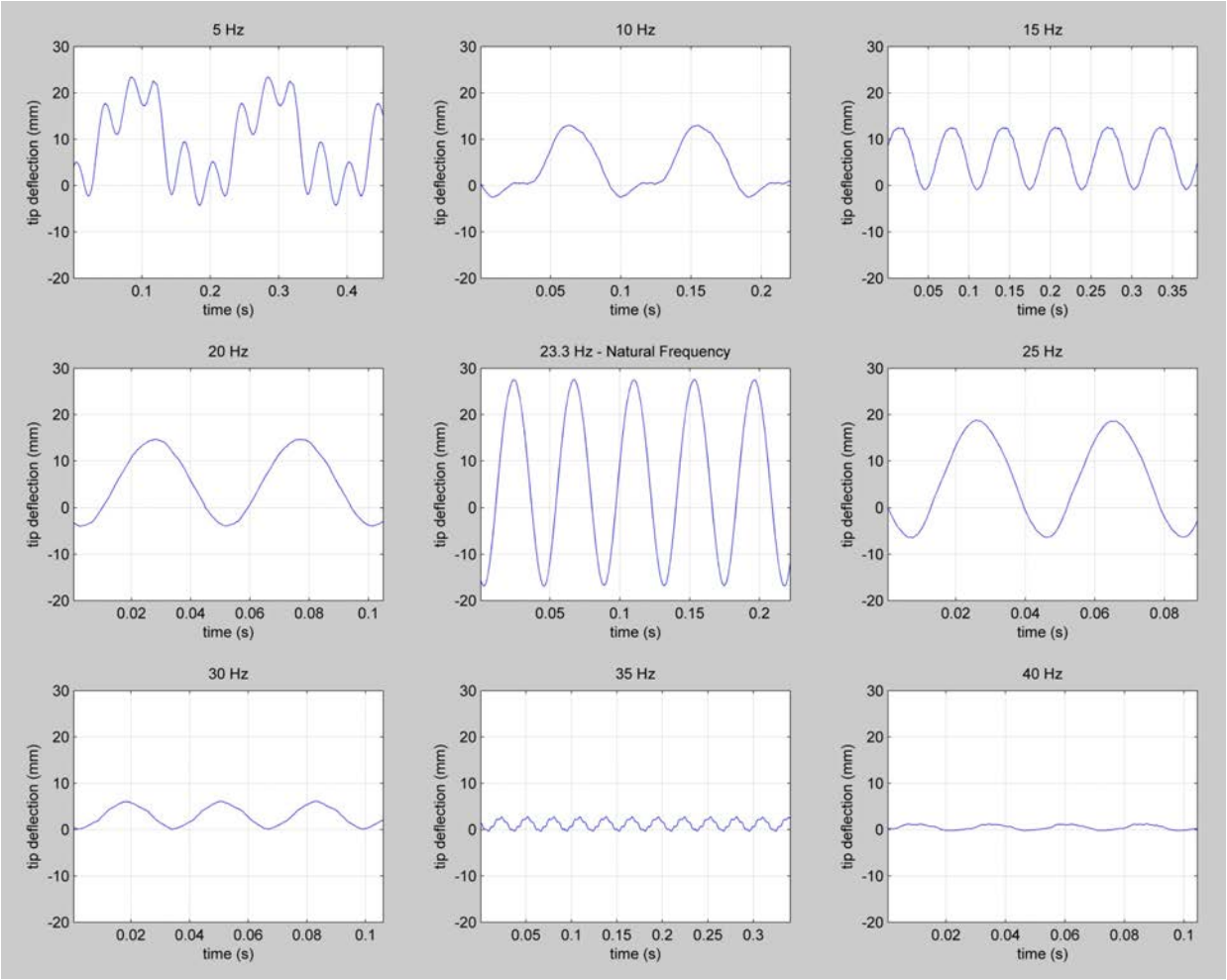

Figure C-4. M8528-P1 unimorph dynamics from 5-40 Hz.

www.manaraa.com

APPENDIX D
MFC1 AND MFC2 WORKBENCH COMPARISONS

D.1 MFC1

Included in this section are additional comparisons for the MFC1 aircraft. The figures compare the ABAQUS FEA model and the experimental tests completed with DIC. The setup and additional details are given in Section 9.6. A diagram explaining the loading direction, Fig. 9-10 can be found in Section 9.4.

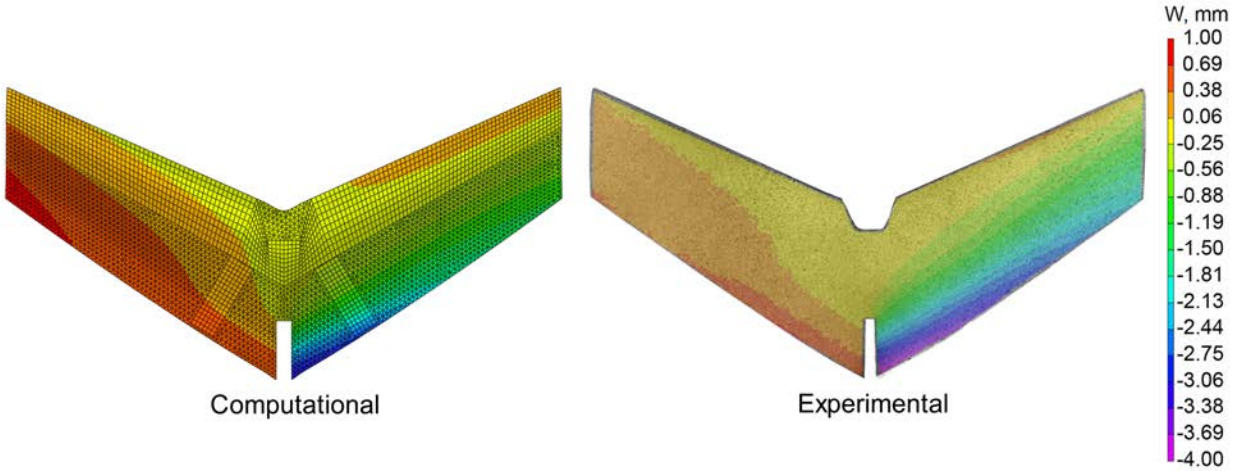

Figure D-1. MFC1 workbench comparison LV0000 RV0000 RPZ20.

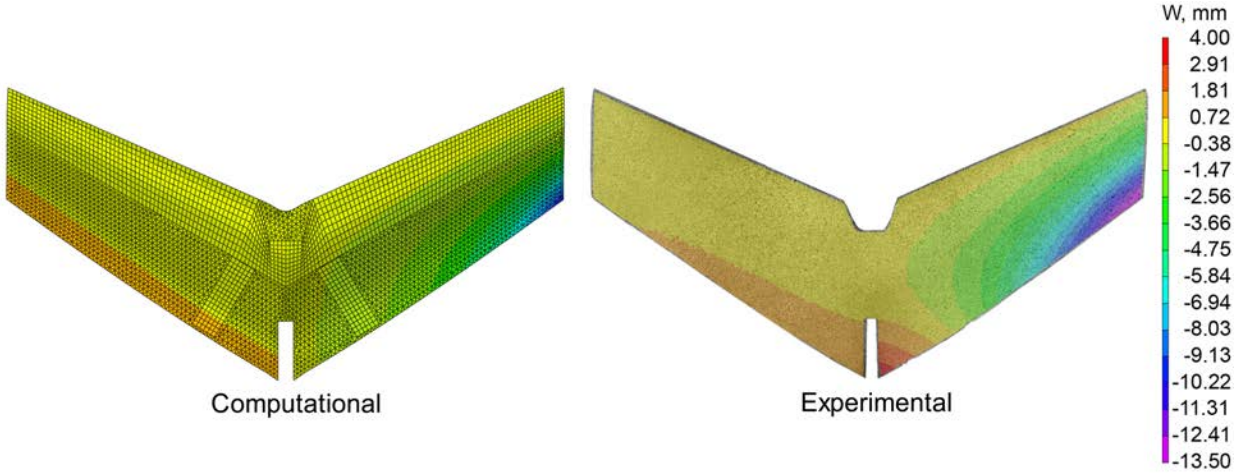

Figure D-2. MFC1 workbench comparison LV0000 RV0000 RTE20.

www.manaraa.com

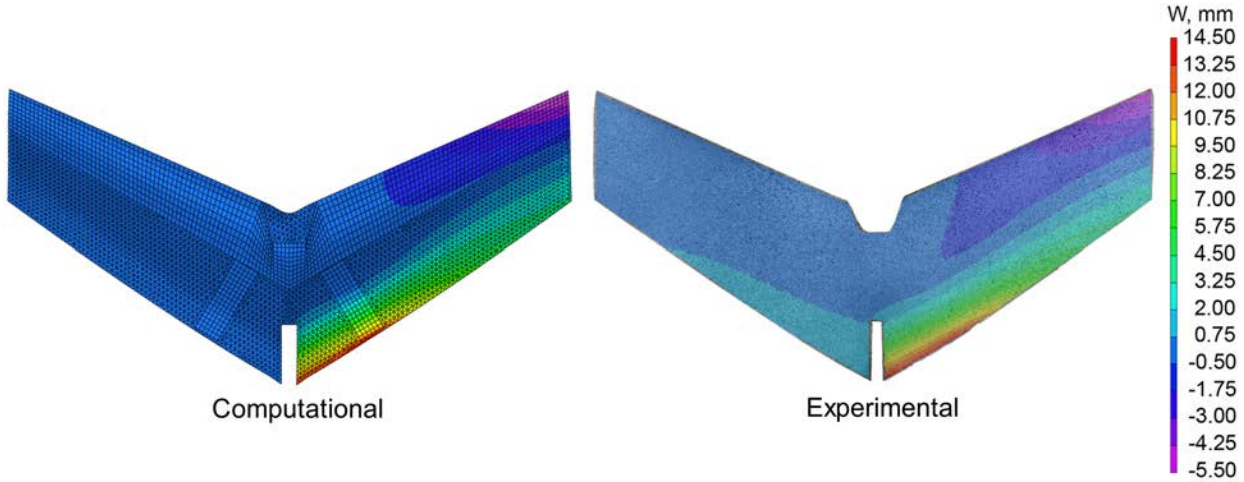

Figure D-3. MFC1 workbench comparison LV0000 RV1500 RLE100.

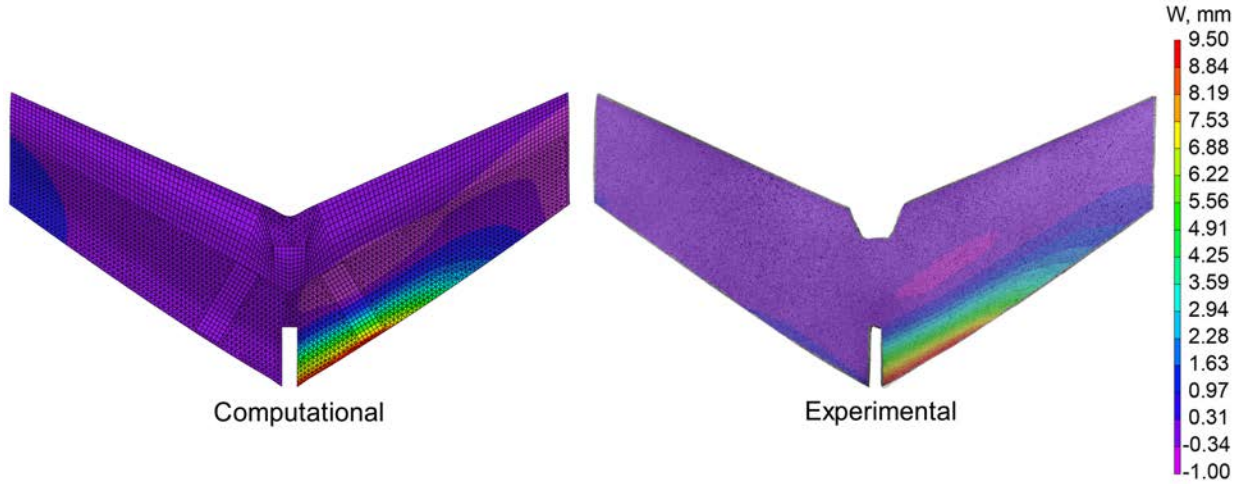

Figure D-4. MFC1 workbench comparison LV0000 RV1500 RPZ20.

www.manaraa.com

D.2 MFC2

Included in this section are additional comparisons for the MFC2 aircraft. The figures compare the ABAQUS FEA model and the experimental tests completed with DIC. The setup and additional details are given in Section 9.6. A diagram explaining the loading direction, Fig. 9-10 can be found in Section 9.4.

D.2.1 No actuation

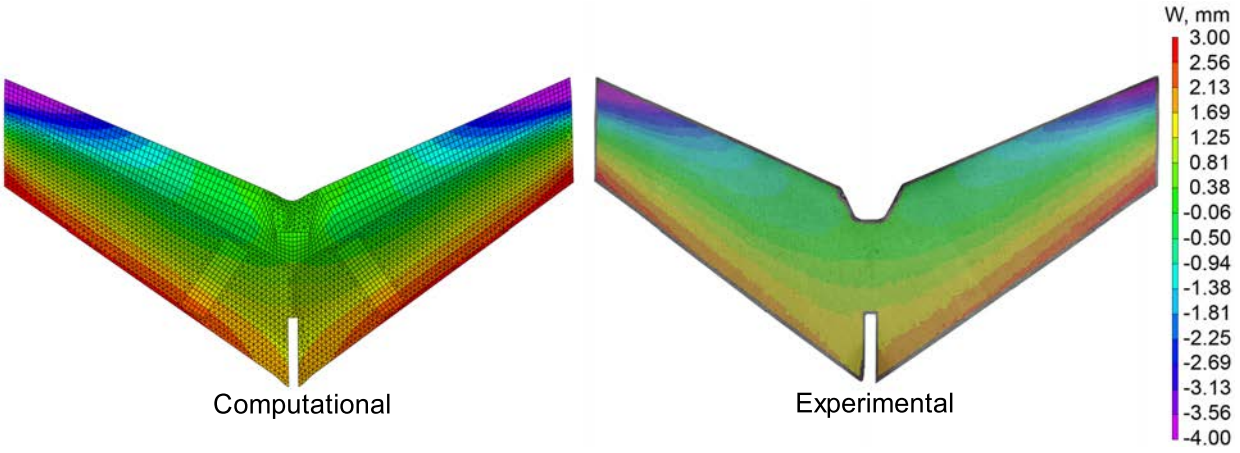

Figure D-5. MFC2 LV0000 RV0000 LLE100g RLE100g.

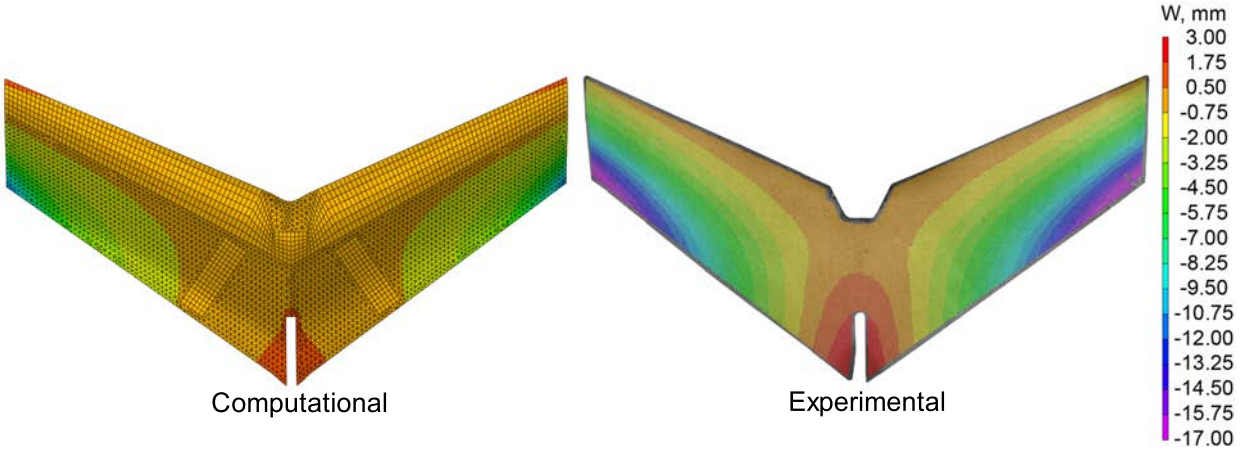

Figure D-6. MFC2 LV0000 RV0000 LTE20g RTE20g.

www.manaraa.com

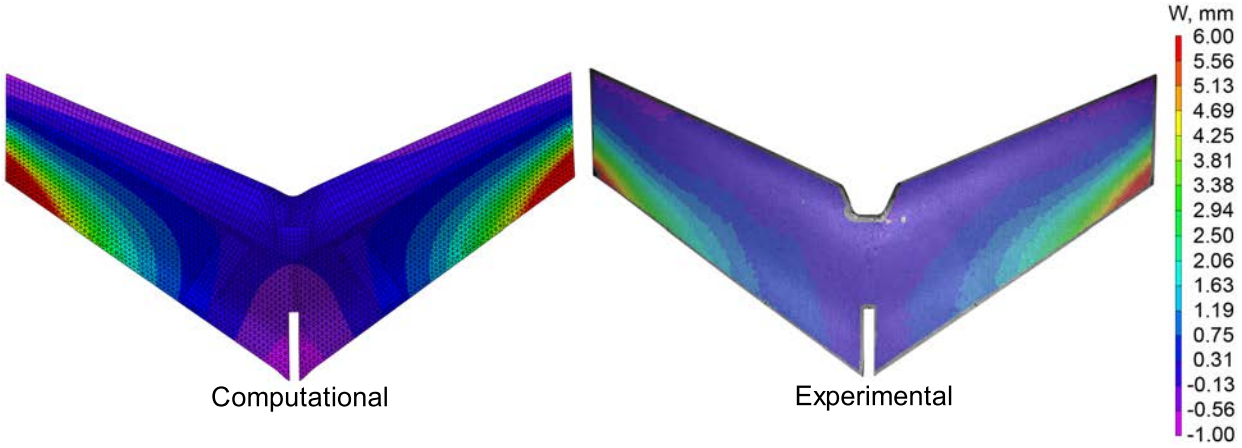

Figure D-7. MFC2 LV0000 RV0000 LTE-20g RTE-20g.

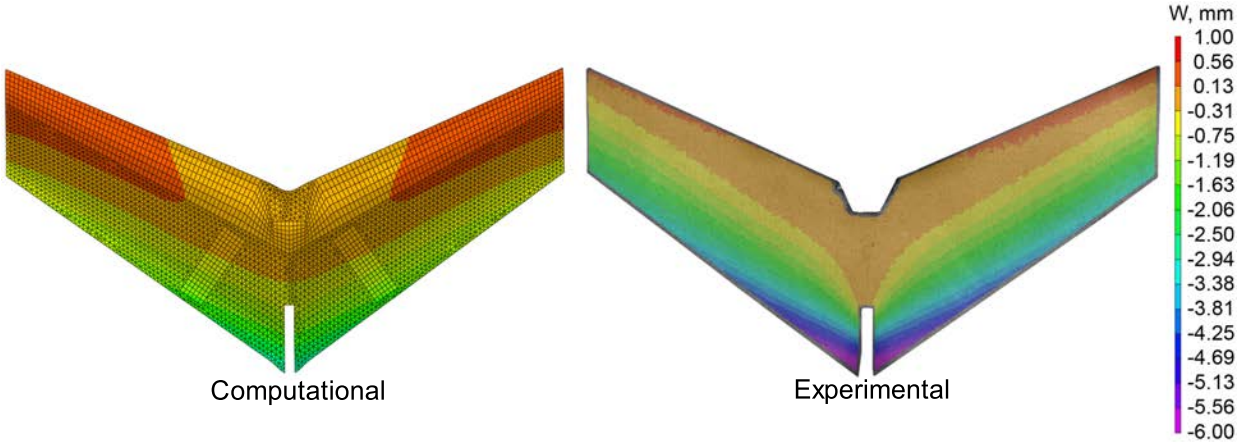

Figure D-8. MFC2 LV0000 RV0000 LPZ20g RPZ20g.

www.manaraa.com

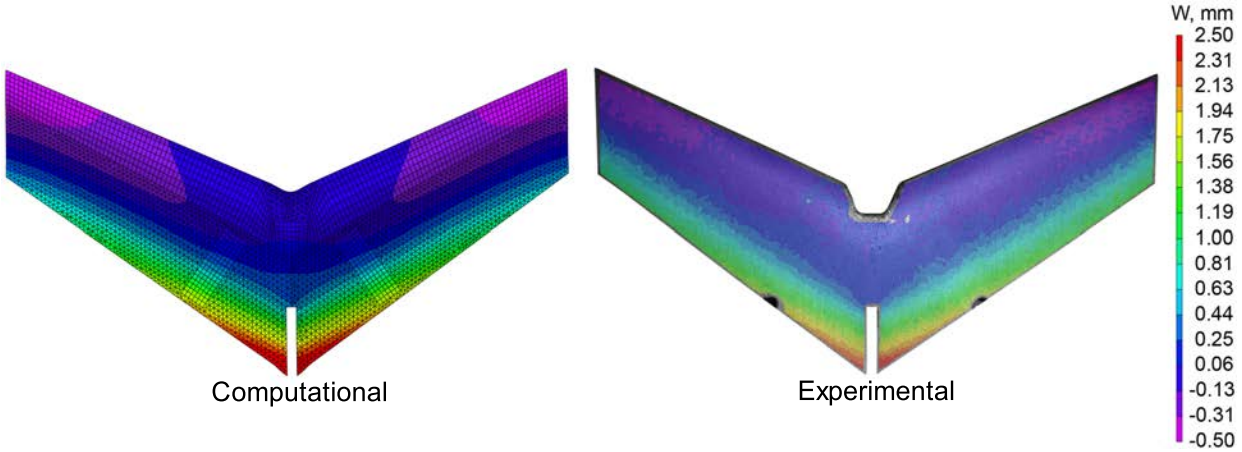

Figure D-9. MFC2 LV0000 RV0000 LPZ-20g RPZ-20g.

D.2.2 No load

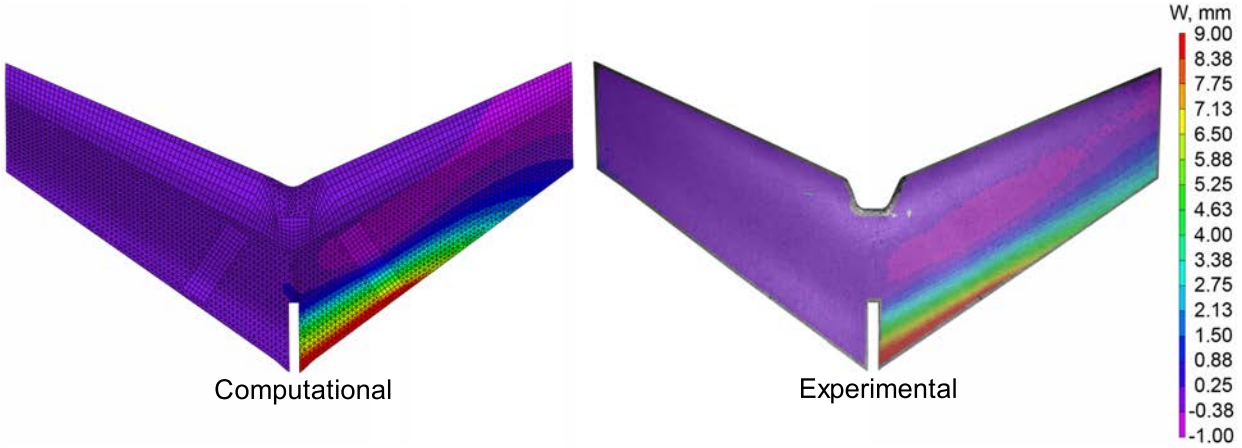

Figure D-10. MFC2 LV0000 RV1500.

www.manaraa.com

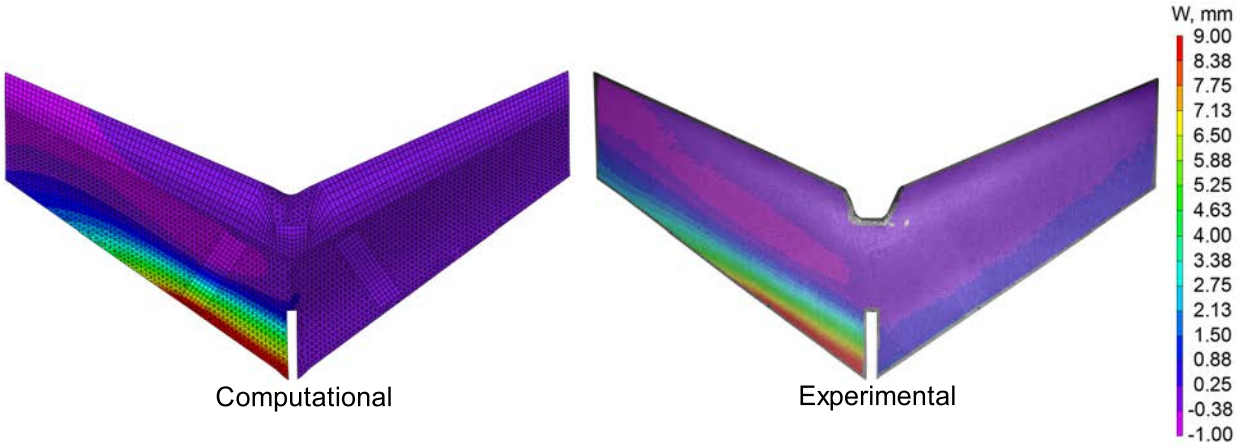

Figure D-11. MFC2 LV1500 RV0000.

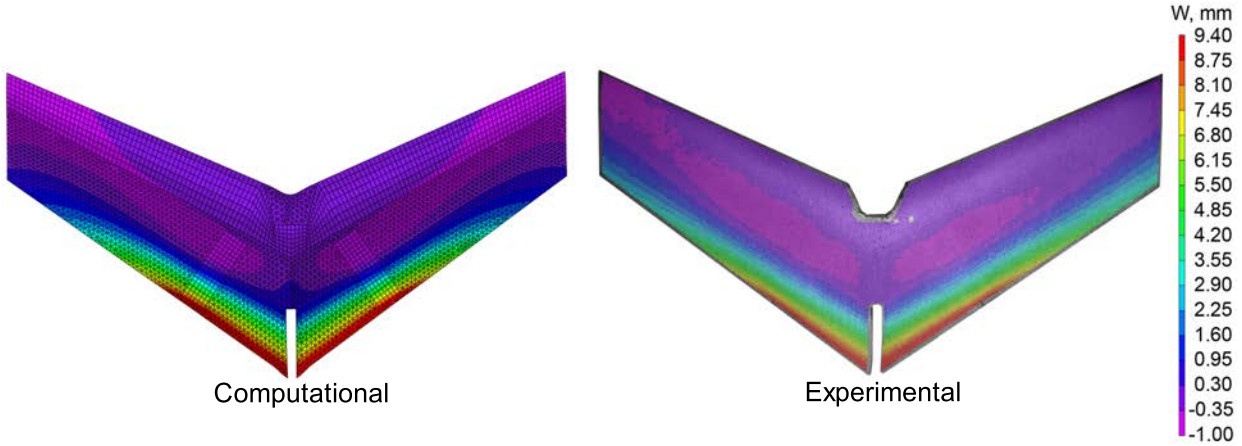

Figure D-12. MFC2 LV1500 RV1500.

www.manaraa.com

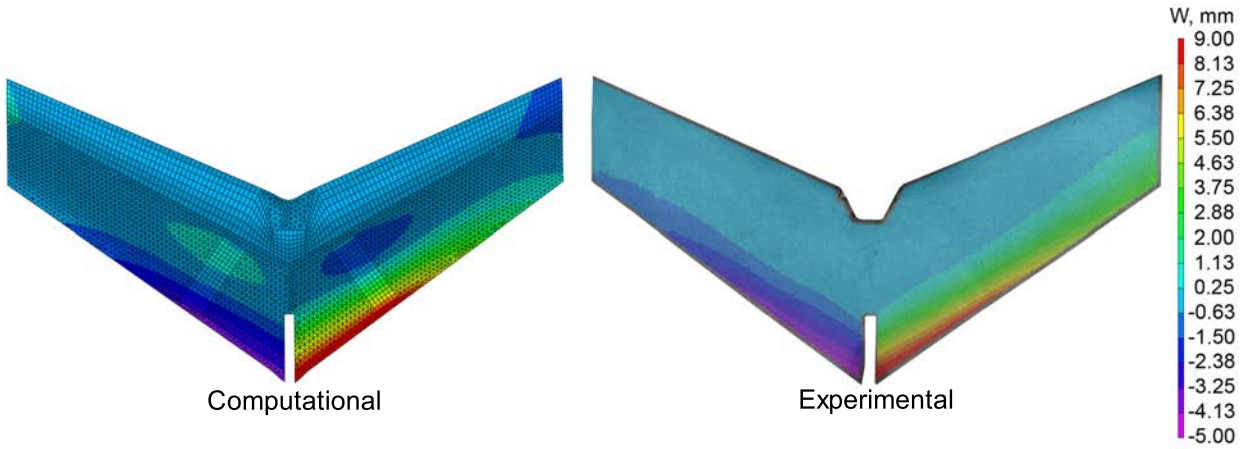

Figure D-13. MFC2 LV-500 RV1500.

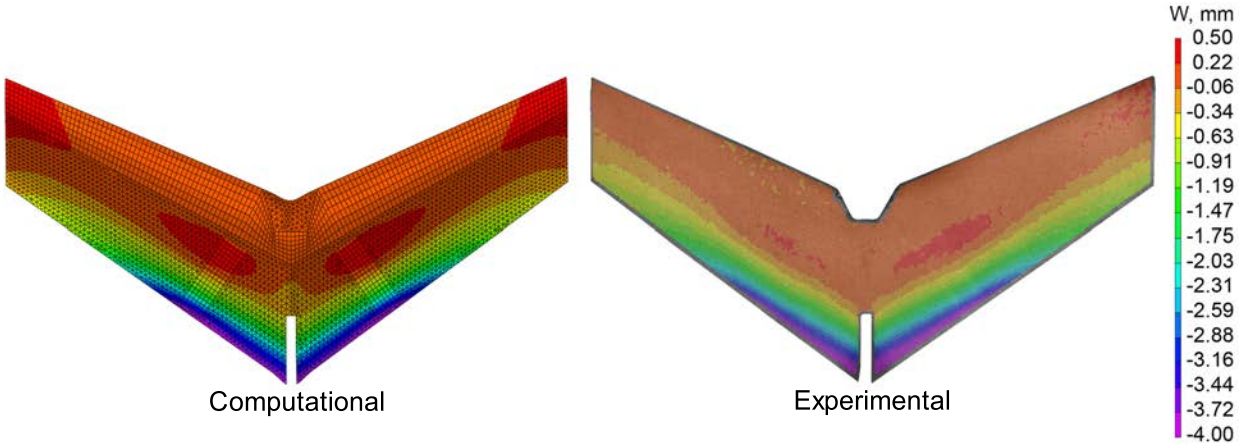

Figure D-14. MFC2 LV-500 RV-500.

www.manaraa.com

D.2.3 LV1500 RV1500

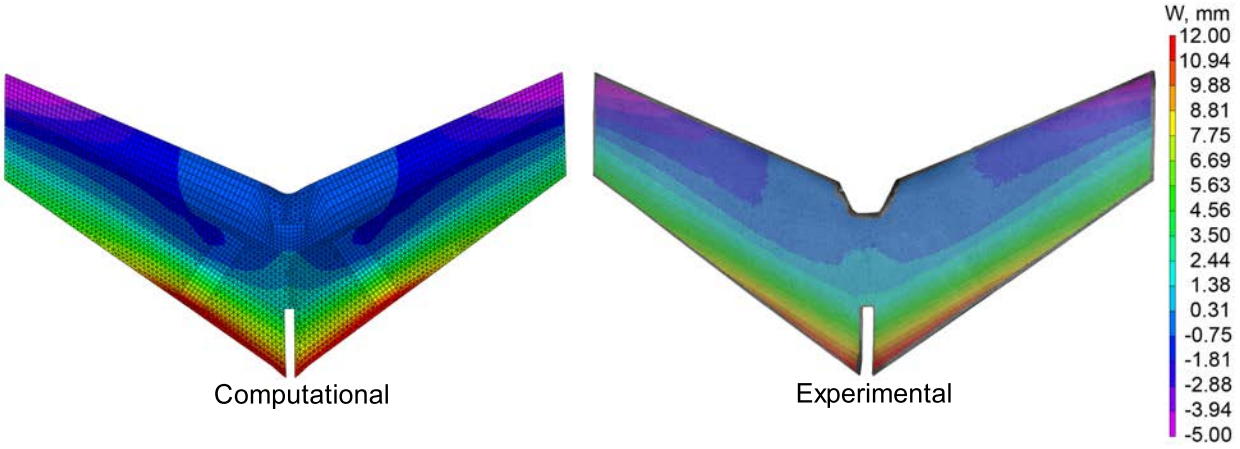

Figure D-15. MFC2 LV1500 RV1500 LLE100g RLE100g.

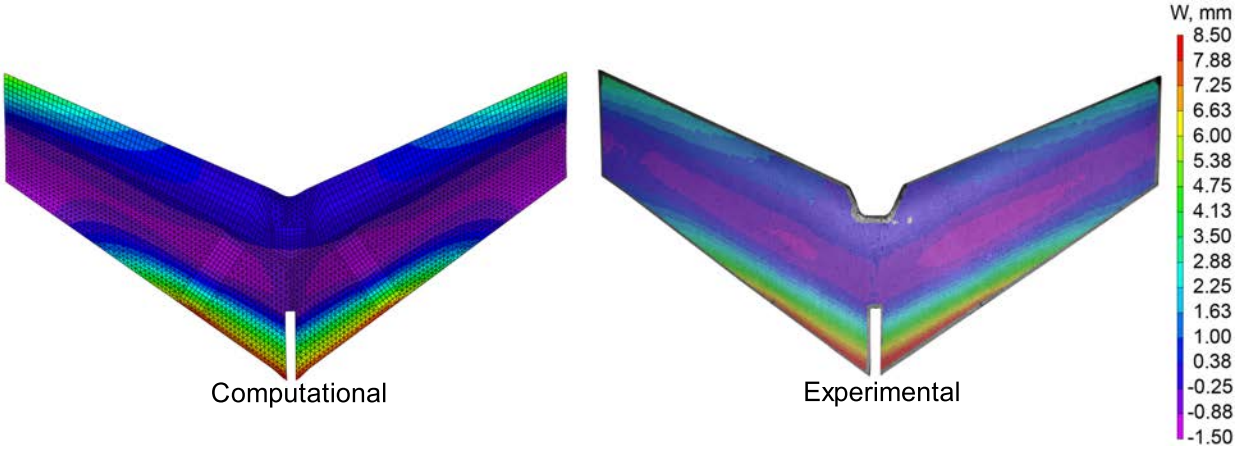

Figure D-16. MFC2 LV1500 RV1500 LLE-100g RLE-100g.

www.manaraa.com

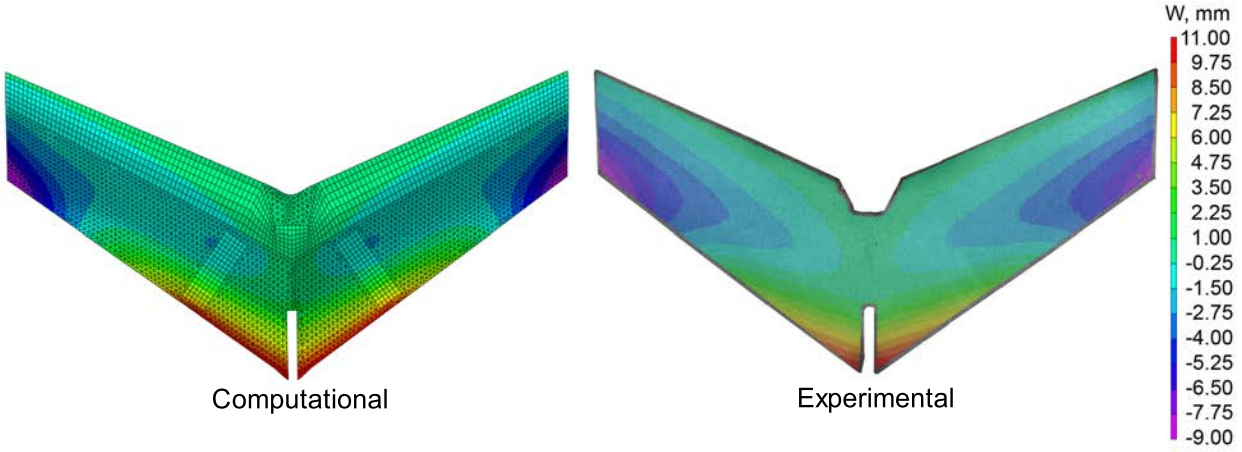

Figure D-17. MFC2 LV1500 RV1500 LTE20g RTE20g.

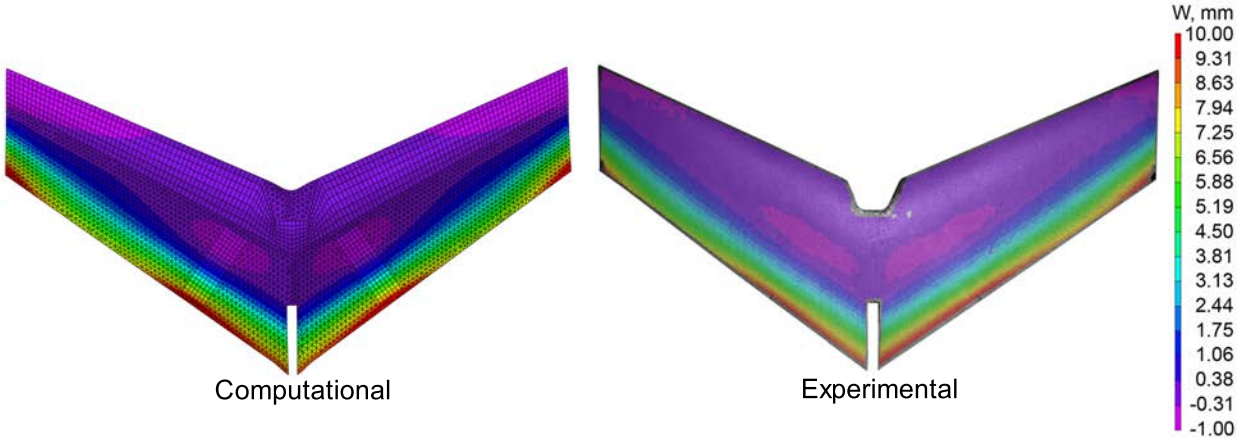

Figure D-18. MFC2 LV1500 RV1500 LTE-20g RTE-20g.

www.manaraa.com

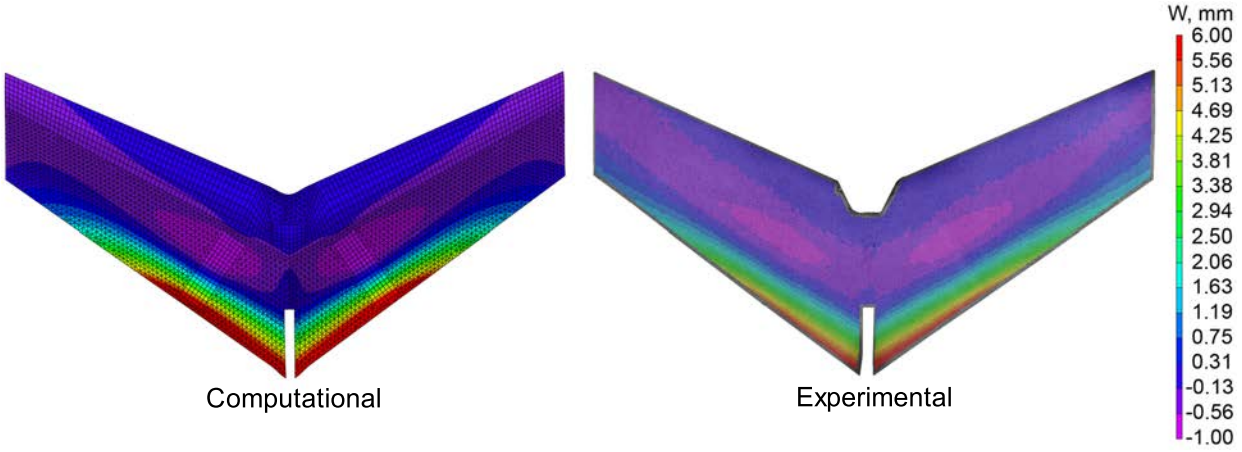

Figure D-19. MFC2 LV1500 RV1500 LPZ20g RPZ20g.

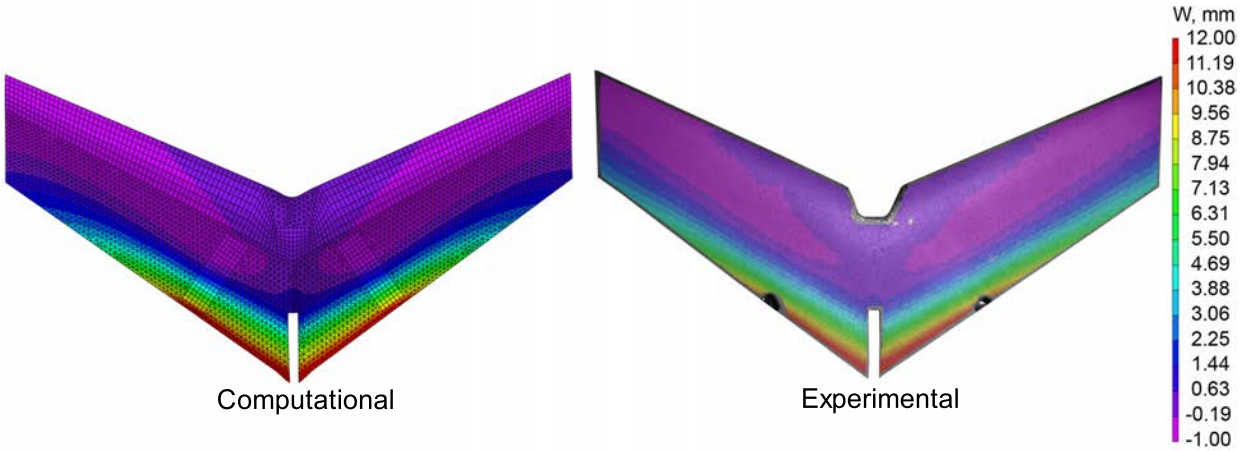

Figure D-20. MFC2 LV1500 RV1500 LPZ-20g RPZ-20g.

www.manaraa.com

D.2.4 LV-500 RV-500

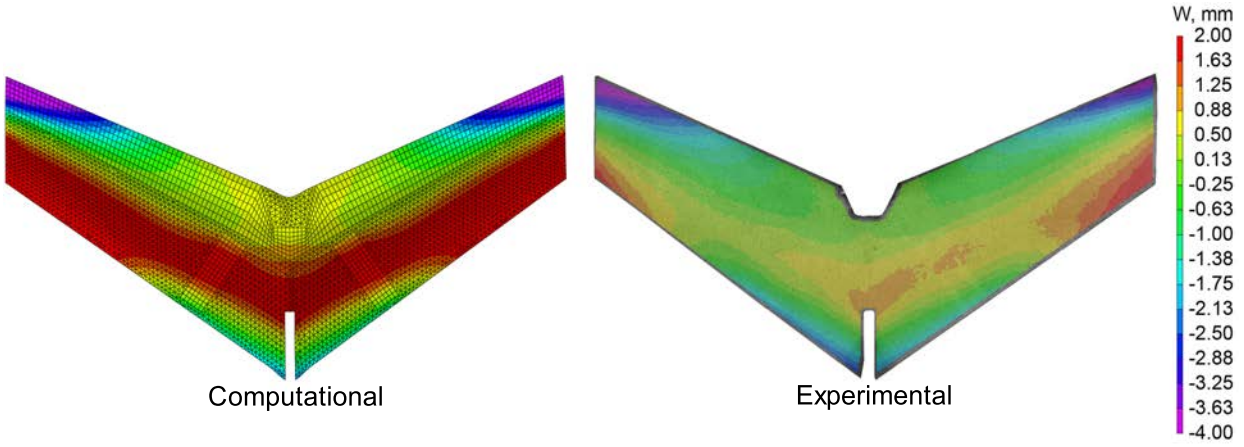

Figure D-21. MFC2 LV-500 RV-500 LLE100g RLE100g.

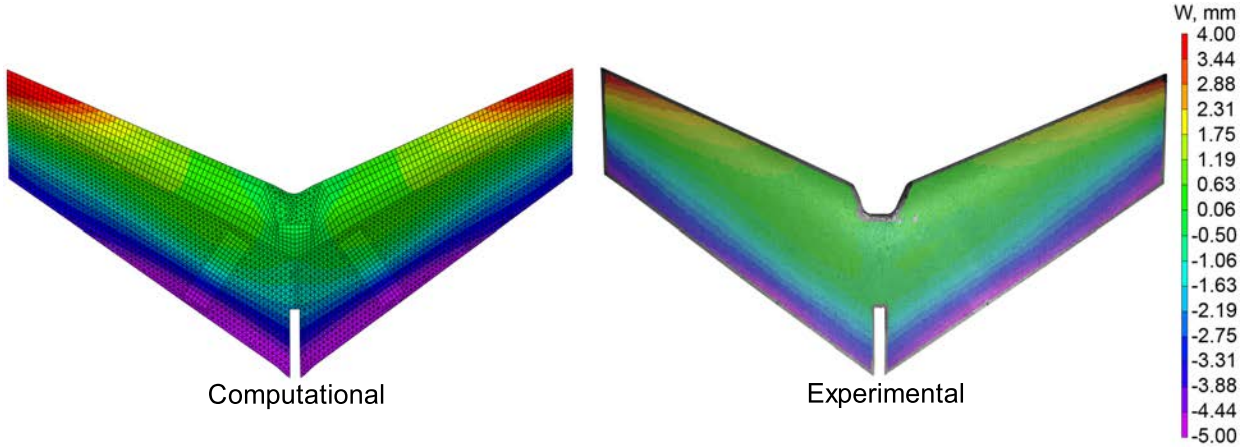

Figure D-22. MFC2 LV-500 RV-500 LLE-100g RLE-100g.

www.manaraa.com

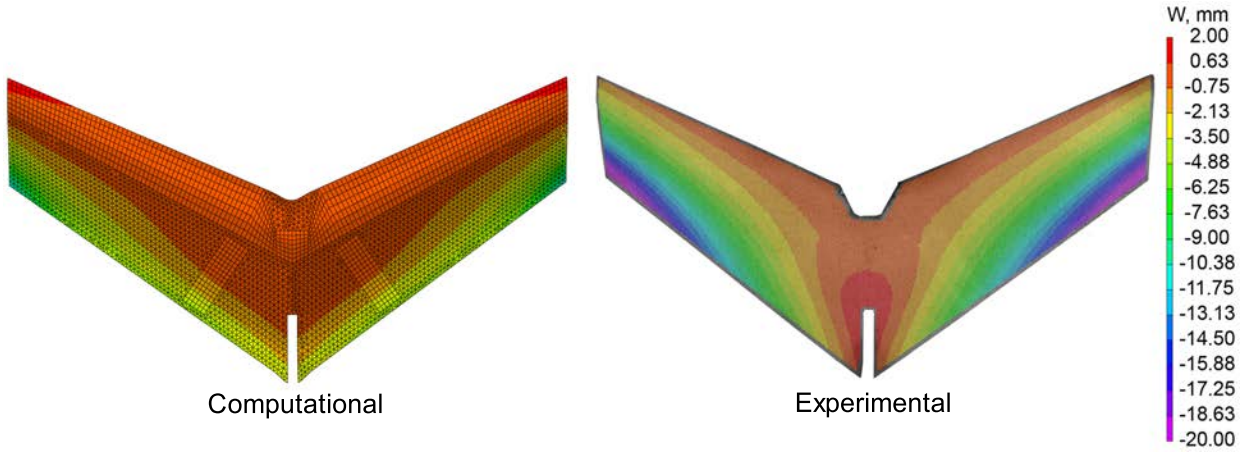

Figure D-23. MFC2 LV-500 RV-500 LTE20g RTE20g.

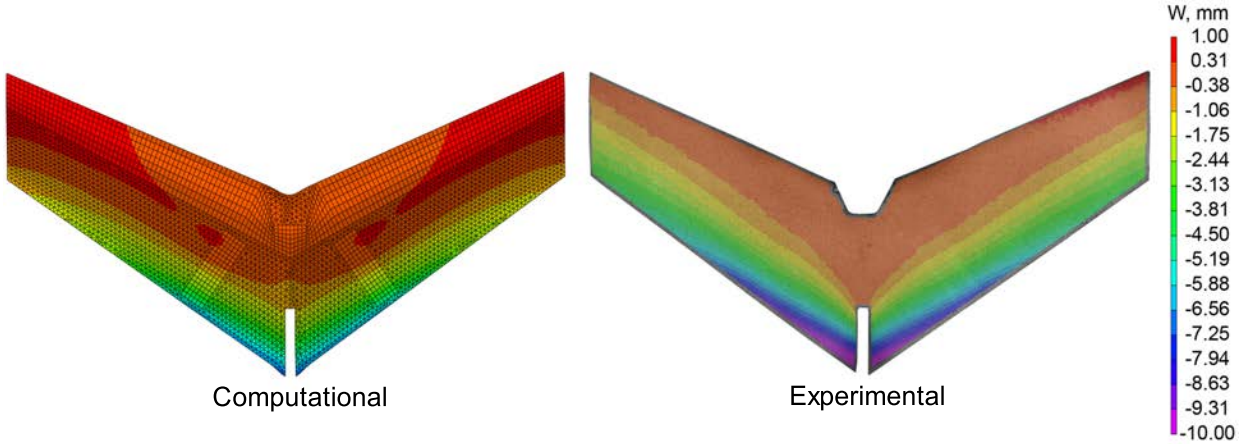

Figure D-24. MFC2 LV-500 RV-500 LPZ20g RPZ20g.

www.manaraa.com

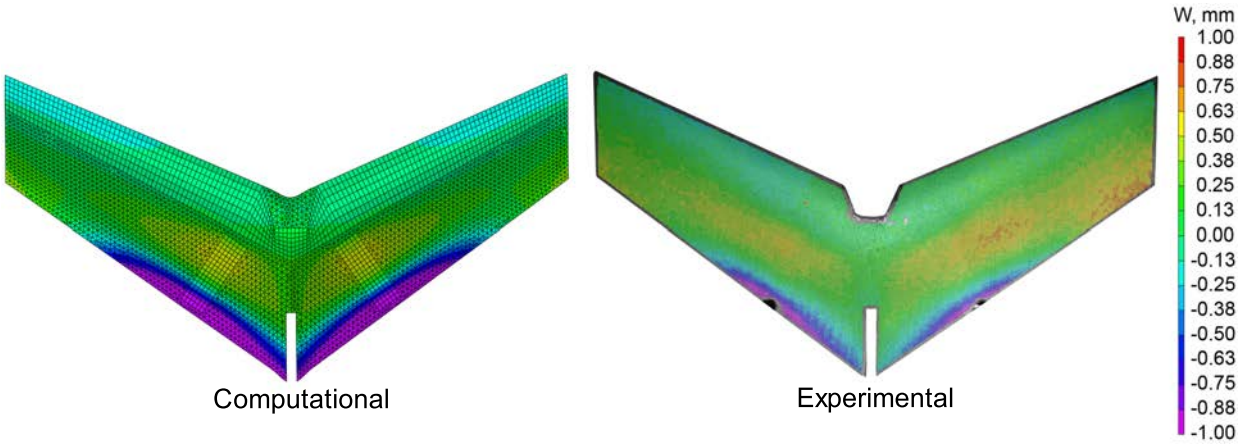

Figure D-25. MFC2 LV-500 RV-500 LPZ-20g RPZ-20g.

www.manaraa.com

D.2.5 Miscellaneous

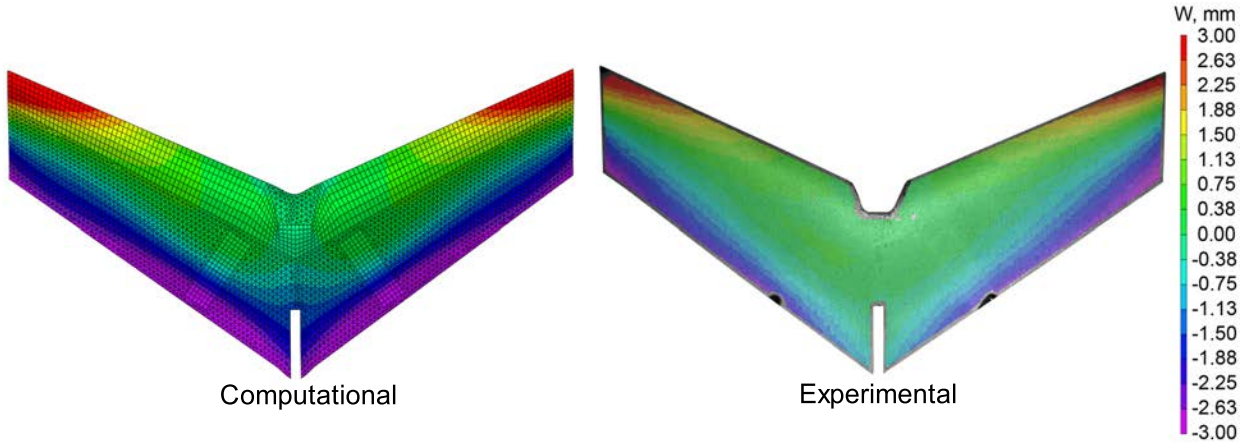

Figure D-26. MFC2 LV-500 RV-500 LPZ-20g RPZ-20g LLE-100g RLE-100g.

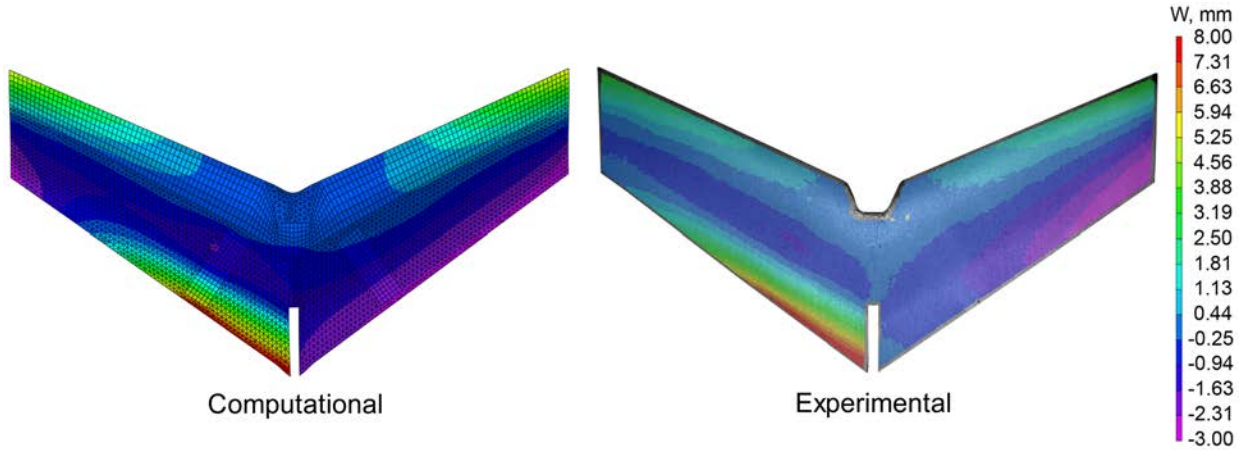

Figure D-27. MFC2 LV1500 RV0000 LLE-100g RLE-100g.

www.manaraa.com

APPENDIX E
MFC1 AEROELASTIC COMPARISONS

This section shows the comparison of the wind tunnel experimental results to the aeroelastic computer model. Additional details can be found in Section 10.3. Due to a failure of the left MFC, only the right side of the MFC1 model is actuated. Figure E-1 shows the results for the actuated wing under static conditions. As stated previously, the results from the unactuated, static conditions are used as a tare for the other cases.

The results in this first set of figures match up well. The results for the 15 m/s test conditions are shown in Fig. E-2. These results differ slightly more, most likely due to the finite element model not being able to model the battens on the MFC1 correctly. The results differ by about 3 mm in some parts of the model.

The fit was optimized and the RMS error for each configuration calculated, as described in Section 10.3. The RMS error is tabulated in Table E-1. As can be seen in the table, an average of slightly more than 45,000 points were analyzed to determine the quality of fit. The RMS error was less than 1 mm for all cases and averaged less than 0.5 mm for the group of configurations.

Table E-1. MFC1 quality of fit for each configuration tested.

Velocity, m/s	Configuration	Number of points	RMS error, mm
0	LV0000 RV0000	45736	0.65
	LV0000 RV1500	45558	0.23
	LV0000 RV-500	45702	0.27
15	LV0000 RV0000	45639	0.46
	LV0000 RV1500	45491	0.57
	LV0000 RV-500	45637	0.49

www.manaraa.com

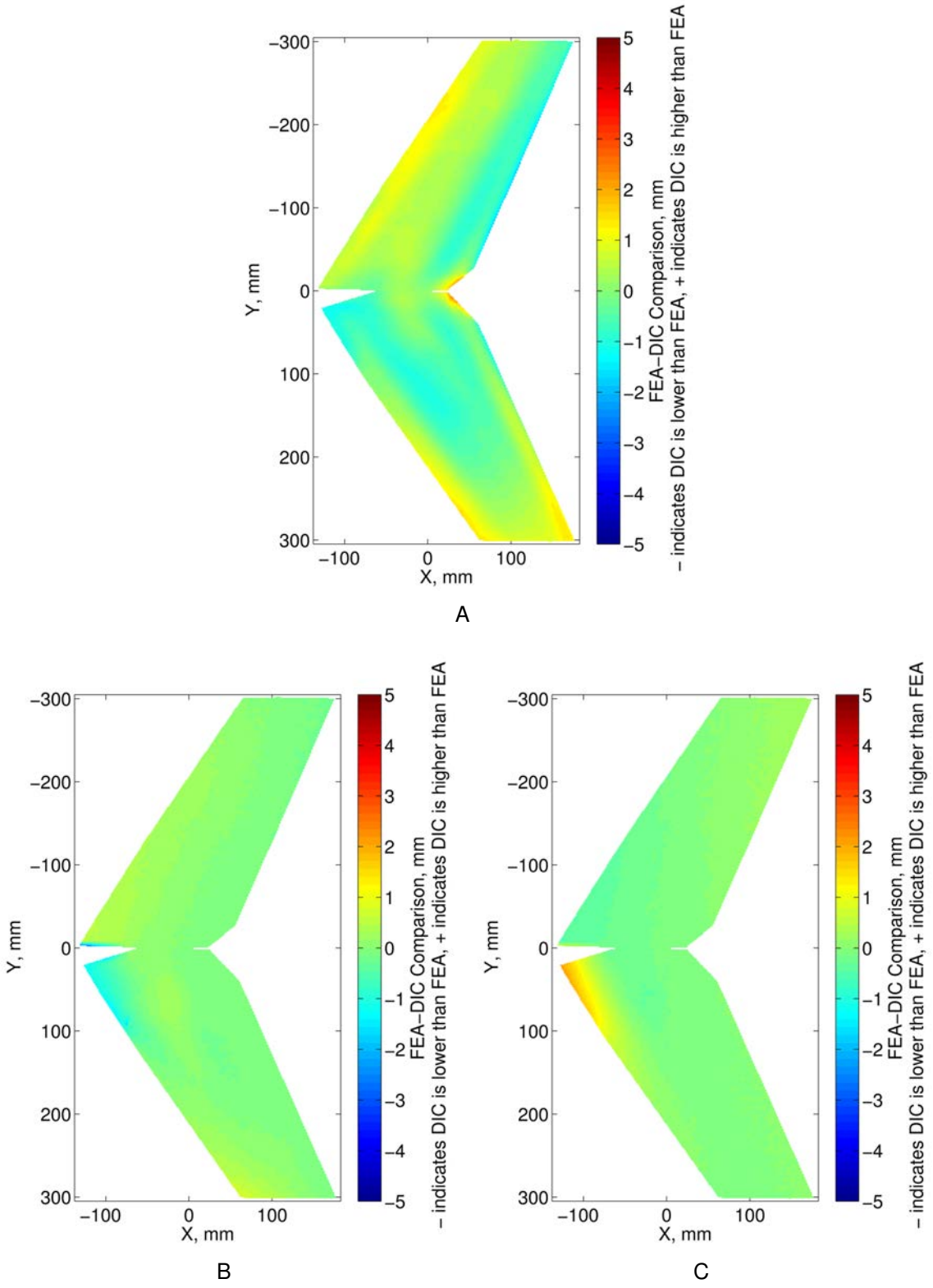

Figure E-1. Comparison of the MFC1 finite element model to the experimental results under static conditions. A) no actuation. B) actuated to LV0000 and RV1500. C) actuated to LV0000 and RV-500.

www.manaraa.com

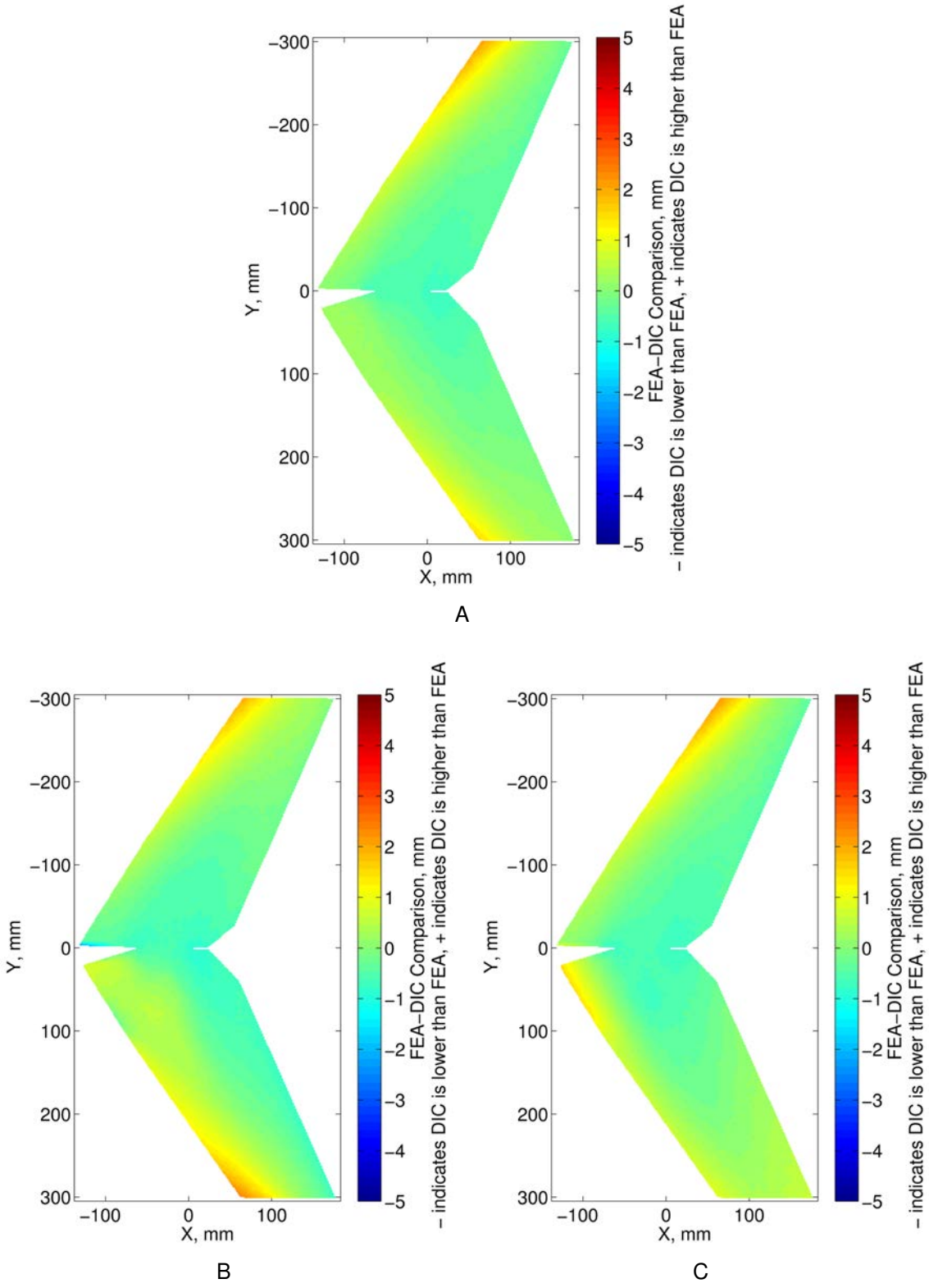

Figure E-2. Comparison of the MFC1 finite element model to the experimental results at 15 m/s. A) no actuation. B) actuated to LV0000 and RV1500. C) actuated to LV0000 and RV-500.

www.manaraa.com

APPENDIX F
SMART MATERIALS CORPORATION'S MFC ENGINEERING PROPERTIES

High-field (|E |>1 kV/mm), biased-voltage-operation piezoelectric constants:		
d33*	4.6E+02 pC/N	4.6E+02 pm/V
d31**	-2.1E+02 pC/N	-2.1E+02 pm/V

Low-field (|E |<1 kV/mm), biased-voltage-operation piezoelectric constants:		
d33*	4.0E+02 pC/N	4.0E+02 pm/V
d31**	-1.7E+02 pC/N	-1.7E+02 pm/V
Free-strain* per volt (low-field - high-field) for d33 MFC(P1)	~0.75-0.9 ppm/V	~0.75-0.9ppm/V
Free-strain* per volt (low-field - high-field) for d31 MFC(P2)	~0.75-0.9 ppm/V	~0.75-0.9ppm/V
Free-strain hysteresis*	~0.2	~0.2
DC poling voltage, Vpol for d33 MFC (P1)	+1500 V	+1500 V
DC poling voltage, Vpol for d31 MFC (P2)	+360 V	+360 V
Poled capacitance @ 1 kHz, roomt temp, Cpol for d33 MFC (P1)	~0.42 nF/cm^2	~2.7 nF/in^2
Poled capacitance @ 1 kHz, roomt temp, Cpol for d31 MFC (P2)	~4.6 nF/cm^2	~29 nF/in^2

Orthotropic Linear Elastic Properties (constant electric field):		
Tensile modulus, E_1*	30.336 GPa	4.4E+06 psi
Tensile modulus, E_1**	15.857 GPa	2.3E+06 psi
Poisson's ratio, ν_{12}	0.31	0.31
Poisson's ratio, ν_{21}	0.16	0.16
Shear modulus, G_{12}***	5.515 GPa	8.0E+05 psi

* Rod direction

** Electrode direction

*** Rules-of-mixture estimate

www.manaraa.com

Operational Parameters:		
Maximum operational positive voltage, V_{max} for d33 MFC (P1)	+1500 V	+1500 V
Maximum operational positive voltage, V_{max} for d31 MFC (P2)	+360 V	+360 V
Maximum operational negative voltage, V_{max} for d33 MFC (P1)	-500 V	-500 V
Maximum operational negative voltage, V_{max} for d31 MFC (P2)	-60 V	-60 V
Linear-elastic strain limit	1000 ppm	1000 ppm
Maximum operational tensile strain	$<$ 4500 ppm	$<$ 4500 ppm
Peak work-energy density	$\sim$6.9 $\mathrm{m \cdot MN/m^3}$	$\sim$1000 $\mathrm{in \cdot lb/in^3}$
Maximum operating temperature - Standard Version	$<$ 80°C	$<$ 176°F
Maximum operating temperature - High Temp Version	$<$ 130°C	$<$ 266°F
Operational lifetime (@ 1kVp-p, in cycles)	$>$ 10E+09	$>$ 10E+09
Operational lifetime (@ 2kVp-p, 500 VDC, in cycles)	$>$ 10E+07	$>$ 10E+07
Operational bandwidth as actuator, high electric field	0 Hz - 10 kHz	0 Hz - 10 kHz
at low electric field levels ($<$33% of max op. voltage)	0 Hz - 700 kHz	0 Hz - 700 kHz

Additional mechanical parameters		
Thickness of all MFC types	300 μm, $\pm$ 10%	12 mil $\pm$ 10%
Volume Density, active area	5.44 g/cm^3	0.197 lb/in^3
Area Density, active area	0.16 g/cm^2	0.328 lb/ft^2

www.manaraa.com

REFERENCES

[1] Lerner, E. K. L. L. and Wilmoth, B., *World of Earth Science*, 2003.

[2] Heywang, W. and Cross, L., *Piezoelectricity*, Vol. 29, Springer Berlin Heidelberg, Sept. 2012.

[3] Worden, K., Bullough, W., and Haywood, J., *Smart Technologies*, World Scientific, 2003.

[4] Cameron, K., Wyatt, R., Mellis, J., Al-Chalabi, S., and Brain, M., "Semiconductor Device and Piezoelectric Stack Optical Mounting Assembly," 1991.

[5] Morita, T., "Miniature piezoelectric motors," *Sensors and Actuators*, Vol. 103, No. 3, Feb. 2003, pp. 291–300.

[6] Uchino, K., *Piezoelectric Actuators and Ultrasonic Motors*, Kluwer Academic Publishers, Norwell, MA, 1997.

[7] Macro Fiber Composite Actuators, *Smart Materials Corp.*, http://www.smart-material.com [Retrieved 6 March 2013].

[8] Wilkie, W. K., Bryant, R. G., High, J. W., Fox, R. L., Hellbaum, R. F., Jalink, Jr., A., Little, B. D., and Mirick, P. H., "Low-cost piezocomposite actuator for structural control applications," *Smart Structures and Materials 2000: Industrial and Commercial Applications of Smart Structures Technologies*, No. 3991, Bremen, Germany, June 2000, pp. 323–334.

[9] Sosnicki, O. and Barillot, F., "Active damping of vibrations applied on ski structures," *Proceedings of the 10th International Conference on New Actuators*, 2006, pp. 932–935.

[10] Bowen, C., "Materials World," *Materials World*, May 2004, pp. 24–26.

[11] Daue, T. P., Kunzmann, J., and Schonecker, A., "Energy Harvesting Systems Using Piezo-electric Macro Fiber Composites," Tech. rep., Smart Material Corp., 1990 Main Street, Suite 750, Sarasota, FL 34236, USA, 2008.

[12] Wilkie, W., Belvin, W., and Park, K., "Aeroelastic analysis of helicopter rotor blades incorporating anisotropic piezoelectric twist actuation," *ASME 1996 World Congress and Exposition, Adaptive Structures Symposium, Proceedings, Aerospace Division*, 1996, pp. 1–11.

[13] Prechtl, E. and Hall, S., "Closed-loop vibration control experiments on a rotor with blade mounted actuation," *41st AIAA Structures, Structural Dynamics and Materials Conference*, Atlanta, GA, 2000, pp. 1–15.

www.manaraa.com

[14] Wickramasinghe, V. K. and Hagood, N. W., "Material characterization of active fiber composites for integral twist-actuated rotor blade application," *Smart Materials and Structures*, Vol. 13, No. 5, Oct. 2004, pp. 1155–1165.

[15] Moses, W., "Vertical Tail Buffeting Piezoelectric Actuators Alleviation Using - Some Results of the Actively Controlled Response Buffet-Affected Tails (ACROBAT) Program," Tech. rep., National Aeronautics and Space Administration - Langley Research Center, Hampton, VA, 1997.

[16] Moses, R., "Active vertical tail buffeting alleviation on an F/A-18 model in a wind tunnel," *Second Joint NASA/FAA/DOD Conference on Aging Aircraft*, Williamsburg, VA, 1998, pp. 1–10.

[17] Wickramasinghe, V., Chen, Y., and Zimcik, D., "Experimental Evaluation of an Advanced Buffet Suppression System on Full Scale F/A-18 Fin," *Journal of Aircraft*, Vol. 44, No. 3, May 2007, pp. 733–740.

[18] Matt, H., Bartoli, I., Salamone, S., Rizzo, P., di Scalea, F. L., Park, G., and Farrar, C., "Automated damage detection in UAV wing skin-to-spar joints based on outlier analysis of guided wave energy," *3rd European Workshop on Structural Health Monitoring*, 2006, pp. 1012–9.

[19] di Scalea, F. L., Matt, H., Bartoli, I., Coccia, S., Park, G., and Farrar, C., "Health Monitoring of UAV Wing Skin-to-spar Joints using Guided Waves and Macro Fiber Composite Transducers," *Journal of Intelligent Material Systems and Structures*, Vol. 18, No. 4, Dec. 2006, pp. 373–388.

[20] Williams, R. B. and Inman, D. J., "An Overview of Composite Actuators with Piezoelectric Fibers," *2002 IMAC-XX: Conference & Exposition on Structural Dynamics*, 2002, pp. 1–7.

[21] High, J. and Wilkie, W., *Method of fabricating NASA-standard macro-fiber composite piezoelectric actuators*, NASA, Langley Research Center, Hampton, Virginia, 2003.

[22] Williams, R. B. and Inman, D. J., *Nonlinear Mechanical and Actuation Characterization of Piezoceramic Fiber Composites*, Phd, Virginia Polytechnic Institute and State University, Blacksburg, VA, 2004.

[23] Jenkins, D. A., Shyy, W., Sloan, J., Klevebring, F., and Nilsson, M., "Airfoil Performance at Low Reynolds Numbers for Micro Air Vehicle Applications," *Thirteenth Bristol International RPV/UAV Conference, University of Bristol*, 1998.

[24] Grzywna, J. W., *A Flight Testbed with Virtual Environment Capabilities for Developing Autonomous Micro Air Vehicles*, Ph.D. thesis, University of Florida, 2004.

www.manaraa.com

[25] Kudva, J., Martin, C., Scherer, L., Jardine, A., McGowan, A., Lake, R., Sendeckyj, G., and Sanders, B., "Overview of the DARPA/AFRL/NASA Smart Wing Program," *SPIE Smart Structures and Materials*, Vol. 3674, 1999, pp. 230–236.

[26] Bilgen, O., Kurdila, A. J., Inman, D. J., Kochersberger, K., Wicks, A. L., and Composite, M. F., *Macro Fiber Composite Actuated Unmanned Air Vehicles : Design , Development , and Testing*, Masters, Virginia Polytechnic Institute and State University, Blacksburg, VA, 2007.

[27] Bilgen, O., Kochersberger, K., Diggs, E. C., Kurdila, A. J., and Inman, D. J., "Morphing Wing Micro-Air-Vehicles via Macro-Fiber- Composite Actuators," *48th AIAA/ASME/ASCE/AHS/ASC Structures, Structural Dynamics, and Materials Conference*, No. April, Honolulu, Hawaii, 2007, pp. 1–16.

[28] Bilgen, O. and Kochersberger, K., "Morphing Wing Aerodynamic Control via Macro-Fiber-Composite Actuators in an Unmanned Aircraft," *AIAA 2007 Conference and Exhibit*, Rohnert Park, California, 2007, pp. 1–17.

[29] Ohanian III, O., Hickling, C., and Stiltner, B., "Piezoelectric Morphing versus Servo-Actuated MAV Control Surfaces," *53rd AIAA/ASME/ASCE/AHS/ASC Structures, Structural Dynamics and Materials Conference*, Honolulu, Hawaii, 2012, pp. 1–18.

[30] Stanford, B., Ifju, P., Albertani, R., and Shyy, W., "Fixed membrane wings for micro air vehicles: Experimental characterization, numerical modeling, and tailoring," *Progress in Aerospace Sciences*, Vol. 44, No. 4, May 2008, pp. 258–294.

[31] Shyy, W., Ifju, P., and Viieru, D., "Membrane Wing-Based Micro Air Vehicles," *Applied Mechanics Reviews*, Vol. 58, No. 4, 2005, pp. 283.

[32] Vos, R., Barrett, R., Breuker, R. D., and Tiso, P., "Post-buckled precompressed elements: a new class of control actuators for morphing wing UAVs," *Smart Materials and Structures*, Vol. 16, No. 3, June 2007, pp. 919–926.

[33] Bramlette, R. B. and Leurck, R. F., "A Method for Control Surface Deflection Utilizing Piezoceramic Bimorph Actuators," *44th AIAA Aerospace Sciences Meeting and Exhibit*, No. January, Reno, Nevada, 2006, pp. 1–10.

[34] Barrett, R., Vos, R., Tiso, P., and Breuker, R. D., "Post-Buckled Precompressed(PBP) Actuators- Enhancing VTOL Autonomous High Speed MAVs," *46 th AIAA/ASME/ASCE/AHS/ASC . . .*, Vol. 3, Austin, TX, 2005, pp. 1–13.

[35] Drela, M. and Youngren, H., "Athena Vortex Lattice (AVL)," http://web.mit.edu/drela/Public/web/avl/ [Retrieved 8 January 2013].

[36] Gomez, J. C. and Garcia, E., "Morphing unmanned aerial vehicles," *Smart Materials and Structures*, Vol. 20, No. 10, Oct. 2011, pp. 103001.

www.manaraa.com

[37] Sofla, A., Meguid, S., Tan, K., and Yeo, W., "Shape morphing of aircraft wing: Status and challenges," *Materials & Design*, Vol. 31, No. 3, March 2010, pp. 1284–1292.

[38] Bilgen, O., Kochersberger, K. B., Inman, D. J., and Ohanian III, O. J., "Macro-Fiber Composite actuated simply supported thin airfoils," *Smart Materials and Structures*, Vol. 19, No. 5, May 2010, pp. 055010.

[39] Bilgen, O., Kochersberger, K. B., Inman, D. J., and Ohanian, O. J., "Novel, Bidirectional, Variable-Camber Airfoil via Macro-Fiber Composite Actuators," *Journal of Aircraft*, Vol. 47, No. 1, Jan. 2010, pp. 303–314.

[40] Bilgen, O., De Marqui, C., Kochersberger, K. B., and Inman, D. J., "Macro-Fiber Composite Actuators for Flow Control of a Variable Camber Airfoil," *Journal of Intelligent Material Systems and Structures*, Vol. 22, No. 1, Dec. 2010, pp. 81–91.

[41] Paradies, R. and Ciresa, P., "Active wing design with integrated flight control using piezoelectric macro fiber composites," *Smart Materials and Structures*, Vol. 18, No. 3, March 2009, pp. 035010.

[42] Wickramasinghe, V., Chen, Y., Martinez, M., Wong, F., and Kernaghan, R., "Design and verification of a smart wing for an extreme-agility micro-air-vehicle," *Smart Materials and Structures*, Vol. 20, No. 12, Dec. 2011, pp. 125007.

[43] Barrett, R., McMurtry, R., Vos, R., Tiso, P., and Breuker, R. D., "Post-buckled precompressed piezoelectric flight control actuator design, development and demonstration," *Smart Materials and Structures*, Vol. 15, No. 5, Oct. 2006, pp. 1323–1331.

[44] Barrett, R. and Vos, R., "Post-buckled precompressed subsonic micro-flight control actuators and surfaces," *Smart Materials and Structures*, Vol. 17, No. 5, Oct. 2008, pp. 055011.

[45] Vos, R., Gurdal, Z., and Abdalla, M., "Mechanism for Warp-Controlled Twist of a Morphing Wing," *Journal of Aircraft*, Vol. 47, No. 2, March 2010, pp. 450–457.

[46] Ohanian III, O. J., David, B. M., Taylor, S. L., Kochersberger, K. B., Probst, T., and Gelhausen, P. A., "Piezoelectric Morphing versus Servo-Actuated MAV Control Surfaces, Part II: Flight Testing," *51st AIAA Aerospace Sciences Meeting including the New Horizons Forum and Aerospace Exposition*, AIAA, Grapevine, TX, Jan. 2013, pp. 1–20.

[47] Yoon, K. J., Shin, S., Park, H. C., and Goo, N. S., "Design and manufacture of a lightweight piezo-composite curved actuator," *Smart Materials and Structures*, Vol. 11, No. 1, Feb. 2002, pp. 163–168.

www.manaraa.com

[48] Goo, N. S., "Validation of a Laminated Beam Model of LIPCA Piezoelectric Actuators," *Journal of Intelligent Material Systems and Structures*, Vol. 16, No. 3, March 2005, pp. 189–195.

[49] Lim, S. M., Lee, S., Park, H. C., Yoon, K. J., and Goo, N. S., "Design and demonstration of a biomimetic wing section using a lightweight piezo-composite actuator (LIPCA)," *Smart Materials and Structures*, Vol. 14, No. 4, Aug. 2005, pp. 496–503.

[50] Strelec, J. K., Lagoudas, D. C., Khan, M. A., and Yen, J., "Design and implementation of a shape memory alloy actuated reconfigurable airfoil," *Journal of Intellegent Material Systems and Structures*, Vol. 14, 2003, pp. 257–273.

[51] Garcia, H. M., *Control of Micro Air Vehicles using wing morphing*, Masters, University of Florida, 2003.

[52] Garcia, H., Abdulrahim, M., and Lind, R., "Roll control for a micro air vehicle using active wing morphing," *AIAA Guidance, Navigation, and Control Conference and Exhibit*, Austin, TX, Aug. 2003, pp. 1–10.

[53] Vos, R., Gurdal, Z., and Abdalla, M., "A Novel Mechanism for Active Wing Morphing," *49th AIAA/ASME/ASCE/AHS/ASC Structures, Structural Dynamics, and Materials Conference*, Schaumburg, IL, 2008.

[54] Vos, R. and Barrett, R., "Post-Buckled Precompressed Techniques in Adaptive Aerostructures: An Overview," *Journal of Mechanical Design*, Vol. 132, No. 3, 2010, pp. 031004.

[55] Ricci, S. and Terraneo, M., "Conceptual Design of an Adaptive Wing for a Three-surface Airplane," *46th AIAA/ASME/ASCE/AHS/ASC Structures, Structural Dynamics, and Materials Conference*, Austin, TX, 2005.

[56] Ricci, S., Scotti, A., and Terraneo, M., "Design , Manufacturing and Preliminary Test Results of an Adaptive Wing Camber Model," *47th AIAA/ASME/ASCE/AHS/ASC Structures, Structural Dynamics, and Materials Conference*, American Institute of Aeronautics and Astronautics, Newport, Rhode Island, May 2006, pp. 1–12.

[57] Bimetallic Strip Differential Bending, http://www.wolframalpha.com/entities/calculators/bimetallic%20strip%20differential%20bending/ri/25/7z/ [Retrieved 15 September 2011].

[58] Gibson, R. F., *Principles of Composite Material Mechanics*, CRC Press, Boca Raton, FL, 2nd ed., 2007.

[59] Paradies, R., Hertwig, M., and Elspass, W. J., "Shape Control of an Adaptive Mirror at Different Angles of Inclination," *Journal of Intelligent Material Systems and Structures*, Vol. 7, No. 2, March 1996, pp. 203–210.

www.manaraa.com

[60] Soykasap, O., "Micromechanical Models for Bending Behavior of Woven Composites," *Journal of Spacecraft and Rockets*, Vol. 43, No. 5, Sept. 2006, pp. 1093–1100.

[61] MFC Engineering Properties, *Smart Materials Corp.,* http://www.smart-material.com/MFC-product-main.html [Retrieved 25 August 2011].

[62] Q Series isolated proportional DC to HV DC converters, *EMCO High Voltage Corporation,* http://www.emcohighvoltage.com/pdfs/qseries.pdf [Retrieved 3 December 2011].

[63] Salichon, M. and Hall, R., "A Neuro-Evolutionary Approach to Micro Aerial Vehicle Control," *Proceedings of the 12th annual conference on genetic and evolutionary computation*, GECCO, Portland, Oregon, 2010, pp. 1123–1130.

[64] Jagdale, V. and Stanford, B., "Experimental Characterization of Load Stiffening Wing for Small UAV," *Experimental Characterization of Load Stiffening Wing for Small UAV*, No. Figure 2, Springfield, MA, 2007.

[65] Jagdale, V., Ifju, P., Stanford, B., and Albertani, R., "A Bendable Load Stiffened Wing for Small UAVs," *International Journal of Micro Air Vehicles*, Vol. 2, No. 4, Dec. 2010, pp. 239–253.

[66] Stewart, K., Wagener, J., Abate, G., and Salichon, M., "Design of the Air Force Research Laboratory Micro Aerial Vehicle Research Configuration," *Proceedings from the AIAA Aerospace Sciences Meeting*, Reno, Nevada, Jan. 2007.

[67] Grant, D. T., Abdulrahim, M., and Lind, R., "Design and analysis of biomimetic joints for morphing of micro air vehicles." *Bioinspiration & biomimetics*, Vol. 5, No. 4, Dec. 2010, pp. 045007.

[68] Stanford, B., Abdulrahim, M., Lind, R., and Ifju, P., "Investigation of Membrane Actuation for Roll Control of a Micro Air Vehicle," *Journal of Aircraft*, Vol. 44, No. 3, May 2007, pp. 741–749.

[69] Stewart, K., Abate, G., and Evers, J., "Flight Mechanics and Control Issues for Micro Air Vehicles," *AIAA Atmospheric Flight Mechanics Conference*, 2006.

[70] Claxton, D., *Development of a Parametric Software Tool for the Design and Manufacturing of Micro Air Vehicles*, Masters, University of Florida, 2007.

[71] Ifju, P., Jenkins, D., Ettinger, S., Lian, Y., and Shyy, W., "Flexible-Wing-Based Micro Air Vehicles," *40th AIAA Aerospace Sciences Meeting Exhibit*, Reno, NV, 2002, pp. 1–13.

[72] Abudaram, Y., Rohde, S., Hubner, J., and Ifju, P., "A Novel Method to Attach Membranes Uniformly on MAV Wings," *Proceedings of the SEM International Conference & Exposition on Experimental and Applied Mechanics*, Costa Mesa, California, USA, 2012.

www.manaraa.com

[73] Bikerman, J. J., *Causes of Poor Adhesion - Weak Boundary Layers*, Industrial and Engineering Chemistry, 1967.

[74] Zhang, D., Sun, Q., and Wadsworth, L. C., "Mechanism of corona treatment on polyolefin films," *Polymer Engineering & Science*, Vol. 38, No. 6, June 1998, pp. 965–970.

[75] Pamadi, B. N., *Performance, Stability, Dynamics, and Control of Airplanes*, American Institute of Aeronautics and Astronautics, 2nd ed., 2004.

[76] Wright, K., *Investigating the Use of Wing Sweep for Pitch Control of a Small Unmanned Air Vehicle*, Masters, University of California, San Diego, 2011.

[77] Bilgen, O., Kochersberger, K., and Inman, D., "Macro-fiber composite actuators for a swept wing unmanned aircraft," *Aeronautical Journal*, Vol. 113, No. 3337, 2009, pp. 385–395.

[78] Drela, M., "ASWING," 2010. http://web.mit.edu/drela/Public/web/aswing/ [Retrieved 24 October 2012].

[79] Jones, D. R., Schonlau, M., and William, J., "Efficient Global Optimization of Expensive Black-Box Functions," *Journal of Global Optimization*, Vol. 13, 1998, pp. 455–492.

[80] Jones, D. R., "A Taxonomy of Global Optimization Methods Based on Response Surfaces," *Journal of Global Optimization*, Vol. 21, 2001, pp. 345–383.

[81] Knowles, J. and Hughes, E. J., "Multiobjective Optimization on a Budget of 250 Evaluations," *Third International Conference, EMO 2005*, Guanajuato, Mexico, 2005, pp. 176–190.

[82] Knowles, J., "ParEGO: a hybrid algorithm with on-line landscape approximation for expensive multiobjective optimization problems," *IEEE Transactions on Evolutionary Computation*, Vol. 10, No. 1, Feb. 2006, pp. 50–66.

[83] Morgans, R. C., Zander, A. C., Hansen, C. H., and Murphy, D. J., "EGO shape optimization of horn-loaded loudspeakers," *Optimization and Engineering*, Vol. 9, No. 4, Nov. 2007, pp. 361–374.

[84] Queipo, N. V., Haftka, R. T., Shyy, W., Goel, T., Vaidyanathan, R., and Kevin Tucker, P., "Surrogate-based analysis and optimization," *Progress in Aerospace Sciences*, Vol. 41, No. 1, Jan. 2005, pp. 1–28.

[85] Schonlau, M., *Computer Experiments and Global Optimization*, Phd, University of Waterloo, 1997.

www.manaraa.com

[86] O'Donnell, Teresa H. Southhall, H., Santarelli, S., and Steyskal, H., "Applying EGO to large dimensional optimizations: a wideband fragmented patch example," *Evolutionary and Bio-Inspired Computation: Theory and Applications IV*, Orlando, FL, 2010.

[87] Southall, H. L., O'Donnell, T. H., and Derov, J. S., "Optimum design of antennas using metamaterials with the efficient global optimization (EGO) algorithm," *Evolutionary and Bio-Inspired Computation: Theory and Applications IV*, Orlando, FL, 2010.

[88] Viana, F. A. C. and Haftka, R. T., "Surrogate-based Optimization with Parallel Simulations using the Probability of Improvement," *13th AIAA/ISSMO Multidisciplinary Analysis Optimization Conference*, Fort Worth, Texas, Sept. 2010, pp. 1–14.

[89] Chaudhuri, A., Haftka, R. T., and Viana, F. A., "Efficient Global Optimization with Adaptive Target for Probability of Targeted Improvement," *53rd AIAA/ASME/ASCE/AHS/ASC Structures, Structural Dynamics and Materials Conference, 20th AIAA/ASME/AHS Adaptive Structures Conference*, AIAA, Honolulu, HI, April 2012, pp. 1–13.

[90] Sutton, M. A., *Springer Handbook of Experimental Solid Mechanics*, Department of Mechanical Engineering, Room 126, Latrobe Hall, The Johns Hopkins University, 3400 North Charles Street, Baltimore, MD 21218-2681, USA, 2008.

[91] Wu, P., Stanford, B., Bowman, W., Schwartz, A., and Ifju, P., "Digital Image Correlation Techniques for Full-Field Displacement Measurements of Micro Air Vehicle Flapping Wings," *Experimental Techniques*, Vol. 33, No. 6, Nov. 2009, pp. 53–58.

[92] Wu, P., Stanford, B., Bowman, W., Schwartz, A., and Ifju, P., "Full-Field Displacement Measurements of Micro Air Vehicle Flapping Wings Using Digital Image Correlation," *Proceedings of the XIth International Congress and Exposition*, Society for Experimental Mechanics, Inc., Orlando, FL, 2008.

[93] Wu, P., Stanford, B., and Ifju, P., "Insect-Inspired Flapping Wing Kinematics Measurements with Digital Image Correlation," *Proceedings of the SEM Annual Conference*, Society for Experimental Mechanics, Inc., Albuquerque, New Mexico, 2009.

[94] Wu, P. and Ifju, P., "Micro Air Vehicle Flapping Wing Effectiveness, Efficiency and Aeroelasticity Relationships," *48th AIAA Aerospace Sciences Meeting Including the New Horizons Forum and Aerospace Exposition*, Orlando, Florida, Jan. 2010.

www.manaraa.com

[95] Rue, J., Chang, K., Ifju, P., Haftka, R., Schmitz, T., McIntire, J., Tyler, C., Ganguly, V., and Chaudhuri, A., "Fabrication and Analysis of Small Flapping Wings," *Proceedings of the SEM International Conference & Exposition on Experimental and Applied Mechanics*, Society for Experimental Mechanics, Inc., Costa Mesa, California, USA, 2012.

www.manaraa.com

BIOGRAPHICAL SKETCH

Bradley's college career began at UF in Fall 2004. First slated towards mechanical engineering, he soon added aerospace engineering to pursue a dual degree. Spending several years in AIAA's Design Build Fly, he quickly learned various manufacturing, design, and testing techniques for small UAVs. He also gained significant commercial airplane experience during his three summer internships with The Boeing Company in the Seattle area.

Brad graduated with dual bachelor degrees in mechanical engineering and aerospace engineering in Spring 2009 and begun his graduate career in the Fall of 2009. His work has been mainly focused on solid mechanics with an application towards micro air vehicles. Through this research, he has gained extensive experience with composite layups, digital image correlation, material testing, and finite element modeling.

www.manaraa.com